Multiphysics modeling and experimental analysis of fiber-reinforced polymers across scales

Von der Fakultät für Bauingenieurwesen
der Rheinisch-Westfälischen Technischen Hochschule Aachen
zur Erlangung des akademischen Grades einer Doktorin der Ingenieurwissenschaften
genehmigte Dissertation

vorgelegt von

Marie-Christine Reuvers, M. Sc.

Berichter*innen: Prof. Dr.-Ing. habil. Stefanie Reese
Prof. Dr.-Ing. habil. Alexander Lion

Tag der mündlichen Prüfung: 20.06.2025

Für mich.

Acknowledgements

Diese kumulative Dissertation ist das Ergebnis meiner Arbeit als Wissenschaftliche Mitarbeiterin am Institut für Angewandte Mechanik (IFAM) an der RWTH Aachen University.

Mein besonderer Dank gilt Frau Prof. Dr.-Ing. Stefanie Reese für die Betreuung meiner Arbeit sowie die Möglichkeit, Teil ihres Aachener Teams sein zu dürfen. Ihre fachliche Expertise und das wissenschaftliche Umfeld, das Sie geschaffen haben, haben meine Arbeit und mich selbst wesentlich geprägt. Ein weiteres Dankeschön gilt Herrn Prof. Dr.-Ing. Alexander Lion für seine fortwährende Unterstützung, die wertschätzende Zusammenarbeit im Rahmen des Thermoformen-Projekts und die Bereitschaft, als Zweitgutachter meiner Dissertation zu fungieren. In diesem Zusammenhang möchte ich mich auch noch einmal ganz herzlich bei Michael Johlitz und Sameer Kulkarni bedanken. Die Zusammenarbeit zwischen unseren Instituten – sowohl fachlich als auch persönlich – im Rahmen des Thermoformen-Projekts hat mir großen Spaß gemacht. Vielen Dank euch beiden für die Unterstützung in den letzten Jahren – und ein ganz besonderer Dank an Sameer für die außergewöhnliche experimentelle Arbeit, die einen zentralen Beitrag zu meiner Dissertation geleistet hat. Schließlich gilt mein Dank auch Herrn Prof. Dr.-Ing. Sven Klinkel, der mich schon während der Masterarbeit begleitet hat und den Vorsitz meiner Promotionskommission übernommen hat.

Darüber hinaus möchte ich mich ganz herzlich bei Tim Brepols bedanken. Deine Unterstützung und deine konstruktive, stets wertschätzende Art der Zusammenarbeit sowie dein unglaublich tiefgehendes Fachverständnis haben meine Forschungsarbeit und das Institut maßgeblich geprägt. Ein weiterer Dank gilt Shahed Rezaei, ohne den ich wahrscheinlich schon im ersten Projekt aufgegeben hätte. Vielen Dank für die zahlreichen Cohesive Zone Diskussionen, deine fortwährende Unterstützung und besonders deine motivierenden Worte. Außerdem gilt ein riesiges Dankeschön allen meinen Kolleginnen und Kollegen am IFAM für die vielen großartigen Momente in den letzten Jahren – auch abseits der Arbeit. Während der Zeit am Institut hatte ich viele tolle Bürokollegen und -kolleginnen, aber wie man so schön sagt: Das Beste kommt zum Schluss. Vielen Dank, Ali, für dein offenes Ohr und die „konstruktiven Gespräche“, die den Arbeitsalltag deutlich angenehmer gemacht haben. Weiterhin hatte ich das Glück, viele tolle Studierende im Rahmen meiner Promotionszeit betreuen zu dürfen, die einen großen Anteil an meiner Forschungsarbeit hatten. Insbesondere möchte ich mich hier bei dir bedanken, Chris, für dein Vertrauen und das freundschaftliche Verhältnis, das sich aus der langjährigen Zusammenarbeit entwickelt hat.

Im Laufe der Jahre sind aus der gemeinsamen Arbeit tiefgehende Freundschaften entstanden – und das ist für mich das Beste, was mir diese Promotion gegeben hat. Vielen Dank an

Christian und Mirjam, dafür, dass ihr immer da seid. Für die gemeinsamen Abende, Urlaube und Samstage auf dem Markt (an dieser Stelle vielen Dank an Max für den Kaffee) und dafür, dass ihr die Hochs und Tiefs mit mir teilt. Meine beiden IFAMs Winest, Johanna und Katharina – wir kamen nie über Folge drei bei *Sex and the City* hinaus, weil wir uns so viel zu sagen haben. Danke euch beiden von Herzen für alles – ihr macht so vieles leichter und so vieles schöner. Mit Katharina kamen Alexander, Konstantin und Isabella in mein Leben – und damit die besten Desserts und ganz viel Freude. An dieser Stelle auch nochmal ein fachliches Danke an Katharina und Alexander, ohne eure Unterstützung wäre das Thermoformen-Beispiel ziemlich sicher nicht so schnell gelaufen.

Großer Dank gilt außerdem den Menschen, die mich schon längere Zeit begleiten und die ich glücklicherweise zu meinen besten Freunden zählen kann. Franzi, die mich – dank Cornelia – schon seit dem Studium begleitet: Vielen Dank für jedes Jahr *Tatsächlich...Liebe* und Raclette, für die gemeinsame Zeit und für Fabi, der mit dir im Paket kam – ihr seid Aachen für mich. Nicht zuletzt möchte ich mich von ganzem Herzen bei dir bedanken, Philipp, meinem Lieblingskarnevalisten. Vielen Dank dafür, dass es mit dir immer wie immer ist, ungeachtet der Zeit, die dazwischen liegt, *dich nicht zu mögen, ist nicht leicht*.

Abschließend möchte ich mich noch bei meiner Schwester Nina bedanken und bei meinen Eltern, für all die Möglichkeiten, die ich dank ihnen hatte und habe. Danke, Mama und Papa, dass ihr mich immer unterstützt und immer für mich da seid, ihr bedeutet mir alles!

Summary

Nowadays, the growing demand for cost-effective, customizable, and reusable materials in the domains of mobility and transport, as well as consumer goods, has led to an increased significance of fiber-reinforced thermoplastics (FRTPs). Nonetheless, the industrial processing of FRTPs in terms of (thermo-)forming processes is still associated with costly and time-consuming trial and error processes to adjust the material design and processing parameters. Still, oftentimes, unwanted deformations or even defects in the components arise due to thermal gradients and residual stresses within the material that need to be eliminated. In this context, numerical simulation tools, such as, for example, digital twins (i.e., the virtual representation of physical objects), can be employed in the conception and development phase of products and processes to improve efficiency, shorten development cycles, and identify potential error sources. In particular, the finite element method (FEM) has established itself as a suitable tool for the simulation of complex technical problems due to steadily increasing computational resources. The accuracy and reliability of the numerical predictions are, however, highly dependent on the quality of the employed material model. Thereby, the material behavior on the structural level is determined by the underlying microstructure and its associated characteristics. Especially fiber-reinforced semi-crystalline polymers (SCPs) represent a challenging material, due to their complex (time-dependent) inelastic deformations and dependencies on both the temperature and the temperature history. Consequently, the internal structure of FRTPs must be taken into account during model development by incorporating information across various scales.

Multiscale modeling schemes can provide valuable insights into the overall constitutive response of the material. However, these simulations are generally computationally expensive. In order to reduce the computational cost and develop frameworks suitable for industry applications, hierarchical approaches have been developed and applied. The objective, and simultaneously the challenge, is to reduce computational costs and experimental effort while preserving high accuracy and validity across a broad spectrum of process parameters.

The given cumulative dissertation comprises a collection of journal articles that contribute to the aforementioned research topics. It aims to develop a multiphysical framework for fiber-reinforced SCPs, including the impact of temperature and temperature history across various scales. Starting with the motivation and corresponding research-relevant questions, followed by an overview of the current literature.

In the first paper, a thermo-mechanically coupled constitutive model is developed for semi-crystalline polyamide 6 blends. Based on an extensive experimental data set, comprising me-

chanical and thermal tests, a visco-elastic, elasto-plastic approach is chosen in which nonlinear relaxation, strain hardening, and a tension-compression asymmetry in yielding are considered. The degree of crystallinity (DOC) serves as a constant input parameter, which significantly influences the material response.

Subsequently, a micromechanical and microthermal analysis is conducted in the second paper, employing the aforementioned matrix framework accompanied by a detailed experimental analysis of the composite's behavior at various temperatures. Thus, an experimental and virtual data base is generated for a wide range of process parameters.

The third paper's objective is to extend the aforementioned micromechanical matrix model to represent glass-fiber reinforced polyamide 6 on the macroscale. Therefore, mechanical and thermal anisotropy is incorporated into the framework and, subsequently, characterized with the data base from the second paper. The DOC is now treated as a non-constant internal variable depending on the temperature history. Finally, a full 3D thermoforming simulation is conducted. The validity of the presented approach is verified by comparison of the numerical material response with experimental data across all material scales.

Zusammenfassung

Die steigende Nachfrage nach kostengünstigen, individualisierbaren und wiederverwendbaren Materialien in den Bereichen Mobilität und Verkehr sowie Konsumgüter hat zu einem zunehmenden Interesse an faserverstärkten Thermoplasten geführt. Die industrielle Verarbeitung dieser Materialien in Form von Umformprozessen wie z.B Thermoformen ist hingegen immer noch mit kostspieligen und zeitaufwändigen Trial-and-Error-Prozessen zur Anpassung des Materialdesigns und der Prozessparameter verbunden. Oftmals kommt es dabei zu unerwünschten Verformungen oder gar Defekten in den Bauteilen aufgrund von thermischen Gradienten und Eigenspannungen im Material, die es zu beseitigen gilt. In diesem Zusammenhang können numerische Simulationswerkzeuge, wie z. B. digitale Zwillinge (d. h. die virtuelle Darstellung physischer Objekte), in der Konzeptions- und Entwicklungsphase von Produkten und Prozessen eingesetzt werden, um die Effizienz zu verbessern, Entwicklungszyklen zu verkürzen und potenzielle Fehlerquellen zu identifizieren. Insbesondere die Finite-Elemente-Methode (FEM) hat sich aufgrund der stetig wachsenden Rechenleistung moderner Computer als geeignetes Werkzeug für die Simulation komplexer technischer Probleme etabliert. Die Genauigkeit und Zuverlässigkeit der numerischen Vorhersagen sind jedoch in hohem Maße von der Qualität des verwendeten Materialmodells abhängig. Dabei wird das Materialverhalten auf der strukturellen Ebene durch die zugrunde liegende Mikrostruktur und deren Eigenschaften bestimmt. Insbesondere faserverstärkte teilkristalline Polymere stellen aufgrund ihrer komplexen (zeitabhängigen) inelastischen Verformungen und ihrer Abhängigkeit von der Temperatur und der Temperaturhistorie eine Herausforderung dar. Folglich muss die innere Struktur von faserverstärkten Thermoplasten durch die Einbeziehung von Informationen sowie die Modellentwicklung über verschiedene Skalen hinweg berücksichtigt werden.

Mehrskalige Modellierungsverfahren können an dieser Stelle wertvolle Einblicke in die konstitutive Reaktion des Materials liefern. Diese Simulationen sind jedoch im Allgemeinen sehr zeit- und rechenintensiv. Um die damit assozierten Kosten zu senken und für industrielle Anwendungen geeignete Frameworks zu entwickeln, wurden hierarchische Ansätze entwickelt und angewandt. Das Ziel und gleichzeitig die Herausforderung besteht darin, die Rechenkosten und den experimentellen Aufwand zu verringern und gleichzeitig eine hohe Genauigkeit und Gültigkeit des Modells über ein breites Spektrum von Prozessparametern zu erhalten.

Die vorliegende kumulative Dissertation umfasst eine Sammlung von Zeitschriftenartikeln, die zu den oben genannten Forschungsthemen beitragen. Sie zielt darauf ab, ein multiphysikalisches Framework für faserverstärkte teilkristalline Polymere zu entwickeln, das den Einfluss von Temperatur und Temperaturhistorie über verschiedene Skalen hinweg berücksichtigt. An-

gefangen mit der Motivation und den entsprechenden forschungsrelevanten Fragen, folgt ein Überblick über die aktuelle Literatur.

In der ersten Veröffentlichung wird ein thermo-mechanisch gekoppeltes konstitutives Modell für teilkristalline Polyamid 6-Blends entwickelt. Auf der Grundlage eines umfangreichen experimentellen Datensatzes, der mechanische und thermische Tests umfasst, wird ein viskoelastischer, elasto-plastischer Ansatz gewählt, bei dem nichtlineare Relaxation- und Verfestigungsprozesse sowie eine Zug-Druck-Asymmetrie in der Plastifizierung berücksichtigt werden. Der Kristallinitätsgrad dient dabei als konstanter Eingangsparameter, der die Materialreaktion erheblich beeinflusst.

Anschließend wird in der zweiten Veröffentlichung eine mikromechanische und mikrothermische Analyse durchgeführt, bei der das oben erwähnte Matrixmodell zusammen mit einer detaillierten experimentellen Analyse des Verhaltens des Verbundwerkstoffs bei verschiedenen Temperaturen verwendet wird. Auf diese Weise wird eine experimentelle und virtuelle Datenbasis für ein breites Spektrum von Prozessparametern geschaffen.

Ziel der dritten Veröffentlichung ist es, das oben erwähnte mikromechanische Matrixmodell zu erweitern, um glasfaserverstärktes Polyamid 6 auf der Strukturebene darzustellen. Dazu wird das Modell um mechanische und thermische Anisotropie erweitert und anschließend mit der Datenbank aus der zweiten Veröffentlichung charakterisiert. Der Kristallinitätsgrad geht nun als nicht konstante interne Variable in Abhängigkeit von der Temperaturhistorie ein. Abschließend wird eine vollständige 3D-Thermoformsimulation durchgeführt. Die Gültigkeit des vorgestellten Ansatzes wird durch den Vergleich der numerischen Materialantwort mit experimentellen Daten über alle Materialebenen hinweg verifiziert.

Contents

1 Introduction

1.1 Motivation

Nowadays, more and more often recyclability and reusability are key factors for the choice and design process of engineering materials, alongside increasing requirements for climate protection. Especially in the fields of mobility and transport as well as consumer goods, tailorable materials with a broad variety of constituents that allow for flexibility, weigth savings, and cost-effective mass production are increasingly sought-after. For these applications, fiber-reinforced polymers (FRPs), in particular thermoplastics, are extensively used due to their low weight in combination with good thermo-mechanical properties. However, despite their popularity in industry and cross-sector usage, the accurate prediction and performance of the manufacturing process, such as, for example, thermoforming, often remains a process of trial and error, where process stability is difficult to ensure. In many cases, the final product exhibits unwanted deformations or even defects after forming that need to be addressed with time-consuming, iterative, and costly experiments, often between different stakeholders until the material as well as the process parameters are adjusted reliably. Thus, process simulation tools, such as, for example, digital twins, are highly desirable from an economic point of view to facilitate time and cost advantages. Steadily growing computational resources increase the popularity for the integration of numerical tools within various engineering disciplines. Still, many manufacturers chose not to simulate the production process or product behavior, primarily due to inadequate prediction quality or inexperience, mostly associated with the choice and accuracy of the underlying material models. Thus, to approximate these complex processes and materials under realistic processing conditions, a strong demand for sophisticated material models has formed, motivating the need for ongoing fundamental research.

Independent of the employed material, the actual forming process generally follows the same sequence. Starting with a heating phase, where the workpiece, which usually comes in the form of a sheet or a foil, is heated close to the melting point to improve its pliability. Subsequently, the desired shape is imprinted by, e.g., pressure- or vacuum-forming, which offers the possibility of achieving complex geometries with relatively low effort. Lastly, the resulting product is

cooled down rapidly before removal from the mold. During the cooling, the interplay between fibers and matrix at their interface and their differences in thermal and mechanical properties significantly influence the behavior of the final product. Moreover, material anisotropy and phase transformations such as crystallization or glass transition facilitate the development of thermal gradients and residual stresses within the final product that can ultimately lead to component distortion or even defects.

From a modeling perspective, thermoforming processes of polymer composites are in particular challenging due to the multitude of influencing factors and the inherent material anisotropy. As a result of the nature of the process, the material typically undergoes large strains and rotations, often including severe nonlinearities and complex (time-dependent) inelastic deformations over a broad range of temperatures. Therefore, necessitating the use of finite strain constitutive theories. In turn, these nonlinear mechanisms induce dissipative effects such as material self-heating and ultimately lead to a change in the temperature that varies with the applied forming rate. Thus, in addition to the mechanical field, the thermal field must also be taken into consideration. Naturally, the backcoupling is not limited to the influence of the mechanical field on the temperature. Similarly, an increase in temperature leads to thermal softening, especially for the polymeric matrix material. Moreover, residual stresses may emerge due to thermal expansion, resulting from the disparity in material properties between the fibers and the matrix, as well as the anisotropy inherent in composite materials. It is therefore necessary to consider complex two-way thermo-mechanical coupling effects as well as the underlying microstructural phenomena.

On the individual constituent level, the evolution of the temperature during thermoforming results in local phase transformations. For instance, the polymer matrix undergoes a second-order phase change around the glass transition regime from a purely amorphous state after the heating phase to a glassy state after cooling. Furthermore, in the case of semi-crystalline polymers (SCPs), the supercooling of the amorphous phase triggers the formation of crystalline configurations. Naturally, both mechanisms significantly alter the underlying morphology and, therefore, strongly influence the effective properties of the resulting component. Noteworthy, the non-isothermal crystallization process occurs within a temperature environment that is both temporally and locally evolving. Due to the exothermic nature of the process, a change in the temperature is triggered, which, in turn, has a significant impact on the relevant parameters for the heat transfer and thus, ultimately, the temperature field within the component. These complex interactions consequently give rise to a fully coupled multiphysics problem, demanding sophisticated and integrated multi-field modeling strategies.

Attentive readers will likely have already noticed that the processes and interactions un-

der discussion occur across multiple material scales. Microscopic mechanisms, such as, for example, crystallization, play a crucial role in describing the material behavior observed at the structural component level. Consequently, accurate modeling of complex engineering processes, such as thermoforming, necessitates the incorporation of information from various material scales into the constitutive formulation. A widely adopted framework to address this complexity is the concept of scale separation, wherein the governing equations are solved independently at each material scale. This approach relies on the assumption that the characteristic length of the current scale is substantially larger than that of the next lower scale. The effective response obtained from the lower scale can then be used to determine the material behavior at the higher scale either by concurrent or hierarchical multiscale approaches. Limiting ourselves to material scales where the theory of continuum mechanics is applicable, typical scales considered for the modeling of fiber-reinforced polymers are the micro-, meso-, and macroscale.

Starting at the microscale, where the internal material geometry is explicitly considered and fibers and matrix are modeled as individual constituents. Besides the complexity of the polymer matrix requiring multiphysical coupling mechanisms, the interaction of the individual constituents on this level can be challenging due to the heterogeneous morphology of the microstructure. Moreover, the randomly oriented fibers result in statistical fluctuation of the effective material response. Moving up, the next level is the mesoscale or ply level, followed by the structural level, where the behavior of the entire component is treated as an effective, homogenized material, approximated by an anisotropic macroscopic material model.

Ideally, to model complex engineering problems that involve specific microstructural effects, information from all material levels should be used to determine and characterize the macroscopic response. In most cases, this is, however, unfeasible, since an extensive amount of experiments would be necessary to characterize the associated material models. Moreover, oftentimes, the material parameters at the lower scales are not known, since (reliable) experimental testing at these levels is extremely challenging. From a numerical perspective, concurrent multiscale methods, such as FE^2 or FE-FFT, can be employed, which connect two or more of the aforementioned scales and, therefore, significantly increase modeling accuracy. These methods, despite their recent and ongoing advances, are, however, not suitable for industry applications because of their extensive computation time. In such cases, hierarchical approaches offer a more reasonable solution, where, first, a micro- or meso-mechanical analysis is conducted on a unit cell. The resulting homogenized material response is then used for model identification on the macroscale. Thus, hierarchical modeling schemes are, essentially, multi-step processes. Nevertheless, despite the considerable time savings of hier-

archical approaches, a sophisticated macroscopic constitutive model is necessary for a reliable prediction.

With the goal in mind to enable modeling of the industrial processing of polymer composites under conditions that increasingly resemble reality, several open questions remain, which provide the need for fundamental research. For instance, which scales and effects must be considered for the development of a sophisticated and reliable material formulation on the macroscale? Furthermore, which experiments are needed to successfully characterize and validate such models, and which experiments can be neglected or reduced? Once the experimental and virtual data is available, the characterization process and the corresponding optimization procedures need to be systematically chosen. In particular, in the context of fiber-reinforced SCPs, which exhibit a wide array of different material phenomena ranging from brittle to glassy to fluid-like behavior and incorporate multiphysical coupling phenomena as well as phase transformations, these questions seem worthwhile to investigate. Despite the existence of numerous phenomenological or physically motivated models in the literature, the range of considered processing parameters is often limited. Furthermore, taking into account all aforementioned mechanisms in a thermodynamically consistent macroscopic theory still is a challenging task, resulting in a limited amount of applicable and comprehensive studies.

Conclusively, this dissertation aims to find a compromise between modeling accuracy and sophisticated model development across various scales and influencing factors while simultaneously reducing the associated experimental effort, enhancing the data base for characterization with virtually generated data where needed. Therefore, a bottom-up approach is chosen, starting with the development of a suitable thermodynamically consistent constitutive model for the polyamide 6 matrix. A comprehensive micromechanical and microthermal analysis allows for the generation of a data base for the identification of the homogenized macroscopic material model. Finally, the macroscopic material formulation is developed based on the underlying matrix model, and the influence of material anisotropy on the thermo-mechanical and thermo-chemical coupling phenomena is experimentally and numerically evaluated. An extensive experimental data set containing carefully selected experiments on individual constituents as well as various material levels allows for model characterization while ensuring an unprecedentedly wide range of process parameters. In this way, new experimental insights and modeling approaches regarding the overall macroscopic material response of FRPs to thermoforming are generated.

1.2 State-of-the-art

In order to contextualize the aforementioned research questions within the broader framework of previously published studies and to motivate the developments of the present dissertation further, a review of the relevant literature is provided below. The focus is primarily on modeling approaches for heterogeneous materials across different length scales as well as continuum mechanical approaches related to modeling polymeric materials and composites.

1.2.1 Modeling strategies for composites across various scales

As previously outlined, reliable material models are essential for the numerical analysis of fiber-reinforced polymers in industrial (thermo-)forming processes. Various modeling strategies have been developed to capture the effective constitutive response at the macroscale. These can generally be categorized into singlescale and multiscale approaches.

Multiscale modeling involves solving separate boundary value problems on two or more distinct material scales, thereby enabling information transfer across scales – typically from the microscale up to the macroscale. In contrast, singlescale approaches involve only one boundary value problem and operate entirely within a single material scale. For the purpose of the present dissertation, this category also includes homogenized microscopic models, often referred to as micromechanical approaches. While these consider the material's individual constituents and the material response derived from such models reflects the effective macroscopic behavior through volume averaging over the microscale domain, they do not propagate this information to solve another boundary value problem on a higher material level. Instead, the analysis remains confined to one scale.

In terms of computational efficiency, macroscopic singlescale methods are the most efficient. Here, the underlying material morphology as well as microstructural effects are not explicitly considered, instead, a phenomenological or micromechanically motivated approach is chosen to account for nonlinear or multiphysical material behavior. Typically, these type of material models are identified with experiments only on the component level. Well-known macroscopic material models for anisotropic fiber-reinforced material systems that laid the foundation for current approaches are presented by, for example, Weiss et al. [1996]; Bonet and Burton [1998]; Holzapfel and Gasser [2001]. While this approach certainly has its advantages, the lack of information about the microstructure results in inferior adaptability to changes in the process parameters, underlying morphology, or material parameters of the constituents. Oftentimes, the model requires time-intensive re-characterization or even re-development for every process modification in order to ensure its predictive capabilities.

Therefore, singlescale methods on the micro- (see e.g. Melro et al. [2013*a*]; Naya et al. [2017]; Chevalier et al. [2019]; Varandas et al. [2020]) and mesoscale (see e.g. Barbero et al. [2005]; Bednarcyk et al. [2015]; Stier et al. [2015*a*]) were introduced. Here, the averaged material response over the chosen microscopic or mesoscopic domain yields the effective macroscopic material behavior. However, only a limited number of studies related to FRPs consider the influence of temperature. For example, Bai et al. [2015] investigated the thermo-visco-plastic behavior of carbon fiber polymer matrix composites by introducing temperature-dependent material parameters via a scaling function and conducting mechanical unit cell simulations at various constant temperatures. A thermo-mechanically coupled approach is available in Sevenois et al. [2022], where mechanical and thermal periodic boundary conditions are employed to investigate the effect of self-heating. Micromechanics incorporating the effect of the degree of crystallinity are only available for the polymeric matrix (see e.g. Nikolov and Doghri [2000]; Van Dommelen et al. [2003]; Shojaei and Li [2013]; van Dommelen et al. [2017]). Here, the microscale is defined as the underlying individual crystalline and amorphous phases, and their homogenized response denotes the matrix behavior.

Despite their high accuracy in reproducing experimental results, homogenized micromechanical or mesomechanical approaches as previously described are generally not suited for use in industrial forming simulations. This is primarily due to their high computational cost, which arises from the explicit modeling of individual constituents such as fibers and matrix or laminate architectures. As a result, their application is often limited to academic studies or small-scale components where computational efficiency is not the primary constraint. Nonetheless, these singlescale methods provide valuable insights into the mechanisms governing complex micromechanical and -thermal phenomena. Thus, they have played a crucial role in demonstrating the importance of incorporating microstructural effects for the prediction of the macroscopic material response. Consequently, integrating these kind of approaches in computationally efficient multiscale modeling strategies is key for reliable and adaptable predictions in industrial applications.

Multiscale methods offer a powerful solution that have seen a continuous increase in popularity due to steadily growing computational resources. Two fundamentally different approaches need to be distinguished: concurrent and hierarchical methods. Concurrent or fully coupled modeling schemes connect two or more material scales by passing the macroscopic deformation to the microscale in every Gauss point, where an additional boundary value problem is solved on a unit cell. The resulting stress state as well as the tangent operator are transferred back to the macroscale as volume averages over the microscopic domain to achieve a global solution. Popular fully coupled methods usually employ the finite element method (FEM) on

the structural scale and different methods on the microscale, such as, for example, FEM or Fast Fourier Transform (FFT), resulting in FE^2 (see e.g. Feyel and Chaboche [2000]; Schröder [2014]; Raju et al. [2021]) or FE-FFT (see e.g. Spahn et al. [2014]; Schneider [2021]; Gierden et al. [2022]) coupling schemes, respectively. A few contributions also address multiphysical problems, as, for example, thermo-mechanical coupling (see e.g. Özdemir et al. [2008]; Temizer and Wriggers [2011]; Li et al. [2019]; Wicht et al. [2021]; Schmidt et al. [2025]). Recent advancements in the field of concurrent multiscale modeling include the replacement of constitutive theories with data-driven methods, such as artificial neural networks or deep material networks, to model the mechanical or thermo-mechanical behavior of composites (see e.g. Gajek et al. [2021, 2022]; Bishara et al. [2023]). In general, concurrent multiscale modeling schemes are able to predict the macroscopic material behavior with a high degree of accuracy given a sufficient separation of scale and an appropriate choice of the microscopic domain. Moreover, these approaches are highly adaptable, since the constituent behavior can be altered without re-characterization of the macroscopic material model. Nonetheless, the associated computational cost is usually very high (cf. Geers et al. [2010]). Therefore, these approaches are not well suited for industry applications. To increase the efficiency, model order reduction techniques have been developed (see e.g. Radermacher and Reese [2016]; Kochmann et al. [2019]) and successfully applied to industrial deep rolling processes (cf. Gierden et al. [2021]).

Hierarchical multiscale approaches, on the other hand, are essentially multi-step processes, where first, depending on the scales of interest, a micro- or meso-mechanical analysis is conducted by subjecting a unit cell to different mechanical or thermal loading conditions. Thereafter, the resulting effective material properties and, in the case of nonlinear material behavior, stress-strain-curves, are used as virtual input data for the identification of a suitable macroscopic material formulation (cf. Aboudi et al. [2012]). Thus, a scale transition is accomplished. For FRPs, these kind of models have been successfully employed in, for example, Reese et al. [2001]; Reese [2003*b*]; Bednarcyk et al. [2015]; Stier et al. [2015*b*]; Rezasefat et al. [2023]. However, these contributions are mostly limited to isothermal problems investigating inelastic phenomena, delamination, or damage. For the polymeric matrix material, hierarchical modeling schemes exist that take into account the degree of crystallinity (cf. Uchida and Tada [2013]). Moreover, data-driven approaches are available (cf. Unger and Könke [2008, 2009]). Here, the artificial neural network was trained by microscale simulations and subsequently used as a constitutive model within the finite element simulation of the macroscopic material behavior. Although hierarchical approaches have been widely applied in composite modeling, the influence of the temperature and the degree of crystallinity within such frameworks –particularly for FRPs– has received comparatively little attention to date (cf. Bouvard et al.

[2009]), revealing the need for further research.

In contrast to concurrent methods, hierarchical approaches rely on a sequential scale transition and require a well-formulated macroscopic material model. While their accuracy and adaptability strongly depend on the quality of the micromechanical analysis as well as the model's ability to capture processing conditions, fiber contents, and underlying morphologies, they significantly reduce computational cost. This trade-off makes them an attractive and efficient choice for industrial applications, balancing reliability with performance.

1.2.2 Multiphysics modeling of semi-crystalline polymers and polymer matrix composites

Multiscale methods commonly rely on the quality of the representation and analysis of the microscale. Hence, suitable domain sizes, geometric approximations, and most importantly, constituent material models need to be chosen in order to gain reliable insights into the material. With regard to fiber-reinforced thermoplastic polymers (FRTPs), particularly the polymeric matrix requires sophisticated modeling schemes, since it exhibits a multitude of inelastic and nonlinear material behaviors within the industrial operating temperature range (see e.g. Ayoub et al. [2010]; Qi et al. [2019]; Felder et al. [2020b]). Hereby, the mechanical behavior is, inter alia, characterized by large (plastic) deformations, loading rate dependency, stress relaxation, and strain hardening as well as tension-compression asymmetry. Semi-crystalline polymers are a subclass of thermoplastics that form crystalline regions during cool-down from the amorphous melt. Therefore, strictly speaking, SCPs are heterogeneous materials themselves, consisting of amorphous and crystalline regions (cf. Dietz [1981]; Wunderlich [2003]).

In the literature, numerous scientific contributions were concerned with the modeling of polymers. Starting with mechanical approaches, many continuum mechanical frameworks for amorphous (see e.g. Anand and Gurtin [2003]; Srivastava et al. [2010]; Barriere et al. [2019]) and semi-crystalline (see e.g. Boyce et al. [2000]; Van Dommelen et al. [2003]; Ayoub et al. [2011]) polymers are based on an additive decomposition into intermolecular and molecular network resistance (cf. Haward and Thackray [1968]; Boyce et al. [1988]). Within the class of phenomenological models, purely visco-elastic (see e.g. Khan et al. [2006]; Ricker et al. [2023]; Kulkarni et al. [2025]) and visco-plastic (see e.g. Kästner et al. [2012]; Cundiff et al. [2022]) approaches are employed, as well as approaches including coupled visco-elastic, elasto-plastic phenomena (see e.g. Gudimetla and Doghri [2017]; Qi et al. [2019]; Wang et al. [2019]; Felder et al. [2020a]; Hao et al. [2022a]). The tension-compression asymmetry of polymers is investigated by, for example, Ghorbel [2008]; Farrokh and Khan [2010]; Vogler

et al. [2013]; Melro et al. [2013*b*]; Bai et al. [2015]; Nguyen et al. [2016]; Manaia et al. [2020], to name a few. Here, experimental studies revealed the need for an appropriate choice of the yield surface, including hydrostatic pressure effects. Moreover, the applicability of associative and non-associative approaches for modeling plasticity is discussed together with the choice of an appropriate plastic potential. However, none of the above-mentioned approaches consider the dependence on both the DOC and temperature in their choice of the yield surface. To account for the well-known Bauschinger effect, several approaches also incorporate kinematic hardening (see e.g. Anand et al. [2009]; Krairi and Doghri [2014]).

In addition to the complex mechanical phenomena, the material behavior of SCPs is highly dependent on the thermal conditions. With regard to thermo-mechanically coupled material modeling schemes, two approaches are commonly used in the literature. Classical thermo-mechanically coupled models start with a general representation of the overall free energy that is obtained from the twice integrated heat capacity (see Chadwick [1974]). Based on this general idea, Reese and Govindjee [1997] proposed an enhanced description of the heat capacity, yielding a non-linear stress-temperature dependence. Here, thermal expansion is defined by an appropriate choice of the Helmholtz free energy. Later, Reese [2003*a*] proposed a continuum mechanical model for finite visco-elasticity, including micro-mechanical considerations based on this framework. Conversely, physically motivated methods employ a multiplicative decomposition of the deformation gradient into a thermal and a mechanical part (see e.g. Stojanovic et al. [1964]; Lu and Pister [1975]; Lion [1997*a*]). Here, the description of thermal expansion within this framework is automatically accomplished by means of the thermal part of the deformation gradient. The experimental verification of this theory is conducted in, for example, Lion [1998, 1997*a*]. Both methods can generally be used interchangeably, however, with regard to damage processes, Felder et al. [2022] showed that the damage growth criterion (cf. Wulfinghoff et al. [2017]) is not easily fulfilled a priori using the classical approach.

The temperature range considered in polymer modeling is typically categorized into studies focusing on behavior below the glass transition regime (e.g. Ames et al. [2009]), near the glass transition (e.g. Shepherd et al. [2006]; Johlitz et al. [2010]), and those that cover a broad spectrum spanning both below and above this phase change (e.g. Srivastava et al. [2010]). The glass transition, which is a characteristic phenomenon of the amorphous phase in polymers, has also been the subject of specific modeling efforts, as shown in Lion et al. [2010, 2011, 2017], to name a few. With regard to semi-crystalline polymers, fewer thermo-mechanically coupled approaches exist despite numerous isothermal contributions. Recent publications include investigations related to material self-heating (see e.g. Ghorbel et al. [2014]; Krairi et al. [2019]; Felder et al. [2020b]), including the double yield phenomenon (cf. Hao et al.

[2022a]) and damage effects (e.g. Shen et al. [2019]).

In addition to the current thermal conditions, the temperature history significantly influences the effective thermo-mechanical behavior of SCPs in terms of the morphology of the underlying microstructure after forming (see e.g. Ayoub et al. [2011]). In order to predict the evolution of the crystalline phase during processing (e.g. the evolution of the degree of crystallinity during cooling from the melt), several approaches were proposed in the past. Based on the isothermal Avrami equation (Avrami [1939]), numerous non-isothermal frameworks were developed that describe the evolution of the DOC (cf. Di Lorenzo and Silvestre [1999]). To account for the heat generation during the exothermic crystallization process, Le Goff et al. [2005]; Zinet et al. [2010] and Kugele [2020] proposed frameworks based on differential scanning calorimetry (DSC) measurements of the enthalpy of fusion. Additionally, the effect of pressure on the crystallization process was described in a thermodynamically consistent manner by Lion and Johlitz [2016], taking into account amorphous and crystalline phases. The influence of the ply thickness on the resulting distribution of the degree of crystallinity is studied in Kulkarni et al. [2023], in the context of thermoforming. Here, a particularly broad range of cooling rates is investigated due to conducting both standard (S-DSC) and flash (F-DSC) differential scanning calorimetry tests.

The effect of the DOC on the mechanical response of SCPs is, however, subject in only a limited number of constitutive models. Several works investigate varying constant degrees of crystallinity at specific temperatures by introducing a rule of mixture for the differentiation between the amorphous and the crystalline regimes (cf. Dusunceli and Colak [2008]) and suggesting a two-phase representation of the microstructure (see e.g. Ayoub et al. [2011]; Abdul-Hameed et al. [2014]; Cundiff et al. [2022]). A particularly wide range of temperatures below and above the glass transition was considered by Felder et al. [2020a], who first introduced both temperature- and crystallinity-dependent material parameters in their modeling scheme, following an extensive experimental investigation. The approach was further extended to a thermodynamically consistent, thermo-mechanically coupled model in Felder et al. [2020b], taking into account the crystallization from the amorphous melt as a separate pre-process. Though significant progress was made, the flexibility of the approach is limited by the considered range of process parameters, especially in terms of the DOC ranging from only 23% to 28%. More recently, Yoshida et al. [2022] experimentally investigated different semi-crystalline polyamides considering their molecular chain structure as well as crystallinity, resulting in a modified modeling approach based on molecular chain networks. This modeling approach was also chosen in Uchida et al. [2024], where prior to modeling, different thermal histories for polyamide were investigated.

As previously discussed, hierarchical multiscale approaches rely on the development of a robust and adaptable macroscopic modeling framework. One effective strategy is a bottom-up approach, in which micro- or mesoscale material models are systematically extended to capture the anisotropic behavior of the composite material. Depending on the level of detail at the microscale, complex micromechanical phenomena, such as thermo-mechanical coupling or the influence of the degree of crystallinity, are directly incorporated into the macroscopic formulation. Moreover, depending on the resolution and scope of the mesoscale, mesomechanical effects, such as fiber-matrix debonding, ply delamination, or interactions arising from woven fiber architecture, may also be accounted for.

Fiber-induced anisotropy, i.e., transversely isotropic or orthotropic material behavior, can be captured by introducing structural tensors into the formulation (see e.g. Boehler [1979]; Holzapfel and Gasser [2001]; Reese et al. [2001]; Reese [2003*b*]; Poggenpohl et al. [2021]; Holthusen et al. [2020]). In Vladimirov et al. [2010], the concept of structural tensors has been used to model anisotropic finite elasto-plasticity, whereas Reese et al. [2021] employed this method to model damage in elasto-plastic materials. Fewer contributions are available in regards to anisotropic thermal phenomena. In this context, Vujošević and Lubarda [2002] developed a theory for anisotropic thermal expansion. Based on this work, Al-Kinani [2014] developed a framework for transversely isotropic materials incorporating a macroscopic description for the anisotropic heat flux. Moreover, the author conducted several numerical studies to investigate thermal anisotropy for FRPs. With regard to classical thermo-mechanically coupled approaches based on the twice integrated heat capacity, to the author's knowledge, only Groß et al. [2019, 2020] incorporated anisotropic thermal expansion via the choice of the free energy. However, no numerical investigations regarding the thermal anisotropy were carried out, and the applicability of the chosen energy terms was not evaluated.

From the above review, a considerable large progress regarding the experimental and numerical investigation of semi-crystalline polymers and polymer matrix composites is apparent. However, most existing models are limited to investigations, either accounting for the impact of the temperature (see e.g. Krairi et al. [2019]; Shen et al. [2019]; Hao et al. [2022a]) or the process-induced crystallinity (see e.g. Dusunceli and Colak [2008]; Ayoub et al. [2011]). Although efforts have been made to investigate both aforementioned influencing factors (see e.g. Felder et al. [2020a,b]), the considered range of processing conditions is still limited and does not yet reflect the broader spectrum required for forming applications (cf. Kulkarni et al. [2022]; Hao et al. [2022b]). Thus, restricting the flexibility of these approaches. Moreover, primarily the polymer matrix is investigated in detail.

More recent studies focused on thermoforming simulations of FRPs include non-isothermal

effects into their modeling frameworks (see e.g. Machado et al. [2016]; Guzman-Maldonado et al. [2016]; Dörr et al. [2019]; Dörr [2021]; Maldonado et al. [2025]). However, with the exception of Dörr et al. [2019]; Dörr [2021], these approaches are typically limited to temperature regimes above the crystallization onset and thus do not account for process-induced crystallization phenomena. Moreover, the majority of these studies rely on macroscopic singlescale approaches (e.g. Vanclooster et al. [2009]; Khan et al. [2010]; Machado et al. [2016]), while only a limited number incorporate mesoscopic effects in a hierarchical manner for (woven) fiber-reinforced thermoplastics (e.g. Boisse et al. [2005]; Guzman-Maldonado et al. [2016]; Dörr et al. [2019]; Dörr [2021]). To the author's knowledge, a fully thermo-mechanically coupled hierarchical modeling approach that accounts for both micromechanical and microthermal effects as well as the process-dependent evolution of the material morphology in terms of the crystallinity has not yet been established in the current literature.

1.3 Outline of the dissertation

The present cumulative dissertation is organized in the following manner. Chapter 2 is concerned with the development and characterization of a thermo-mechanically coupled model formulation for the polyamide 6 matrix. In Chapter 3, the matrix model is employed in the context of a micromechanical analysis on repeating unit cells to generate an experimental and virtual data base. Finally, in Chapter 4, a homogenized macroscopic approach for unidirectionally fiber-reinforced polyamide 6 is proposed as an extension of the previously developed theory. In this instance, the experimental and virtual data base from Chapter 3 is used for model identification and the framework is employed to conduct a full thermoforming simulation.

In more detail, in Chapter 2 a comprehensive mechanical and thermal experimental study on polyamide 6 blends is used to identify the dependencies of the material on the temperature, strain rate, and the underlying morphology in terms of the degree of crystallinity. Therefore, various loading conditions, such as monotonic and cyclic tension and compression, are tested, and relaxation tests as well as a thermal analysis are conducted. The use of blends instead of pure polyamide 6 ensures testing on a stable, temperature-independent crystalline state and, simultaneously, extends the range of tested DOCs tremendously. Based on the experimental findings, a thermo-mechanically coupled continuum approach is proposed, which combines nonlinear visco-elastic and elasto-plastic effects. In this thermodynamically consistent framework, the degree of crystallinity serves as a constant input quantity, which affects the overall constitutive behavior. To account for the tension-compression asymmetry characteristic for polymeric materials, a tension-compression asymmetry in yielding is incorporated via the

choice of the yield surface incorporating a dependence on both the DOC and the temperature, combined with nonlinear kinematic hardening of Armstrong-Frederick type and a nonlinear relaxation behavior. In this way, the material behavior in terms of loading-rate dependency, strain hardening and stress relaxation can be accurately predicted over a wide range of process parameters.

Next, the polymeric matrix model is employed for a micromechanical and microthermal analysis on repeating unit cells in Chapter 3. Therefore, firstly, various randomization methods are tested to generate the unit cells and replicate the composites' random fiber distribution with a focus on process automation. A statistical evaluation is conducted to determine the size of the unit cell, taking into account the statistical fluctuations related to the random fiber distribution. Subsequently, the effective mechanical and thermal material properties are derived, combining the aforementioned polyamide 6 matrix formulation with a thermo-elastic model for the glass fibers. The virtual results of the micromechanical analysis are successfully compared to an experimental study on glass fiber reinforced polyamide 6 at various temperatures. Thus, enabling the development of a virtual and experimental data base for the identification of a homogenized macroscopic material model in Chapter 4.

As previously mentioned, Chapter 4 is concerned with the extension of the polymeric matrix model from Chapter 2 to a homogenized macroscopic approach for unidirectional fiber-reinforced polyamide 6. The fiber-induced anisotropy is accounted for by an additional transverse isotropic thermo-elastic energetic contribution in combination with a macroscopic description for anisotropic thermal conduction. Furthermore, the crystallization kinetics are introduced as an independent thermo-chemical process to include the impact of the temperature history on the overall mechanical material behavior. Hence, the degree of crystallinity is now treated as a temperature-rate-dependent internal variable to account for the evolution of the underlying crystalline phase. The influence of the mechanical and thermal material anisotropy on different phenomena such as thermal expansion, self-heating, and crystallization is carefully examined in various numerical examples, including a 3D thermoforming simulation in comparison to experimental results.

2 Article 1: A thermo-mechanically coupled constitutive model for semi-crystalline polymers at finite strains: Mechanical and thermal characterization of polyamide 6 blends

This article was published as:

Reuvers, M., Kulkarni, S., Boes, B., Felder, S., Wutzler, A., Johlitz, M., Lion, A., Brepols, T. and Reese, S. [2024], 'A thermo-mechanically coupled constitutive model for semi-crystalline polymers at finite strains: Mechanical and thermal characterization of polyamide 6 blends', *Continuum Mechanics and Thermodynamics* **36**, 657 – 698.

Disclosure of the individual authors' contributions to the article:

M. Reuvers revieved the existing literature, derived the constitutive framework, implemented the material model as a user-defined material model into the commercial Finite Element software *ABAQUS*/Standard, was responsible for model identification and validation, performed all computations, interpreted the results and wrote the article. S. Kulkarni and A. Wutzler provided the experimental data and contributed to the interpretation of the results. B. Boes implemented parts of the material routine and investigated different yield criteria. S. Felder contributed parts of the visco-elastic material routine. M. Johlitz, A. Lion, T. Brepols and S. Reese gave conceptual advice, contributed to the discussion, proofread the article and made valuable suggestions for improvement. All authors approved the publication of the final version of the manuscript.

2.1 Abstract

In the field of material modeling, thermoplastic polymers are often studied because of their complex material behavior and their prevalence in industry applications due to their low cost and wide range of applications. Nowadays, where reusability becomes more and more important, materials which can undergo reversible thermomechanical deformations are appealing for, e.g., the construction of car body components. To predict such complex forming processes with multiple influencing factors, such as temperature, strain rate or underlying material morphology, model formulations are needed that account for these influences simultaneously and are validated against experimental data. Unfortunately, up to now only a few contributions are available which consider all these phenomena. In addition, the range of process parameters considered is often narrow due to the experimental effort required for testing. This usually results in limited predictive capabilities of the model. To overcome these limitations, in this work, a thermo-mechanically coupled material model is developed, that accounts for the underlying morphology in terms of the degree of crystallinity (DOC). The model formulation is derived in a thermodynamically consistent manner, incorporating coupled nonlinear visco-elastic and elasto-plastic material behavior at finite strains. To characterize and further validate the model, mechanical as well as thermal experiments are conducted for polyamide 6 (PA6). Here, a blending strategy of PA6 together with an amorphous co-polymer is introduced during specimen production to achieve a wider range of stable DOCs(approximately 15%). The model formulation is successfully applied to experimental results and its predictions are in good agreement with experimental observations.

Abbreviations

a, A	Scalar quantity
$\boldsymbol{a}$	First order tensor
$\boldsymbol{A}$	Second order tensor
$\boldsymbol{I}$	Identity tensor
$\mathbb{A}$	Fourth order tensor
$\dot{(*)}$	Total derivative with respect to time
$(\boldsymbol{A})^T$	Transpose of $\boldsymbol{A}$
$(\boldsymbol{A})^{-1}$	Inverse of $\boldsymbol{A}$
$\text{tr}(\boldsymbol{A})$	Trace of $\boldsymbol{A}$
$\det(\boldsymbol{A})$	Determinant of $\boldsymbol{A}$
$\text{sym}(\boldsymbol{A})$	$\frac{1}{2}(\boldsymbol{A} + \boldsymbol{A}^T)$
$\text{dev}(\boldsymbol{A})$	$\boldsymbol{A} - \frac{1}{3}\,\text{tr}(\boldsymbol{A})\boldsymbol{I}$
$\text{Grad}(\boldsymbol{A})$	Gradient of $\boldsymbol{A}$ with respect to the reference configuration
$\text{Div}(\boldsymbol{A})$	Divergence of $\boldsymbol{A}$ with respect to the reference configuration
:	Double contraction
$\lvert\boldsymbol{A}\rvert$	$\sqrt{\text{tr}(\boldsymbol{A}^T\boldsymbol{A})}$
$(*)_n$	Quantity from last converged time step
$\bar{(*)}$	Quantity in the reference configuration
$\hat{(*)}$	Quantity in Nye Notation $\big((11),(22),(33),(12),(13),(23)\big)^T$

2.2 Introduction

Polymers are marcomolecules consisting of repeating units (monomers) with linear, branched or cross-linked structures. They are typically classified on the basis of their origin (synthetic, natural, modified natural), the origin of their ressources (renewable, fossil), their biodegradability, or their physiochemical properties (thermoplastics, thermosets, elastomers) in terms of their arrangement of monomers on the microlevel. The latter is of interest in industrial applications, for example in automotive or aerospace industry, where polymers are used as engineering materials due to their beneficial high strength to weight ratio, as well as their eligibility for cost-effective mass-production. In contrast to three dimensional cross-linked network structures, highly pronounced in thermosets and less distinct in elastomers, thermoplastics primarly consist of long linear or branched polymer chains without cross-links. This underlying morphology allows for reversible thermoplastic deformations, needed for technical forming or moulding processes, as e.g. for car components. Thermoplastics can either be purely amorphous or semi-crystalline polymers (SCPs), depending on their chain morphology. Amorphous polymers mainly consist of disordered (coiled) chains that undergo a change from a glassy to a rubbery state around the glass transition temperature. In contrast, SCPs contain

disordered (amorphous) and ordered (crystalline) regions, resulting in a recrystallization behavior during cool-down from the melt (Strobl [1997]; Cowie and Arrighi [2007]; Young and Lovell [2011]). Hereby, the cooling rate and the production method (e.g. extrusion, injection molding, blow molding, compaction etc.) have a crucial impact on the resulting degree of crystallinity (DOC). In industrial applications, the process stability is most important, therefore additives such as softening agents, stabilizers, crystallization agents, dyes or fillers to enhance the mechanical properties are commonly used in plastics manufacturing. Nonetheless, these are not the only influencing factors on the resulting material behavior. Besides production parameters, temperature, heating or loading rate as well as moisture content or ageing factors, such as UV radiation or other environmental factors, can alter the material characteristics. Hence, it is crucial to consider multiple influencing factors over a wide range when formulating and identifying a material model to reliably predict the material behavior of plastics.

Over the past decades, multiple models were proposed to simulate the material behavior of polymers under various influencing factors. Here, contributions for thermoplastic materials are of particular interest. Based on the modeling approach by Haward and Thackray [1968] for glassy polymers and the idea of a split into a molecular network as well as an intermolecular resistance (Boyce et al. [1988]), several phenomenological models were developed for amorphous (e.g. Anand and Gurtin [2003]; Mulliken and Boyce [2006]; Barriere et al. [2019]) and semi-crystalline (e.g Boyce et al. [2000]; Ayoub et al. [2010]; Felder et al. [2020a]) polymers. Within the class of phenomenological models, the approaches differ between purely viscoelastic formulations (e.g. Müller et al. [2011]; Kästner et al. [2012]) and models that cover the elasto-visco-plastic material behavior (e.g. Lion [1997*a*]; Boyce et al. [2000]; Felder et al. [2020a]). Several works additionally account for the Bauschinger-like effect upon unloading (e.g. Anand et al. [2009]; Srivastava et al. [2010]; Krairi and Doghri [2014]).

Modeling the yielding behavior of thermoplastics requires the identification of an appropriate yield surface. Here, the well-known von Mises yield criterion, which depends on a single material parameter only (i.e. yield stress) and originates from the analysis of the inelastic behavior of metals, is not suitable, since it neglects the hydrostatic pressure dependence known for polymers, see for example Mears et al. [1969]; Ghorbel [2008]. Possible alternatives are, for example, the Drucker-Prager yield surface Drucker and Prager [1952], or the paraboloid yield surface by Tschoegl [1971]. Both offer the possibility to consider tension-compression asymmetry in yielding, by introducing separate yield stresses in tension and compression. This effect is also visible in experiments. Nguyen et al. [2016] showed e.g. a tension-compression asymmetry in the onset of yielding for glassy polymers at room temperature, where the stiffer compressive response resulted from the effect of hydrostatic pressure. The temperature and

strain rate sensitivity of yielding under compression was discussed in Richeton et al. [2006]. However, the ratio of the tensile and compressive yield stresses is not affected by the strain rate, as concluded by Ghorbel et al. [2014]. Manaia et al. [2020] investigated the mechanical response of various semi-crystalline polymers and found out that PA6, among others, shows a strain-rate dependent yielding together with a higher yield stress in compression. At higher temperatures, Rae et al. [2007] tested the response of polyether-ether-ketone (PEEK) and compared the resulting yield stresses in tension and compression. Their difference decreased with increasing temperature, especially close to or above the glass transition. Further testing by Ghorbel [2008] revealed that yield criteria based on the hydrostatic stress and second invariant of the deviatoric stress are not sufficient to predict biaxial stress states or shear banding. In these cases, the third invariant of the deviatoric stress needs to be considered as well. Another possibility are yield criteria derived from mechanical testing, see e.g. Farrokh and Khan [2010]. These approaches are, however, tailored to a specific material and can therefore not be used for other cases.

Some works considered additional effects at the microlevel, as, for example, plastic flow occurring via crystallographic slip in the crystalline phase (Van Dommelen et al. [2003]) or a change of the plastic flow depending on the glass transition (Richeton et al. [2007]). Naturally, the morphology of the underlying microstructure, e.g. crystal configuration, lamellae thickness etc., has a significant influence on the overall material response. This motivated modeling formulations that take into account molecular dynamics or the microstructual constituents, employing analytical or FE-based homogenization schemes to arrive at the macroscopic material response, see e.g. Nikolov et al. [2002]; Bouvard et al. [2009]; Uchida and Tada [2013]; Popa et al. [2014]; Pisani et al. [2019]. However, due to experimental limitations it is in general difficult and costly to obtain the required physical data for characterizing the microscopic material behavior. Especially semi-crystalline polymers prove to be difficult in terms of their different molecular arrangements. With the growing interest in artificial intelligence and machine learning, efforts have been made to use neural networks for describing the temperature dependence of mechanical properties of polyurethane (Kopal et al. [2017]) and the temperature- and rate-dependence of polypropylene in terms of a hybrid model approach, combining constitutive and data-based modeling (Jordan et al. [2020]). Additional applications included material development, as e.g. rubber blend optimization by tracing back targeted visco-elastic material properties Román et al. [2022] or polymer identification Rabiej and Rabiej [2021]. Similar to micromechanical approaches, the generation of experimental data sets remains cost- and time-intensive.

The influence of the internal microstructure on the macroscopic material response is only

taken into account in a limited number of works. For example, the amount of crystal volume fraction was taken into account in Ayoub et al. [2010, 2011], who incorporated a two-phase representation of the intermolecular resistance, whereas in Dusunceli and Colak [2008] and Regrain et al. [2009] mixture rules based on a crystallinity ratio were used to distinguish between the amorphous and the crystalline phase. Hachour et al. [2014] developed a micromechanics-based criterion for the yielding of SCPs, based on the amorphous volume fraction. In most cases, however, crystalline and amorphous phases are treated in a smeared manner and the degree of crystallinity serves as a constant input parameter, see e.g. Felder et al. [2020a]. Several works additionally considered the evolution of the DOC as a stress-free pre-process, resulting during cool-down from the molten state (Felder et al. [2020b]), or elaborated a full coupling scheme (e.g. Cundiff et al. [2022] based on Doufas et al. [2000]; Ahzi et al. [2003]). However, the validation of such approaches remains cumbersome, since the DOC cannot be measured directly during experimental testing and additional changes in the sample cannot be excluded, if tested afterwards. Commonly, no further differentiation between fully extended (α-form) and twisted (γ-form) polymer chains is made.

Thermal effects in semi-crystalline polymers need to be accounted for, due to the inherent structural changes occuring at the lamallae level. In literature, multiple approaches exist for polymers that take into account a coupling with the temperature field (e.g. Arruda et al. [1995]; Anand et al. [2009]). Here, the approaches differ in terms of the treatment of thermal softening with increasing temperature. Reese and Govindjee [1997] and Lion [1997*b*], for example, considered material degradation, whereas in the works of e.g. Johlitz et al. [2010]; Johnsen et al. [2019]; Felder et al. [2020b], the material parameters themselves are dependent on the temperature. In regards to the considered temperature range, Ames et al. [2009] identified the model framework below the glass transition, whereas Shepherd et al. [2006] considered processing cases close to the glass transition. In contrary, Srivastava et al. [2010] conducted a modeling framework that spans a wide temperature range independent of the phase change. Significant self-heating effects were visible in experiments from Ghorbel et al. [2014] for polyamide (PA66), polymethylmethacrylate (PMMA) and polycarbonate (PC) and in experiments from Krairi et al. [2019] for PA66 and polypropylene. In a recent publication, Hao et al. [2022a] studied the material behavior of PA6 under large deformations including the self-heating effect, prominent at high loading rates.

Other influencing factors were investigated in, for example, Sharma et al. [2020], who investigated the effects of a change in moisture content on the mechanical properties of PA6 by coupling a nonlinear diffusion model with a visco-elastic material model. In Kehrer et al. [2023], the thermoviscoelastic behavior of PA6 is explored by means of dynamical

mechanical analysis (DMA) under varying moisture contents. Further, Rodriguez et al. [2020] experimentally investigated the effect of UV-aging on polyethylene, whereas Bahrololoumi et al. [2022] incoporated the effect of thermal-aging into a micromechanical constitutive model. Besides the influence of environmental factors, multiple attempts were made to model the failure regime of SCPs. Krairi and Doghri [2014] modeled e.g. ductile damage in polypropylene, nylon 101 and high-density polyethylene, whereas Shen et al. [2019] introduced a thermo-elastic-viscoplastic-damage model for PA6. A gradient-damage approach was used in Narayan and Anand [2021] to overcome pathological mesh-dependence issues in the simulation of PMMA and polycarbonate (PC) fracture.

Concluding from the review above, considerable efforts were made in the experimental and numerical analysis of SCPs. However, in most of these works the influencing factors on the material behavior are considered separately. Only a few works consider multiple influences at once. Especially regarding the temperature and process induced morphology, as the degree of crystallinity, a strongly limited number of contributions is available that covers their correlations over a wide process range (Felder et al. [2020a]). In these cases, mostly the mechanical model response is investigated, whereas the influence of the DOC on the thermal properties is neglected, in particular for temperatures above the glass transition. At the same time, the considered range of process parameters in experimental testing is often limited. Therefore, a broad overview of the material response is missing. As a result, material models identified from experimental data are often valid only for small regions, e.g. a small range of DOCs, limiting the predictive capability of the model for various applications and process induced morphologies. Additionally, the production of temperature stable specimens with a significant range of crystallinities remains a challenge, since quenching during cool-down or post-production treatments, as for example anealing, yield only small changes in the DOC that are unstable in temperature and time. Here, additives like crystallization agents or fillers are needed, to achieve significant and stable changes in the materials' crystal content. Compounding such materials with designed properties is a separate research field in terms of identification of a suitable blend partner, blend composition, mixing technology and chemical reactions initiated between the components that may require the use of compatibilizers, see e.g. Doshev et al. [2005]; Ozkoc et al. [2007]; Lin et al. [2020]; Perin et al. [2023]. Further testing is required to validate the newly generated materials prior to mechanical testing, which increases the experimental effort.

The objective of this work is to evaluate the influence and interplay between strain rate, temperature and degree of crystallinity collectively over a wide range of process parameters and develop a corresponding thermo-mechanical constitutive theory. Therefore, in a first step

(see Sec. 2.3) a thermodynamically consistent finite strain formulation is derived, where the temperature serves as an additional field variable. The degree of crystallinity is accounted as an additional constant input quantity. In line with previous works, a coupled visco-elastic, elasto-plastic model is developed that includes nonlinear kinematic hardening of Armstrong-Frederick type. The formulation is extended with a tension-compression asymmetry in yielding, necessitating experimental results in tension and compression to characterize the model. Further, the model is identified in a staggered manner with new experimental results from polyamide 6 cyclic-olefin-copolymer (COC) blends with a range of 15 % to 29% DOC (see Sec. 2.4). Tension, compression and relaxation tests are carried out for temperatures below and above the glass transition with an emphasis on a wide range of variation in the tested strains and strain rates. Here, several functions for a nonlinear relaxation time are tested and compared to experimental data. Additional thermal tests, as, for example, thermal conductivity measurements or specific heat capacity measurements, are carried out to identify the models' thermal properties and their dependence on the underlying morphology. Following model verification, numerical examples are shown and discussed in Sec. 2.5. Finally, a conclusion and outlook are given in Sec. 2.6.

2.3 Constitutive modeling of semi-crystalline polymers

The experimental findings of e.g. Felder et al. [2020a] imply that, to accurately represent the material behavior of SCPs, a coupled visco-elastic, elasto-plastic framework, incorporating nonlinear relaxation behavior as well as strain hardening, is required. To this end, the corresponding modeling strategy is presented in a schematic one dimensional rheological illustration (Fig. 2.1 a) to allow a better understanding of the following derivation.

2.3.1 Kinematics

In the finite strain regime, the previous assumptions lead to a multiplicative decomposition of the deformation gradient $\boldsymbol{F}$ into an elastic ($\boldsymbol{F}_{e1}$) and a plastic ($\boldsymbol{F}_{p}$) part (see e.g. Eckart [1948]; Kröner [1959]; Lee [1969]) as well as an elastic ($\boldsymbol{F}_{e2}$) and viscous ($\boldsymbol{F}_{v}$) contribution (see e.g. Sidoroff [1974]; Lubliner [1985]; Lion [1997a]; Reese and Govindjee [1998])

$$\boldsymbol{F} = \boldsymbol{F}_{e1}\,\boldsymbol{F}_{p} = \boldsymbol{F}_{e2}\,\boldsymbol{F}_{v}, \tag{2.1}$$

see Fig. 2.1. To model nonlinear kinematic hardening, an additional, physically motivated split of the plastic deformation gradient $\boldsymbol{F}_p = \boldsymbol{F}_{pe}\,\boldsymbol{F}_{pi}$ is introduced, according to Lion [2000]; Dettmer and Reese [2004]. Naturally, the above decompositions of the deformation gradient result in the local intermediate configurations ic_1, ic_1^v and ic_2 for plasticity, kinematic hardening and viscosity, respectively, with rc defining the reference and cc the current configuration (cf. Fig. 2.1).

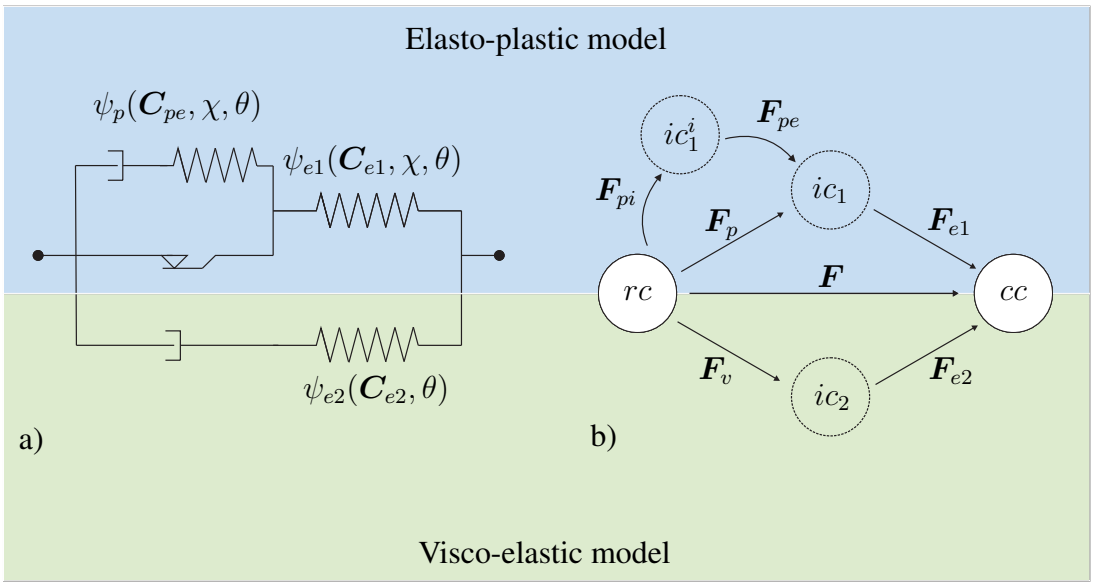

Figure 2.1: a) Schematic illustration of the constitutive model b) Multiplicative splits of the deformation gradient.

2.3.2 Helmholtz free energy

The total Helmholtz free energy per unit mass, as the state potential of the model, is expressed in terms of physically reasonable deformation measures in the intermediate configurations. Therefore, next to the symmetric right Cauchy-Green tensor $\boldsymbol{C} = \boldsymbol{F}^T\boldsymbol{F}$, the elastic and plastic Cauchy-Green-like tensors

$$\boldsymbol{C}_{e1} = \boldsymbol{F}_{e1}^T\,\boldsymbol{F}_{e1} = \boldsymbol{F}_p^{-T}\,\boldsymbol{C}\,\boldsymbol{F}_p^{-1}, \quad \boldsymbol{C}_{pe} = \boldsymbol{F}_{pe}^T\,\boldsymbol{F}_{pe}, \quad \boldsymbol{C}_{e2} = \boldsymbol{F}_{e2}^T\,\boldsymbol{F}_{e2} = \boldsymbol{F}_v^{-T}\,\boldsymbol{C}\,\boldsymbol{F}_v^{-1} \tag{2.2}$$

are introduced, according to Vladimirov et al. [2008]; Brepols et al. [2020]. Here, the general form of the total Helmholtz free energy ψ is additively decomposed, following the idea presented in Fig. 2.1

$$\psi(\boldsymbol{C}_{e1}, \boldsymbol{C}_{e2}, \boldsymbol{C}_{pe}, \chi, \theta) = \psi_1(\boldsymbol{C}_{e1}, \boldsymbol{C}_{pe}, \chi, \theta) + \psi_2(\boldsymbol{C}_{e2}, \theta) + \psi_c(\chi, \theta), \tag{2.3}$$

where ψ_1 and ψ_2 denote the energies related to the elasto-plastic and visco-elastic contributions, respectively. Analogously to Anand et al. [2009]; Ames et al. [2009]; Felder et al. [2020b, 2022], the state potential is extended by a caloric contribution ψ_c in order to ensure flexibility regarding the function for the heat capacity c_T derived in Sec. 2.3.5. As indicated in (2.3), all energetic contributions jointly depend on the temperature field via the absolut temperature θ. The first term ψ_1 contains an elastic part ψ_{e1} based on the elastic right Cauchy-Green tensor $\boldsymbol{C}_{e1}$ and the degree of crystallinity χ

$$\psi_1(\boldsymbol{C}_{e1}, \boldsymbol{C}_{pe}, \chi, \theta) = \psi_{e1}(\boldsymbol{C}_{e1}, \chi, \theta) + \psi_p(\boldsymbol{C}_{pe}, \chi, \theta), \tag{2.4}$$

to account for the influence of the microstructural morphology. Note here that no distinction is made between the underlying crystal configurations and that the DOC in this framework serves as a constant input quantity. In addition, a defect energy ψ_p related to kinematic hardening is introduced, depending on $\boldsymbol{C}_{pe}$ as well as χ. The energy related to viscous effects ψ_2, is expressed in terms of the elastic right Cauchy-Green-like tensor $\boldsymbol{C}_{e2}$ as the sole deformation measure.

2.3.3 Second law of thermodynamics: Clausius-Duhem inequality

To ensure non negative internal dissipation, the model equations need to fulfill the second law of thermodynamics. Therefore, the state relations are derived from the local form of the Clausius-Duhem inequality:

$$\boldsymbol{S} : \frac{1}{2}\dot{\boldsymbol{C}} - \rho_0(\dot{\psi} + \eta\dot{\theta}) - \frac{1}{\theta}\,\boldsymbol{q}_0 \cdot \mathrm{Grad}(\theta) \geq 0. \tag{2.5}$$

Here, $\boldsymbol{S}$ is the second Piola-Kirchhoff stress tensor, ρ_0 represents the material density per unit reference volume and η the entropy. The heat flux with respect to the reference configuration is introduced as $\boldsymbol{q}_0$. Considering the assumed form of ψ_1 and ψ_2 in Eq. 2.3, the time derivative of the Helmholtz free energy is expressed as

$$\dot{\psi} = \frac{\partial \psi_{e1}}{\partial \boldsymbol{C}_{e1}} : \dot{\boldsymbol{C}}_{e1} + \frac{\partial \psi_p}{\partial \boldsymbol{C}_{pe}} : \dot{\boldsymbol{C}}_{pe} + \frac{\partial \psi_2}{\partial \boldsymbol{C}_{e2}} : \dot{\boldsymbol{C}}_{e2} + \frac{\partial \psi}{\partial \theta}\,\dot{\theta} \tag{2.6}$$

The reader is kindly reminded that the derivatives with respect to χ vanish, since the DOC is assumed to be constant in this constitutive framework. Now, using the chain rule of differentiation and additionally the relation $\boldsymbol{L}_p = \dot{\boldsymbol{F}}_p \boldsymbol{F}_p^{-1}$ and $\boldsymbol{L}_{pi} = \dot{\boldsymbol{F}}_{pi} \boldsymbol{F}_{pi}^{-1}$ for the velocity

gradients, the derivatives of $\boldsymbol{C}_{e1}$ and $\boldsymbol{C}_{pe}$ can be reformulated as

$$\dot{\boldsymbol{C}}_{e1} = -\boldsymbol{L}_p^T \boldsymbol{C}_{e1} + \boldsymbol{F}_p^{-T} \dot{\boldsymbol{C}} \boldsymbol{F}_p^{-1} - \boldsymbol{C}_{e1} \boldsymbol{L}_p, \quad \dot{\boldsymbol{C}}_{pe} = -\boldsymbol{L}_{pi}^T \boldsymbol{C}_{pe} + \boldsymbol{F}_{pi}^{-T} \dot{\boldsymbol{C}}_p \boldsymbol{F}_{pi}^{-1} - \boldsymbol{C}_{pe} \boldsymbol{L}_{pi}. \tag{2.7}$$

Here, the identities $\dot{\boldsymbol{F}}_p^{-1} = -\boldsymbol{F}_p^{-1}\, \dot{\boldsymbol{F}}_p^{-1}\, \boldsymbol{F}_p^{-1}$ and $\dot{\boldsymbol{F}}_p^{-T} = -\boldsymbol{F}_p^{-T}\, \dot{\boldsymbol{F}}_p^{T}\, \boldsymbol{F}_p^{-T}$ have been used for the derivation of $\dot{\boldsymbol{C}}_{e1}$ and $\dot{\boldsymbol{F}}_{pe}^{\ -1} = -\boldsymbol{F}_{pe}^{-1}\, \dot{\boldsymbol{F}}_{pe}^{-1}\, \boldsymbol{F}_{pe}^{-1}$ and $\dot{\boldsymbol{F}}_{pe}^{-T} = -\boldsymbol{F}_{pe}^{-T}\, \dot{\boldsymbol{F}}_{pe}^{T}\, \boldsymbol{F}_{pe}^{-T}$ for the derivation of $\dot{\boldsymbol{C}}_{pe}$. The viscous deformation rate $\dot{\boldsymbol{C}}_{e2}$ is derived analogously using the corresponding inelastic velocity gradient $\boldsymbol{L}_v = \dot{\boldsymbol{F}}_v\, \boldsymbol{F}_v^{-1}$. In the next step, ψ_{e1} is assumed to be an isotropic function of $\boldsymbol{C}_{e1}$, therefore coaxiality between $\boldsymbol{C}_{e1}$ and $\partial\psi_{e1}/\partial\boldsymbol{C}_{e1}$ can be shown. Together with the relation for a scalar product of two second-order tensors ($\boldsymbol{A} : \boldsymbol{B} = \mathrm{tr}(\boldsymbol{A}^T\boldsymbol{B}) = \mathrm{tr}(\boldsymbol{A}\boldsymbol{B}^T)$) this results in the identity

$$\frac{\partial \psi_{e1}}{\partial \boldsymbol{C}_{e1}} : \boldsymbol{C}_{e1} \boldsymbol{L}_p = \boldsymbol{C}_{e1} \frac{\partial \psi_{e1}}{\partial \boldsymbol{C}_{e1}} : \boldsymbol{L}_p = \boldsymbol{C}_{e1} \frac{\partial \psi_{e1}}{\partial \boldsymbol{C}_{e1}} : \boldsymbol{D}_p. \tag{2.8}$$

Here, the velocity gradient $\boldsymbol{L}_p$ can be replaced by its symmetric part $\mathrm{sym}\boldsymbol{L}_p = \boldsymbol{D}_p$, the plastic rate of deformation tensor, since the product of $\boldsymbol{C}_{e1}$ and $\partial\psi_{e1}/\partial\boldsymbol{C}_{e1}$ is symmetric. Analogously, ψ_p and ψ_{e2} are assumed to be isotropic functions of $\boldsymbol{C}_{pe}$ and $\boldsymbol{C}_{e2}$, respectively. Thus, similar relations as in Eq. 2.8 are obtained for these quantities. Now, the reformulated energy rate $\dot{\psi}$ is inserted back into Eq. 2.5

$$\begin{aligned}
&\left(\boldsymbol{S} - 2\rho_0 \boldsymbol{F}_p^{-1} \frac{\partial \psi_{e1}}{\partial \boldsymbol{C}_{e1}} \boldsymbol{F}_p^{-T} - 2\rho_0 \boldsymbol{F}_v^{-1} \frac{\partial \psi_{e2}}{\partial \boldsymbol{C}_{e2}} \boldsymbol{F}_v^{-T} \right) : \frac{1}{2} \dot{\boldsymbol{C}} \\
&+ \left(2\rho_0 \boldsymbol{C}_{e1} \frac{\partial \psi_{e1}}{\partial \boldsymbol{C}_{e1}} - 2\rho_0\, \boldsymbol{F}_{pe} \frac{\partial \psi_p}{\partial \boldsymbol{C}_{pe}} \boldsymbol{F}_{pe}^T \right) : \boldsymbol{D}_p + \left(2\rho_0\, \boldsymbol{C}_{pe} \frac{\partial \psi_p}{\partial \boldsymbol{C}_{pe}} \right) : \boldsymbol{D}_{pi} \\
&+ \left(2\rho_0 \boldsymbol{C}_{e2} \frac{\partial \psi_{e2}}{\partial \boldsymbol{C}_{e2}} \right) : \boldsymbol{D}_v + \rho_0 \left(\frac{\partial \psi}{\partial \theta} + \eta \right) \dot{\theta} - \frac{1}{\theta}\, \boldsymbol{q}_0 \cdot \mathrm{Grad}(\theta) \geq 0,
\end{aligned} \tag{2.9}$$

using the relation $\dot{\boldsymbol{D}}_p = \dfrac{1}{2}\, \boldsymbol{F}_p^{-T} \boldsymbol{C}_p \boldsymbol{F}_p^{-1}$. For arbitrary $\dot{\boldsymbol{C}}$, the second Piola-Kirchhoff stress tensor $\boldsymbol{S}$ is chosen according to the Coleman-Noll procedure Coleman and Noll [1961] as

$$\boldsymbol{S} = \boldsymbol{S}_1 + \boldsymbol{S}_2, \tag{2.10}$$

where $\boldsymbol{S}_1$ and $\boldsymbol{S}_2$ represent the second Piola-Kirchhoff stresses corresponding to the elasto-plastic and visco-elastic model, respectively

$$\boldsymbol{S}_1 = 2\rho_0 \boldsymbol{F}_p^{-1} \frac{\partial \psi_{e1}}{\partial \boldsymbol{C}_{e1}} \boldsymbol{F}_p^{-T}, \quad \boldsymbol{S}_2 = 2\rho_0 \boldsymbol{F}_v^{-1} \frac{\partial \psi_2}{\partial \boldsymbol{C}_{e2}} \boldsymbol{F}_v^{-T}. \tag{2.11}$$

In addition, definitions for the Mandel stresses $\boldsymbol{M}_1$ and $\boldsymbol{M}_2$ in the intermediate configurations ic_1 and ic_2 are introduced

$$\boldsymbol{M}_1 = 2\rho_0 \boldsymbol{C}_{e1} \frac{\partial \psi_{e1}}{\partial \boldsymbol{C}_{e1}}, \quad \boldsymbol{M}_2 = 2\rho_0 \boldsymbol{C}_{e2} \frac{\partial \psi_2}{\partial \boldsymbol{C}_{e2}}. \tag{2.12}$$

Moreover, the back stress $\boldsymbol{X}$ related to kinematic hardening in ic_1 and the Mandel stress corresponding to kinematic hardening $\boldsymbol{M}_{1,\text{kin}}$ follow to

$$\boldsymbol{X} = 2\rho_0 \, \boldsymbol{F}_{pe} \frac{\partial \psi_p}{\partial \boldsymbol{C}_{pe}} \boldsymbol{F}_{pe}^T, \quad \boldsymbol{M}_{1,\text{kin}} = 2\rho_0 \, \boldsymbol{C}_{pe} \frac{\partial \psi_p}{\partial \boldsymbol{C}_{pe}}. \tag{2.13}$$

The entropy is specified as

$$\eta = -\partial\psi/\partial\theta \tag{2.14}$$

to a priori fullfill the thermodynamic restrictions and a heat flux according to Fourier's law in the reference configuration

$$\boldsymbol{q}_0 = -J \, \lambda_T \, \boldsymbol{C}^{-1} \, \text{Grad}(\theta) \tag{2.15}$$

is chosen with $J = \det\boldsymbol{F}$ and $\lambda_T(\theta)$ denoting the temperature dependent heat conductivity. Exploiting Eq. 2.9, together with Eq. 2.10 - 2.15 leads to a reduced form of the Clausius-Duhem inequality

$$(\boldsymbol{M}_1 - \boldsymbol{X}) : \boldsymbol{D}_p + \boldsymbol{M}_{1,\text{kin}} : \boldsymbol{D}_{pi} + \boldsymbol{M}_2 : \boldsymbol{D}_v \geq 0. \tag{2.16}$$

2.3.4 Evolution equations and proof of thermodynamic consistency

2.3.4.1 Yield function and elasto-plastic evolution

Following Tschoegl [1971]; Ghorbel [2008]; Melro et al. [2013*b*], a Tschoegl-type or paraboloid yield criterion

$$\Phi_p = 3J_2 + (m-1)\,\sigma_t^0 I_1 - m\,(\sigma_t^0)^2 \leq 0 \tag{2.17}$$

is considered, which includes a tension-compression asymmetry in yielding. It depends on the first ($I_1 = \text{tr}(\boldsymbol{\Sigma})$) and second ($J_2 = 1/2\,\text{tr}(\text{dev}((\boldsymbol{\Sigma}))^2)$) invariant of the relative stress $\boldsymbol{\Sigma} = \boldsymbol{M}_1 - \boldsymbol{X}$ and thus accounts for the effects of hydrostatic pressure on the yielding behavior. The tension-compression flow asymmetry is introduced via the ratio m

$$m = \frac{\sigma_c^0(\chi,\theta)}{\sigma_t^0(\chi,\theta)}, \tag{2.18}$$

between the initial yield stresses in tension σ_t^0 and compression σ_c^0. Note here that both material quantities are assumed to depend independently on the degree of crystallinity and the temperature, resulting in a varying ratio m with temperature evolution. Under the assumption of associative plasticity, the evolution equation for the plastic strain rate follows to

$$\boldsymbol{D}_p = \dot{\lambda}_p \frac{\partial \Phi_p}{\partial \boldsymbol{\Sigma}} = \dot{\lambda}_p \Big(3\,\mathrm{dev}(\boldsymbol{\Sigma}) + (m-1)\,\sigma_t^0\,\boldsymbol{I} \Big), \tag{2.19}$$

where $\dot{\lambda}_p$ denotes the plastic multiplier. The evolution equation for $\boldsymbol{D}_{pi}$ is chosen to model nonlinear Armstrong-Frederick kinematic hardening according to Armstrong et al. [1966]

$$\boldsymbol{D}_{pi} = \dot{\lambda}_p \frac{b}{c} \mathrm{dev}(\boldsymbol{M}_{1,\mathrm{kin}}), \tag{2.20}$$

with the corresponding material parameters b and c. Since the Mandel stress of kinematic hardening depends on c (Eq. 2.37,2.39), the ratio b/c is introduced for dimensional reasons. Finally, the Karush-Kuhn-Tucker conditions complete the constitutive equations for the elasto-plastic model part, i. e.

$$\dot{\lambda}_p \geq 0, \quad \Phi_p \leq 0, \quad \dot{\lambda}_p\,\Phi_p = 0. \tag{2.21}$$

2.3.4.2 Visco-elastic evolution

The evolution equation for the visco-elastic part in the intermediate configuration ic_2 is chosen according to Reese and Govindjee [1998]

$$\boldsymbol{D}_v = \frac{\partial g}{\partial \boldsymbol{M}_2} = \frac{1}{2\tau\mu_2} \mathrm{dev}(\boldsymbol{M}_2) + \frac{1}{9\tau K_2} \mathrm{tr}(\boldsymbol{M}_2)\,\boldsymbol{I}, \tag{2.22}$$

where $g(\boldsymbol{M}_2)$ is a potential introduced in Reese and Govindjee [1998]. Thereby, the bulk modulus $K_2(\theta)$ as well as the shear modulus $\mu_2(\theta)$ are temperature dependent quantities related to the material stiffness defined in Sec. 2.3.7. The relaxation time τ determines how fast the material releases stresses and must therefore be larger than zero. In this work, $\tau(\boldsymbol{\tau}_2, \theta)$ is chosen as a function of the Kirchhoff stress of the visco-elastic part ($\boldsymbol{\tau}_2$) as well as the temperature. For the specific function, the reader is referred to Sec. 2.4.

Note on thermodynamic consistency

For a more detailed derivation of the elasto-plastic part, the reader is kindly referred to Vladimirov et al. [2008]; Brepols et al. [2020]. In these works, the classical von Mises yield criterion is exploited, in a framework considering isotropic and kinematic hardening, to

derive the plastic flow rule and prove the thermodynamic consistency. The thermodynamic consistency of the constitutive model presented here can be shown in a similar manner, using the approach of Reese and Govindjee [1998] for the visco-elastic part.

2.3.5 First law of thermodynamics: energy balance

In the following section, the local form of the energy balance with respect to the reference configuration

$$\rho_0 \, \dot{e} + \mathrm{Div}(\boldsymbol{q}_0) - \boldsymbol{S} : \frac{1}{2} \dot{\boldsymbol{C}} = 0 \tag{2.23}$$

is evaluated to derive the heat generation in a thermodynamically consistent manner. Therefore, the time derivative of the internal energy

$$\dot{e} = \dot{\psi} + \dot{\eta} \, \theta + \eta \, \dot{\theta} \tag{2.24}$$

is exploited. Subsequently, the rate of the total Helmholtz free energy (Eq. 2.6) is inserted in Eq. 2.23 and Eq. 2.14 is recalled to derive the entropy rate $\dot{\eta} = -\partial \dot{\psi} / \partial \theta$. Using the relations derived in Eq. 2.7- 2.13 as well as Eq. 2.16, the partial differential equation for the temperature field follows to

$$\rho_0 \, c_T \, \dot{\theta} = r_e + r_p + r_v - \mathrm{Div}(\boldsymbol{q}_0) \tag{2.25}$$

$$r_e = \theta \left(\frac{\partial \boldsymbol{S}_1}{\partial \theta} : \frac{1}{2} \dot{\boldsymbol{C}} + \frac{\partial \boldsymbol{S}_2}{\partial \theta} : \frac{1}{2} \dot{\boldsymbol{C}} \right) \tag{2.26}$$

$$r_p = \left(\boldsymbol{M}_1 - \theta \, \frac{\partial \boldsymbol{M}_1}{\partial \theta} \right) : \boldsymbol{D}_p - \left(\boldsymbol{X} - \theta \, \frac{\partial \boldsymbol{X}}{\partial \theta} \right) : \boldsymbol{D}_p + \left(\boldsymbol{M}_{1,\mathrm{kin}} - \theta \, \frac{\partial \boldsymbol{M}_{1,\mathrm{kin}}}{\partial \theta} \right) : \boldsymbol{D}_{pi} \tag{2.27}$$

$$r_v = \left(\boldsymbol{M}_2 - \theta \, \frac{\partial \boldsymbol{M}_2}{\partial \theta} \right) : \boldsymbol{D}_v \tag{2.28}$$

Here, the specific heat capacity was introduced as

$$c_T = -\theta \, \frac{\partial^2 \psi}{\partial \theta^2}. \tag{2.29}$$

From Eq. 2.29 it can be seen, that the heat capacity in theory is a complex function of all internal variables. However, coming back to the definition of the total Helmholtz free energy in Eq. 2.3, a caloric energy term ψ_c was added to ensure flexibility regarding the function for the heat capacity which otherwise would be a priori defined. In reality it is hard to asses these energetic contributions experimentally for inelastic materials and thus derive the heat capacity

in closed form Anand et al. [2009]; Ames et al. [2009]; Felder et al. [2022]. Therefore, in this work, the heat capacity is approximated by a constant value $c_T = c_T(\chi, \theta)$ for each DOC and test temperature according to cited literature. In Sec. 2.4, experiments are conducted to determine the specific heat capacity for the underlying morphology.

2.3.6 Representation of the constitutive equations in the reference configuration

In the preceding sections, the constitutive equations of the model were derived in a thermodynamically consistent manner, resulting in quantities in multiple configurations. However, since the intermediate configurations are non-unique, all quantities defined with respect to ic_1, ic_1^i and ic_2 can not be computed directly without further treatment (Holthusen et al. [2023]). Thus, several pull-back operations are needed to arrive at unique and therefore calculable quantities in the reference configuration. Simultaneously, this procedure allows the application of an exponential map algorithm (Vladimirov et al. [2008]) to integrate the evolution equations which automatically preserves the symmetry of the internal variables as well as the material's incompressibility.

Since ψ_{e1} and ψ_{e2} are isotropic functions of $\boldsymbol{C}_{e1}$ and $\boldsymbol{C}_{e2}$, respectively, one can directly show that $\boldsymbol{S}_1$ and$\boldsymbol{S}_2$ are unique using the concept of invariants Spencer [1971]. Now, the relations from Eq. 2.2 can be used to reformulate the Second Piola-Kirchhoff stresses in terms of $\boldsymbol{C}$ and $\boldsymbol{C}_p$ or $\boldsymbol{C}_v$. A similar observation can be made for the back stress tensor in the reference configuration $\bar{\boldsymbol{X}}$. The rates of the plastic and viscous right Cauchy-Green-like tensors are defined as

$$\dot{\boldsymbol{C}}_p = 2\,\boldsymbol{F}_p^T\,\boldsymbol{D}_p\,\boldsymbol{F}_p, \quad \dot{\boldsymbol{C}}_{pi} = 2\,\boldsymbol{F}_{pi}^T\,\boldsymbol{D}_{pi}\,\boldsymbol{F}_{pi}, \quad \dot{\boldsymbol{C}}_v = 2\,\boldsymbol{F}_v^T\,\boldsymbol{D}_v\,\boldsymbol{F}_v. \tag{2.30}$$

Using the aforementioned relations together with Eq. 2.19, 2.20 and 2.22, the evolution equations can be represented in the refererence configuration as

$$\dot{\boldsymbol{C}}_p = 2\,\dot{\lambda}_p\,\boldsymbol{F}_p^T\,\frac{\partial \Phi_p}{\partial \boldsymbol{\Sigma}}\,\boldsymbol{F}_p, \quad \dot{\boldsymbol{C}}_{pi} = 2\,\dot{\lambda}_p\,\frac{b}{c}\,\boldsymbol{F}_{pi}^T\,\mathrm{dev}(\boldsymbol{M}_{1,\mathrm{kin}})\,\boldsymbol{F}_{pi}, \quad \dot{\boldsymbol{C}}_v = 2\,\boldsymbol{F}_v^T\,\frac{\partial g}{\partial \boldsymbol{M}_2}\,\boldsymbol{F}_v. \tag{2.31}$$

Next, the thermodynamic driving forces of the elasto-plastic part are pulled-back to the reference configuration

$$\boldsymbol{M}_1 = 2\,\rho_0\,\boldsymbol{C}_{e1}\,\frac{\partial \psi_{e1}}{\partial \boldsymbol{C}_{e1}} = 2\rho_0 \boldsymbol{F}_p^{-T}\boldsymbol{C}\boldsymbol{F}_p^{-1}\frac{\partial \psi_{e1}}{\partial \boldsymbol{C}_{e1}}\boldsymbol{F}_p^{-T}\boldsymbol{F}_p^{T} = \boldsymbol{F}_p^{-T}\boldsymbol{C}\boldsymbol{S}_1\boldsymbol{F}_p^{T} \tag{2.32}$$

$$\begin{aligned}\boldsymbol{X} &= 2\,\rho_0\,\boldsymbol{F}_{pe}\,\frac{\partial \psi_p}{\partial \boldsymbol{C}_{pe}}\,\boldsymbol{F}_{pe}^{T} = 2\rho_0\,\boldsymbol{F}_p\,\boldsymbol{F}_{pi}^{-1}\,\frac{\partial \psi_p}{\partial \boldsymbol{C}_{pe}}\,\boldsymbol{F}_{pi}^{-T}\,\boldsymbol{F}_p^{T} = \boldsymbol{F}_p\,\bar{\boldsymbol{X}}\,\boldsymbol{F}_p^{T} \\ &= \boldsymbol{F}_p^{-T}\boldsymbol{F}_p^{T}\,\boldsymbol{F}_p\,\bar{\boldsymbol{X}}\,\boldsymbol{F}_p^{T} = \boldsymbol{F}_p^{-T}\,\boldsymbol{C}_p\,\bar{\boldsymbol{X}}\,\boldsymbol{F}_p^{T}\end{aligned} \tag{2.33}$$

$$\begin{aligned}\boldsymbol{M}_{1,\text{kin}} &= 2\rho_0\,\boldsymbol{C}_{pe}\,\frac{\partial \psi_p}{\partial \boldsymbol{C}_{pe}} = 2\rho_0\,\boldsymbol{F}_{pi}^{-T}\,\boldsymbol{C}_p\,\boldsymbol{F}_{pi}^{-1}\,\frac{\partial \psi_p}{\partial \boldsymbol{C}_{pe}}\,\boldsymbol{F}_{pi}^{-T}\,\boldsymbol{F}_{pi}^{T} \\ &= \boldsymbol{F}_{pi}^{-T}\,\boldsymbol{C}_p\,\bar{\boldsymbol{X}}\,\boldsymbol{F}_{pi}^{T} = \boldsymbol{F}_{pi}^{-T}\,\boldsymbol{Y}_{\text{kin}}\,\boldsymbol{F}_{pi}^{T}\end{aligned} \tag{2.34}$$

showing that $\boldsymbol{M}_1$ and $\boldsymbol{C}\,\boldsymbol{S}_1$ as well as $\boldsymbol{X}$ and $\boldsymbol{C}_p\,\bar{\boldsymbol{X}}$ are similar tensors [1] and share the same eigenvalues. Now, the relative stress can be reformulated as

$$\boldsymbol{\Sigma} = \boldsymbol{M}_1 - \boldsymbol{X} = \boldsymbol{F}_p^{-T}\,(\boldsymbol{C}\,\boldsymbol{S}_1 - \boldsymbol{C}_p\,\bar{\boldsymbol{X}})\,\boldsymbol{F}_p^{T} = \boldsymbol{F}_p^{-T}\,\boldsymbol{Y}\,\boldsymbol{F}_p^{T}. \tag{2.35}$$

Thus, since the yield function Φ_p is an isotropic function of $\boldsymbol{\Sigma}$, it can equally be expressed as $\Phi_p = \Phi_p(\boldsymbol{\Sigma}) = \Phi_p(\boldsymbol{Y})$. In the same manner, pull-back operations for the visco-elastic part can be deduced (see Tab. 2.1), since it can be shown that $\boldsymbol{M}_2$ and $\boldsymbol{C}\boldsymbol{S}_2$ are similar. Regarding the internal dissipative heat sources, pull-back operations need to be applied to r_p and r_v as well. Here, it is made use of Eq. 2.30-2.34, to arrive at the final form. Finally, all quantities are expressed in terms of $\boldsymbol{C}$ and the internal variables $\boldsymbol{C}_p$, $\boldsymbol{C}_{pi}$ and $\boldsymbol{C}_v$. An overview of the constitutive equations in the reference configuration is given in Tab. 2.1.

2.3.7 Specific choice of the Helmholtz free energy

Until this point, the constitutive framework has been presented in a quite general manner, to allow for a flexible adaption of the model to other polymeric materials. To proceed with the identification of the model using the experimental results in Section 2.4, however, a particular choice for the energetic contributions is required. Note, for consistency the subsequent energies are expressed in terms of the elastic right Cauchy-Green tensors $\boldsymbol{C}_{e1}$ and $\boldsymbol{C}_{e2}$ in the intermediate configurations. They can of course be equivalently reformulated in terms of the corresponding quantities of the reference configurations $\boldsymbol{C}, \boldsymbol{C}_p$ and $\boldsymbol{C}_v$ as well.

[1] Two arbitrary tensors $\boldsymbol{A}$ and $\boldsymbol{B}$ are similar if $\boldsymbol{A} = \boldsymbol{C}\,\boldsymbol{B}\,\boldsymbol{C}^{-1}$ holds for invertible $\boldsymbol{C}$. By evaluating the characteristic polynomial, it can be shown that $\boldsymbol{A}$ and $\boldsymbol{B}$ share the same eigenvalues and thus the same physical interpretation. Consequently, the invariants of $\boldsymbol{A}$ and $\boldsymbol{B}$ are interchangeable.

For the elasto-plastic model part, the elastic contribution ψ_{e1} is chosen as a compressible Neo-Hookean-type energy

$$\begin{aligned}\psi_{e1} = &\frac{\mu_1}{2}\left(\text{tr}(\boldsymbol{C}_{e1}) - 3\right) - \mu_1 \ln\left(J_{e1}\right) + \frac{\Lambda_1}{4}\left(\det(\boldsymbol{C}_{e1}) - 1 - 2\ln(J_{e1})\right) \\ &- 3\,K_1\alpha_T\,\Delta\theta\ln(J_{e1}),\end{aligned} \tag{2.36}$$

including the two Lamé constants $\mu_1(\chi,\theta)$ and $\Lambda_1(\chi,\theta)$ dependent on the DOC and temperature. Here, $J_{e1} = \det(\boldsymbol{F}_{e1})$ is the determinant of the elastic deformation gradient $\boldsymbol{F}_{e1}$. The elastic energy is extended by a term related to volumetric thermal expansion with the elasto-plastic bulk modulus[2] $K_1(\theta)$, the coefficient of thermal expansion $\alpha_T(\theta)$ and the temperature difference $\Delta\theta = \theta - \theta_0$ between the current temperature θ and the reference temperature θ_0. Alongside the elastic energy, a nonlinear plastic defect energy is introduced to account for kinematic hardening

$$\psi_p = \frac{c}{2}\left(\text{tr}(\boldsymbol{C}_{pe}) - 3\right) - c\ln(\sqrt{J_{pe}}), \tag{2.37}$$

where $J_{pe} = \det(\boldsymbol{C}_{pe})$ holds. Here, $c(\chi,\theta)$ and the second dimensionless parameter $b(\chi,\theta)$, that only shows up in the evolution equation of $\boldsymbol{D}_{pi}$ or $\dot{\boldsymbol{C}}_{pi}$, are material parameters (cf. Armstrong et al. [1966]). With Eq. (2.11) and (2.13), the second Piola Kirchhoff stress for the elasto-plastic part and the thermodynamic conjugate force for kinematic hardening in the reference configuration follow to

$$\boldsymbol{S}_1 = \mu_1(\boldsymbol{C}_p^{-1} - \boldsymbol{C}^{-1}) + \frac{\Lambda_1}{2}\left(\frac{\det(\boldsymbol{C})}{\det(\boldsymbol{C}_p)} - 1\right)\boldsymbol{C}^{-1} - 3K_1\alpha_T(\theta-\theta_0)\boldsymbol{C}^{-1} \tag{2.38}$$

$$\bar{\boldsymbol{X}} = c\,(\boldsymbol{C}_{pi}^{-1} - \boldsymbol{C}_p^{-1}). \tag{2.39}$$

Similar to ψ_{e1}, the visco-elastic energy contribution is defined as

$$\begin{aligned}\psi_2 = &\frac{\mu_2}{2}\left(\text{tr}(\boldsymbol{C}_{e2}) - 3\right) - \mu_2\ln(J_{e2}) + \frac{\Lambda_2}{4}\left(\det(\boldsymbol{C}_{e2}) - 1 - 2\ln(J_{e2})\right) \\ &- 3\,K_2\alpha_T(\theta-\theta_0)\ln(J_{e2}),\end{aligned} \tag{2.40}$$

where $\mu_2(\theta)$ and $\Lambda_2(\theta)$ are the viscous Lamé constants and K_2 is the visco-elastic bulk modulus[2]. The determinant J_{e2} for volumetric thermal expansion is defined as $J_{e2} = \det(\boldsymbol{F}_{e2})$.

[2]The bulk moduli $K_*, * = 1, 2$ are defined by the two Lamé constants μ_* and Λ_* as $K_* = \Lambda_* + \frac{2\mu_*}{3}$.

Following Eq. 2.11, the inelastic second Piola-Kirchhoff tensor $\boldsymbol{S}_{e2}$ takes the form

$$\boldsymbol{S}_2 = \mu_2(\boldsymbol{C}_v^{-1} - \boldsymbol{C}^{-1}) + \frac{\Lambda_2}{2}\left(\frac{\det(\boldsymbol{C})}{\det(\boldsymbol{C}_v)} - 1\right)\boldsymbol{C}^{-1} - 3K_2\alpha_T\,\Delta\theta\,\boldsymbol{C}^{-1}. \tag{2.41}$$

2.3.8 Numerical implementation

The presented thermo-mechanically coupled modeling framework is implemented as a user material subroutine UMAT and UMATHT into the commercial FEM software ABAQUS/Standard. During the solution of a thermo-mechanically coupled boundary value problem, at each Gaussian integration point, the deformation gradient $\boldsymbol{F}$, the temperature θ and the spatial temperature gradient grad(θ) are passed down to the subroutine together with a vector containing all internal variables from the last converged time step. Here, for the time discretization of the local residuals of $\dot{\boldsymbol{C}}_p$, $\dot{\boldsymbol{C}}_{pi}$ and $\dot{\boldsymbol{C}}_v$, the exponential map algorithm is exploited as an implicit time integration scheme. The starting point is a reformulation of the evolution equations from Tab. 2.1:

$$\dot{\boldsymbol{C}}_p = \dot{\lambda}_p\,\boldsymbol{f}_1(\boldsymbol{C},\boldsymbol{C}_p,\boldsymbol{C}_{pi},\theta) = \dot{\lambda}_p\,\boldsymbol{g}_1(\boldsymbol{C},\boldsymbol{C}_p,\boldsymbol{C}_{pi},\theta)\,\boldsymbol{C}_p \tag{2.42}$$

$$\dot{\boldsymbol{C}}_{pi} = \dot{\lambda}_p\,\boldsymbol{f}_{1,\text{kin}}(\boldsymbol{C},\boldsymbol{C}_p,\boldsymbol{C}_{pi},\theta) = \dot{\lambda}_p\,\boldsymbol{g}_{1,\text{kin}}(\boldsymbol{C},\boldsymbol{C}_p,\boldsymbol{C}_{pi},\theta)\,\boldsymbol{C}_{pi} \tag{2.43}$$

$$\dot{\boldsymbol{C}}_v = \boldsymbol{f}_2(\boldsymbol{C},\boldsymbol{C}_v,\theta) = \boldsymbol{g}_2(\boldsymbol{C},\boldsymbol{C}_v,\theta)\,\boldsymbol{C}_v \tag{2.44}$$

with the second order tensors

$$\boldsymbol{f}_1 = (6\,\text{dev}(\boldsymbol{Y}) + 2\,(m-1)\,\sigma_t^0)\,\boldsymbol{C}_p, \qquad \boldsymbol{g}_1 = \boldsymbol{f}_1\boldsymbol{C}_p^{-1} \tag{2.45}$$

$$\boldsymbol{f}_{1,\text{kin}} = 2\,\frac{b}{c}\,\text{dev}(\boldsymbol{Y}_{\text{kin}})\,\boldsymbol{C}_{pi}, \qquad \boldsymbol{g}_{1,\text{kin}} = \boldsymbol{f}_{1,\text{kin}}\boldsymbol{C}_{pi}^{-1} \tag{2.46}$$

$$\boldsymbol{f}_2 = \left(\frac{1}{\tau\mu_2}\,\text{dev}(\boldsymbol{C}\boldsymbol{S}_2) + \frac{2}{9\tau K_2}\,\text{tr}(\boldsymbol{C}\boldsymbol{S}_2)\,\boldsymbol{I}\right)\boldsymbol{C}_v, \quad \boldsymbol{g}_2 = \boldsymbol{f}_2\boldsymbol{C}_v^{-1} \tag{2.47}$$

To integrate equations (2.42) - (2.44), an exponential map algorithm proposed by Reese and Christ [2008]; Vladimirov et al. [2008] is used. This leads to the final form of the discretized evolution equations, displayed in a residuum format together with the yield surface:

$$\boldsymbol{r}_{1,p} = -\boldsymbol{C}_{p,n}^{-1} + \boldsymbol{U}_p^{-1}\exp\left(\Delta\lambda_p\,\boldsymbol{U}_p^{-1}\boldsymbol{f}_1\boldsymbol{U}_p^{-1}\right)\boldsymbol{U}_p^{-1} = \boldsymbol{0} \tag{2.48}$$

$$\boldsymbol{r}_{1,pi} = -\boldsymbol{C}_{pi,n}^{-1} + \boldsymbol{U}_{pi}^{-1}\exp\left(\Delta\lambda_p\,\boldsymbol{U}_{pi}^{-1}\boldsymbol{f}_{1,\text{kin}}\,\boldsymbol{U}_{pi}^{-1}\right)\boldsymbol{U}_{pi}^{-1} = \boldsymbol{0} \tag{2.49}$$

$$r_{1,\sigma} = \Phi_p = 0 \tag{2.50}$$

$$\boldsymbol{r}_{2,v} = -\boldsymbol{C}_{v,n}^{-1} + \boldsymbol{U}_v^{-1}\exp\left(\Delta t\,\boldsymbol{U}_v^{-1}\boldsymbol{f}_2\boldsymbol{U}_v^{-1}\right)\boldsymbol{U}_v^{-1} = \boldsymbol{0} \tag{2.51}$$

Here, the relations $\Delta\lambda_p = \Delta t\,\dot{\lambda}_p$, $\boldsymbol{U}_p = \sqrt{\boldsymbol{C}_p}$, $\boldsymbol{U}_{pi} = \sqrt{\boldsymbol{C}_{pi}}$ and $\boldsymbol{U}_v = \sqrt{\boldsymbol{C}_v}$ are introduced. The index n refers to quantities from the last time step, whereas quantities without index n relate to the current time step. For a more detailed description of the time integration procedure, the reader is kindly referred to Vladimirov et al. [2008]; Brepols et al. [2020]. Due to the symmetry of the internal variables, a system of 13 nonlinear equations, corresponding to the local plastic residual vector $\boldsymbol{r}_{1,\text{loc}} = (\boldsymbol{r}_{1,p}, \boldsymbol{r}_{1,pi}, r_{1,\sigma})^T = \boldsymbol{0}$ must be solved for the elasto-plastic part. Using the Newton-Raphson scheme, the plastic solution vector $\boldsymbol{x}_{1,\text{loc}} = (\hat{\boldsymbol{U}}_p^{-1}, \hat{\boldsymbol{U}}_{pi}^{-1}, \Delta\lambda_p)^T$ is obtained. This procedure requires an additional linearization of the residuals (for constant $\boldsymbol{C}$ and θ) and the calculation of the Jacobian matrix $\boldsymbol{J}_1 = \partial\boldsymbol{r}_{1,\text{loc}}/\partial\boldsymbol{x}_{1,\text{loc}}$. The latter is obtained by automatic differentiation using the software *AceGen* (cf. Korelc [2009]). Likewise, for the visco-elastic part a system of 6 nonlinear equations $\boldsymbol{r}_{2,\text{loc}} = \boldsymbol{r}_{2,v} = \boldsymbol{0}$ is solved for $\hat{\boldsymbol{U}}_v^{-1}$.

After local convergence is achieved, ABAQUS requires the Cauchy stress tensor $\boldsymbol{\sigma}$ and the volumetric heat generation r from the UMAT and the heat flux $\boldsymbol{q}$ from the UMATHT together with the material sensitivities for the global Newton iteration. The rate of the right Cauchy-Green tensor needed for the calculation of the internal heat generation is approximated by $\dot{\boldsymbol{C}} \approx (\boldsymbol{C} - \boldsymbol{C}_n)/\Delta t$. Since the heat generation and the heat flux are derived with respect to the reference configuration (see Tab. 2.1), they firstly need to be related to the current configuration

$$\boldsymbol{q} = -\lambda_T\,\text{grad}(\theta) \tag{2.52}$$

$$r = \frac{1}{J}\,(r_e + r_1 + r_2). \tag{2.53}$$

In terms of the material sensitivies, ABAQUS requires the material tangent modulus $\mathbb{C}_{\boldsymbol{D}}^{\boldsymbol{\sigma}} = 1/J\,\mathbb{C}_{\boldsymbol{D}}^{\boldsymbol{\tau}}$ (DDSDDE), which is related to the tangent modulus tensor $\mathbb{C}_{\boldsymbol{D}}^{\boldsymbol{\tau}}$ for the Jaumann rate of the Kirchhoff stress tensor $\boldsymbol{\tau}$. The linearized incremental form of the Kirchhoff stress can be expressed as

$$\Delta\boldsymbol{\tau} - \Delta\boldsymbol{W}\boldsymbol{\tau} - \boldsymbol{\tau}\Delta\boldsymbol{W}^T = \mathbb{C}_{\boldsymbol{D}}^{\boldsymbol{\tau}}\Delta\boldsymbol{D}, \tag{2.54}$$

where $\Delta\boldsymbol{D}$ and $\Delta\boldsymbol{W}$ refer to the incremental symmetric and antisymmetric parts of the incremental velocity gradient $\Delta\boldsymbol{L}$, respectively. Further, the thermal tangent modulus $\boldsymbol{C}_\theta^{\boldsymbol{\sigma}}$ (DDSDDT) and the derivatives of the internal heat sources with respect to the strain increment

$\boldsymbol{C}_{\boldsymbol{D}}^{r}$ (DRPLDE) and the temperature $C_{\theta}^{\boldsymbol{\sigma}}$ (DRPLDT) are needed:

$$\Delta\boldsymbol{\sigma} = \boldsymbol{C}_{\theta}^{\boldsymbol{\sigma}}\,\Delta\theta \tag{2.55}$$

$$\Delta r = \boldsymbol{C}_{\boldsymbol{D}}^{r} : \Delta\boldsymbol{D} \tag{2.56}$$

$$\Delta r = C_{\theta}^{r}\Delta\theta. \tag{2.57}$$

These quantities are obtained in a consistent manner from the corresponding expressions in the reference configuration utilizing the algorithmic differentiation tool *AceGen*. Thus, quadratic convergence within the global Newton-Raphson iteration is achieved. The push forward operations can be found in Appendix 2.7.1 alongside a more detailed derivation of the tangent operators.

Table 2.1: Overview over the constitutive equations in the reference configuration.

Elasto-plastic contribution	Visco-elastic contribution
Stresses $\boldsymbol{S}_1 = \mu_1(\boldsymbol{C}_p^{-1} - \boldsymbol{C}^{-1}) + \frac{\Lambda_1}{2}\left(\frac{\det(\boldsymbol{C})}{\det(\boldsymbol{C}_p)} - 1\right)\boldsymbol{C}^{-1} - 3K_1\alpha_T(\theta-\theta_0)\boldsymbol{C}^{-1}$ $\bar{\boldsymbol{X}} = c\,(\boldsymbol{C}_{pi}^{-1} - \boldsymbol{C}_p^{-1})$ $\boldsymbol{Y} = \boldsymbol{C}\boldsymbol{S}_1 - \boldsymbol{C}_p\bar{\boldsymbol{X}}, \quad \boldsymbol{Y}_{\text{kin}} = \boldsymbol{C}_p\bar{\boldsymbol{X}}$ Yield function $\Phi_p = 3\,J_2 + (m-1)\,\sigma_t^0\,I_1 - m\,(\sigma_t^0)^2$ $I_1 = \text{tr}(\boldsymbol{Y}), \quad J_2 = \frac{1}{2}\,\text{tr}((\text{dev}(\boldsymbol{Y}))^2)$ Evolution equation $\dot{\boldsymbol{C}}_p = \dot{\lambda}_p\,(6\,\text{dev}(\boldsymbol{Y}) + 2\,(m-1)\,\sigma_t^0)\,\boldsymbol{C}_p, \quad \dot{\boldsymbol{C}}_{pi} = 2\,\dot{\lambda}_p\,\frac{b}{c}\,\text{dev}(\boldsymbol{Y}_{\text{kin}})\,\boldsymbol{C}_{pi}$ Heat generation due to plastic dissipation $r_1 = \bar{r}_p = \frac{1}{2}\,\boldsymbol{C}\left(\boldsymbol{S}_1 - \theta\,\frac{\partial \boldsymbol{S}_1}{\partial\theta}\right) : \boldsymbol{C}_p^{-1}\,\dot{\boldsymbol{C}}_p - \frac{1}{2}\left(\bar{\boldsymbol{X}} - \theta\,\frac{\partial\bar{\boldsymbol{X}}}{\partial\theta}\right) : \dot{\boldsymbol{C}}_p$ $+\frac{1}{2}\,\boldsymbol{C}_p\left(\bar{\boldsymbol{X}} - \theta\,\frac{\partial\bar{\boldsymbol{X}}}{\partial\theta}\right) : \boldsymbol{C}_{pi}^{-1}\,\dot{\boldsymbol{C}}_{pi}$	Stress $\boldsymbol{S}_2 = \mu_2(\boldsymbol{C}_v^{-1} - \boldsymbol{C}^{-1}) + \frac{\Lambda_2}{2}\left(\frac{\det(\boldsymbol{C})}{\det(\boldsymbol{C}_v)} - 1\right)\boldsymbol{C}^{-1}$ $-3\,K_2\,\alpha_T\,(\theta-\theta_0)\boldsymbol{C}^{-1}$ Evolution equation $\dot{\boldsymbol{C}}_v = \left(\frac{1}{\tau\mu_2}\,\text{dev}(\boldsymbol{C}\boldsymbol{S}_2) + \frac{2}{9\tau K_2}\,\text{tr}(\boldsymbol{C}\boldsymbol{S}_2)\,\boldsymbol{I}\right)\boldsymbol{C}_v$ Heat generation due to viscous dissipation $r_2 = \bar{r}_v = \frac{1}{2}\,\boldsymbol{C}\left(\boldsymbol{S}_2 - \theta\,\frac{\partial \boldsymbol{S}_2}{\partial\theta}\right) : \boldsymbol{C}_v^{-1}\,\dot{\boldsymbol{C}}_v$
Second Piola-Kirchhoff stress $\boldsymbol{S} = \boldsymbol{S}_1 + \boldsymbol{S}_2$	Elastic heat generation $r_e = \theta\left(\frac{\partial \boldsymbol{S}_1}{\partial\theta} : \frac{1}{2}\,\dot{\boldsymbol{C}} + \frac{\partial \boldsymbol{S}_2}{\partial\theta} : \frac{1}{2}\,\dot{\boldsymbol{C}}\right)$
Heat flux $\boldsymbol{q}_0 = -J\,\lambda_T\,\boldsymbol{C}^{-1}\,\text{Grad}(\theta)$	

2.4 Parameter identification procedure

In this section, a staggered parameter identification scheme is described, to obtain a set of material parameters for each test temperature. Therefore, firstly the experimental data base is discussed (see Sec. 2.4.1), followed by a successive model characterization with a focus on the dependence on the degree of crystallinity and the temperature.

2.4.1 Experimental data base

2.4.1.1 Specimen preparation

All experimental results used in this work for model identification purposes were conducted at the Institute of Mechanics, University of the German Federal Armed Forces, Munich. To that end, the required test specimens were injection moulded at Polymer Service GmbH Merseburg (PSM) as type 1A and 1BA specimens of DIN EN ISO 527-2:2012. In the following, 1BA specimens were used for monotonic tension as well as relaxation tests, whereas the 1A specimens were used to cut smaller specimens (10x4x50 mm^3) from the middle section for compression tests in line with DIN EN ISO 604:2003. Prior to specimen production, the PA6 type B granulate, kindly provided by Bond Laminates (Lanxess), was compounded with an amorphous co-polymer (cyclic olefin copolymer (COC), type: Topas 9506F-500) in four different ratios PA6:COC (1:0, 0.85:0.15, 0.70:0.30, 0.55:0.45). The test specimens were then injection moulded from the granulates. The idea of this blending technique is to achieve different thermally stable volume-crystallinities with a wide range of DOCs, where the change in DOC stems purely from the change in the PA6 mass content to the total compound mass. The resulting material behavior of the blends should therefore reflect the material behavior of pure PA6. Consequently, the blend partner COC was chosen to have a similar glass transition temperature compared to PA6, as well as a stiffness around 4 GPa which corresponds to the stiffness of the amorphous phase of pure PA6 below T_g. Below the glass transition, the material behavior of the blends is influenced by both the amorphous and the crystalline phase. In this case, the similarity of the chosen blend partner to the amorphous PA6 phase should result in a comparable material behavior to pure PA6. Above the glass transition, the stiffness of the amorphous phase reduces to individual MPa, therefore the crystalline phase is mainly responsible for the material performance. Here, the blending technique should enable testing on a broad variety of DOCs, while at the same time post crystallization is avoided. Other methods that alter the DOC, as for example quenching at the end of the injection moulding process or post-processing methods, like annealing, where the specimens are stored at high temperatures

for several hours to enforce further crystallization, result in recrystallization when tested above the glass transition. Here, annealed specimes behave more thermally stable compared to quenched specimens, however, the change in DOC in annealed specimens is only minor and unpredictable. On the other hand, the use of blends should ensure a broad, predictable and most important controllable variety of DOCs, outweighing the complex manufacturing. After the production process, the specimens were stored in a dry chamber (*MP Dry Cabinet IV ST*) at $40°$ C, until the moisture content, obtained from an *Aquatrack* measurement, measured less then $0.1\,\%$.

Blend ratio [%]		DOC [%]		
PA6	COC	1st heating run	1st cooling run	2nd heating run
100	0	29	40	40
85	15	24	34	34
75	25	18	28	28
55	45	15	24	24
0	100	< 1	< 1	< 1

Table 2.2: Differential scanning caliometry (DSC) results for four different blends as well as pure COC. Experimental results from green colored blends are used for model identification, blue colored blends are used for verification purposes.

2.4.1.2 Differential scanning caliometry (DSC)

In a first step, the degree of crystallinity of each blend was determined by differential scanning caliometry (DSC), using a *Q2000* machine from *TA instruments*. Samples of between 5 and 8 mg were cut from the 1BA specimens and heated up from room temperature way above the melting point with a constant heating rate of 10 K/min, repeating the process for each blend. The heat absorption during the endothermic melting of the crystalline regime or, more specifically, the integrated heat flow over time of the melting peak yielded the change in specific enthalpy ΔH_m. Together with the specific fusion enthalpy for a hypothetical 100% crystalline material as $\Delta H_0 = 190\ J/g$ from Campoy et al. [1998], the absolute DOC is obtained by

$$\chi = \frac{\Delta H_m}{\Delta H_0^{100}}. \tag{2.58}$$

In this way, the four DOCs 0.29, 0.24, 0.18 and 0.15 (from highest to lowest PA6 content) were obtained, which will be used for model identification and verification. It should be noted that the DOC for pure PA6 multiplied by the respective blend ratio corresponds well with the measured DSC results for the three blends. Therefore, the authors conclude that the DOC

of polyamide 6 blends can be approcimated with the DSC results for pure PA6 together with the respective blend ratio leading to a possible reduction in experimental effort. Additional measurements conducted by PSM Merseburg GmbH in the first cooling and second heating run confirmed a predictable DOC based on blending ratios. The reproducible DOCs measured 0.4, 0.34, 0.28 and 0.24 from highest to lowest PA6 content. Further, a DSC measurement on pure COC showed a DOC lower then 1% which confirmed that the addition of the co-polymer does not change the resulting crystallization behavior in the specimens. An overview of the DSC results for all four PA6 blends as well as COC can be found in Tab. 2.2. For model identification and verification, the DSC results from the first heating run are used. These results were obtained from samples untreated after injection moulding and therefore contain the production history in terms of, e.g. cooling rate. Since no further (thermal) treatment is applied on the remaining test specimens, the DOC of the first heating run reflects the experimentally tested material morphology. In addition, the glass transition temperature was identified from DSC results. All specimens showed a glass transition temperature at around 58°C, independent of the blend ratio, which supports the hypothesis of an unaltered caloric material behavior through the blending strategy.

2.4.1.3 Monotonic tension tests

For the mechanical tests, a *Zwick/Roell Z020* machine with 2000 N and 500 N force sensors was used, together with a temperature furnace for the test temperatures above room temperature. Preliminary simulations by Kulkarni et al. [2022] identified the relevant magnitude of experimental inputs such as for example strain and strain rates. Concomitant, the specimens were subjected to displacement controlled loading at various loading rates between 0.05 and 1 % per second. Each loading procedure was repeated several times for all four blends at temperatures below and above the glass transition, namely at 23° C, 50° C, 100° C, 130° C and 150° C.

In Fig. 2.2, the results of the monotonic uniaxial tension tests above the glass transition (T_g) for an exemplary loading rate of 0.05 % per second are shown for a stretch of approximately 20%. The true (Cauchy) stress over the logarithmic strain in the loading direction is determined under the assumption of incompressible material behavior, which is reasonable comparing the experimentally determined Poisson's ratio (cf. Sec. 2.4.2). The interested reader is referred to Appendix 2.7.3 for the conversion between engineering (1. Piola-Kirchhoff) and true (Cauchy) stress. In addition, the true stress relation allowed for the investigation of self-heating effects at higher loading rates, which generally lead to thermal softening in polymers. This effect

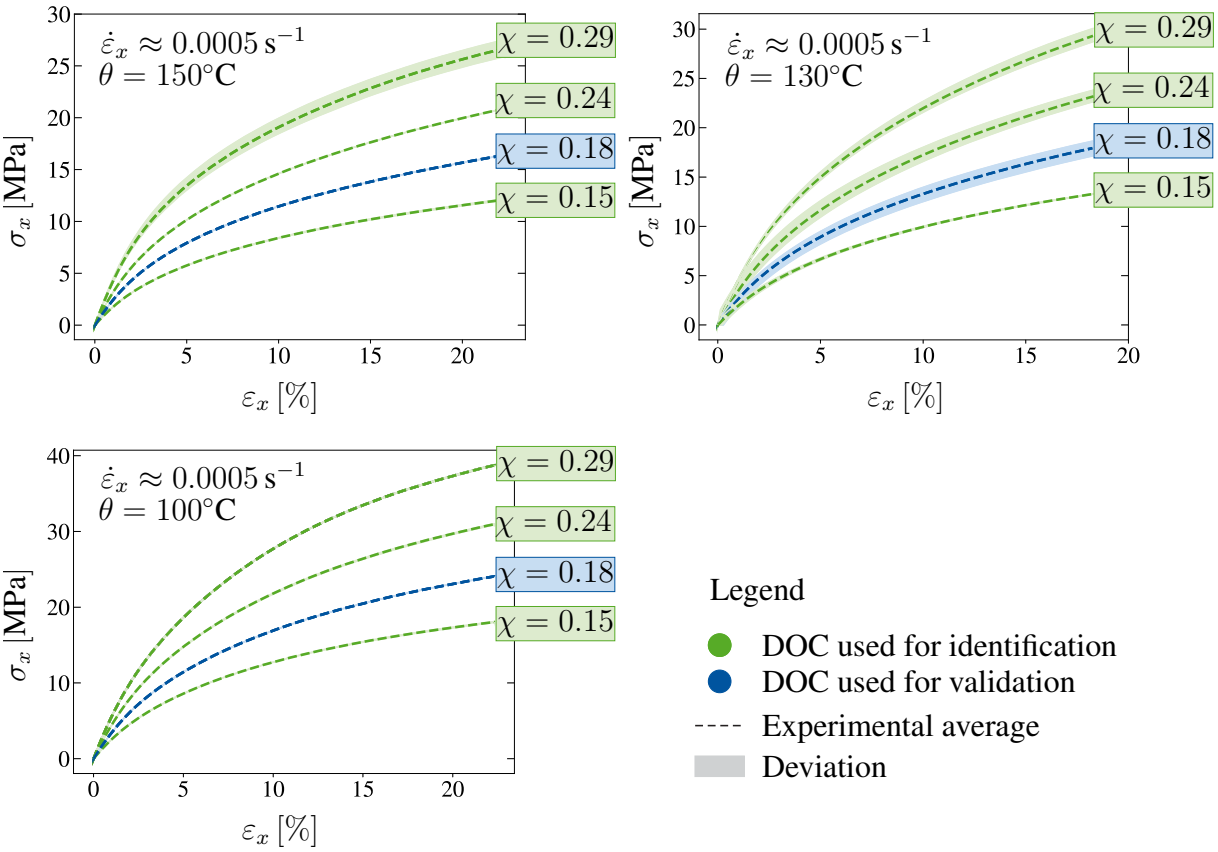

Figure 2.2: Monotonic uniaxial extension: Experimental true strain and stress curves at $\dot{\varepsilon}_x \approx 0.0005\,\mathrm{s}^{-1}$ for multiple degrees of crystallinity (DOC) and temperatures above the glass transition regime.

cannot be accurately identified using the engineering (1. Piola-Kirchhoff) stress, since relating the current force to the reference area results in additional geometric softening at high strains. As a result, both effects overlap and no clear distinction can be made. Here, the dashed lines represent the mean values used in the following sections for identification (green) and validation (blue), whereas the deviation of the experimental results is plotted in terms of minimum and maximum values. Note here that the number of tests per DOC and temperature was too small for the calculation of further statistical measures (e.g. standard deviation) with a useful significance. As expected, a pronounced influence of the temperature and the degree of crystallinity on the material response is visible, in line with e.g. Richeton et al. [2006]; Shan et al. [2007]; Parodi et al. [2018]; Felder et al. [2020a]. An increase in temperature led to a decrease in the overall material stiffness, whereas an increase in crystallinity resulted in a higher initial stiffness, hardening and yield stress. In addition, a gradual roll-over to yielding is apparent, therefore the yield stress in tension cannot be determined directly from

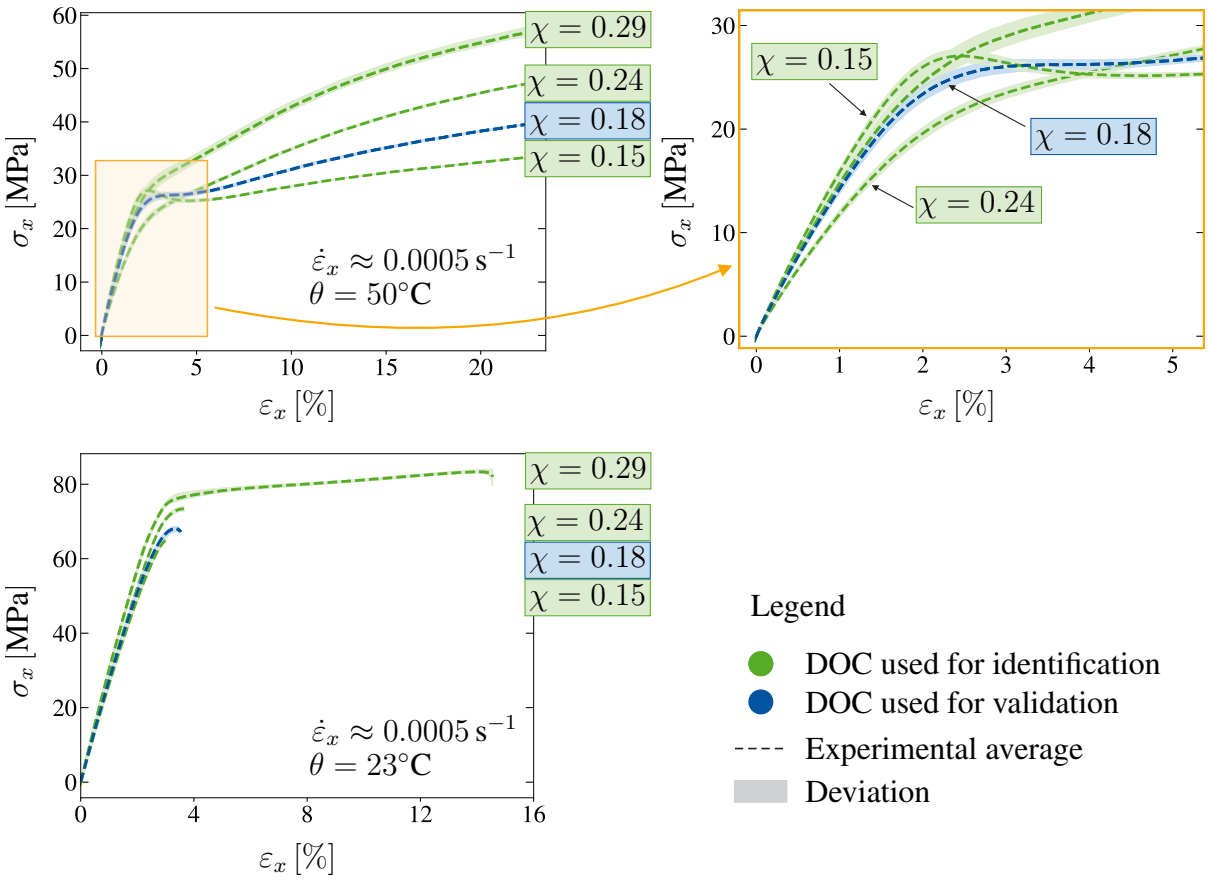

Figure 2.3: Monotonic uniaxial extension: Experimental true strain and stress curves at $\dot{\varepsilon}_x \approx 0.0005\,\mathrm{s}^{-1}$ for multiple degrees of crystallinity (DOC) and temperatures below the glass transition regime.

the peak in the stress-strain curve, nor from the intersection of the initial slope and the hardening slope (e.g. Rae et al. [2007]). Hence, it is chosen as an additional fitting parameter for the identification of the plastic regime. Note here that a similar observation is made for the compressive yield stress, see Fig. 2.6. Below the glass transition, the influence of the DOC is less pronounced, see Fig. 2.3, which can be related to a lower chain mobility in the amorphous phase (Felder et al. [2020a]). Interestingly, at 23° C the blends of PA6 and COC failed earlier than the samples consisting of pure PA6 with a higher total stiffness. This effect can be related to the additional phase boundaries introduced by creating blends. Although binding agents were introduced during compounding to prevent this effect, the apparent heterogeneity of the blends contradicts the hypothesis of an unaltered material behavior below the glass transition temperature. To investigate the material behavior of PA6 for a wide range of crystallinities below the glass transition, other methods as for example the addition of nucleation agents (see e.g. Mudra and Balázs [1998]; Nagarajan et al. [2000]; Menyhárd and Varga [2006]) to pure

PA6 or different compatibilizers in the blends could be tested to improve the results. At 50° C, the experimental results showed the distinct influence of the crystallinity at large strains above 5%. Similar to the test results above T_g, the total stress increased with increasing DOC. However, this trend was not visible in the elastic regime and equally during plastic yielding (see Fig. 2.3). Here, the results from the two blends with the highest COC content ($\chi = 0.18$ and $\chi = 0.15$) differed severly from the results for $\chi = 0.29$ and $\chi = 0.24$ for all measured strain rates. Both curves showed a high initial stiffness and a first yield point, followed by a stress reduction and a second yielding around 10 % strain. This effect is similar to the double yield (DY) phenomenon, reported for amorphous polymers (Boyce et al. [1988]) and polyamide 6 in e.g. Luo et al. [2009]; Parodi et al. [2018]; Hao et al. [2022a]. The first yield point is related to the amorphous phase (Van Dommelen et al. [2003]), whereas the second yield point corresponds to the crystalline regime Hao et al. [2022a]. At this point, it is unclear why this effect was only visible for the two lowest DOCs, however, the authors believe that it could be related to the higher amount of amorphous phase in these specimens. Nevertheless, micromechanical analysis, as for example the determination of crystal configurations via X-ray diffraction and DSC (Fornes and Paul [2003]) or aditional density measurements, would be necessary, to further investigate whether the observed effects are related to the blend composition. In the elastic regime, the influence of the DOC on the initial stiffness differed from the observations made for the other test temperatures. Here, especially for $\chi = 0.29$ and $\chi = 0.24$ a softening in the elastic regime is visible, before the onset of yield is reached. To investigate this phenomenon, an additional dynamic mechanical analysis (DMA) was conducted to determine the storage modulus (stored elastic energy) over the temperature (see Appendix 2.7.2). Here, the decrease in material stiffness started already at around 45°C with a slightly later beginning with decreasing DOC. The glass transition temperature obtained from DMA lies around 58°C as determined in the DSC tests. The authors therefore conclude, that the tests at 50°C were conducted in the glass transition regime of the specimens, where changes in the underlying morphology of the amorphous phase led to a change in the initial stiffness. Here, the glass transition started earlier for blends with a higher DOC, consequently this effect was more pronounced for these blends since their stiffness degradation was further along.

The influence of the loading rate on the material behavior of PA6 is depicted in Fig. 2.4 for various temperatures and a DOC of $\chi = 0.29$. Here, four different strain rates in the range of nearly two decades were tested. In line with findigs from Shan et al. [2007]; Felder et al. [2020a], the initial elastic material response appeared to be mainly independent of the strain rate, especially below the glass transition. In the visco-elastic, elasto-plastic regime, an increasing velocity led to an increase of hardening, especially for temperatures below T_g. In

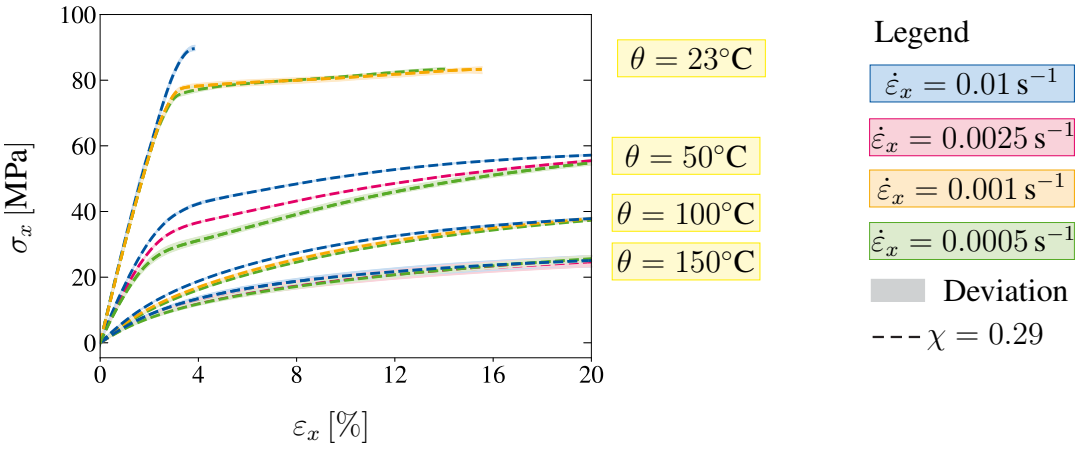

Figure 2.4: Monotonic uniaxial extension: Results for $\chi = 0.29$ at various temperatures and strain rates.

this temperature regime, the failure behavior is affected as well, with a premature failure at high loading rates, corresponding to the increase in the yield stress (cf. $\chi = 0.29$ and $\dot{\varepsilon}_x = 0.01\,\mathrm{s}^{-1}$). Above the glass transition, the influence of the strain rate is less pronounced. These observations correspond with those of Shan et al. [2007], who stated that the yield stress increased logarithmically with an increasing loading rate and that the influence of the velocity reduces in general with increasing temperatures. In addition, thermal softening due to dissipative effects related to material self-heating is observed at higher strain rates (see e.g. Maurel-Pantel et al. [2015]). This effect is mainly visible for temperatures below T_g, where the slope of the stress-strain curve for $\dot{\varepsilon}_x = 0.001\,\mathrm{s}^{-1}$ decreased, compared to the curve corresponding to a velocity of $\dot{\varepsilon}_x = 0.0005\,\mathrm{s}^{-1}$. The curves intersect already at moderate strains of approximately 7%. For temperatures above T_g, this intersection is slightly delayed to strains of around 15%, nontheless, also here self-heating is prominent. To further investigate this effect, experiments using infrared thermography (IR) would be necessary, as done for example in Felder et al. [2020a].

2.4.1.4 Relaxation tests

Moreover, longterm relaxation test data was obtained at all test temperatures and various strains, to provide additional insight into the time dependent material response. To investigate the visco-elastic regime, relaxation tests at 1% strain were carried out, whereas the visco-elastic, elasto-plastic regime was tested at around 19% strain. The experimental results are shown in Fig. 2.5 for exemplary temperatures of 130 °C and 150 °C. Noteworthy, due to the extensive relaxation times (cf. Fig. 2.5), it was not possible to repeat this test with the current

set of specimens. In contrast to e.g. Felder et al. [2020a], the total relaxation time throughout all samples was very high, with a low initial relaxation time and therefore sudden stress reduction in the beginning of the relaxation step. Similar to the tension tests, a temperature depencence was present also in the relaxation tests, where the relaxation time decreased with increasing temperature (see also Sec. 2.4.3). Furthermore, the amount of stress relaxation in the beginning of the relaxation step increased notably at higher strains. This influence, as well as the impact of the degree of crystallinity that is not visible directly from the experimental results, is studied in detail in Sec. 2.4.3., where a post-processing method by Amin et al. [2006] is applied to the experimental data.

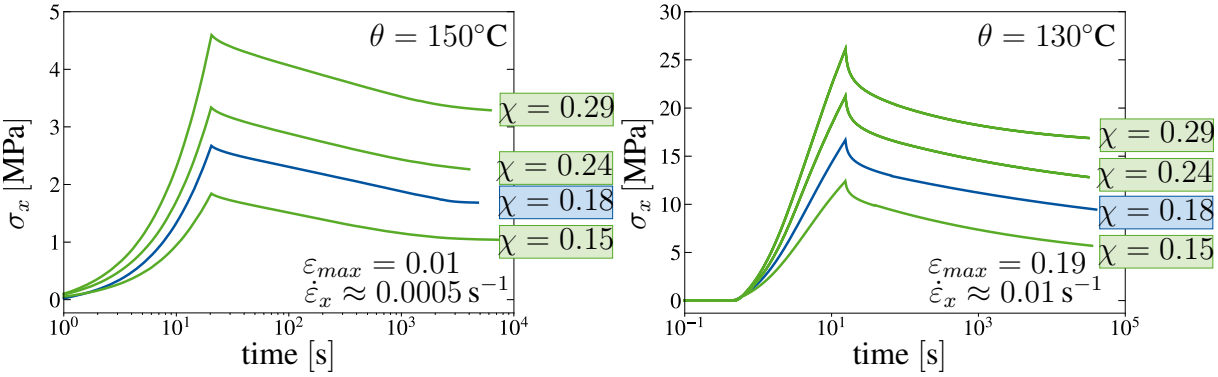

Figure 2.5: Longterm stress relaxation: Experimental true stress over time curves for multiple degrees of crystallinity (DOC) at small strains and 150° C and finite strains and 130° C.

2.4.1.5 Compression tests

To obtain insights into the deformation under compression, monotonic uniaxial compression tests were conducted at various temperatures for $\chi = 0.29$ and $\chi = 0.15$. Therefore, additional samples were cut with a cross-section of approximately 3.77 x 10 mm^2 and tested at $\dot{\varepsilon}_x = 0.0005\,\mathrm{s}^{-1}$ with a *Zwick/Roell Z020* machine under 23° C and 130° C. Additional measurements were carried out at PSM for temperatures of 100° C and 150° C. However, no complete data set for all DOCs was available at the present point of time. The experimental results are displayed in Fig. 2.6. Here, a significant stiffening at high strains, typical for materials under compression, can be observed for all specimens, except for $\chi = 0.15$ at 150° C. Similar to the results in tension, no yield stress was directly detectable from the stress-strain curve for temperatures above the glass transition. The observed influence of temperature and degree of crystallinity is in agreement with the tensile results, where an increasing temperature led to a decrease in stiffness and an increasing DOC resulted in a generally stiffer material response.

Further tests for the remaining blend ratios and test temperatures are necessary to confirm these findings in the future.

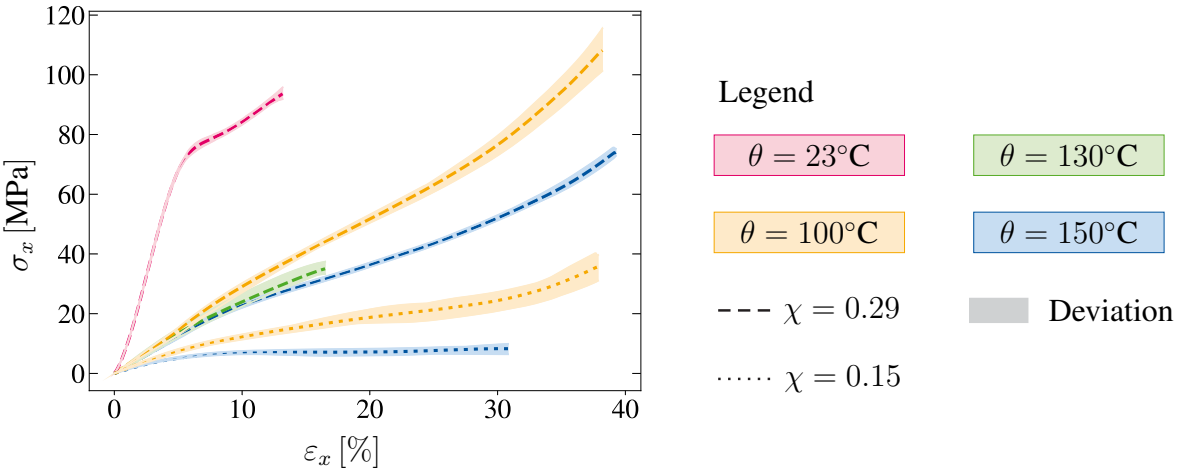

Figure 2.6: Compression tests for $\chi = 0.29$ and $\chi = 0.15$ at various temperatures below and above the glass transition.

2.4.1.6 Thermomechanical analysis (TMA)

To conclude the set of experimental results, additional measurements were conducted to obtain insights into the thermal properties of the material. A thermomechanical analysis (TMA) was conducted on a TMA/SDTA841e from *Mettler Toledo* to obtain the coefficient of thermal expansion (CTE) α_T. The results are shown in Fig. 2.7 a), where the thermal expansion is plotted against the temperature for all DOCs. The corresponding plot of the evaluated CTE (gradient of the graph of dimensional change vs. temperature) plotted over the DOC can be found in Sec. 2.4.5. The CTE generally depends on the glass transition, since thermal expansion is enforced by molecular motions and mobility which are low in the glassy state of the amorphous phase and higher in the rubbery state above the glass transition. This was also visible in the experimental results (cf. Fig. 2.7), where the thermal expansion increased significantly above the glass transition. The dependence of the CTE on the DOC was not pronounced below the glass transition, whereas above T_g a decrease of α_T with increasing DOC was visible. In semi-crystalline polymers, the crystalline phases are interspersed with amorphous regions, therefore their thermal expansion behavior is more complex as in purely amorphous polymers. For example, amorphous regions close or connected to the crystalline phases, the so-called rigid amorphous phase, show less thermal mobility than the bulk amorphous phase (e.g. Menczel and Prime [2009]; Saba and Jawaid [2018]). In addition, the amorphous blend

partner COC adds separate amorphous regions with particular characteristics, therefore the combatibility of the two materials was important during blend composition.

2.4.1.7 Specific heat capacity

To determine the specific heat capacity and its dependence on temperature and DOC, the DSC measurements conducted at PSM Merseburg were evaluated further. To that end, the evolution of the specific heat capacity with increasing temperature is shown in Fig. 2.7 b) for all four blend ratios. The heat capacity can then be identified as the tangent to the experimental curve, with the remaining changes corresponding to structural changes associated with melting of the crystalline phase. There is no clear dependence on the DOC in the experimental results. However, the specific heat increases linearly with increasing temperature, with a lower total value below the glass transition (see Fig. 2.7).

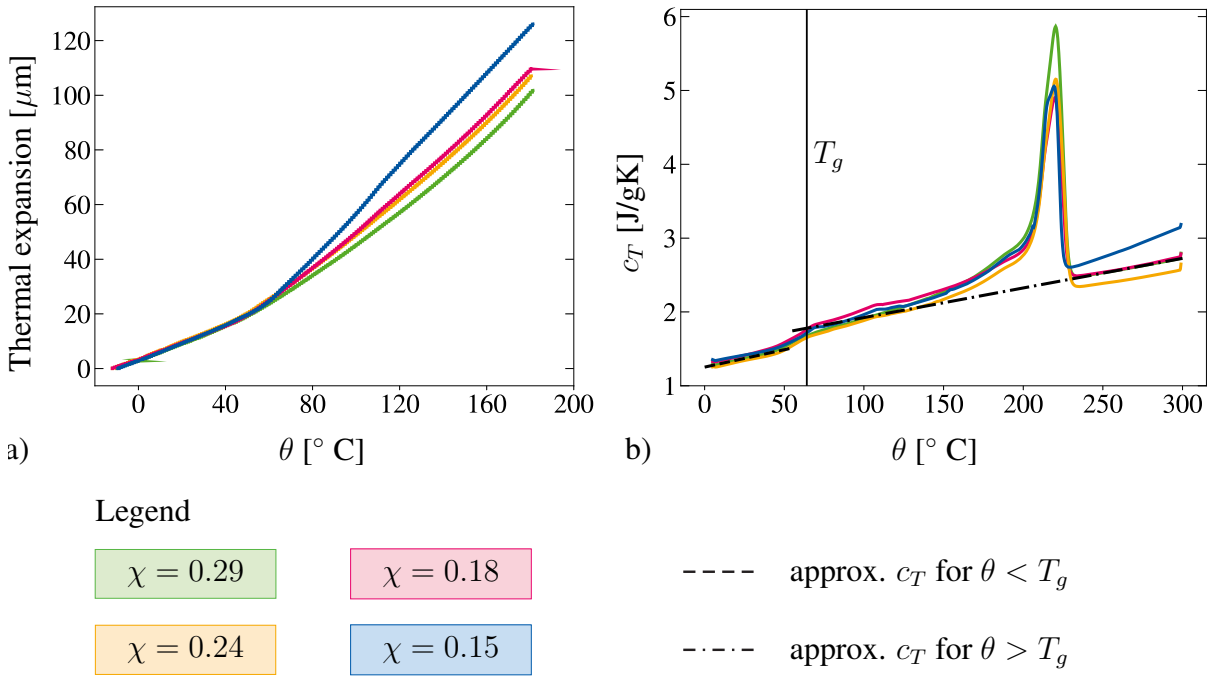

Figure 2.7: a) Thermomechanical analysis (TMA): Thermal expansion over the temperature for all blends. b) Specific heat capacity from DSC measurements for all blends. The trend lines are of the form $c_T(\chi) = c_1\chi + c_2$.

2.4.1.8 Thermal conductivity measurement

The thermal conductivity λ_T was measured using the *Hot-Disc* method, in which a temperature sensor is placed between two samples that are subjected to a defined heating protocol. Subse-

quently, the thermal conductivity was derived from the temperature profile over the time as the average of several measurements. To that end, *Hot-Disc* measurements were taken for multiple test temperatures and a DOC of $\chi = 0.29$, as well as all DOCs at a temperature of 130° C, see Fig. 2.8. The experiments showed an inconclusive dependence of the thermal conductivity on the temperature (see Fig. 2.8 a), where the thermal conductivity firstly increased with increasing temperature and then decreased for all temperatures above the glass transition. The thermal conductivity can be related to the product of thermal diffusivity, density and specific heat capacity (see eg. dos Santos et al. [2013]). While the heat capacity increases with increasing temperature (cf. Fig. 2.7), the thermal diffusivity as well as the density decrease simultaneously (cf. dos Santos et al. [2005, 2013]). Consequently, the effect of the temperature on the thermal conductivity can be related to the change in the afforementioned quantities. Here, further measurements on the density and thermal diffusivity at various temperatures and for all other DOCs would be necessary to clearly explain the changes in the thermal conductivity. Since the changes in the thermal conductivity with increasing temperature are only small, the temperature dependence is neglected in this work. In terms of the crystal content, an increase with increasing DOC is visible. Consequently, for the identification procedure described in Sec. 2.4.5, the thermal conductivity is assumed to depend only on the DOC, hence $\lambda_T(\chi)$.

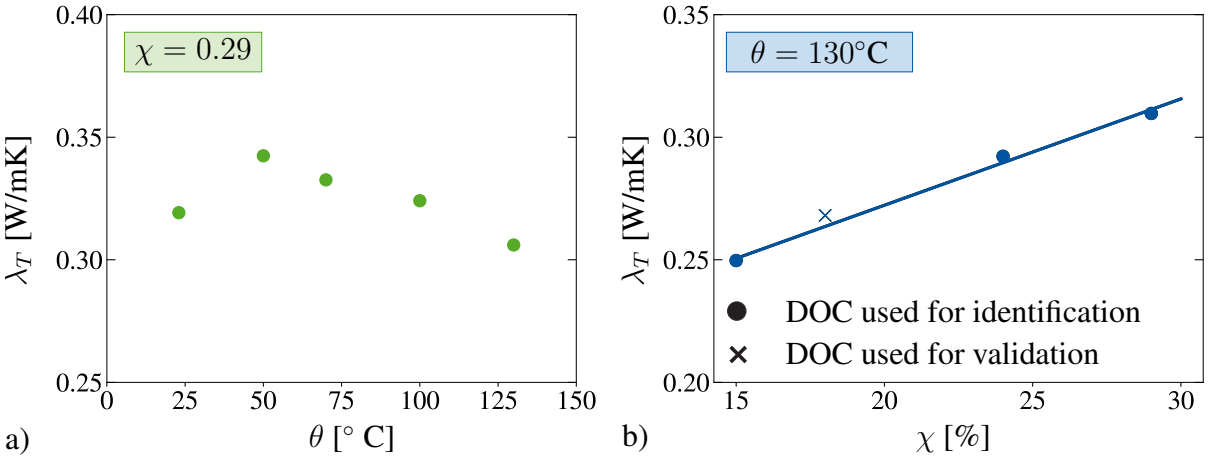

Figure 2.8: Thermal conductivity measurements: a) for $\chi = 0.29$ and various temperatures b) for all blends at 130° C. The linear trend line is of the form $\lambda_T(\chi) = c_1\chi + c_2$.

2.4.1.9 Density measurements

Lastly, density measurements were carried out at room temperature, using a gas pycnometer by the company *Anton Paar*. The resulting density showed an increase with increasing DOC

(see Fig. 2.9) which was expected due to the higher density of crystalline phases compared to amorphous regions.

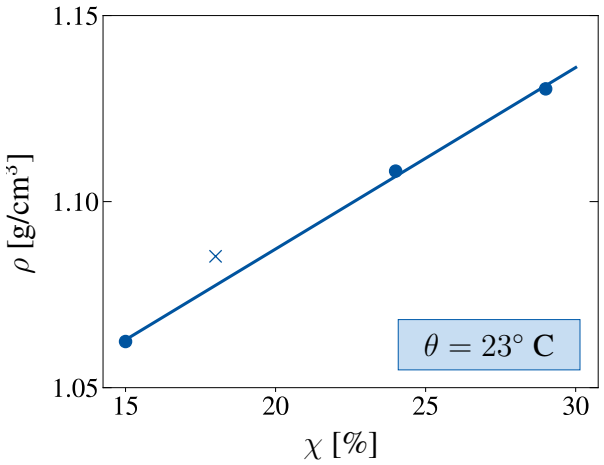

Figure 2.9: Density measurements at room temperature. The linear trend line is of the form $\rho(\chi) = c_1\chi + c_2$.

2.4.2 Elastic constants

The elastic constants, in terms of the Youngs' modulus and the Poisson's ratio, are obtained from the initial elastic response from uniaxial monotonic tension tests at all respective test temperatures. Here, the total Young's Modulus $E_{tot}(\chi, \theta)$ is determinded for each blend, according to DIN EN ISO 527-2:2012, and plotted over the DOC in Fig. 2.10. Next, the dependence of E_{tot} on the DOC is examined, therefore the Trust-Region algorithm in the software tool *MATLAB* is exploited. The data shows an exponential relation of the form

$$E_{\text{tot}}(\chi, \theta) = C_1(\theta)\exp(C_2(\theta)\,\chi). \tag{2.59}$$

Here, C_1 and C_2 are temperature dependent material parameters. Interestingly, the nonlinear dependence of E_{tot} on the DOC is more pronounced for temperatures above the glass transition. As suspected, at 50° C no trend is found, due to the differences in the elastic regime between the samples with different COC content (cf. Fig. 2.3), which is related to testing in the glass transition region. Therefore, during identification, for the temperature of 50° C only two DOCs will be considered, i.e. $\chi = 0.29$ and $\chi = 0.24$. From the experimentally identified E_{tot}, the Youngs' moduli E_1 and E_2 for the elasto-plastic and visco-elastic part, respectively, are determined using longterm relaxation data at small strains. With regard to Felder et al. [2020a], who conducted cylic loading-unloading-recovery experiments at room-temperature

for polyamide 6 with 23 % DOC, it can be concluded that at 1% strain the material still behaves visco-elastically and no plastic deformation has occured yet. Hence, the equilibrium stress, measured at the end of the relaxation step, is assumed to correspond soley to the elastic spring of the elasto-plastic part of the model (see Fig. 2.1). Concomitant, E_1 is determined using Eq. 2.38 and the relations for the Lamé constants[3]. Interestingly enough, the ratio m_E between the Young's modulus of the elasto-plastic part E_1 and the total Young's modulus E_{tot} is found to be crystallinity dependent, with values ranging from 0.5 for $\chi = 0.15$ to approx. 0.72 for $\chi = 0.29$. This finding corresponds to the blend composition and, for example, the density measurements, where a lower DOC means a higher content of amorphous phase and therefore increased viscous behavior. A clear dependence on the temperature is not visible, therefore this influence is neglected. The ratio $m_E(\chi)$ is approximated by a linear function and the Young's modulus for the elasto-plastic term is determined according to $E_1 = m_E\, E_{\text{tot}}$. The Youngs' modulus for the visco-elastic part followed from $E_2 = E_{\text{tot}} - E_1$.

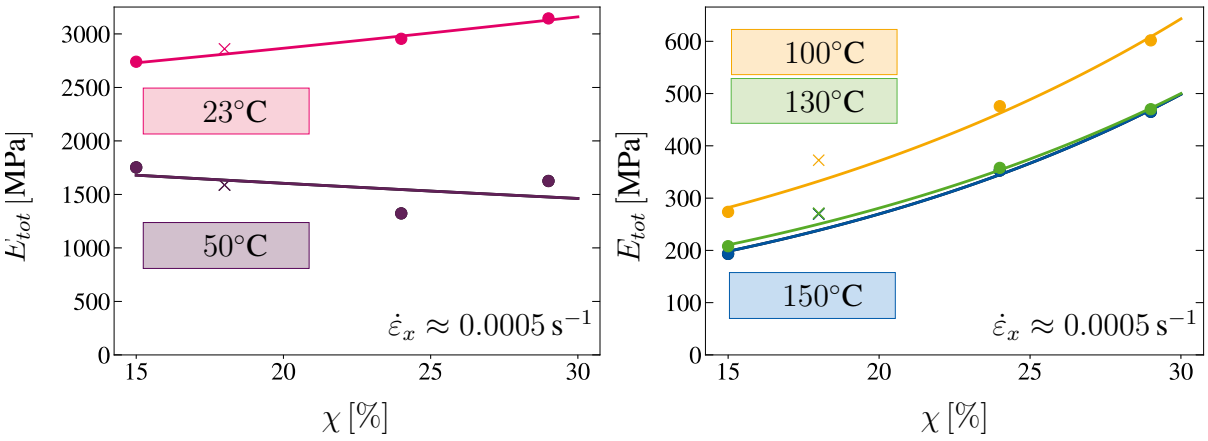

Figure 2.10: Crystallinity dependence of the total Young's modulus below and above the glass transition temperature.

To obtain the Poisson's ratio, 2D measurements evaluated using digital image correlation (DIC) are necessary. The corresponding tests were conducted using a *Limess Q400* system. Following Sec. 2.3 and the assumptions made therein, the Poission's ratio is chosen to be constant in this work, i.e. $\nu_{tot}(\theta) = \nu_1 = \nu_2$. No trend on the DOC was visible in the experimental results, therefore the dependence on the crystallinity is neglected. Furthermore,

[3]The 1. Lamé constant is calculated using the relation $\lambda = (E_{\text{tot}}\nu_{\text{tot}})/((1+\nu_{\text{tot}})(1-2\nu_{\text{tot}}))$ and the shear modulus as (2. Lamé constant) $\mu = E_{\text{tot}}/(2(1+\nu_{\text{tot}}))$.

the dependence of the Poission's ratio on the temperature is observed to be relatively small above the glass transition, thus a constant value of $\nu_{\text{tot,Above Tg}} = 0.45$ is concluded, which is close to incompressible material behavior. For temperatures below T_g, the experimentally determined Poission's ratio was lower compared to the results above the glass transition. However, the experimental data showed a pronounced strain rate dependence that is not yet clarified. Therefore, the Poission's ratio below the glass transition is approximated with $\nu_{\text{tot,Below Tg}} = 0.35$.

2.4.3 Viscous quantities: Nonlinear relaxation function

To represent the relaxation behavior of semi-crystalline polymers, a single Maxwell element in combination with a constant relaxation time τ generally is not sufficient (see e.g. Reese and Govindjee [1997]; Lion [1997*a*]; Amin et al. [2006]). Therefore, other approaches must be utilized, as for example combining several Maxwell elements or employing a nonlinear relation for the relaxation time (e.g. Lion [1997*b*]; Amin et al. [2006]; Felder et al. [2020a]). In this work, the latter approach is chosen, since the addition of further Maxwell elements increases the number of material parameters significantly. With the governed elastic constants, a post-processing scheme, originally proposed by Amin et al. [2006] for the identification of the viscosity and adapted for the relaxation time in the three-dimensional case by Felder et al. [2020a], is applied. Here, longterm relaxation test data at large strains (see Fig. 2.5) is used for identification purposes, whereas results at small strains and stepwise tests are utilized for model validation. The relaxation tests at small total strains were explicitly excluded from identification where possible, since Felder et al. [2020a] concluded that the nonlinearity of the relaxation time is more pronounced at finite strains. At 23° C only experimental data at small strains was available, due to early failure in three of the four blends.

To this end, a uniaxial tension test is conducted, where the loading direction coincided with the direction of the principal stretch λ_x. The specimen is loaded until a maximum total strain of approximately 19% is reached, followed by a constant displacement ($\boldsymbol{u} = \text{constant}$) during the relaxation step. At the termination point of the experiment, stress equilibrium was assumed, where the remaining or equilibrium stress ($\sigma_{1,x}$) corresponded to the contribution of the elasto-plastic part of the model. Note here that a polynomial function is fitted to the results to reduce the oscillations in the experimental data, related to readjustments of the machine during testing. In general, experimental noise likely yields non-physical results and results in spikes when evaluating the relaxation time. During testing, DIC is used to obtain two-dimensional deformation data in terms of the stretches in the principal directions λ_x and λ_y to determine the deformation gradient $\boldsymbol{F}$ for every experimental time step. In the third direction, the evolution

of the stretch λ_z is assumed to be equal to λ_y, according to Felder et al. [2020a]. Subsequently, the true (Cauchy) stress σ_x in loading direction is obtained by relating the machine force to the current area $A = A_0\,\lambda_y\,\lambda_z$, which is calculated using the reference area A_0, as well as the corresponding stretches in y- and z-direction. The overstress $\sigma_{2,x}$ in loading direction corresponding to the visco-elastic part is then calculated at each experimental time step by $\sigma_{2,x}(t) = \sigma_x(t) - \sigma_{1,x}$ and used together with the deformation gradient $\boldsymbol{F}$ as input data for the post-processing scheme. The associated coefficient matrices read:

$$F = \begin{pmatrix} \lambda_x & 0 & 0 \\ 0 & \lambda_y & 0 \\ 0 & 0 & \lambda_z \end{pmatrix}, \qquad \sigma_2(t) = \begin{pmatrix} \sigma_x(t) - \sigma_{1,x} & 0 & 0 \\ 0 & 0 & 0 \\ 0 & 0 & 0 \end{pmatrix} \tag{2.60}$$

From the experimental data, the second Piola-Kirchhoff stress during the relaxation step is obtained by a pull-back operation $\boldsymbol{S}_2(t) = J\,\boldsymbol{F}^{-1}\boldsymbol{\sigma}_2(t)\boldsymbol{F}^{-T}$. Subsequently, Eq. 2.41 is solved for the viscous right-Cauchy-Green like tensor $\boldsymbol{C}_v$ at each experimental time step. The corresponding evolution of the viscous stretch $\lambda_{v,x}$ in loading direction over the time is shown in Fig. 2.11 exemplary for all DOCs at 100° C. Exploiting the exponential map algorithm, Eq. 2.31 is integrated over the time

$$\boldsymbol{C}_v = \exp\left(\Delta t \left(\frac{1}{\tau\,\mu_2}\mathrm{dev}\left(\boldsymbol{C}\boldsymbol{S}_2\right) + \frac{2}{9\,\tau\,K_2}\mathrm{tr}\left(\boldsymbol{C}\boldsymbol{S}_2\right)\boldsymbol{I}\right)\right)\boldsymbol{C}_{v,n} \tag{2.61}$$

and further solved for the relaxation time τ. Here, the index $(*)_n$ indicates quantities from the last converged time step t_n, whereas quantities from the current time step t_{n+1} are given without index. Since the coefficient matrices from the preceding time step are known and all tensor valued quantities commute, Eq. 2.61 can be solved in terms of a system of scalar-valued equations. The resulting relaxation time at each experimental time step is plotted in Fig. 2.11 over the Kirchhoff stress $\tau_{2,x}$ for an exemplary temperature of 100° C. Similar to Amin et al. [2006]; Felder et al. [2020a], a nonlinear relation of the relaxation time is observed, despite the slight noise in the data. However, no clear dependence of the relaxation time on the DOC is visible in the results of the post-processing procedure (see Fig. 2.11), the same holds for the other test temperatures. Thus, the relaxation time is concluded to be independent of the DOC. Furthermore, a significant decrease of the relaxation time with increasing temperature is observed as well as a nonlinear dependence on the overstress (see Fig. 2.11). These findings motivate the use of a nonlinear function for the relaxation time, depending on the temperature and the overstress.

Following the findings from Ricker et al. [2023], who investigated various functions for the

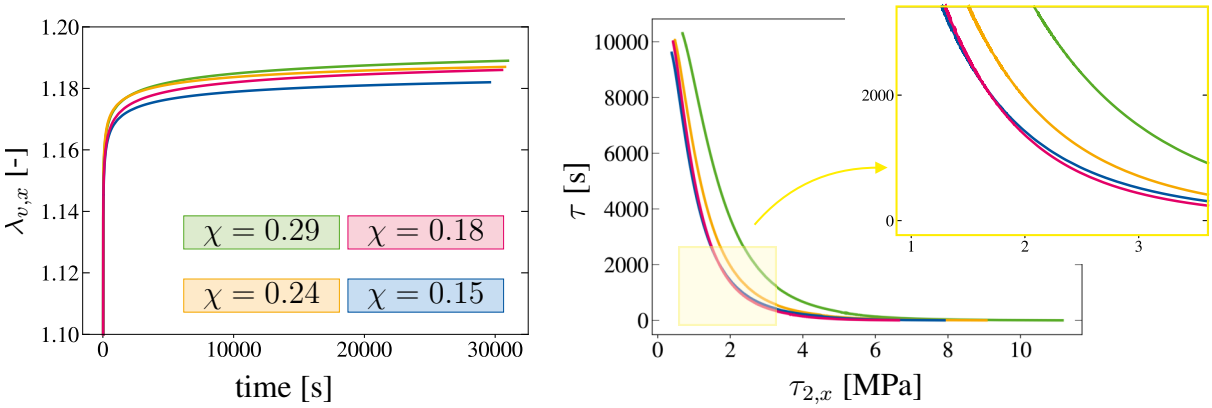

Figure 2.11: Results of the visco-elastic post-processing procedure: Inelastic stretch over time and relaxation time over Kirchhoff stress at 100° C for all DOCs.

viscosity in the context of viscoelasticity models for rubber and brain tissue, several functions for the relaxation time are identified with the results from the post-processing method and compared to experimental data. Here, only functions are tested that showed an improvement in Ricker et al. [2023] for rubber compared to a constant viscosity and that have a relatively low number of material parameters (see Tab. 2.3). A constant relaxation time serves as the benchmark. Functions 2-4 depend purely on the stress in terms of the Kirchhoff overstress $\boldsymbol{\tau}_2$, whereas in function 5 an additional dependence on the total deformation in terms of the left Cauchy-Green tensor $\boldsymbol{B} = \boldsymbol{F}\boldsymbol{F}^T$ is introduced. From function 6 onwards, a dependence on the inelastic deformation is assumed. Here, it is made use of the equivalence of the norm $||\boldsymbol{B}_v|| = ||\boldsymbol{C}_v||$ and $||\boldsymbol{B}_v^{-1}|| = ||\boldsymbol{C}_v^{-1}||$ as well as the trace $I_{1,v} = \text{tr}(\boldsymbol{B}_v) = \text{tr}(\boldsymbol{C}_v)$. Unlike all other functions, function 6 contains a dependence on the visco-elastic Mandel stress $\boldsymbol{M}_2$ which can be related to the viscous Kirchhoff stress as $\boldsymbol{M}_2 = \boldsymbol{F}_{e2}^T \boldsymbol{\tau}_2 \boldsymbol{F}_{e2}^{-T}$. Therefore, $\boldsymbol{M}_2$ and $\boldsymbol{\tau}_2$ share the same eigenvalues and $||\boldsymbol{M}_2|| = ||\boldsymbol{\tau}_2||$ holds. Additionally, a modified version of the function from Lion [1997a] is proposed in function 7, depending on the Kirchhoff stress $\boldsymbol{\tau}_2$ and the inelastic deformation $\boldsymbol{B}_v^{-1}$. An overview of the functions adapted for the relaxation time is given in Tab. 2.3. For a detailed description and investigation of further functions for the viscosity, the reader is kindly referred to Ricker et al. [2023] or the literature cited therein.

To identify the function best suited to describe the present behavior of the relaxation time, the Trust-Region algorithm is exploited in *MATLAB*. A least squares problem is solved, where the residual is defined as the sum of the squared differences between the experimentally post-processed relaxation time τ (see Fig. 2.11) and the corresponding function value (see Tab. 2.3). In accordance with Ricker et al. [2023], the range of feasible material parameter values for the identification procedure is chosen such that the second law of thermodynamics

No.	Name & source for corresponding viscosity function	Relaxation time function [s]	Para.
1	Const. relaxation time	τ_0	1
2	Power law Norton [1929]	$\tau_0 \, \|\|\boldsymbol{\tau}_2\|\|^{-\delta}$	2
3	Exponential law, Schmid and Boas [2013]	$\tau_0 \exp(-\delta \, \|\|\boldsymbol{\tau}_2\|\|)$	2
4	Hyperbolic sine power law, Garofalo [1963]	$\tau_0 \left(\sinh(\delta \, \|\|\boldsymbol{\tau}_2\|\|)\right)^{-\gamma}, \quad \gamma > 0$	3
5	Amin and Lion, Amin et al. [2006]	$\tau_0 \dfrac{\|\|\boldsymbol{B}\|\|^{\gamma}}{\|\|\boldsymbol{M}_2\|\|^{\delta}}$	3
6	Lion, Lion [1997a]	$\tau_0 \exp\left(-\delta \dfrac{\|\|\boldsymbol{M}_2\|\|}{\|\|\boldsymbol{B}_v^{-1}\|\|^3}\right)$	2
7	Modified Lion	$\tau_0 \, \|\|\boldsymbol{B}_v\|\|^{\gamma} \exp(-\delta \, \|\|\boldsymbol{\tau}_2\|\|)$	3
8	Bergström & Boyce Bergström and Boyce [1998]	$\tau_0 \, \|\|\boldsymbol{\tau}_2\|\|^{-\delta} \left(\sqrt{\dfrac{I_{1,v}}{3}} - 1 + \varphi\right)^{\gamma}, \quad \varphi = 0.01 \text{ (const.)}$	3

Table 2.3: Overview of investigated functions for the relaxation time, based on Ricker et al. [2023] (Para. stands for number of material parameters).

is satisfied ($\tau > 0$). The fitting results for all functions are shown in Fig. 2.12 together with the corresponding fitted material parameters. Note here that each function was identified simultaneously for all DOCs. Function 1 with a constant relaxation time clearly yielded an insufficient approximation of the nonlinear behavior of the relaxation time. Thus, it served as the reference solution for the comparison. In contrast, all other tested functions showed a significant improvement. The power law-type functions 2, 5 and 8 are, however, inferior to the exponential approaches as well as to the hyperbolic sine power law (function 4), which behaves like a power law for small stresses and as an exponential law for large stresses. Interestingly, the identified parameters for the relaxation time τ_0 in function 3, 4 and 6 (cf. Fig. 2.12), reflected the extrapolated value for the relaxation time at the termination point of the relaxation step, where the overstress is zero. Hence, this value could be determined during post-processing, reducing the number of material parameters during identification. The errors for function 3, 4 and 6 are almost identical (cf. Fig. 2.12), therefore these approaches can be seen as equally suited to model the nonlinear relaxation time. In combination with the findings about the initial relaxation time τ_0 and considering the number of material parameters, function 3 and 6 are best suited. However, function 7 shows an even lower error, compared to function 3 and 6. Here, the influence of the inelastic deformation is considered, depending on the exponent γ, whereas function 6 assumed a constant ratio between overstress and viscous deformation.

For a temperature of 23° C, longterm relaxation data was only available at a total strain of

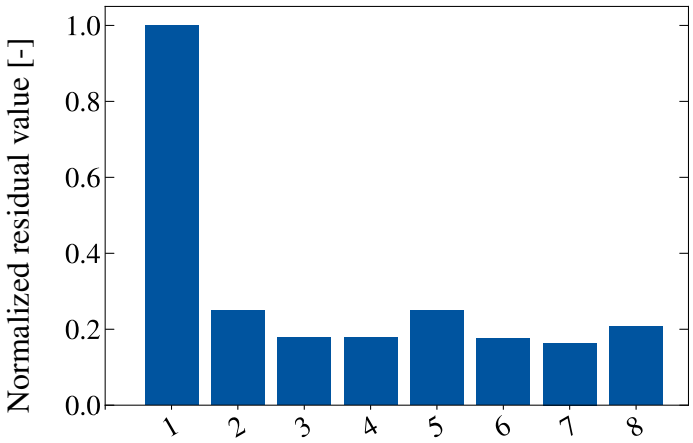

No.	τ_0 [s]	δ	γ
1	6866.265	-	-
2	6315.281	0.7069	-
3	14168.876	0.7741	-
4	14168.876	18.6377	0.0415
5	874.003	0.7069	3.2029
6	14509.6144	4.4946	-
7	1035.2382	0.75906	4.30
8	148999.982	0.6817	0.8754

Figure 2.12: a) Identification results for the nonlinear relaxation time functions from Tab. 2.3 at 100° C normalized to a constant relaxation time. b) Corresponding material parameters.

0.5 %. Applying the post-processing scheme to the experimental data, a rather linear relation for the relaxation is visible (see Fig. 2.13), similar to the results of Felder et al. [2020a]. When comparing different nonlinear functions for the relaxation time, this resulted in a comparatively weaker improvement, compared to the constant relaxation time (see Fig. 2.13). Here, the use of multiple Maxwell elements with different relaxation time functions could improve the results. However, this investigation is beyond the scope of this paper. Function 8 performed worse than the benchmark test and is therefore excluded from the plot. In the case of small strains, function 7 yielded similar improvement, compared to function functions 3, 4 and 6. Finally, function 7 is identified for all remaining tests temperatures and further implemented in a *ABAQUS* user material subroutine UMAT. The comparison of the identification results at the other test temperatures is given in Appendix 2.7.5 and the corresponding material parameters for function 7 in Tab. 2.5.

2.4.4 Plastic material parameters

In the final identification step for the mechanical parameters of the isothermal model, the remaining parameters related to plastic deformations are characterized. These are the parameters $c(\chi, \theta)$ and $b(\chi, \theta)$ that describe the nonlinear kinematic hardening behavior. Due to the inconclusive data for the yield stresses in tension and compression above the glass transition, also the parameters $\sigma_t(\chi, \theta)$ and $\sigma_c(\chi, \theta)$ are still undetermined. Therefore, a nonlinear multi curve fitting procedure in *MATLAB* is used together with monotonic tensile data to identify these four parameters for all DOCs at each test temperature. A least-squares problem is formulated,

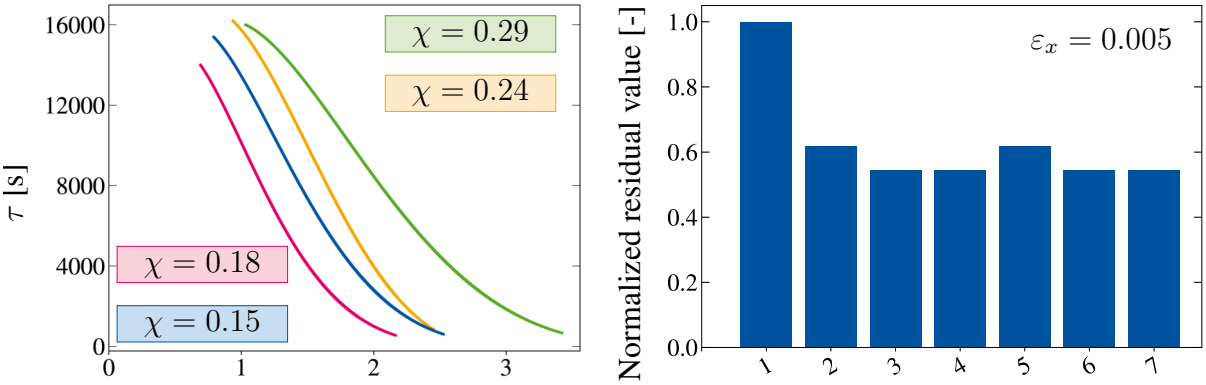

Figure 2.13: Results of the visco-elastic post-processing procedure: a) Relaxation time over Kirchhoff stress at 23° C for all DOCs. b) Fitting results for the nonlinear relaxation time functions from Tab. 2.3.

where the error is defined as the squared difference between the experimental true stress in loading direction and the Cauchy stress obtained from a single element test. Thus, in each iteration of the optimization, *ABAQUS* and the corresponding UMAT are called with the current set of plastic parameters. The boundary value problem for the single element test is displayed in Fig. 2.25 in the Appendix. For the discretization in *ABAQUS*, a single C3D8T element is used together with isothermal boundary conditions. Concerning the optimization, the genetic algorithm is used in series with the Downhill-Simplex algorithm. This procedure is favorable, since the parameter range, apart from the yield stresses, is kept relatively large and for the Downhill-Simplex algorithm alone no restrictions can be applied to the parameter domain. Consequently, also negative, non-physical values are possible. Furthermore, convergence is unlikely if the initial parameters are too far away from their final values. The genetic algorithm therefore narrows down the range of possible solutions and its best fitted parameter set serves as the starting values for the Downhill-Simplex algorithm. In contrast to the gradient based Levenberg-Marquardt algorithm or the closely related Trust-Region algorithm, the genetic algorithm as well as the geometrical Downhill-Simplex algorithm are gradient free and due to their construction not restricted in the direction of the iteration. Thus, in comparison they are more robust when used in combination with numerical simulations.

Similar to [Johlitz et al., 2010], who investigated the thermo-viscoelastic material behavior of polyurethane and introduced temperature dependent shift functions to relate the identified value at room temperature to higher temperatures, in this work a function for each material parameter depending on the DOC is identified. In this way, a parameter set for each test temperature is

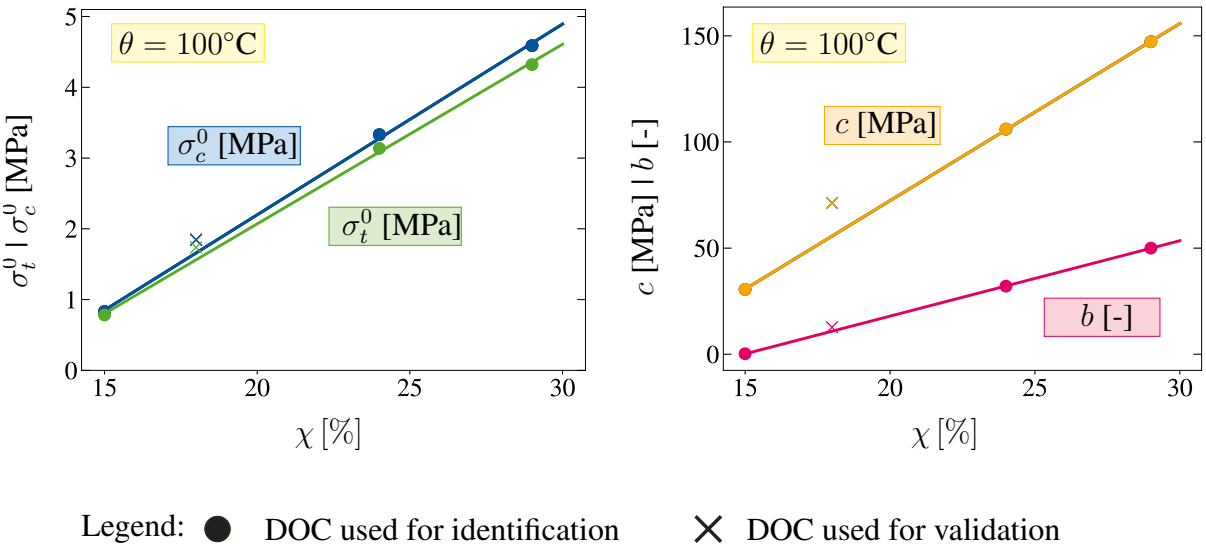

Figure 2.14: Results for the parameter identification from single curve fits at 100° C. The linear trend line is of the form $(\bullet) = c_1\,\chi + c_2$, with $(\bullet) = \sigma_t^0, \sigma_c^0, c, b$.

found. Therefore, in a first step single fits at each constant temperature and for each DOC need to be conducted using the aforementioned nonlinear optimization procedure. Besides the yield stresses, for which the parameter range can be restrained by identifying the intersection of the initial slope of the stress-strain curve with the inconclusive hardening slopes, the parameter range for the hardening parameters is kept large for the identification. The resulting plastic parameters for each blend are subsequently plotted against the degree of crystallinity (see Fig. 2.14). Now, the dependence of each parameter on the DOC can be determined as a post-processing step, by exploiting the Trust-Region algorithm in *MATLAB*. As done in all previous identification steps, the blend with $\chi = 0.18$ is not considered for identification and serves for validation purposes. Here, a linear ansatz is chosen and the identified relation is visualized exemplary for a temperature of 100° C in Fig. 2.14. For the identification, only experimental curves from three degrees of crystallinity ($\chi = 0.15, 0.24, 0.29$) are taken into account. Notably, the identified parameters for $\chi = 0.18$ are overall in good agreement with the parameters of the other DOCs. Only for the kinematic hardening parameter c a higher deviation is visible which is also apparent in the result for $\chi = 0.15$. The results for the other temperatures above the glass transition can be found in Appendix 2.7.6. For the temperatures below T_g, the fitting results are not visualized, since at 23° C three of the four blends failed before significant plastification, therefore the parameters, apart from the onset of yielding, are identified with a single fit for $\chi = 0.29$. At 50° C the blends with $\chi = 0.18$ and $\chi = 0.15$ were excluded from identification, since inconclusive material behavior occured, related to testing

in the glass transition regime. Thus, only two blends remain for the characterization, therefore the fitted linear trend line agrees perfectly with the results, leaving no possibility for validation. The identified parameters for the linear functions for all plastic parameters are listed in Tab. 2.5.

2.4.5 Thermal quantities

To obtain an expression for the coefficient of thermal expansion, it is calculated by $\alpha_T = \Delta L/\Delta T$ from the thermal expansion curve in Fig. 2.7 for every blend at each test temperature. Here, ΔL is the thermal expansion, L is the initial length of the specimen and ΔT the temperature difference. Next, the Trust-Region algorithm is exploited in the commercial software tool *MATLAB* to describe α_T as a function of the degree of crystallinity for each test temperature separately. Again, $\chi = 0.18$ is only used for validation purposes. The results are shown in Fig. 2.15, where it can be seen that the characterized curves are in good agreement with the experimental results. However, it is not clear as to why the behavior at 100° C differs so much from the remaining temperatures above T_g. A possible explanation could be changes in the ratio of the amorphous to the crystalline phase, related to post-crystallization.

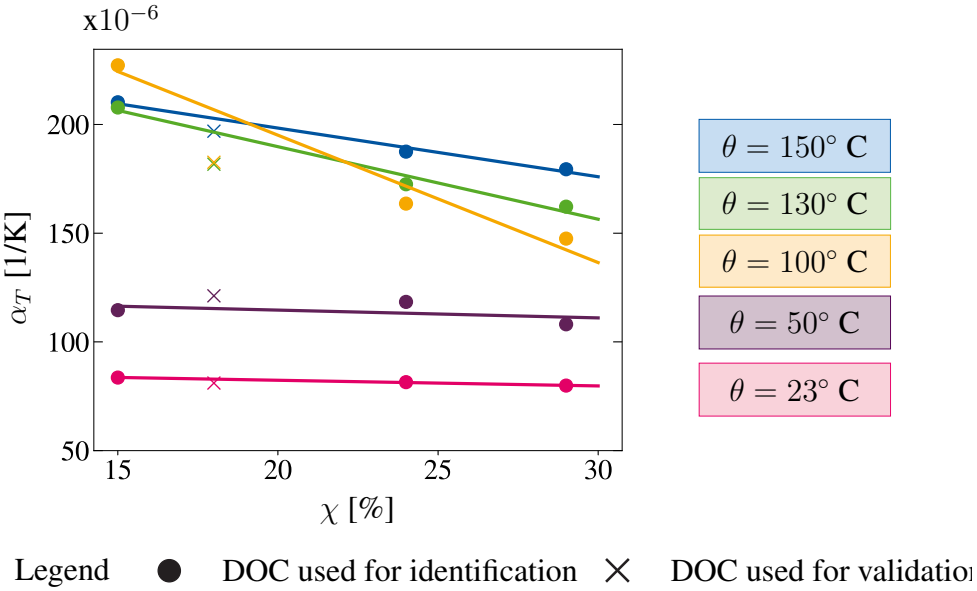

Figure 2.15: Coefficient of thermal expansion at different temperatures and DOCs. The linear trend line is of the form $\alpha_T(\chi) = c_1\chi + c_2$.

Concerning the specific heat capacity c_T, the results of the identification procedure were already shown in Fig. 2.7. The corresponding material parameters are summarized in Tab. 2.4. Note here that no clear dependence on the DOC is present. For the thermal conductivity,

a multifit using the Trust-Region algorithm in *MATLAB* is conducted, corresponding to Sec. 2.4.4. The results of the fitting procedure are visualized in Fig. 2.8. An overview of the thermal parameters including the density is given in Tab. 2.4.

2.4.6 Identification results

The results of the identification procedure can be seen in Fig. 2.16 for all temperatures above the glass transition and in Fig. 2.17 for the temperatures below T_g. Good agreement of the identification results with the experimental data can be observed, which is especially remarkable keeping in mind the extensive range of DOCs to be described by the model. The model prediction for $\chi = 0.18$ also captures the experimental results well, especially the elastic regime and the onset of yielding. However, at large strains the deviation between model and experiment is notable. This can be traced back to the deviation between the function for each plastic parameter compared to the plastic parameters obtained in a single fit for $\chi = 0.18$ (cf. Fig. 2.14 and 2.27). For instance, at a temperature of 100° C, the initial elastic response as well as the yield stress are accurately captured. However, the prediction of the hardening slope is inaccurate, since the hardening parameter c is not in good agreement with the single fit results (cf. Fig. 2.14). Similar observations can be made for the other temperatures above T_g, though here, additionally the onset of yielding differs from the identified relation through the multifit.

Below T_g, the results for a temperature of 23° C in Fig. 2.17 are in good agreement with the experimental data. Here, the elastic regime as well as the onset of yielding are accurately captured. Regarding the hardening slope, only results for one blend were available for identification, therefore, naturally, the hardening behavior is well represented. For a temperature of 50° C, the model response already differs from the experimental results in the elastic regime, though the hardening behavior is well captured. This difference results from a material softening visible in the experimental data (see Sec. 2.4.1) and the DMA results in Appendix 2.7.2, where the slope of the experimental curve flattens compared to the initial material stiffness before the onset of plastic yielding is reached at around 2.5 % strain. The authors believe, that this behavior is related to testing in the glass transition regime. Since the gradual transition of the underlying morphology of the amorphous phase and its associated effect are however not incorporated in the model formulation the difference is expected.

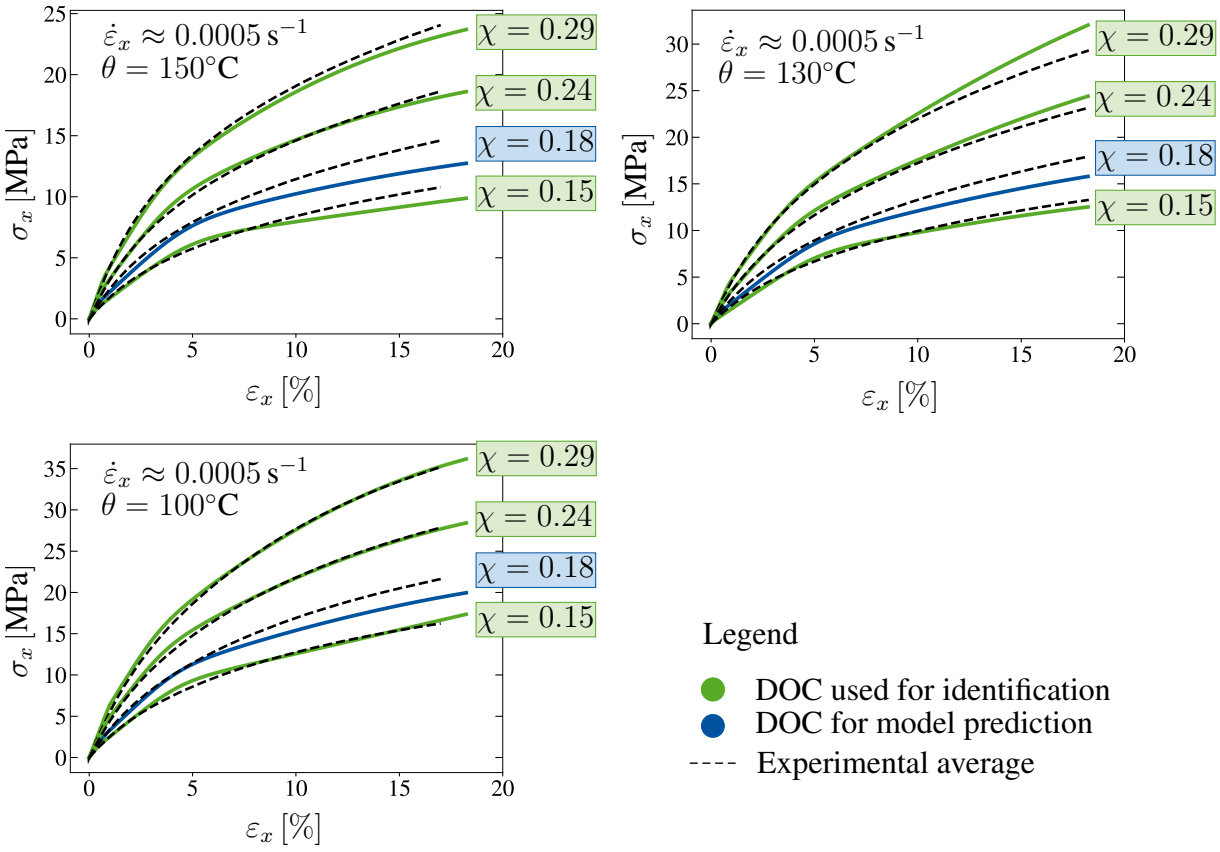

Figure 2.16: Monotonic, uniaxial extension: Identification results for multiple degrees of crystallinity (DOC) and temperatures above the glass transition regime.

Table 2.4: Set of thermal material parameters at different temperatures.

Function	Parameter at:	23° C	50° C	100° C	130° C	150° C
$\alpha_T(\chi) = c_9(\theta)\chi + c_{10}(\theta)$	$c_9[10^{-4}/\mathrm{K}]$	-0.2601	-0.3586	-5.857	-3.336	-2.238
	$c_{10}[10^{-4}/\mathrm{K}]$	0.8756	1.218	3.122	2.565	2.431
$c_T(\chi) = c_{11}(\theta)\,\theta + c_{12}(\theta)$	$c_{11}[\mathrm{J/gK^2}]$	0.00471	0.00401	0.00401	0.00401	0.00401
	c_{12} [J/gK]	1.25313	1.52299	1.52299	1.52299	1.52299
$\lambda_T(\chi) = c_{13}\chi + c_{14}$	c_{13}[W/mK]	0.4338	0.4338	0.4338	0.4338	0.4338
	c_{14}[W/mK]	0.1855	0.1855	0.1855	0.1855	0.1855
$\rho_0(\chi) = c_{15}\chi + c_{16}$	c_{15} [g/mm^3]	0.4878	0.4878	0.4878	0.4878	0.4878
	c_{16} [g/mm^3]	0.9897	0.9897	0.9897	0.9897	0.9897

Remark: The reader is kindly reminded, that although some coefficients of the identified functions determining the material parameters, are negative, the material parameters themselves are always positive for the range of DOCs ($\chi = 0.15 - 0.29$) the model spans.

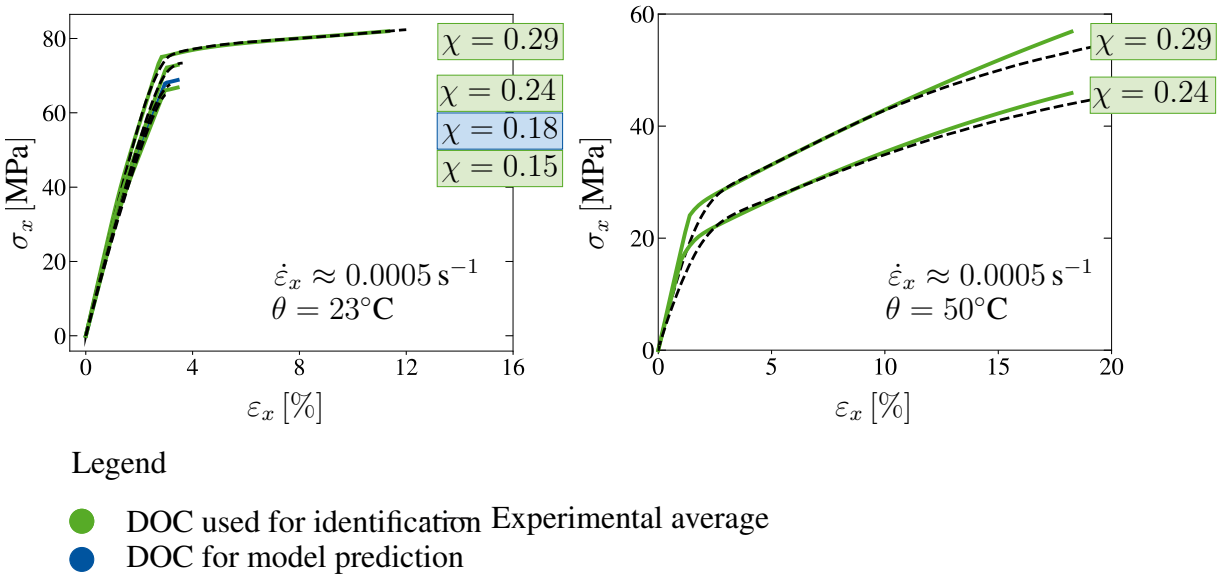

Figure 2.17: Monotonic uniaxial extension: Identification results for multiple degrees of crystallinity (DOC) and temperatures below the glass transition regime.

2.4.7 Model validation

In order to validate the proposed constitutive framework, further results are compared to the test data. Therefore, only experimental data that has not been used for identification is compared to the corresponding model response. The boundary value problem, in terms of a single element test, is given in Fig. 2.25 in the Appendix. In a first step, the model prediction for the long-term relaxation behavior corresponding to Fig. 2.5 is shown for $\chi = 0.18$ and all temperatures above the glass transition. It should be emphasized that the relaxation function was identified with experimental results for the other three blends only. Therefore, the specimens were loaded with $\dot{\varepsilon}_x = 0.01\,\mathrm{s}^{-1}$ to a strain level of approximately $\varepsilon_x = 0.19$ and subsequently relaxed for 32000 s. The corresponding model response for $\chi = 0.18$ is given in Fig. 2.18. Overall the model prediction is in good agreement with the experimental data, especially at 100° C.

To validate the small strain regime, a stepwise loading-unloading test is carried out for a DOC of 29% at 130° C. Here, the specimen undergoes a stepwise deformation of $\varepsilon_x = 0.01$, until a maximum strain of $\varepsilon_{\mathrm{max},x}$ is reached (see Fig. 2.19). Subsequently, the specimen is unloaded at the same pace up into the compression regime. The corresponding loading rate was $\dot{\varepsilon}_x = 0.0001\,\mathrm{s}^{-1}$ and the specimen was held at constant strain for 15000 s in each step. In comparison to the experimental results, the model prediction underestimated the material behavior, especially at larger strains. However the shape of the model curve corresponds well

Table 2.5: Set of mechanical material parameters at different temperatures.

Function	Parameter at:	23° C	50° C	100° C	130° C	150° C
$E_{\text{tot}}(\chi) = C_1(\theta)\exp(C_2(\theta)\,\chi)$	C_1 [MPa]	2397	2270*	143.1	96.875	102.1
$E_2 = E_{\text{tot}} - E_1$	C_2 [-]	0.9106	-0.8716*	5.133	5.565	5.373
$E_1 = m_E(\chi)E_{\text{tot}}$	m_E [-]					
$m_E = 107.143\chi + 38.935$						
$\nu_{\text{tot}}(\theta) = \nu_1 = \nu_2$	[-]	0.35	0.45	0.45	0.45	0.45
$\sigma_c^0 = c_1(\theta)\chi + c_2(\theta)$	c_1 [MPa]	72.19	138.8	26.95	20.86	13.19
	c_2 [MPa]	41.96	-21.913	-3.192	-2.969	-1.436
$\sigma_t^0 = c_3(\theta)\chi + c_4(\theta)$	c_3 [MPa]	72.19	131.24	25.38	20.27	12.93
	c_4 [MPa]	41.96	-20.984	-3.006	-2.884	-1.407
$c = c_5(\theta)\chi + c_6(\theta)$	c_5 [MPa]	$c = 17.756$**	20.86	834.5	597.3	523.8
	c_6 [MPa]		92.213	-94.56	-69.42	-67.89
$b = c_7(\theta)\chi + c_8(\theta)$	c_7 [-]	$b = 1.276$**	0	355.4	150.2	196.3
	c_8 [-]		60.438	-53.15	-22.39	-28.3
$\tau = \tau_0(\theta)\,\|\|\boldsymbol{B}_v\|\|^{\gamma(\theta)}\exp(-\delta(\theta)\,\|\|\boldsymbol{\tau}_2\|\|)$	τ_0 [s]	1853.653	1511.952	1035.238	737.245	573.899
	γ [-]	4.57	4.416	4.3	4.872	4.289
	δ [-]	0.539	0.814	0.759	0.866	0.873

* inconsistent results due to testing in the glass transition regime

** constant values obtained for $\chi = 0.29$ only, due to early failure of the remaining blends

Remark: The reader is kindly reminded, that although some coefficients of the identified functions determining the material parameters, are negative, the material parameters themselves are always positive for the range of DOCs ($\chi = 0.15 - 0.29$) the model spans.

to the experimental data. The authors believe that this behavior results from the identification and characterization process to finite strain data only. As previously seen for small strain test data at 23° (cf. Fig. 2.13), the nonlinear function for the relaxation time does not fit the linear relation between relaxation time and stress. As suggested in Ricker et al. [2023], the use of a second Maxwell element, identified with the relaxation behavior at small strains, could lead to an improvement. Moreover, it should be noted that the corresponding strain rate of $\dot{\varepsilon}_x = 0.0001\,\text{s}^{-1}$ has not been used for identification of either tensile, compressive or relaxation data and differs by two decades from the strain rate used for identification of the relaxation function ($\dot{\varepsilon}_x = 0.01\,\text{s}^{-1}$).

Besides stepwise tests at small strains, also stepwise tests at large strains were conducted for $\dot{\varepsilon}_x = 0.0001\,\text{s}^{-1}$ (see Fig. 2.20). Therefore, the specimens were exposed to a maximum strain of $\varepsilon_{\text{max},x} = 0.16$, distributed over four load steps of 4 % strain each. The holding period was 15000 s per step. Again, the model predictions are less accurate, while the shape of the curves is in good agreement. Nevertheless, the predictions are good, keeping in mind that the strain rate is two decades lower than the one used for identification. Compared to the small strain case in Fig. 2.19 for the same strain rate, the experimental results for the large strain case are in better agreement with the test data. This supports the findings made in Sec. 2.4.3 that the

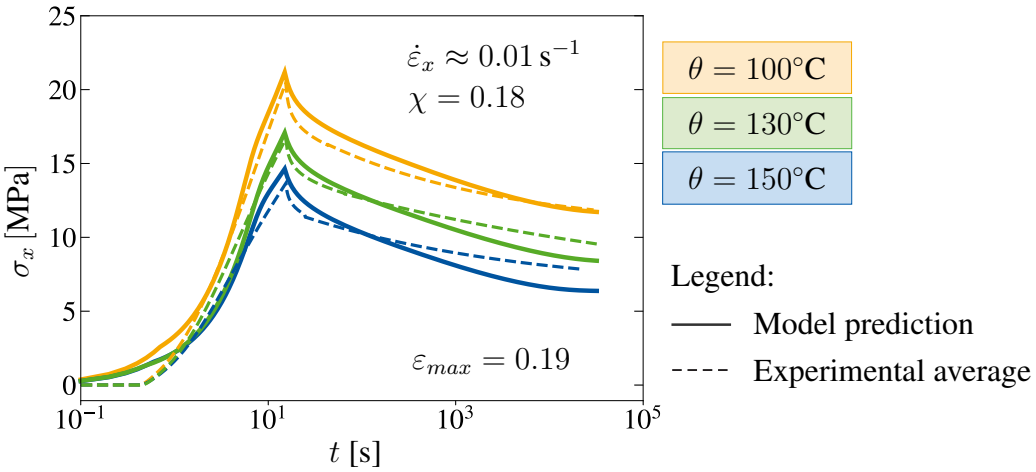

Figure 2.18: Long-term stress-relaxation at finite strains for temperatures above T_g. Experimental stress over time data and corresponding model predictions ($\chi = 0.18$).

chosen function for the relaxation time works best for finite strains. As mentioned earlier, the addition of further Maxwell elements could improve the model results.

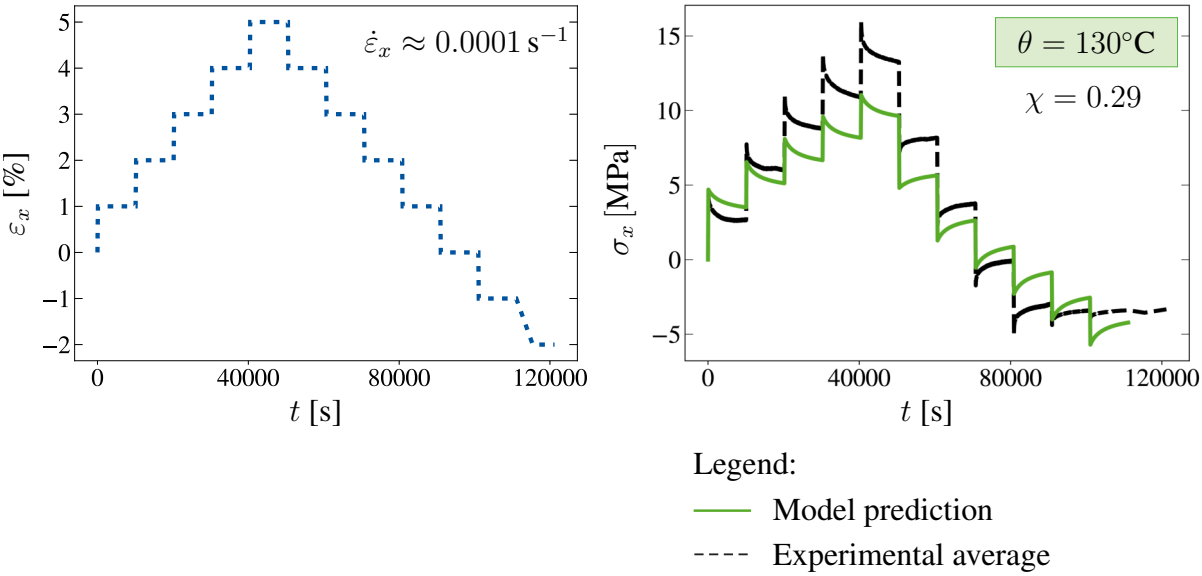

Figure 2.19: Stepwise long-term stress-relaxation at small strains for $\chi = 0.29$ at 130° C. Experimental strain and stress over time data and corresponding model predictions.

The validation for the tensile tests is already given in Fig. 2.16 and 2.17 for $\chi = 0.18$. Overall, as discussed in Sec. 2.4.6, the prediction is in good agreement with the experimental results. Especially the elastic regime and the onset of yielding are accurately captured, only the hardening behavior is underestimated. Unfortunately, it was not possible to validate the

compression regime, since all available test data was used for identification. In the future, further compression tests on the remaining blends and temperatures are planned to close this gap.

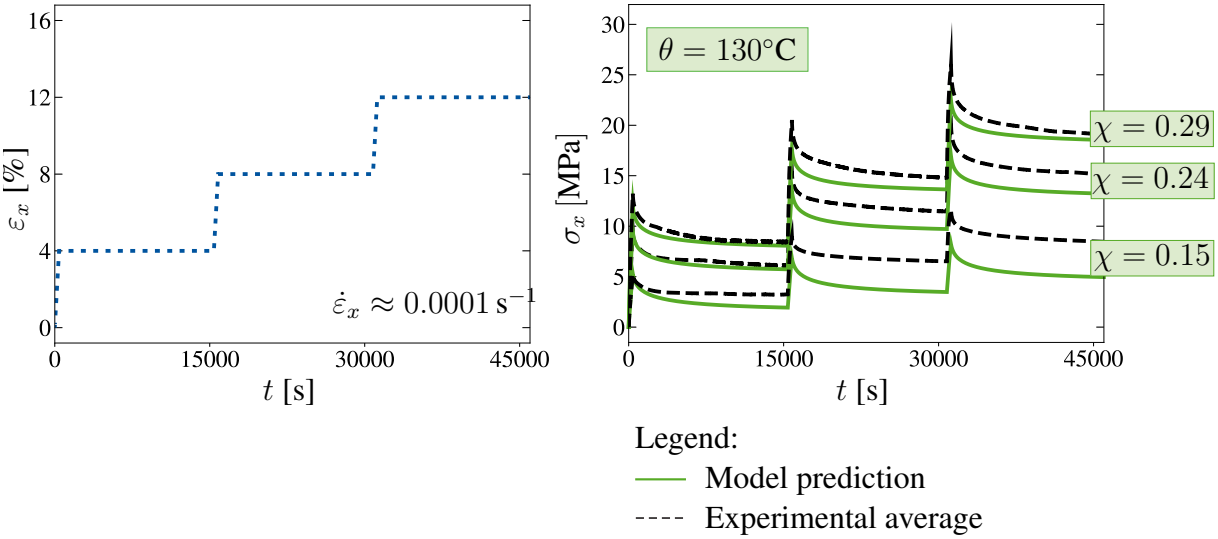

Figure 2.20: Stepwise long-term stress-relaxation at large strains for multiple DOCs at 130° C. Experimental strain and stress over time data and corresponding model predictions.

2.5 Numerical example

To demonstrate the capabilities of the developed and validated constitutive framework in capturing the material response in multi-axial stress-states, a structural example at ambient ($\theta = 23°$ C) and elevated ($\theta = 100°$ C) temperature is conducted. To this end, type 1BA (ISO 527-2:2012) specimens were modified by drilling a circular hole with approximately 1mm diameter into the center of the measurement area (cf. Fig. 2.21). Here, various DOCs were tested to validate the model response. At room temperature, only the highest DOC ($\chi = 0.29$) was tested, since the other DOCs suffered from early failure (cf. Fig. 2.3). For a temperature of 100° C, three DOCs were tested, $\chi = 0.29$ and $\chi = 0.24$ which served for identification purposes and $\chi = 0.18$ that is used for prediction only. The loading rate was controlled by the cross head speed of the *Zwick/Roell Z020* machine and prescribed to $\dot{\varepsilon}_x \approx 0.0005\,\mathrm{s}^{-1}$. During testing, the heterogeneous strain field around the hole was measured using the *Q-4xx Istra 4D* digital image correlation (DIC) system. The corresponding measurment area is highlighted in light blue in Fig. 2.21. Each experiment was repeated only two to three times due to good

reproducibility and only small scatter in the recorded force over time data (cf. Fig. 2.21).
To reduce computation time, the symmetry of the specimen is exploited. Consequently, only one eigth of the specimen is modeled. The corresponding specimen dimensions were approximated from ISO 527-2:2012. Similar to Felder et al. [2020a], at the boundary of the measurement area, the evolution of the cross section was calculated from the initial cross section $A_0 = 5 \cdot 2\,\mathrm{mm}^2$ and the measured mean stretch in y-direction by $A(t) = \lambda_y(t)^2 A_0$. Note here, that the assumption $\lambda_y(t) \approx \lambda_z(t)$ is made in line with the findings from Felder et al. [2020a]. In this way, the evolution of the true stress in longitudinal direction could be computed from the recorded force data and the deformed cross section as $\sigma_x(t) = F(t)/A(t)$. In the following, the respective true stress over time relation served as a traction boundary condition for the finite element model. In Fig. 2.21, the geometry for the FEM simulation is presented, where reduced eight-node solid elements (C3D8RT) from the ABAQUS/Standard element library are used for discretization. Note here, that for visualization purposes a coarse mesh is shown. Prior to obtaining the simulation results, a mesh convergence study was conducted and a finer mesh distribution was chosen. The corresponding material parameters for each DOC are taken from Tab. 2.5 and 2.4.

Fig. 2.22 and 2.23 show the comparison of the true strain contours in longitudinal (x) and transverse (y) direction, obtained from both, the finite element simulation and the DIC images. For $\chi = 0.29$ at room temperature two time steps A ($t = 25$ s) and B ($t = 50$ s), highlighted in Fig. 2.21 are presented. At $100°$ C, the results are shown at $t = 75$ s (point C) and $t = 150$ s (point D) for all three DOCs and at $t = 225$ s (point E) for $\chi = 0.24$ only.

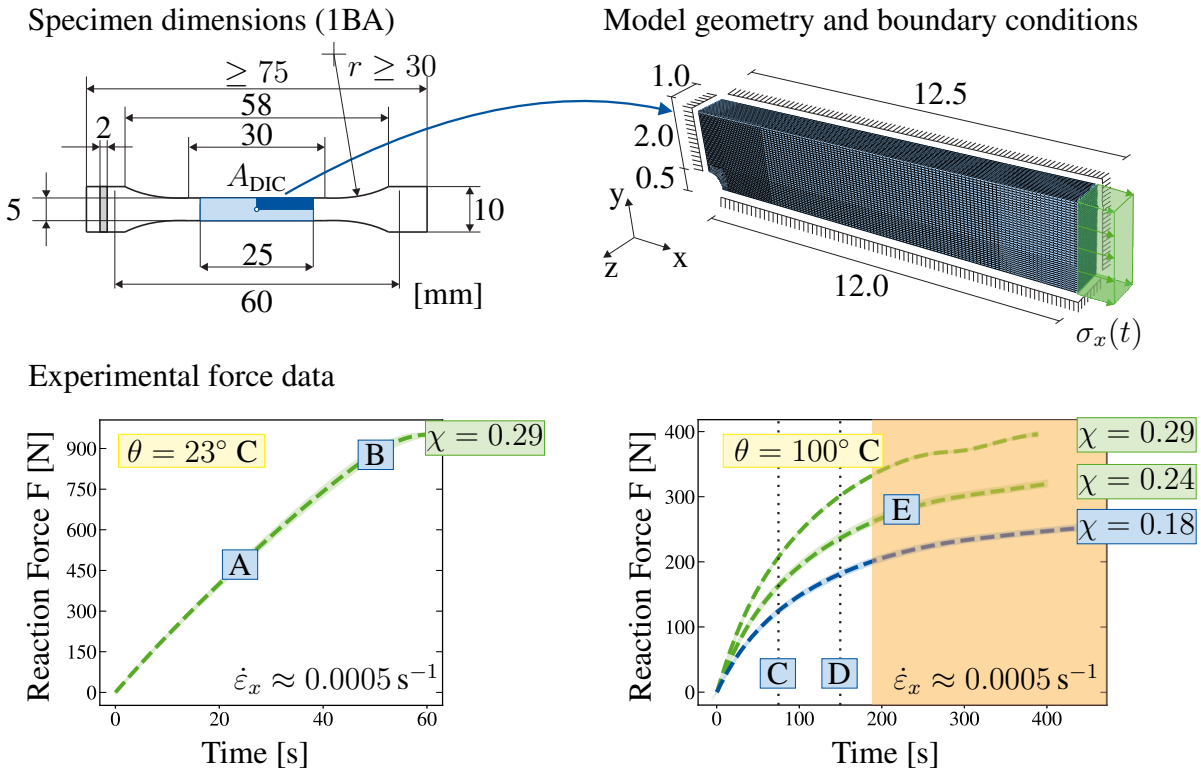

Figure 2.21: Top: Geometry and boundary value problem of type 1BA (ISO 527-2:2012) with circular hole, including DIC measurement area. Bottom: Recorded force data for various DOCs at room ($\theta = 23°$C) and elevated ($\theta = 100°$C) temperature. **Note:** The orange area indicates where the evaluation of the DIC measurement was not possible or only possible with the exclusion of larger areas around the hole, due to large deformations and flaked off DIC pattern.

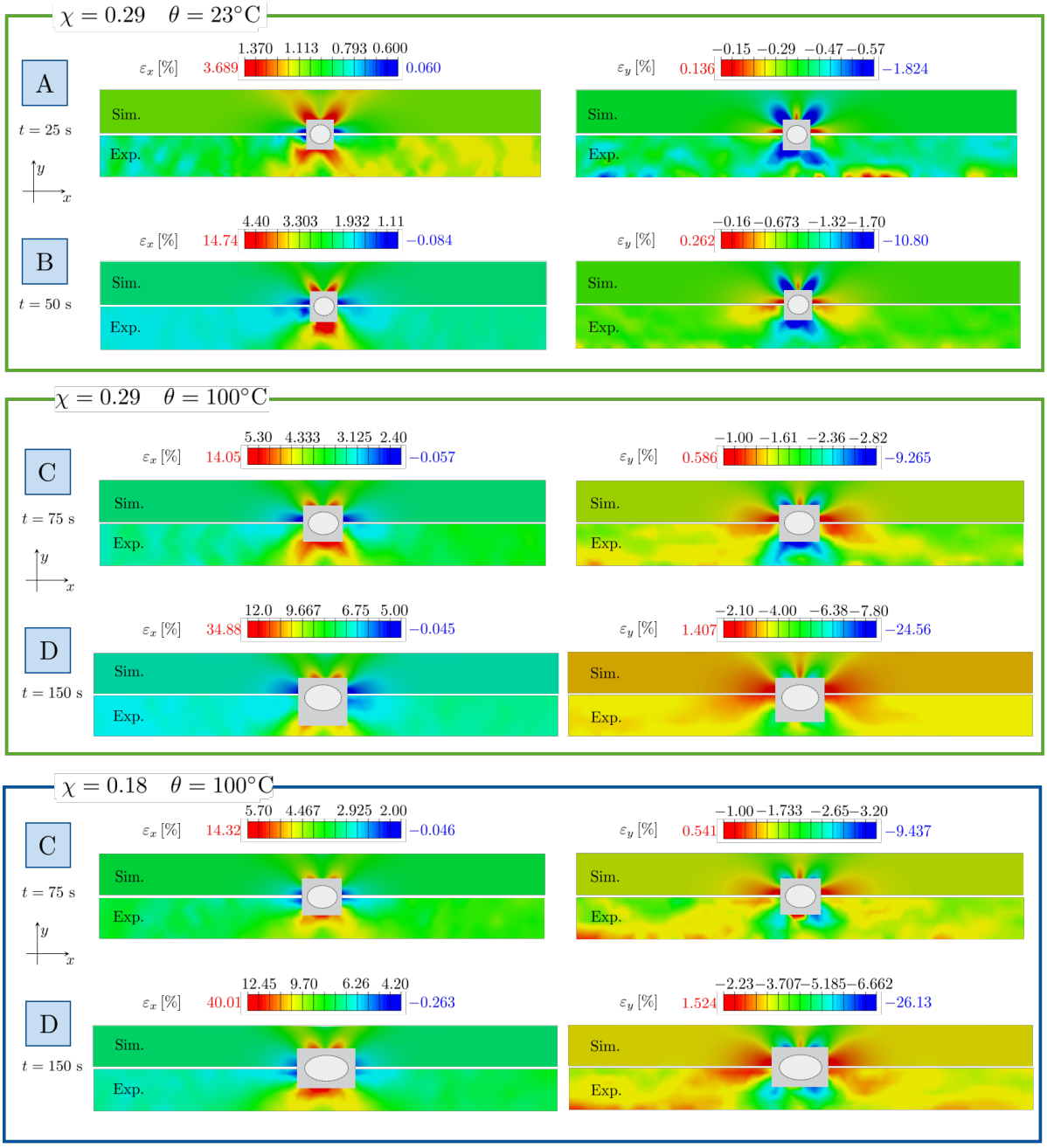

Figure 2.22: True strain contours in longitudinal and transverse direction: Comparison between experiment and model response for different temperatures and DOCs. Note here that the red and blue coloured values correspond to the simulation extrema in the area close to the hole.

Since the area close to the hole cannot be evaluated in the DIC data due to the chosen facet size and since therefore no strains are available, this area is excluded from the comparison with a light-gray patch. The size of the light-gray patch was chosen such that any area of the DIC where no strain data was available at that experimental time step was covered. Consequently, the patch size increased with increasing time (cf. Fig. 2.22 and 2.23). For the contour plots of the simulation, the chosen patch was mirrored at the x-axis and the legend of the DIC results was adopted for plotting. In the region close to the hole, however, the extreme values of the simulations occur. Thus, the extrema are included in red and blue colour next to the legends.

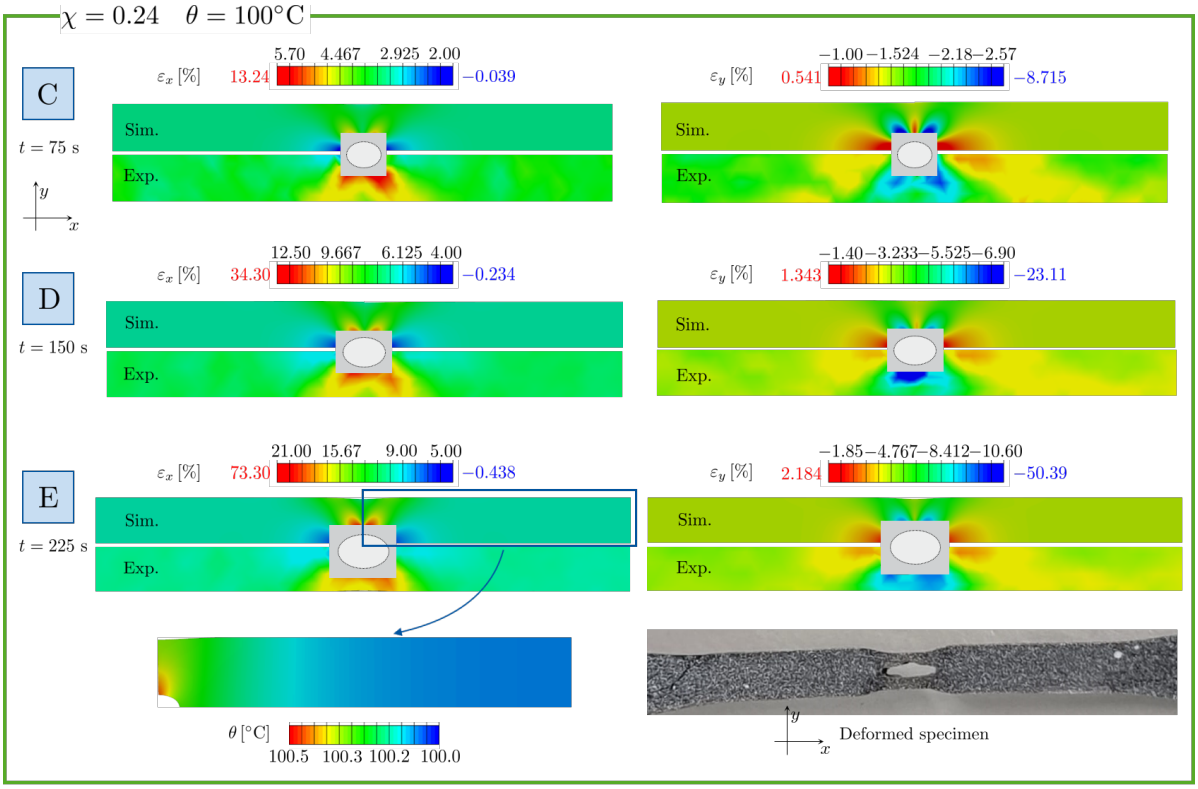

Figure 2.23: True strain contours in longitudinal and transverse direction: Comparison between experiment and model response for different temperatures and DOCs. Note here that the red and blue coloured values correspond to the simulation extrema in the area close to the hole.

The predicted strain fields in longitudinal and transverse direction are in vergy good agreement with the experimental results. Considering the formation of a multi-axial strain field close to the hole, the prediction is especially impressive, since the constitutive model was identified with uniaxial test data only. In addition, for model identification no DIC data apart from the Poisson's ratio was available and the true stress-strain data was obtained via the assumption of

incompressibility. In terms of the results for $\chi = 0.18$ (cf. Fig. 2.22) which is used purely for model validation, no big differences compared to the other DOCs can be observed, confirming the validity of the model for polyamide 6. For $\chi = 0.24$ at $100°$ C, a third time step E at $t = 225$ is evaluated. Here, the deformation of the specimen in the region close to the hole was already very large, therefore a bigger area needed to be grayed out. To provide a better understanding, the resulting deformation of the specimen after testing is visualized in a photograph in Fig. 2.23. In addition, for this time step the temperature field is given as well, indicating a slight increase in temperature for the whole specimen originating from the area close to the hole, where large strains in longitudinal direction are present. Infrared thermography measurements during mechanical testing would be needed to validate this result in the future, which is caused by dissipative heating.

2.6 Conclusion and outlook

In this work, a thermo-mechanically coupled constitutive framework was presented to predict the material behavior of semi-crystalline polymers at finite strains. To this end, a visco-elastic and an elasto-plastic contribution were combined to capture the complex nonlinear material behavior. Hereby, the derivation of the model equations was carried out in a thermodynamically consistent manner. To account for the Bauschinger effect, nonlinear kinematic hardening of Armstrong-Frederick type was incorporated together with a tension-compression asymmetry in yielding. The corresponding yield surface incorporates a hydrostatic pressure sensitivity, typically observed in polymers. Besides the strain-rate dependency, the temperature was considered as an influencing factor, therefore the temperature-field was fully coupled with the mechanical part of the model to account for self-heating effects. Moreover, the degree of crystallinity served as a constant input parameter to predict the effect of the underlying material morphology on the material behavior, as well as the interplay between the biphasic microstructure and applied thermal conditions. The implementation in the commercial FEM software ABAQUS/Standard, together with the use of the algorithmic differentiation tool ACEGEN, provided a flexible framework for current and future model adjustments.

To identify and validate the constitutive framework, an extensive experimental study was conducted, including a wide range of temperatures, finite strains as well as strain rates over two decades. Here, a novel blending technique was used during specimen production to achieve a wide range of degress of crystallinitys that were stable regarding time and temperature. In total, a range of approximately 15 % DOC, ranging from $\chi = 0.15$ to $\chi = 0.29$, was realized in the specimens. However, the addition of a co-polymer also had negative effects on the material

response. Monotonic tensile tests, revealed that the material strength below the glass transition regime is drastically reduced due to the increasing number of phase boundaries. Above T_g no such effects were visible. In order to investigate the complex visco-elastic, elasto-plastic material behavior, different loading procedures (i.e. monotonic tension, monotonic compression and relaxation tests) were conducted. The set of experimental data was completed by thermal experiments (i.e. TMA, DSC, Hot-Disc measurements, density measurements). The conducted experimental study provided important insights into the complex dependencies of temperature, strain rate and DOC and closed several gaps left in earlier works. Nonetheless, also further questions arose, especially related to the field of blend production. Here, further additives should be tested in the future. Especially the comparison of blends produced with a co-polymer or with crystallizations agents could be of interest when it comes to producing specimens with a wide range of DOCs. In addition, the influence of adding different compatibilizers on the material response below the glass transition regime should be examined carefully.

Based on the experimental data base, a successive identification procedure for the proposed framework was presented to obtain a set of material parameters for each test temperature. At the same time, various functions for a nonlinear relaxation time were compared to a benchmark test to identify the best suited relation. Lastly, against the odds, the evaluation of the crystallinity dependence of the thermal quantities revealed that the influence was less pronounced as in the mechanical tests, apart from the thermal expansion coefficient.

Subsequently, validation studies were performed that showed good agreement with the experimental data in the case of monotonic tension. The prediction for the relaxation tests was, however, less accurate for strain rates that were not used during identification. Probably, this can be accounted to the range of two decades that were considered during experimental testing. Overall, the constitutive framework was able to predict the material behavior of PA6, as demonstrated in the structural examples, where experimental data for various DOCs and temperatures was considered. Here, the temperature field was visualized as well, demonstrating a slight increase in the overall specimen temperature due to dissipation.

In the future, forming experiments are planned, where large variations in temperature during the heating, consolidation and cooling steps will demonstrate the need for the thermo-mechanical coupling in a more elaborate way. Furthermore, the experimental data set will be completed with additional compression tests for the remaining blends and cyclic tension and compression tests to analyze the hysteresis loop. Further, experiments on more complex loading scenarios, as for example pure shear, are planned to validate the choice of the yield surface with respect to experimental findings. Finally, crystallization kinetics will be incorporated

into the constitutive framework to study the effect of strain induced crystallization as well as cold-crystallization for further use in thermoforming simulations.

2.7 Appendix

2.7.1 Consistent tangent operators

In this section, the computation of the consistent tangent operators required by ABAQUS (cf. Sec. 2.3.8) is discussed in more detail. Since all model quantities are computed in the reference configuration (cf. Sec. 2.3.6), push forward operations are needed before use in ABAQUS. Without further derivation, the linearization of the weak forms of the balance of linear momentum as well as the energy balance are given as

$$\Delta \boldsymbol{S} = \mathbb{K}_E \left[\frac{1}{2} \Delta \boldsymbol{C} \right] + \boldsymbol{K}_\theta \Delta\theta \tag{2.62}$$

$$\Delta r = \boldsymbol{L}_E : \frac{1}{2} \Delta \boldsymbol{C} + L_\theta \Delta\theta. \tag{2.63}$$

The Jaumann rate of the Kirchhoff stress tensor from Eq. 2.54 can be reformulated to

$$\boldsymbol{\tau} - \boldsymbol{W}\boldsymbol{\tau} - \boldsymbol{\tau}\boldsymbol{W}^T = \mathring{\boldsymbol{\tau}} + \boldsymbol{D}\boldsymbol{\tau} + \boldsymbol{\tau}\boldsymbol{D} = \mathbb{C}^{\boldsymbol{\tau}}_{\boldsymbol{D}}[\boldsymbol{D}], \tag{2.64}$$

using the Lie derivative $(\mathring{*})$ of the Kirchhoff stress (cf. Stein and Sagar [2008])

$$\mathring{\boldsymbol{\tau}} = \boldsymbol{F} \underbrace{\left(\frac{d}{dt} (\boldsymbol{F}^{-1} \boldsymbol{\tau} \boldsymbol{F}^{-T}) \right)}_{\dot{\boldsymbol{S}}} \boldsymbol{F}^T = \Delta\dot{\boldsymbol{\tau}} - \boldsymbol{L}\boldsymbol{\tau} - \boldsymbol{\tau}\boldsymbol{L}^T. \tag{2.65}$$

With the definition of the stress rate of the second Piola-Kirchhoff tensor $\dot{\boldsymbol{S}} = 1/2\, \mathbb{K}_E[\dot{\boldsymbol{C}}]$ and the rate of deformation $\dot{\boldsymbol{C}} = 2\boldsymbol{F}^T\boldsymbol{D}\boldsymbol{F}$, the material tangent modulus $\mathbb{C}^{\boldsymbol{\tau}}_{\boldsymbol{D}}$ can now be calculated. The push forward operations for the remaining three material sensitivies are defined in the following

$$\boldsymbol{C}^{\boldsymbol{\sigma}}_{\theta} = \frac{1}{J}\, \boldsymbol{F}\, \boldsymbol{K}_\theta\, \boldsymbol{F}^T \tag{2.66}$$

$$\boldsymbol{C}^{r}_{\boldsymbol{D}} = \frac{2}{J}\, \boldsymbol{F}\, \boldsymbol{L}_E\, \boldsymbol{F}^T \tag{2.67}$$

$$C^{r}_{\theta} = \frac{1}{J}\, L_\theta. \tag{2.68}$$

Here, the algorithmic tangents corresponding to the stress increment $\Delta \boldsymbol{S}$ and the derivatives related to the increment of the internal heat generation Δr are expressed as

$$\mathbb{K}_E = 2\,\frac{\partial \boldsymbol{S}}{\partial \boldsymbol{C}}\bigg|_{\theta} = 2\left(\frac{\partial \boldsymbol{S}}{\partial \boldsymbol{C}}\bigg|_{\Gamma/\boldsymbol{C}} + \frac{\partial \boldsymbol{S}}{\partial \boldsymbol{U}_p^{-1}}\bigg|_{\Gamma/\boldsymbol{U}_p^{-1}} : \frac{\partial \boldsymbol{U}_p^{-1}}{\partial \boldsymbol{C}}\bigg|_{\theta} + \frac{\partial \boldsymbol{S}}{\partial \boldsymbol{U}_v^{-1}}\bigg|_{\Gamma/\boldsymbol{U}_v^{-1}} : \frac{\partial \boldsymbol{U}_v^{-1}}{\partial \boldsymbol{C}}\bigg|_{\theta}\right) \tag{2.69}$$

$$\boldsymbol{K}_{\theta} = \frac{\partial \boldsymbol{S}}{\partial \theta}\bigg|_{\boldsymbol{C}} = \frac{\partial \boldsymbol{S}}{\partial \theta}\bigg|_{\Gamma/\theta} + \frac{\partial \boldsymbol{S}}{\partial \boldsymbol{U}_p^{-1}}\bigg|_{\Gamma/\boldsymbol{U}_p^{-1}} : \frac{\partial \boldsymbol{U}_p^{-1}}{\partial \theta}\bigg|_{\boldsymbol{C}} + \frac{\partial \boldsymbol{S}}{\partial \boldsymbol{U}_v^{-1}}\bigg|_{\Gamma/\boldsymbol{U}_v^{-1}} : \frac{\partial \boldsymbol{U}_v^{-1}}{\partial \theta}\bigg|_{\boldsymbol{C}} \tag{2.70}$$

$$\begin{aligned}\boldsymbol{L}_E = 2\,\frac{\partial r}{\partial \boldsymbol{C}}\bigg|_{\theta} = 2\Bigg(&\frac{\partial r}{\partial \boldsymbol{C}}\bigg|_{\Upsilon/\boldsymbol{C}} + \frac{\partial r}{\partial \boldsymbol{U}_p^{-1}}\bigg|_{\Upsilon/\boldsymbol{U}_p^{-1}} : \frac{\partial \boldsymbol{U}_p^{-1}}{\partial \boldsymbol{C}}\bigg|_{\theta} + \frac{\partial r}{\partial \boldsymbol{U}_{pi}^{-1}}\bigg|_{\Upsilon/\boldsymbol{U}_{pi}^{-1}} : \frac{\partial \boldsymbol{U}_{pi}^{-1}}{\partial \boldsymbol{C}}\bigg|_{\theta} \\ &+ \frac{\partial r}{\partial \lambda_p}\bigg|_{\Upsilon/\lambda_p} \frac{\partial \lambda_p}{\partial \boldsymbol{C}}\bigg|_{\theta} + \frac{\partial r}{\partial \boldsymbol{U}_v^{-1}}\bigg|_{\Upsilon/\boldsymbol{U}_v^{-1}} : \frac{\partial \boldsymbol{U}_v^{-1}}{\partial \boldsymbol{C}}\bigg|_{\theta}\Bigg)\end{aligned} \tag{2.71}$$

$$\begin{aligned}L_{\theta} = \frac{\partial r}{\partial \theta}\bigg|_{\boldsymbol{C}} = &\frac{\partial r}{\partial \theta}\bigg|_{\Upsilon/\theta} + \frac{\partial r}{\partial \boldsymbol{U}_p^{-1}}\bigg|_{\Upsilon/\boldsymbol{U}_p^{-1}} : \frac{\partial \boldsymbol{U}_p^{-1}}{\partial \theta}\bigg|_{\boldsymbol{C}} + \frac{\partial r}{\partial \boldsymbol{U}_{pi}^{-1}}\bigg|_{\Upsilon/\boldsymbol{U}_{pi}^{-1}} : \frac{\partial \boldsymbol{U}_{pi}^{-1}}{\partial \theta}\bigg|_{\boldsymbol{C}} \\ &+ \frac{\partial r}{\partial \lambda_p}\bigg|_{\Upsilon/\lambda_p} \frac{\partial \lambda_p}{\partial \theta}\bigg|_{\boldsymbol{C}} + \frac{\partial r}{\partial \boldsymbol{U}_v^{-1}}\bigg|_{\Upsilon/\boldsymbol{U}_v^{-1}} : \frac{\partial \boldsymbol{U}_v^{-1}}{\partial \theta}\bigg|_{\boldsymbol{C}} \quad .\end{aligned} \tag{2.72}$$

To indicate which variables are held constant for the respective partial derivative, the set $\Gamma = \{\boldsymbol{C}, \boldsymbol{U}_p^{-1}, \boldsymbol{U}_v^{-1}, \theta\}$ was introduced for the stress. Likewise, for the internal heat generation the set $\Upsilon = \{\boldsymbol{C}, \boldsymbol{U}_p^{-1}, \boldsymbol{U}_{pi}^{-1}, \lambda_p, \boldsymbol{U}_v^{-1}, \theta\}$ was introduced for brevity and a more clear representation. As dicussed in detail in Sec. 2.3.8, the automatic differention tool *AceGen* is used to obtain the partial derivatives for the algorithmic tangents. Here, firstly the functions for the stress and the internal heat generation are implemented and $\boldsymbol{C}, \boldsymbol{U}_p^{-1}, \boldsymbol{U}_{pi}^{-1}, \lambda_p, \boldsymbol{U}_v^{-1}$ and θ, as well as all internal variables from the last converged time step, serve as input quantities. Consequently, the derivatives of $\boldsymbol{S}$ and r can be obtained rather easily after reaching local convergence. In the next step, the remaining derivatives of the two solution vectors $\boldsymbol{x}_{1,\text{loc}} = (\hat{\boldsymbol{U}}_p^{-1}, \hat{\boldsymbol{U}}_{pi}^{-1}, \lambda_p)^T$ and $\boldsymbol{x}_{2,\text{loc}} = (\hat{\boldsymbol{U}}_v^{-1})^T$ with respect to the global unknowns $\boldsymbol{x}_{\text{glo}} = (\boldsymbol{C}, \theta)^T$ are derived. For the elasto-plastic part, an additional linearization of the converged local residual vector $\boldsymbol{r}_{1,\text{loc}} = (\boldsymbol{r}_{1,p}, \boldsymbol{r}_{1,pi}, r_{1,\sigma})^T$ is performed and implemented in *AceGen*.

$$\begin{aligned}\mathbf{0} &= \underbrace{\boldsymbol{r}_{1,\mathrm{loc}}}_{=\mathbf{0}} + \left.\frac{\partial \boldsymbol{r}_{1,\mathrm{loc}}}{\partial \boldsymbol{x}_{1,\mathrm{loc}}}\right|_{\substack{\boldsymbol{C}\\ \theta}} \cdot \Delta \boldsymbol{x}_{1,\mathrm{loc}} + \left.\frac{\partial \boldsymbol{x}_{1,\mathrm{loc}}}{\partial \hat{\boldsymbol{C}}}\right|_{\substack{\theta\\ \boldsymbol{x}_{1,\mathrm{loc}}}} : \Delta \hat{\boldsymbol{C}} + \left.\frac{\partial \boldsymbol{r}_{1,\mathrm{loc}}}{\partial \theta}\right|_{\substack{\boldsymbol{C}\\ \boldsymbol{x}_{1,\mathrm{loc}}}} \Delta\theta \\ &= \left.\frac{\partial \boldsymbol{r}_{1,\mathrm{loc}}}{\partial \boldsymbol{x}_{1,\mathrm{loc}}}\right|_{\substack{\boldsymbol{C}\\ \theta}} \cdot \Delta \boldsymbol{x}_{1,\mathrm{loc}} + \left.\frac{\partial \boldsymbol{r}_{1,\mathrm{loc}}}{\partial \boldsymbol{x}_{\mathrm{glo}}}\right|_{\boldsymbol{x}_{1,\mathrm{loc}}} \cdot \Delta \boldsymbol{x}_{1,\mathrm{glo}} = \boldsymbol{J}_1 \Delta \boldsymbol{x}_{1,\mathrm{loc}} + \boldsymbol{J}_2 \Delta \boldsymbol{x}_{1,\mathrm{glo}}. \end{aligned} \tag{2.73}$$

Using the relation above, the incremental change of the local elasto-plastic variables $\boldsymbol{x}_{1,\mathrm{loc}}$ with respect to an incremental change of the global variables $\boldsymbol{x}_{1,\mathrm{glo}}$ can be expressed by $\boldsymbol{J} = -\boldsymbol{J}_1^{-1}\boldsymbol{J}_2$. From this expression, the remaining derivatives for the elasto-plastic part can be exracted. The derivatives for the visco-elastic part are obtained in the same manner and therefore not further discussed.

2.7.2 Dynamical Mechanical Analysis (DMA)

The DMA tests were conducted on a *TA instruments AR-G2* rheometer.

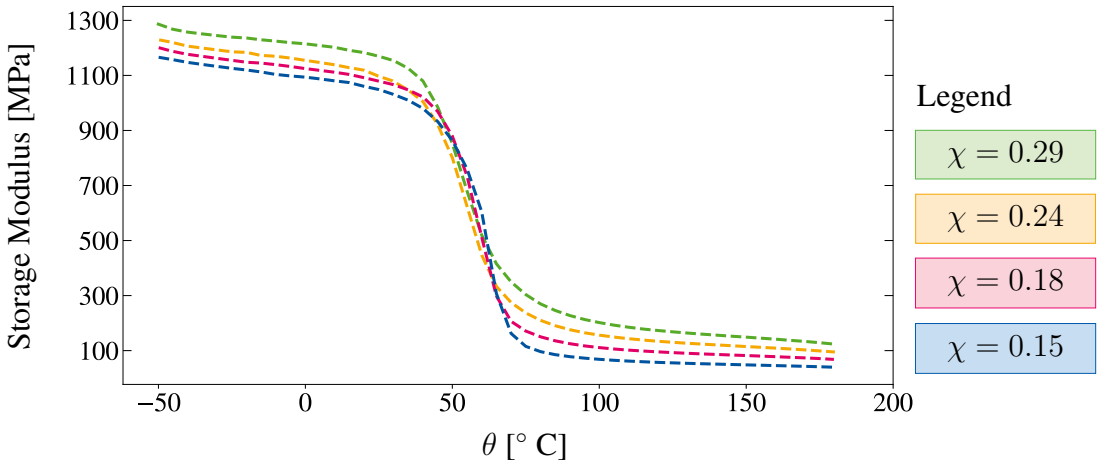

Figure 2.24: Dynamical mechanical analysis - Storage modulus for various DOCs.

2.7.3 Conversion between engineering and true stress

The engineering or nominal stress in terms of the 1. Piola-Kirchoff stress ($\boldsymbol{P}$) is converted to the true (Cauchy) stress ($\boldsymbol{\sigma}$) under the assumption of perfect incompressibility

$$J = \det(\boldsymbol{F}) = 1. \tag{2.74}$$

Using Eq. 2.74, the deformation gradient for uniaxial monotonic tension or compression can be obtained by means of the experimentally measured stretch in loading (x-) direction

$$\boldsymbol{F} = F_{\text{exp}} = \begin{pmatrix} \lambda_x & 0 & 0 \\ 0 & 1/\sqrt{\lambda_x} & 0 \\ 0 & 0 & 1/\sqrt{\lambda_x} \end{pmatrix}. \tag{2.75}$$

Now, the true (Cauchy) stress is calculated by a pushforward of the 1. Piola-Kirchhoff to the current configuration

$$\boldsymbol{\sigma} = J^{-1}\, \boldsymbol{P}\, \boldsymbol{F}^T. \tag{2.76}$$

Here, $\boldsymbol{P}$ is the engineering or nominal stress,

$$\boldsymbol{P} = P_{\text{exp}} = \begin{pmatrix} F/A_0 & 0 & 0 \\ 0 & 0 & 0 \\ 0 & 0 & 0 \end{pmatrix}, \tag{2.77}$$

which, in the case of uniaxial tension or compression, is the current experimentally measured force (F) in loading (x-) direction over the reference cross section (A_0).

2.7.4 Single element boundary value problem

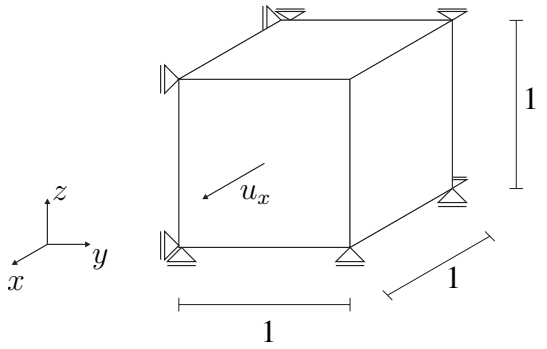

Figure 2.25: Single element test - Boundary value problem for a uniaxial monotonic tension/compression test.

2.7.5 Results at remaining temperatures for the comparison of different nonlinear functions for the relaxation time

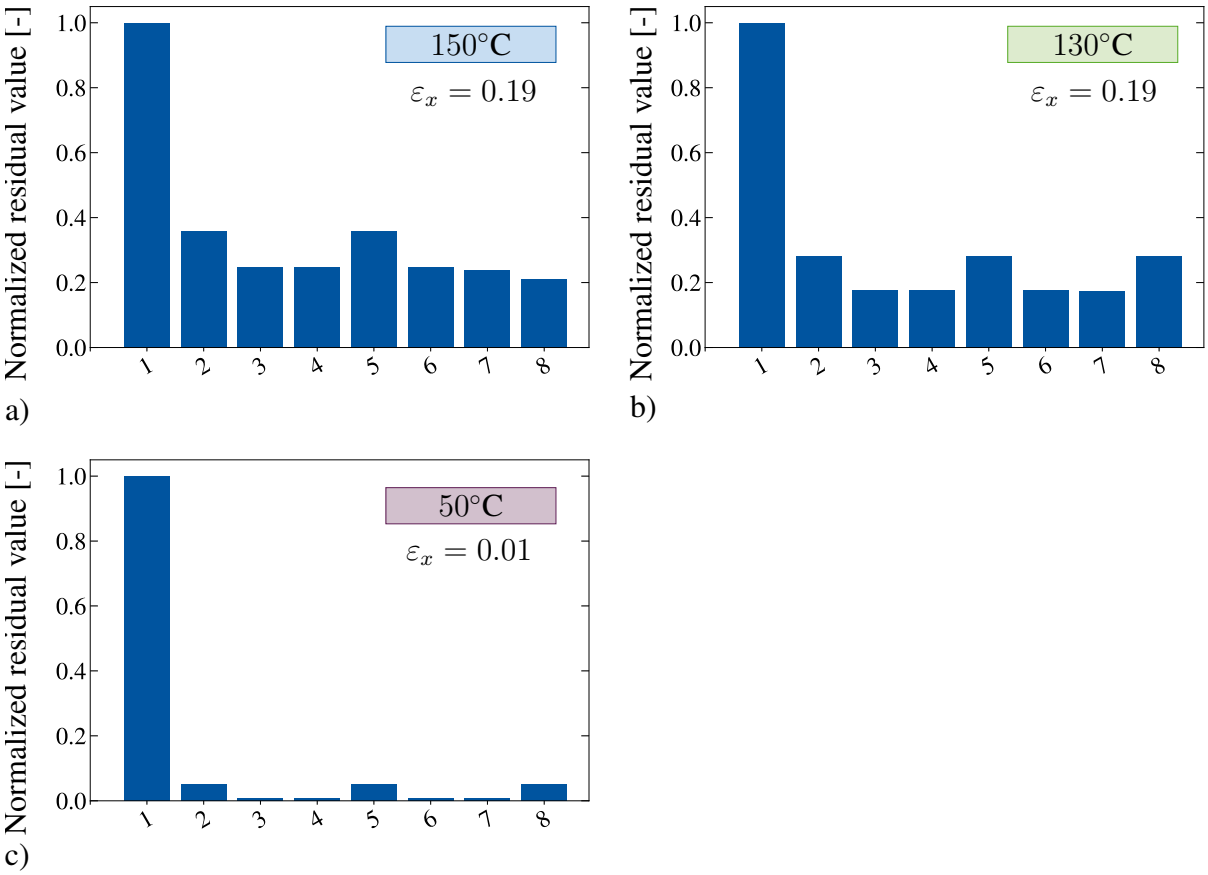

Figure 2.26: Fitting results for different nonlinear functions for the relaxation time: a) and b) above the glass-transition regime c) at 50° C. Note here that due to the reduced set of experimental data (only $\chi = 0.29$ and $\chi = 0.24$ were considered at this temperature), a comparatively better fit is achieved.

2.7.6 Results at remaining temperatures for the parameter identification from single curve fits

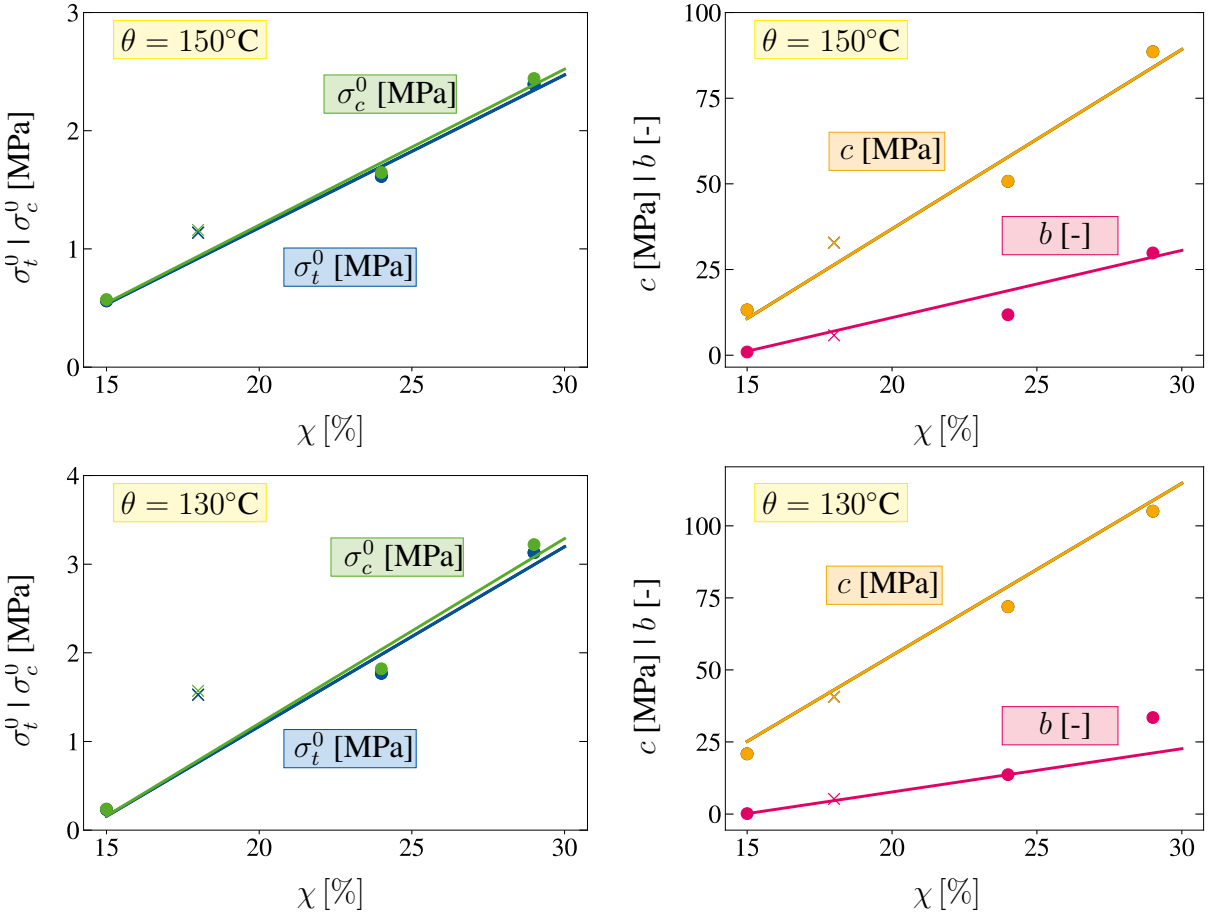

Legend: ● DOC used for identification × DOC used for validation

Figure 2.27: Results for the parameter identification from single curve fits for temperatures above T_g. The linear trend line is of the form $(\bullet) = c_1\,\chi + c_2$, with $(\bullet) = \sigma_t, \sigma_c, c, b$. Note here that the fit for parameter b is weighted for both temperatures to avoid a function that leads to negative results for $\chi = 0.15$.

3 Article 2: Experimental investigation and micromechanical analysis of glass fiber reinforced polyamide 6

This article was published as:

Reuvers, M., Dannenberg, C., Kulkarni, S., Loos, K., Johlitz, M., Lion, A., Reese, S. and Brepols, T. [2024], 'Experimental investigation and micromechanical analysis of glass fiber reinforced polyamide 6', *Mechanics of Materials* **199**, 105144.

Disclosure of the individual authors' contributions to the article:

M. Reuvers revieved the relevant existing literature, developed the conceptual design of the experimental study, evaluted the experiments, was responsible for model identification and validation and performed all computational examples, interpreted the results and wrote the article. C. Dannenberg developed the algorithm for the automated generation of repeating unit cells using the Abaqus-Python interface and generated all corresponding unit cells. S. Kulkarni provided the thermal analysis and the microscopic images and contributed to the discussion of the results. K. Loos, M. Johlitz, A. Lion, T. Brepols and S. Reese gave conceptual advice, contributed to the discussion of the results, proofread the article and gave valuable suggestions for improvement. All authors approved the publication of the final version of the manuscript.

3.1 Abstract

Achieving process stability in the thermoforming of fiber reinforced polymer materials (FRPs) for aerospace or automotive manufacturing is usually associated with a costly trial-and-error process, where experimental boundary conditions and other influencing factors, such as, for example, material composition, need to be adjusted over time. This is especially true when material phenomena on the microlevel, such as the crystallization kinetics of the polymer matrix or resulting stresses from temperature gradients, are the cause of the process instability. To reduce the experimental effort and reliably predict the material behavior during thermoforming, finite element simulation tools on multiple scales are a useful solution. Hereby, incorporating micromechanical phenomena into the model approaches is crucial for an accurate prediction by further reducing the deviation between simulation and experiment, in particular with regard to the underlying nonlinear material behavior. In this work, unit cell simulations on the microscale of a unidirectional glass fiber reinforced polymer (UD GFRP) are conducted to predict effective thermomechanical properties of a single material ply and ascertain the effect of individual ply constituents on the homogenized material behavior. The polymeric matrix material model used was identified in a prior publication with experimental data at various temperatures for polyamide 6 blends with varying degrees of crystallinities. Various randomization methods are tested to generate the unit cells and replicate the composites' random fiber distribution, with a focus on process automation. The simulative results are successfully compared to an experimental study on glass fiber reinforced polyamide 6 tested at various temperatures, demonstrating the potential of the approach to reduce both time and cost required for material characterization. Finally, the unit cells are used to generate a database to predict untested load cases that will be used in future work to characterize a homogenized macroscopic material model.

3.2 Introduction

Nowadays, fiber reinforced polymers (FRPs) are extensively used in applications where good thermomechanical properties are required in combination with weight savings and cost-effective mass production. These composite materials are manufactured with a broad variety of constituents and more and more often recyclability and reusability are key factors for the design process. However, despite their popularity in industry and cross-sector usage the accurate prediction and performance of forming processes such as e.g. thermoforming often remains a process of trial and error. In many cases, the final product exhibits unwanted deformations

after forming that need to be eradicated with time-consuming and costly experiments until all process parameters are dialed in. Especially, the complex behavior of the polymeric matrix material undergoing a second order phase change around the glass transition regime is difficult to predict and still an ongoing research topic on its own today (see e.g. Hadipeykani et al. [2020]; Xie et al. [2020]). In the case of a semi-crystalline polymer matrix, the recrystallization during cooling is another process that is crucial not only for the resulting material performance but also for the interplay between fiber and matrix at their interface is a challenging factor.

Experimentally obtained results for one specific FRP system cannot be extrapolated to other configurations with different fiber volume fractions or constituent properties, such as for example the matrix degree of crystallinity (DOC). Therefore, to characterize material model formulations for various material systems, experiments need to be repeated, leading to a massive investment for model identification and verification (see e.g. Naya et al. [2017]). To consider micromechanical effects, which are often critical to understanding material failure during a forming process, additional experiments are required to account for the individual constituents, even though the material behavior of the composite may already be known. In addition, the simultaneous consideration of an increasing number of boundary conditions and material phenomena, such as temperature, moisture content, environmental factors, time-dependent material behavior, underlying morphology, kinematic rotation of the fibers during forming, or damage, dramatically increases the number of experiments required. Consequently, computational approaches are needed to reduce the set of experiments without compromising on data and at the same time increasing the reusability for different material systems through a universal approach.

To investigate micromechanical effects and further incorporate them on the macrolevel without conducting new experiments, several computational approaches exist Geers et al. [2010]. Classical, fully coupled modeling schemes such as FE^2 (see e.g. Feyel and Chaboche [2000]; Schröder [2014]; Raju et al. [2021]) or FE-FFT (see e.g. Spahn et al. [2014]; Schneider [2021]; Gierden et al. [2022]) pass the macroscopic deformation to the microscale in every Gauss point, where an additional boundary value problem is solved on a unit cell. The resulting stress state as well as the tangent operator are transferred back to the macroscale as volume averages over the microscopic domain to achieve a global solution. Herein, several contributions also address multiphysical problems such as, for example, thermomechanical coupling (see e.g. Özdemir et al. [2008]; Temizer and Wriggers [2011]; Li et al. [2019]; Wicht et al. [2021]; Schmidt et al. [2023]) or damage (see e.g. Spahn et al. [2014]). These approaches are known to predict the macroscopic material behavior with a high degree of accuracy, provided that there is sufficient separation of scales. However, the computational

cost is usually very high (cf. Geers et al. [2010]). Another method to achieve the homogenized macroscopic solution are uncoupled multiscale approaches, where numerical simulations on a representative part of the composite microstructure are used as virtual experiments to generate input data for the characterization of the material models on the macroscale (see e.g. Naya et al. [2017]). Thereby, the homogenized microscopic response in terms of e.g. effective material properties is in close agreement with experimental data on the higher scale given an appropriate choice of the microscopic domain. In addition to the lower computational cost associated with the uncoupled solution, complex experimental stress or strain conditions such as multiaxial loadings can be reproduced without the corresponding experimental effort. Furthermore, varying boundary conditions can easily be applied on the microstructure and their effect on the macroscale can be investigated in detail.

In the context of FRPs, computational micromechanics have been used intensively to study the composites failure behavior. Melro et al. [2013*b*], for example, developed a constitutive damage model for an epoxy matrix that was used in a micromechanical analysis with unidirectional (UD) fiber reinforcement to predict ply properties in Melro et al. [2013*a*]. Apart from the matrix damage, the delamination between fibers and matrix at their interface was studied using cohesive zone elements. Similar investigations were conducted by Naya et al. [2017], who further incorporated a cohesive damage-friction model for fiber matrix debonding and validated the numerical results against experimental data. Interfiber/interlaminar failure prediction was studied by Hinton et al. [2004]; Daniel et al. [2009], whereas Selmi et al. [2011] used mean-field homogenization to investigate the biaxial yield as well as the plastic regime of short glass fiber reinforced polyamide. More recent publications from Poggenpohl et al. [2022*b*,*a*] focused on the development of a homogenization approach for the failure zone of carbon fiber reinforced polymers (CFRPs). The generation of statistically equivalent fiber distributions in unit cells was discussed by e.g. Vaughan and McCarthy [2010]; Wang et al. [2016]; Bargmann et al. [2018], while the influence of the shape of the individual fibers on the resulting macroscopic material behavior was investigated by, for example, Herráez et al. [2016]. The influence of the fiber volume content and the fiber length distribution on the elastic and thermoelastic behavior of short fiber composites were studied by Hine et al. [2002], whereas the influence of the thermal history on the interfacial properties of carbon fiber reinforced polyamide 6 composites was studied by Li et al. [2016]. In terms of multiphysical micromechanical investigations, especially regarding the thermomechanical behavior of FRPs, only a few contributions are available, where, to the authors' knowledge, the influence of the DOC is not taken into account yet. Therefore, in this work, a micromechanical analysis will be conducted on glass fiber reinforced polyamide 6 repeating unit cells (RUCs) and extended

to account for the effective thermal material response in order to generate a virtual data basis for the identification of a homogenized macroscopic material model. For validation purposes, an experimental study is carried out on the composite.

In contrast to existing publications, this approach employs a thermomechanically coupled matrix material formulation developed by Reuvers et al. [2024a]; Kulkarni et al. [2022, 2023] in a preceding step. This formulation has been validated through extensive mechanical and thermal experimental studies conducted on polyamide 6 blends. Its applicability is demonstrated across a wide range of crystallinities and temperatures. Consequently, the authors are able to generate virtual composite data for a wide range of matrix degrees of crystallinity (DOCs) and temperatures after validating the results of the micromechanical analysis for one DOC. This approach thus leads to a significant decrease in the overall experimental effort without any compromise to the experimental findings. In other words, the presented approach allows for the generation of experimental data in a virtual manner, thereby enabling the testing of a broad variety of boundary conditions or load cases that would otherwise require an extensive amount of time if tested experimentally. Furthermore, the integration of further micromechanical phenomena related to the polymeric matrix, such as damage or moisture dependence, is straightforward. The same methodology can be applied to other semi-crystalline thermoplastic composite materials in the future.

The accompanying experimental preparation and procedure are stated in Sec. 3.3, where a direction dependent mechanical and thermal analysis is carried out. Next, in Sec. 3.4 the thermodynamically consistent, thermomechanically coupled material model formulation for the polyamide 6 matrix is briefly summarized. Here, the degree of crystallinity serves as a constant input variable. Visco-elastic and elasto-plastic contributions are combined together with a nonlinear kinematic hardening of Armstrong-Frederick type and a tension-compression asymmetry in yielding. In Sec. 3.5, the generation of repeating unit cells is discussed using various different randomization methods with a focus on process automation. Moreover, a statistical analysis is carried out to determine the resulting mesh and RUC size. The identification of the matrix model with experiments carried out on polyamide 6 blends in Reuvers et al. [2024a] is briefly summarized in Sec. 3.6 together with an extension of the parameter range to account for the composite material. Subsequently, the numerical results are compared to experimental findings to examine the validity of the RUCs. Further mechanical and thermal numerical results enrich the data basis for the characterization of a macroscopic material model formulation. Finally, in Sec. 3.7 a conclusion is drawn, and an outlook is given.

3.3 Experimental investigation

3.3.1 Specimen preparation

The objective of the experimental investigation was to obtain engineering stress-strain data for various constant temperatures and strain rates in the direction of the fibers (x-direction) and perpenpendicular to them (y- and z-direction). Therefore, unidirectionally (UD) fiber reinforced plates were manufactured by Bond Laminates (Lanxess) as 102-RGUDm317 Tepex® dynalite sheets with 40 % fiber volume content and a polyamide 6 matrix[1]. To ensure comparability with the experiments conducted to characterize the existing matrix material model (see Reuvers et al. [2024a]), the same PA6 granulate was used for the production of the plates. Here, randomly distributed UD roving glass fibers with a diameter of approximately 17 μm were used for UD tape production and stacked in 16 or 32 layers for manufacturing to achieve two material thicknesses of 5 and 10 mm, respectively. In the following, the 5 mm plates were used for all tension and bending tests as well as for the thermomechanical analysis (TMA) and the dynamical mechanical analysis (DMA), whereas the 10 mm plate served for compression and conduction tests. After production, the plates were cut into 100x5x10 mm^3 and 100x5x20 mm^3 specimens for the tension tests in fiber direction and perpendicular to it, in line with DIN EN ISO 527-5. Note here that all tests under varying fiber angle were performed with the latter specimen size as well. For the compression tests, smaller samples with 10x10x10 mm^3 were needed according to DIN EN ISO 604. For the three-point bending experiments in y- and z-direction, the specimens were cut into strips of 100x15x5 mm^3 in line with DIN EN ISO 14125. An overview of the sample geometries and the coordinate system that will be used throughout this work is provided in Fig. 3.1. For cutting, a diamond saw was utilized together with a water jet for cooling purposes, since the heat generated during sawing could potentially alter the degree of crystallinity of the polyamide 6 matrix. Afterwards, the wet specimens were stored in a *MP Dry Cabinet IV ST* (MP Elektronik Technologie, Svitávka, Czech Republic) until the moisture content obtained from an *Aquatrack* (Brabender (Anton Paar), Duisburg, Germany) measurement was less than 0.1 %. Until testing, the specimens were stored in vacuum sealed aluminum bags to prevent water absorption due to the hygroscopic matrix material.

[1]The thermal histories associated with the production of the tape and laminate are not available due to the commercial nature of the product.

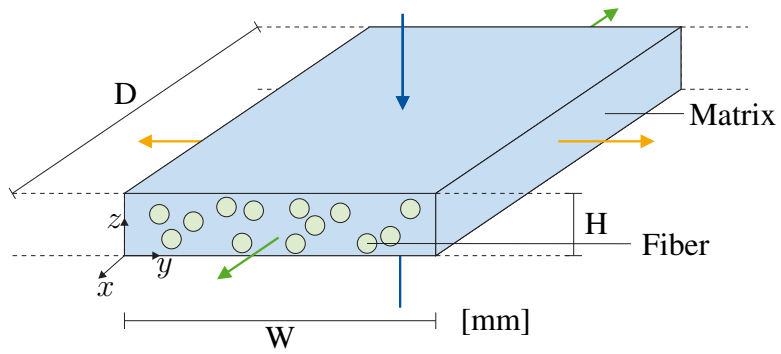

Orientation to fiber direction	Load case	Width [mm]	Depth [mm]	Height[mm]
∥	Tension	10	100	5
⊥	Tension	100	20	5
⊥	Compression	10	10	10
∥	Three-point bending	15	100	5
⊥	Three-point bending	100	15	5

Figure 3.1: Schematic overview of the sample geometries and mechanical test cases.

3.3.2 Differential scanning calorimetry

Prior to the mechanical and thermal experimental investigations, the degree of crystallinity of the composite was determined via differential scanning calorimetry (DSC) at the Polymer Service GmbH Merseburg (PSM) Germany. For this procedure, only a small fraction of material (ideally < 10 mg) is needed. However, due to the random dispersion of the glass fibers in the polyamide 6 matrix, cutting and testing a small part of a specimen does not guaranty the desired 40 % fiber volume content in the probe. To overcome this problem and to achieve sample material with the correct fiber volume content, slices from four different measurement positions of a specimen were taken and subsequently ground to powder. Next, a fraction of the powder was used for the DSC analysis and afterwards burned via thermogravimetric analysis (TGA) to determine the true amount of glass fibers in the tested sample. As can be seen in Tab. 3.1, the four locations yielded similar results in the DSC analysis and the TGA confirmed that the correct amount of fibers was met when calculating the volume percentage with the fiber density. Next, the melting enthalpy ΔH_m obtained from the integrated area under the peak of the heat flow over time of the first and second heating run was corrected with the PA6 mass fraction to resemble a material with 100 % PA6 content ($\Delta H_m^{100,\mathrm{PA6}}$). Together with the specific fusion enthalpy for a hypothetically 100 % crystalline material ($\Delta H_0^{100} = 190$ J/g

from Campoy et al. [1998]), the absolute DOC of the matrix was calculated by

$$\chi = \frac{\Delta H_m^{100,\mathrm{PA6}}}{\Delta H_0^{100}}. \tag{3.1}$$

The mean value for the first heating run of the four test locations was found to be $\chi \approx 0.41$. This value will be used in the following to obtain the matrix properties together with the results of the identification procedure in Reuvers et al. [2024a].

Similar to Reuvers et al. [2024a] for pure PA6, the glass transition temperature of the composite was around 58° C. The authors anticipated this outcome, given that the same PA6 granulate was used for specimen production and the glass fibers behave purely amorphously.

	Weight[mg]	Melting enthalpy [J/g]		GF content [mass-%]	corrected melting enthalpy [J/g]		DOC [%]	
		1.HR	2. HR		1.HR	2. HR	1.HR	2. HR
M1	6.48	29.77	30.36	0.6274	79.90	81.48	42.05	42.88
M2	6.72	28.26	28.75	0.6334	77.09	78.42	40.57	41.28
M3	7.68	27.27	29.04	0.6396	75.67	80.58	39.82	42.41
M4	7.10	31.39	31.46	0.6047	79.41	79.59	41.79	41.89
Avg.	7.00	29.173	29.903	0.6263	78.015	80.017	41.06	42.11

Table 3.1: Differential scanning calorimetry (DSC) and thermogravimetric analysis (TGA): Results and average at four different measuring locations.

3.3.3 Microscopic examination

To gain a direct insight into the materials' microstructure for the unit cell generation in Sec. 3.5, microscopic in-ply images were taken on a *Zeiss Axiophot* (Zeiss, Oberkochen, Germany) microscope with *ProgRes SpeedXT Core 5* (Jenoptik, Jena, Germany) camera at the Institute of Mechanics, University of the German Federal Armed Forces, Munich. Therefore, a small sample of the composite material was enclosed in epoxy, and further ground and polished with a *LaboSystem LaboPol-30* and *LaboForce-100* (Struers, Champigny sur Marne cedex, France) machine until a clear image was visible under the microscope. In Fig. 3.2, two material sections are shown with different magnification. As indicated in the picture, the glass fibers are randomly distributed in the polyamide 6 matrix. Additionally, supporting fibers in weft direction are visible, which are necessary to ensure stability during the production process. According to the manufacturer specifications, only three percent of the total fiber volume content are supporting fibers, hence, these fibers are neglected for the unit cell generation in Sec. 3.5. Moreover, the glass fibers show a variation in cross-sectional area. To incorporate this phenomenon, further microscopic images on a range of samples would be necessary in

combination with statistical investigations which is beyond the scope of this work. Therefore, the authors chose to approximate the cross section of the glass fibers as circular disks with a constant diameter of 17 μm according to the manufacturer. Interestingly enough, in the left image in Fig. 3.2 a laminate like pattern is visible, where layers consisting predominantly of matrix material separate layers including fibers.

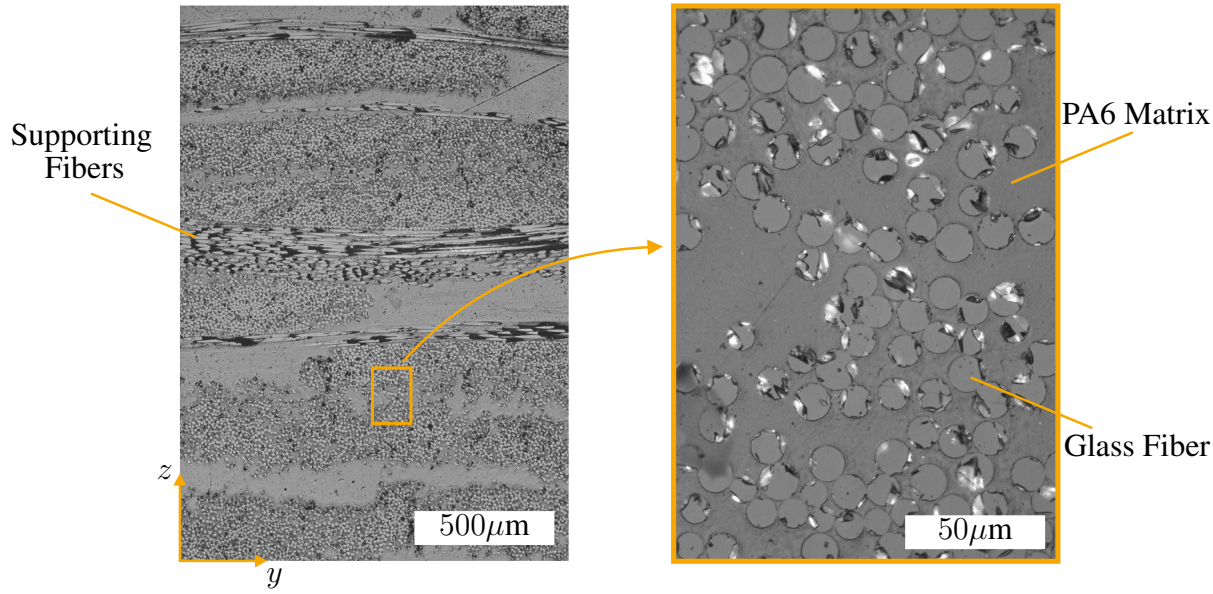

Figure 3.2: Microscopic pictures showing the random fiber distribution and the layer structure of the composite.

This effect stems from the production process, where firstly prepregs are produced out of a single layer of unidirectional glassfibers coated with PA6 powder. In the next processing step, several prepreg rolls are layered and combined to a composite during an impregnation and consolidation step. Here, the PA6 powder melts under temperature and forms the matrix. The application of pressure ensures an air pocket free composite in which every fiber is surrounded by the thermoplastic matrix. In our case, 16 and 32 layers were realized for a resulting composite thickness of 5 and 10 mm, respectively. Naturally, the layered structure remains even after consolidation, resulting in areas where only matrix material is present.

3.3.4 Mechanical testing

3.3.4.1 Experimental setup and boundary conditions

For the mechanical tests, a *ZwickRoell Z005* (ZwickRoell, Ulm, Germany) universal testing machine was utilized together with a 10 kN force cell. Additionally, a temperature furnace

(ZwickRoell, Ulm, Germany) was incorporated in the experimental set-up for all test temperatures above room temperature. Monotonic, uniaxial tension tests were conducted in fiber direction (x-direction) and perpendicular to the fibers (y-direction) as displayed in Fig. 3.1 together with cyclic tests in both directions. In addition, monotonic uniaxial compression tests (z-direction) were performed to complete the set of in-plane material characteristics and determine differences in the material related to the loading direction. Here, cyclic tests were conducted as well. For all compression tests, a load string with a reversal cage was used that converts tensile forces to a compressive load to reduce the effort in changing the experimental set-up from tension to compression. In addition, a lubricant was used to reduce bulging of the specimens in line with DIN EN ISO 604.

To gain insight into the material behavior for multiaxial strain states, monotonic tension tests under varying fiber angle (15°, 30°, 45°, 60°) were conducted as well at room temperature and one elevated temperature (150°). For these tests, material from a second order was used that was made several month after the first one, thus a comparison between first and second batch of material will be given as well.

To obtain non-tactile displacement measurements, an *ARAMIS 4M* (Zeiss, Oberkochen, Germany) digital image correlation (DIC) system was exploited during testing. Therefore, the specimens were primed with a white color coat, on which graphene speckles were applied in a secondary step to generate a stochastic pattern visible for the DIC system. Outside the temperature furnace, 3D DIC measurements were taken with two cameras for all tension tests, while testing at elevated temperatures required changing to a 2D set-up with one camera due to the small window of the temperature furnace and the reflections caused by the window pane. In these cases, major attention was paid to achieve a perpendicular alignment between the specimen surface and the camera lens with a translative motion test serving as a verification. The effect of barrel distortion or thinning of the specimen (change in distance to the camera) that could lead to differences between 2D and 3D measurements was tested in advance with several 2D room temperature tensile tests in the temperature furnace compared to the 3D results outside the temperature chamber (see Fig. 3.6 a). In general, the 2D measurements resulted in a softer material behavior compared to the measurements with two cameras. The deviation in y-direction is negligible, in x-direction, however, a significant change in stiffness is present. The authors believe that this difference does not only result from the change between 2D and 3D DIC measurements but is influenced by several factors such as the window pane of the temperature chamber and the smaller specimen size. As a consequence of the blurring effect of the window pane and the increased distance between camera and specimen, it was necessary to adjust the stochastic pattern to a coarser grid. This resulted in a reduction in the number of

interpretable data points, particularly in x-direction, where the number of available data points was significantly decreased due to the smaller specimen dimensions. Without the change in speckle size, however, the camera was unable to focus, and thus the adjusted stochastic pattern served to mitigate the issue caused by the temperature furnace. Though explainable, the measurement differences will be visible in the upcoming results in fiber direction and need to be interpreted with care. Here, a better camera system and more light sources, especially in the blue light range, could lead to an improvement. Additionally, indirect lighting from the side window of the temperature furnace could be considered. In terms of the compression tests, only 2D DIC measurements were possible at room temperature since the distance between the specimen and the camera needed to be reduced due to the small specimen size. For the compression tests above room temperature, unfortunately, no DIC measurements were possible. This can be attributed mostly to the reversal cage that caused severe shadowing on the backwards offset specimen in combination with the light sources arranged at an angle to the window pane to reduce reflection. The use of compression plates that were not available at that time would improve the set-up and reduce shadowing. Nonetheless, the increased distance between the camera and the specimen due to the temperature furnace would need to be resolved as well.

In total, experiments were conducted at three distinct temperatures, both below and above the glass transition temperature of the matrix material ($T_g \approx 58°$ C, cf. Reuvers et al. [2024a]): 23° C, 100° C, and 150° C. The heating time for achieving a homogeneous temperature distribution across the specimens measured 15 minutes prior to testing for the tensile specimens and 30 minutes for the compression specimens due to the increased thickness. To allow for thermal expansion, the tension specimens were clamped only at the upper part during heating.

To ensure comparability with the tests conducted in Reuvers et al. [2024a], two strain rates ($\dot{\varepsilon}^t_{\text{min}} = 2.1$ mm/min and $\dot{\varepsilon}^t_{\text{max}} = 4.2$ mm/min) were prescribed for all tension tests independent of the fiber direction to study the rate dependent material behavior that is reported for PA6 (see e.g. Shan et al. [2007]; Ayoub et al. [2011]). Hereby, the loading rate was controlled by the cross head speed of the machine. In terms of the loading rate for the compression tests $\dot{\varepsilon}^c_{\text{min}} = 0.3$ mm/min and $\dot{\varepsilon}^c_{\text{max}} = 3.0$ mm/min were used. Converted to the dimensions of the respective specimens, the lowest loading rate for each test corresponds to 0.0005s^{-1}, as used for the experiments on PA6 blends in Reuvers et al. [2024a]. The tests were terminated once the specimen broke or the maximum force of the testing machine (5 kN) was reached. Each procedure was repeated three to four times. The strain data was obtained using the DIC data averaged over the whole specimen domain, whereas the force data was taken directly from the $ZwickRoell$ machine. To avoid effects due to imperfect stochastic pattern or imperfections

during cutting, the area close to the specimen edge was excluded from the evaluation of the DIC measurements. All results are given in terms of engineering stress ($P = F/A_0$) ,defined as the current force F divided by the undeformed cross-sectional area A_0, over engineering strain ($\varepsilon = \Delta L/L$) ,defined as the ratio of the change in length ΔL to the original length of the specimen L.

Lastly, three-point bending tests were conducted at room temperature in x- and y-direction to determine the Young's modulus in bending as well as the flexural stress-strain response of the material. Here, DIC measurements were omitted, due to the short distance between load cell and cross head in this set-up which reduces the slip significantly.

3.3.4.2 Experimental results

Fig. 3.3 shows the results for the monotonic tension tests in and perpendicular to the fiber direction at room and elevated tests temperatures. Here, the experimental average is given together with the deviation in terms of maximum and minimum stress of the test series. In fiber direction ($x-$direction), the material response is linear at room temperature and only slightly nonlinear for elevated temperatures due to the high material stiffness and the machine limit of 5 kN. A clear temperature dependence is visible in y-direction, where a higher temperature generally leads to a reduction in material stiffness. The temperature dependence in $x-$direction most likely results from the difference in 2D between 3D DIC measurements, as discussed in Sec. 3.3.4.1. Furthermore, the strain rate dependence is more pronounced at higher temperatures. Unfortunately, the tests in $x-$direction for the lowest strain rate at 150° C are not usable since the exposure to temperature during pre-heating, combined with the longer testing time, led to sliding of the specimens in the clamping area. After testing, shear marks were visible on the specimens in the clamping area (see Fig. 3.3), where the bracket was in contact with the fibers due to the increased viscosity of the PA6 matrix at 150° C. Consequently, the low friction resistance of the glass fibers compared to the polymer matrix caused sliding. A reinforcement with CFK at the clamping area did not improve the test results. Consequently, they were left out of the plot. Here, pneumatic grips might improve the test situation. For the tests with higher velocity, the problem was less pronounced due to the reduced contact time. Note here that sliding occurred only in fiber direction. Compared to the tests in fiber direction, in transverse direction, the temperature dependence of the material response is more pronounced in line with Gröger et al. [2021] who tested the same material system. Here, the matrix material, which shows a pronounced temperature sensitivity (cf. Shan et al. [2007]; Felder et al. [2020a]; Reuvers et al. [2024a]) in the considered temperature range, dominates the material response. Moreover, a more gradual roll-over to yielding is observed for temperatures

above the glass transition, where a highly nonlinear material response is visible. Overall, the strain rate dependence is more distinct in y-direction. Similarly to the results in x-direction, the sensitivity to the loading velocity increases with increasing temperature. Fiber sliding was observed in both directions, especially at room temperature, where the matrix material is less ductile. Here, the debonding or rupture of individual fibers led to kinks in the individual force displacement curves and, therefore, resulted in a higher deviation at elevated strains. In compression, the tests were conducted at two different strain rates with a decade difference. Therefore, here the dependence of the material response on the loading rate is more pronounced compared to the tensile tests.

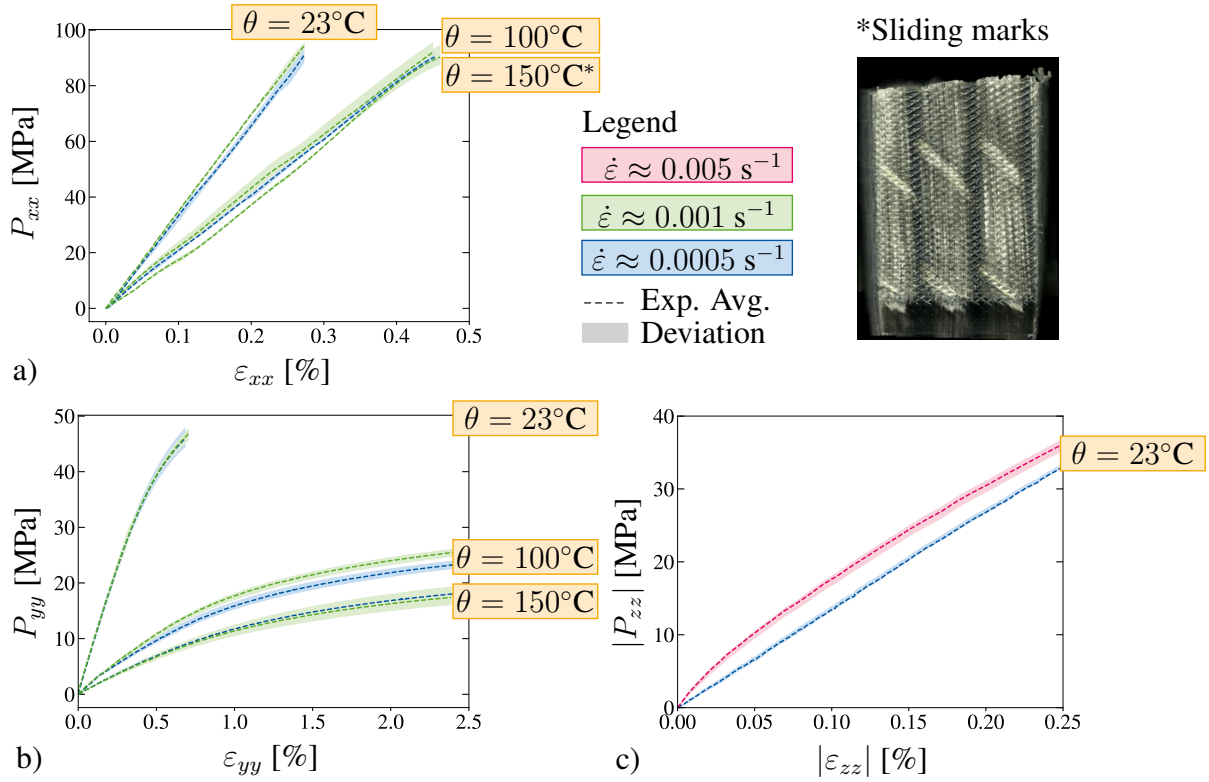

Figure 3.3: a) Montonic, uniaxial extension in fiber direction. *Results only available for $\dot{\varepsilon} \approx 0.001\ \mathrm{s}^{-1}$ due to sliding at the clamp. b) Montonic, uniaxial extension results in transverse direction. c) Monotonic, uniaxial compression in transverse direction for various strain rates.

In Fig. 3.4, the boundary conditions as well as the results for the stepwise cyclic tension tests are shown for an exemplary temperature of 150°C. During the experimental procedure, the specimens were subjected to displacement controlled loading followed by an unloading step until the force equaled zero. A subsequent recovery step to distinguish between time-dependent and time-independent remaining deformations was omitted here due to the extensive relaxation

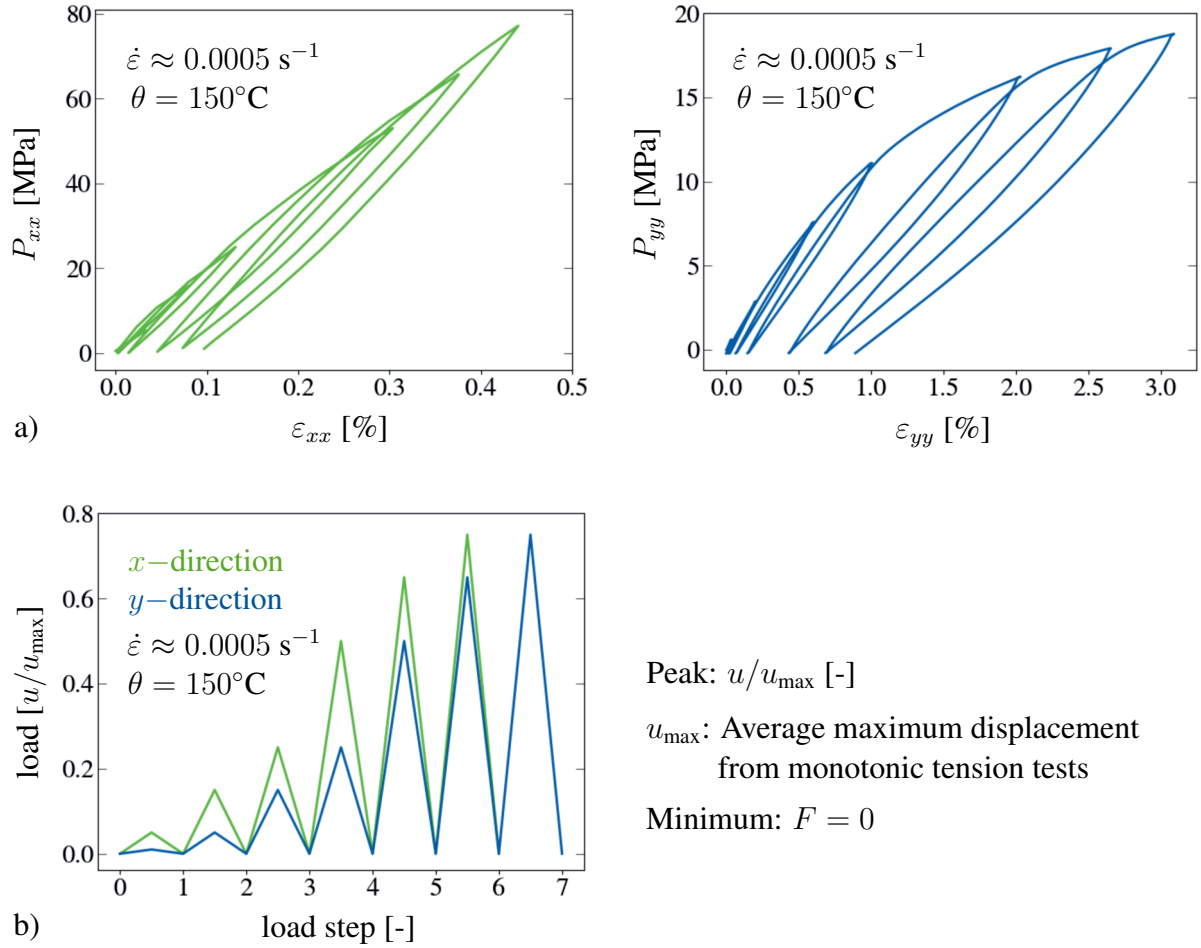

Figure 3.4: a) Cyclic tension results in fiber and transverse direction at 150°C. b) Boundary conditions for the cyclic tension tests.

times of the matrix material detected in Reuvers et al. [2024a]. The target displacements were determined based on the machine results from the monotonic tension tests to ensure comparability between the varying material directions. Moreover, high displacements were deliberately omitted to avoid slipping at the clamping areas, as observed in the monotonic tension tests (cf. Fig. 3.3). Due to the lower stiffness perpendicular to the fiber direction, an additional load step with $u_i/u_{\max,i} = 1\%$ was included to determine the elastic regime. The results of the cyclic tension tests at elevated temperature (see Fig. 3.4) show a distinct nonlinearity in the loading and unloading paths in both directions, however, more pronounced perpendicular to the fiber direction. In fiber direction, no remaining deformation is present for the first two load cycles. Thus, the authors conclude that plastic deformation occurs from the third load cycle onwards. The remaining deformation at the end of the loading-unloading procedure, however, measured only 0.1 %. Perpendicular to the fiber direction,

plastic deformations were already visible in the 5 % load step, corresponding to the lower material stiffness in y-direction. Here, the final strain after testing measured approximately 1 %. Interestingly enough, the hysteresis energy (area under the curve of each load step) seemed to increase with increasing deformation, especially for the results in y-direction. This observation suggests a deformation dependent visco-elastic material behavior as indicated by e.g. Reese and Govindjee [1998]; Lion [1999]; Holmes et al. [2006]; Amin et al. [2006] for the viscosity of polymeric materials and experimentally detected for PA6 by Felder et al. [2020a]; Reuvers et al. [2024a].

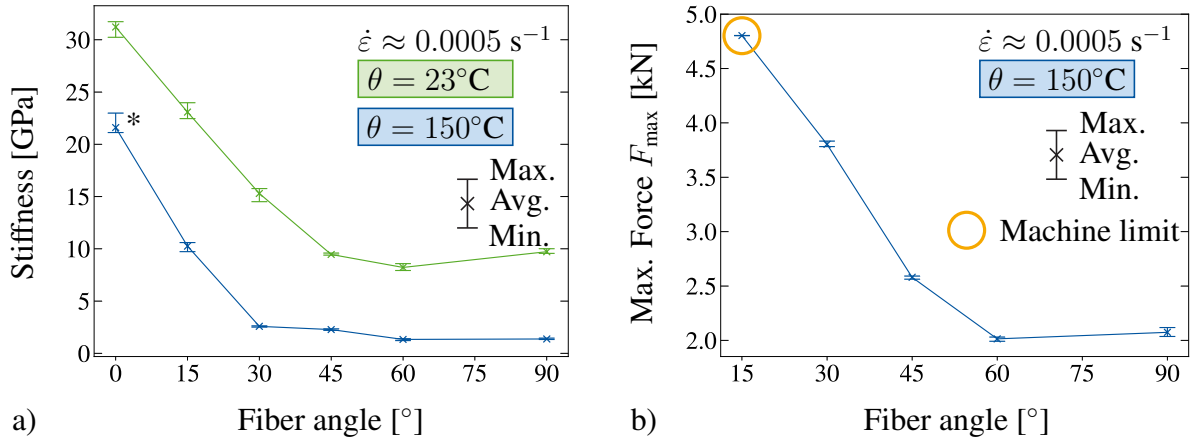

Figure 3.5: Experiments under varying fiber angle a) Material stiffness at various temperatures (* indicates sliding marks) b) Maximum force.

In Fig. 3.5, the results for the experiments under varying fiber angle are shown. Firstly, the average material stiffness in GPa for each fiber angle is calculated from the monotonic tension tests according to DIN EN ISO 527-5 and plotted over the fiber angle. A severe and nonlinear reduction in material resistance is visible between the stiffness in fiber direction (°) and perpendicular to it (90°). Initially the material stiffness reduces drastically between fiber angles of 0° and 30°. Afterwards, the changes are only marginal, suggesting that between 45° and 90° the matrix material dominates the material response. Interestingly enough, the influence of the fibers on the overall material response appears to be temperature dependent. With increasing temperature, the fiber influence vanishes already at 30° which could be related to a weakened fiber-matrix-interface due to the increased matrix ductility. This trend, however, is only visible in the material stiffness and does not translate to the maximum force of the material shown in Fig. 3.5 b). Here, the fiber influence is still clearly visible at 30°. Note here that the test in fiber direction (0°) is left out since the machine maximum (≈ 5 kN) is already reached for a fiber angle of 15°. In both comparisons, the results for 90° lie slightly above the

minima at 60° which can be attributed to testing on two material batches. During specimen production, the use of the diamond cutting blade, together with a water jet for cooling purposes, led to more offcuts. Consequently, a second order of material needed to be placed to substitute the loss. To ensure comparability, monotonic tension tests in x- and $y-$direction were repeated with the second batch and compared to the results for the first batch, see Fig. 3.6 b. In fiber direction, no difference apart from the expected material scatter is visible. On the contrary, perpendicular to the fiber direction the response of the second batch appears to be slightly softer. The authors believe that the changes in the two batches stem purely from the polyamide 6 matrix and are therefore only prominently visible when testing perpendicular to the fibers, since the fibers themself dominate in this case. Though the orders were placed at different times, with significant temporal distance inbetween, the authors suspect that inconsistency in the individual components (PA6 granulate, roving glass sheets) is most likely not the reason for the differences. During production, the polyamide 6 matrix undergoes a phase transition from melt to solid and, additionally, crystallizes over a period of time. Here, the cooling rate mainly determines the resulting amount of crystalline phase. In contrast, the fibers do not change their material characteristics during the consolidation process. Moreover, the tested plates are not mass produced but rather a custom-built research material due to the non-standard material thickness. This high plate thickness could lead to unwanted temperature gradients during cooling down from the melt, and therefore to an inhomogeneous crystallization distribution. For this reason, the authors believe that the crystal configuration most likely differs between the plates and that the variance in the two batches (and most likely the majority of the material scatter as well) stems from the polyamide 6 matrix. Nonetheless, the differences between both material batches are negligibly small, and can only be seen in Fig. 3.5 where results from both batches are combined. In all other figures, either results from batch one or batch two are used.

The results of the three-point bending tests are shown in Tab. 3.2. Here, the test data at room temperature was enriched with results conducted at the Polymer Service Merseburg GmbH (PSM) at room and elevated test temperatures in line with DIN EN ISO 14125. The Young's modulus in bending E_f in x- and y-direction was measured together with the flexural strength σ_{fM} and the corresponding strain ε_{fM}. Where available, the breaking stress σ_{fB} and strain ε_{fB} are provided as well. Each test was repeated at least five times, hence all values are given as the statistical mean and the standard deviation s is shown as well below the results.

The results from Tab. 3.2 support the findings from the tensile tests in Fig. 3.3 and 3.5, where the material stiffness is temperature dependent and an increase in temperature generally leads to a decrease in material stiffness, especially perpendicular to the fibers. This relation holds for the maximum stress and the failure stress as well. However, here the temperature

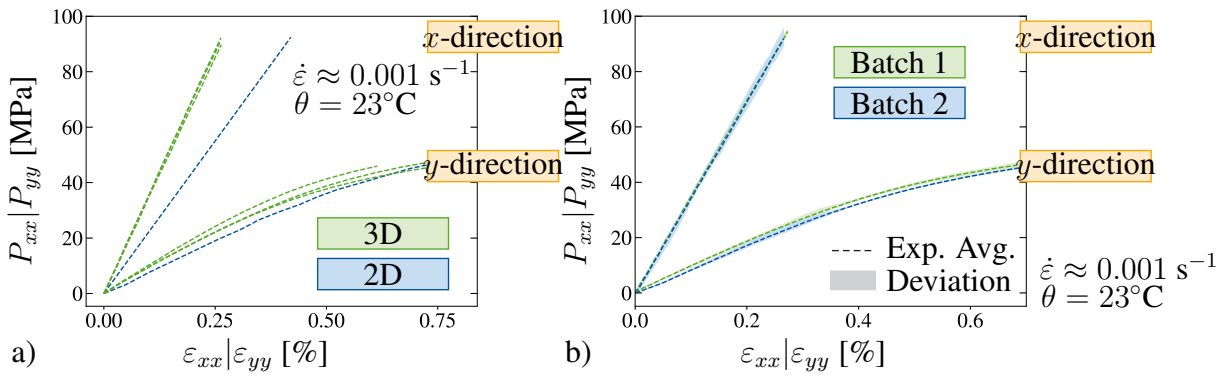

Figure 3.6: Additional tests: a) Comparison of 2D (inside the temperature furnace) and 3D (outside the temperature furnace) DIC measurements at room temperature. b) Comparison of different material batches in x- and y-direction.

dependence is pronounced in x-direction as well. Moreover, at room temperature the failure behavior is brittle corresponding to $\sigma_{fM} = \sigma_{fB}$, whereas for elevated temperature a more ductile failure is observed. In x- direction, the material failed due to a combination of tension and compression, whereas in y-direction a tension failure was observed independent of the temperature.

3.3.5 Thermal analysis

The thermal analysis of the material was conducted at the Institute of Mechanics, University of the German Federal Armed Forces, Munich and Polymer Service GmbH Merseburg (PSM).

To obtain insights into the expansion of the material under temperature, a thermomechanical analysis was conducted on a TMA/SDTA841e from *Mettler Toledo* (Mettler Toledo, Columbus, USA) in all three material directions. In Fig. 3.7 a, the resulting coefficients of thermal expansion (CTEs) α_T are plotted over the temperature. Here, the thermal expansion in fiber direction (x-direction) is least pronounced and reflects the lower thermal expansion of glass fibers according to the manufacturer ($\alpha = 4.9 - 5.1\,10^{-6}/K$) and in line with experiments from Segal [1979]. Additionally, no distinct temperature influence is observed in this direction. On the other hand, the in-plane thermal expansion coefficients react sensitively to temperature, especially above the glass transition. However, interestingly enough, the thermal expansion in y- and z-direction does not coincide. Considering the microscopic images in Fig. 3.2, the authors believe that this observation is related to the production process (cf. Sec. 3.3.3), where the consolidation of prepregs results in a layer structure in z-direction. Consequently, in this direction, the polymeric matrix behavior is most pronounced, leading to an increased thermal

	Temperature [°C]	Direction	E_f [MPa]	σ_{fM} [MPa]	ε_{fM} [%]	σ_{fB} [MPa]	ε_{fB} [%]
	23	x	30531	850	2.78	850	2.78
s			650	28.3	0.11	28.8	0.092
	23	y	7327	96.3	1.97	96.3	1.97
s			303	3.22	0.146	3.22	0.146
	100	x	27388	353	1.40	285	2.53
s			916	17.5	0.04	32.5	0.0923
	100	y	2445	57.2	4.07	52.8	4.24
s			82	1.34	0.17	2.52	0.21
	150	x	25415	269	1.47	242	2.85
s			609	4.91	0.78	13.7	0.11
	150	y	1738	43.0	3.85	37.8	4.03
s			64	2.81	0.41	4.36	0.38

Table 3.2: Three-point bending results in x- and y-direction at room and elevated temperatures.

expansion together with a strong temperature dependence above the glass transition, in line with the results for pure PA6 in Reuvers et al. [2024a]. In y-direction, the CTE lies in-between the results for the other two directions.

The thermal conductivity was measured on a *Hot-Disk* TPS 2500S (Hot Disk, Gothenburg, Sweden). For testing, the 1D *Hot-Disk* method was employed, utilizing a sensor with a diameter of 12.8 mm. This was deemed an appropriate choice given that larger sensors generally yield more accurate results. The method requires a cylindrical specimen with a diameter that is 2 mm greater than that of the sensor. Consequently, only the thickness direction (z-direction) was tested using the measured composite density of $\rho = 1.8$ g/cm^3 since the maximum thickness of the composite plate measured 10 mm in total. It it important to note that smaller sensors were available for testing, however, they did not produce reliable results for the polymeric material, which is generally low in conductivity. In Fig. 3.7 b, the resulting thermal conductivity is plotted over the temperature. The composites' thermal conductivity is higher compared to that of pure PA6 which can be attributed to the influence of the glass fibers ($\lambda_{\textit{glass fiber}} \approx 1.28$ W/mK). Similar to the results in Reuvers et al. [2024a] for PA6, the influence of temperature on the resulting thermal conductivity is negligible, see also Kugele [2020]. Therefore, from this point onwards, a transverse thermal conductivity of $\lambda_{T,\perp} = \lambda_{T,y} = \lambda_{T,z} = 0.6365$ W/mK is used in all calculations. Additionally, the authors expect to see no significant difference between the results in fiber and transverse direction in line with results from Kalaprasad et al. [2000] since the heat conductivity of the glass fibers is isotropic. To verify the assumption, virtual thermal experiments on the unit cell will be conducted in Sec. 3.6.2 in all material

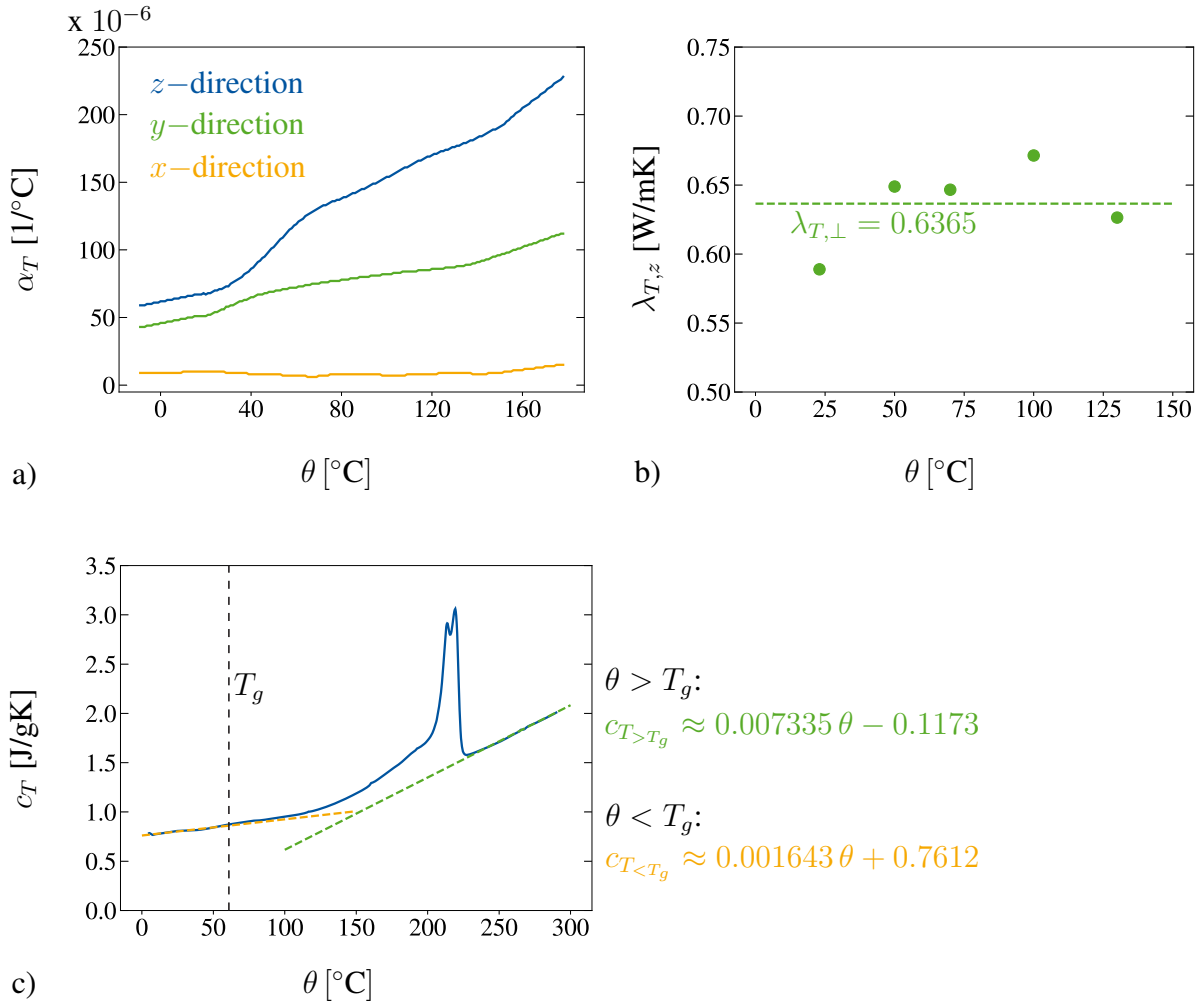

Figure 3.7: Thermal analysis a) Direction dependent coefficient of thermal expansion (TMA measurement) b) Thermal conductivity measurement in z-direction c) Specific heat capacity from DSC measurements in the second heating run.

directions. Furthermore, the specific heat capacity is derived from the second heating run of the composite DSC experiments in Sec. 3.3.1. Here, the tangent to the experimental curve yields the specific heat capacity above and below the glass transition T_g, which increases with increasing temperature (see Fig. 3.7 c). Note here that the steep incline of the heat capacity after the melting of the crystalline phase is unexpected. Generally, the slope of c_T should be approximately equal below and above the glass transition. Thus, the authors suspect that structural changes might be the reason for this uncertainty.

3.4 Polymeric matrix material model formulation

The following section provides a brief overview of the material model utilized for the polyamide 6 matrix. For a more detailed description, the reader is kindly referred to Reuvers et al. [2024a], where the full derivation of the framework is presented together with the numerical implementation as a user material subroutine UMAT and UMATHT for the commercial finite element method (FEM) software Abaqus/Standard (Dassault Système, Vélizy-Villacoublay, France). Throughout the text, the subsequent notational conventions are employed:

a, A	Scalar quantity
$\boldsymbol{a}$	First order tensor
$\boldsymbol{A}$	Second order tensor
$\boldsymbol{I}$	Identity tensor
$\mathbb{A}$	Fourth order tensor
$\dot{(*)}$	Total derivative with respect to time
$(\boldsymbol{A})^T$	Transpose of $\boldsymbol{A}$
$(\boldsymbol{A})^{-1}$	Inverse of $\boldsymbol{A}$
$\mathrm{tr}(\boldsymbol{A})$	Trace of $\boldsymbol{A}$
$\det(\boldsymbol{A})$	Determinant of $\boldsymbol{A}$
$\mathrm{dev}(\boldsymbol{A})$	$\boldsymbol{A} - \frac{1}{3}\,\mathrm{tr}(\boldsymbol{A})\boldsymbol{I}$
$\mathrm{Grad}(\boldsymbol{A})$	Gradient of $\boldsymbol{A}$ with respect to the reference configuration
$\mathrm{Div}(\boldsymbol{A})$	Divergence of $\boldsymbol{A}$ with respect to the reference configuration
:	Double contraction
$\bar{(*)}$	Quantity in the reference configuration

To accurately capture the material behavior of semi-crystalline polymers (SCPs), a coupled visco-elastic, elasto-plastic framework is chosen, according to Reuvers et al. [2024a]. A schematic overview in the form of a 1D rheological representation of the model assumptions is provided in Fig. 3.8. Here, a multiplicative split of the deformation gradient $\boldsymbol{F}$

$$\boldsymbol{F} = \boldsymbol{F}_{e1}\,\boldsymbol{F}_p = \boldsymbol{F}_{e2}\,\boldsymbol{F}_v, \tag{3.2}$$

into elastic ($\boldsymbol{F}_{e1}$) and plastic ($\boldsymbol{F}_p$) (see e.g.Eckart [1948]; Kröner [1959]; Lee [1969]) as well as an elastic ($\boldsymbol{F}_{e2}$) and viscous ($\boldsymbol{F}_v$) part (see e.g. Sidoroff [1974]; Lubliner [1985]; Lion [1997a]; Reese and Govindjee [1998]) is introduced. Further, an additional split of the plastic part of the deformation gradient $\boldsymbol{F}_p = \boldsymbol{F}_{pe}\,\boldsymbol{F}_{pi}$ (cf. Lion [2000]; Dettmer and Reese [2004]) is performed to model nonlinear kinematic hardening.

The Helmholtz free energy per unit mass is expressed in terms of symmetric elastic deformation measures only, namely the elastic right Cauchy-Green tensors $\boldsymbol{C}_{e1}$, $\boldsymbol{C}_{pe}$ and $\boldsymbol{C}_{e2}$

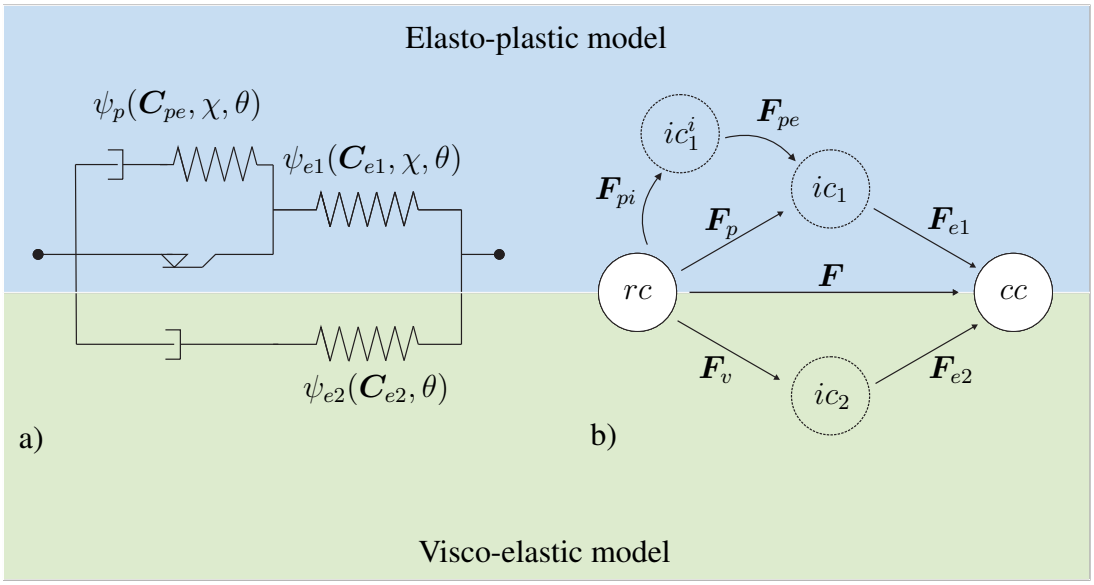

Figure 3.8: a) Schematic illustration of the constitutive model b) Multiplicative splits of the deformation gradient (reference (rc) and current (cc) configurations, local intermediate configurations ic_1, ic_1^i and ic_2 for plasticity, kinematic hardening and viscosity).

defined as

$$\boldsymbol{C}_{e1} = \boldsymbol{F}_{e1}^T \boldsymbol{F}_{e1}, \quad \boldsymbol{C}_{pe} = \boldsymbol{F}_{pe}^T \boldsymbol{F}_{pe}, \quad \boldsymbol{C}_{e2} = \boldsymbol{F}_{e2}^T \boldsymbol{F}_{e2}. \tag{3.3}$$

Here, $\boldsymbol{C} = \boldsymbol{F}^T \boldsymbol{F}$ denotes the right Cauchy-Green tensor and $\boldsymbol{C}_p = \boldsymbol{F}_p^T \boldsymbol{F}_p$ the plastic right Cauchy-Green tensor. Following the assumptions made in Fig. 3.8, the total specific Helmholtz free energy

$$\psi(\boldsymbol{C}_{e1}, \boldsymbol{C}_{e2}, \boldsymbol{C}_{pe}, \chi, \theta) = \psi_1(\boldsymbol{C}_{e1}, \boldsymbol{C}_{pe}, \chi, \theta) + \psi_2(\boldsymbol{C}_{e2}, \theta) + \psi_c(\theta) \tag{3.4}$$

is additively decomposed into elasto-plastic (ψ_1) and visco-elastic (ψ_2) energetic contributions accompanied by an unspecified caloric part ψ_c to ensure flexibility regarding the choice of the function for the heat capacity c_T (cf. Felder et al. [2022]; Reuvers et al. [2024a]). Here, the first term ψ_1 contains an elastic part ψ_{e1} as well as a defect energy ψ_p related to kinematic hardening

$$\psi_1(\boldsymbol{C}_{e1}, \boldsymbol{C}_{pe}, \chi, \theta) = \psi_{e1}(\boldsymbol{C}_{e1}, \chi, \theta) + \psi_p(\boldsymbol{C}_{pe}, \chi, \theta), \tag{3.5}$$

both dependent on the crystallization state of the material via the degree of crystallinity χ. The energy contributions related to the elasto-plastic model part ψ_1 are chosen as a compressible

Neo-Hookean-type energy ψ_{e1} in combination with a nonlinear plastic defect energy ψ_p to account for Armstrong-Frederick kinematic hardening

$$\psi_{e1} = \frac{\mu_1}{2}\left(\text{tr}(\boldsymbol{C}_{e1}) - 3\right) - \mu_1 \ln\left(J_{e1}\right) + \frac{\Lambda_1}{4}\left(\det(\boldsymbol{C}_{e1}) - 1 - 2\ln(J_{e1})\right) - 3\,K_1\alpha_T\,\Delta\theta\ln(J_{e1}), \tag{3.6}$$

$$\psi_p = \frac{c}{2}\left(\text{tr}(\boldsymbol{C}_{pe}) - 3\right) - c\ln(\sqrt{J_{pe}}). \tag{3.7}$$

Here, $J_{e1} = \det(\boldsymbol{F}_{e1})$ is the determinant of the elastic part of the deformation gradient $\boldsymbol{F}_{e1}$ and $J_{pe} = \det(\boldsymbol{C}_{pe})$ holds. In terms of the material quantities, the two Lamé constants $\mu_1(\chi,\theta)$ and $\Lambda_1(\chi,\theta)$ are introduced in ψ_{e1} and $c(\chi,\theta)$ in the defect energy ψ_p. The expression for the elastic energy ψ_{e1} in Eq. 3.6 is extended with a term related to volumetric thermal expansion incorporating the elasto-plastic bulk modulus[2] $K_1(\theta)$, the coefficient of thermal expansion $\alpha_T(\theta)$ and the temperature difference $\Delta\theta = \theta - \theta_0$ between the current temperature θ and the reference temperature θ_0. All material properties of the elasto-plastic part depend on both the DOC and temperature. Similarly to Eq. 3.6, the visco-elastic part of the Helmholtz free energy ψ_{e2} is defined as

$$\psi_2 = \frac{\mu_2}{2}\left(\text{tr}(\boldsymbol{C}_{e2}) - 3\right) - \mu_2\ln(J_{e2}) + \frac{\Lambda_2}{4}\left(\det(\boldsymbol{C}_{e2}) - 1 - 2\ln(J_{e2})\right) - 3\,K_2\alpha_T(\theta-\theta_0)\ln(J_{e2}), \tag{3.8}$$

where $\mu_2(\theta)$ and $\Lambda_2(\theta)$ are the visco-elastic Lamé constants and K_2 is the visco-elastic bulk modulus[2]. Furthermore, $J_{e2} = \det(\boldsymbol{F}_2)$ holds. As indicated in Eq. 3.4, all energetic contributions jointly depend on the temperature θ.

Next, the constitutive equations are derived from the local form of the Clausius-Duhem inequality

$$\boldsymbol{S} : \frac{1}{2}\dot{\boldsymbol{C}} - \rho_0(\dot{\psi} + \eta\,\dot{\theta}) - \frac{1}{\theta}\,\boldsymbol{q}_0 \cdot \text{Grad}(\theta) \geq 0. \tag{3.9}$$

Here, $\boldsymbol{S}$ is the second Piola-Kirchhoff stress tensor and ρ_0 represents the material density per unit reference volume. The entropy is introduced via the parameter η and the heat flux in the reference configuration is denoted by $\boldsymbol{q}_0$ with the temperature dependent heat conductivity $\lambda_T(\theta)$. Following several mathematical operations (cf. Reuvers et al. [2024a]) the stress quantities are introduced as:

[2]The bulk moduli $K_*, * = 1, 2$ are defined by the two Lamé constants μ_* and Λ_* as $K_* = \Lambda_* + \frac{2\mu_*}{3}$.

Second Piola-Kirchhoff stresses:

$$\boldsymbol{S}_1 = 2\rho_0 \boldsymbol{F}_p^{-1} \frac{\partial \psi_{e1}}{\partial \boldsymbol{C}_{e1}} \boldsymbol{F}_p^{-T}, \qquad \boldsymbol{S}_2 = 2\rho_0 \boldsymbol{F}_v^{-1} \frac{\partial \psi_2}{\partial \boldsymbol{C}_{e2}} \boldsymbol{F}_v^{-T}$$

Mandel stresses:

$$\boldsymbol{M}_1 = 2\rho_0 \boldsymbol{C}_{e1} \frac{\partial \psi_{e1}}{\partial \boldsymbol{C}_{e1}}, \qquad \boldsymbol{M}_2 = 2\rho_0 \boldsymbol{C}_{e2} \frac{\partial \psi_2}{\partial \boldsymbol{C}_{e2}}.$$

Back stress:

$$\boldsymbol{X} = 2\rho_0 \, \boldsymbol{F}_{pe} \frac{\partial \psi_p}{\partial \boldsymbol{C}_{pe}} \boldsymbol{F}_{pe}^T$$

Mandel stress related to kinematic hardening:

$$\boldsymbol{M}_{1,\text{kin}} = 2\rho_0 \, \boldsymbol{C}_{pe} \frac{\partial \psi_p}{\partial \boldsymbol{C}_{pe}}$$

In terms of the evolution equations (see Tab. 3.3) a Tschoegl-type or paraboloid yield criterion (see e.g. Tschoegl [1971]; Ghorbel [2008]; Melro et al. [2013*b*]) is adopted for the elasto-plastic part introducing the initial yield stress in compression σ_c^0 and tension σ_t^0. For the evolution of plasticity an associative flow rule is chosen together with the classical evolution equation for nonlinear Armstrong-Frederick kinematic hardening (Armstrong et al. [1966]). Here, the plastic multiplier $\dot{\lambda}_p$ is introduced, as well as the hardening material parameters b and c. The evolution equation for the visco-elastic part is based on a potential from Reese and Govindjee [1998]. For the specific choice of the nonlinear function for the relaxation time τ, the reader is kindly referred to Sec. 3.6. In addition, the local form of the energy balance

$$\rho_0 \left(\dot{\psi} + \dot{\eta}\,\theta + \eta\,\dot{\theta}\right) + \text{Div}(\boldsymbol{q}_0) - \boldsymbol{S} : \frac{1}{2}\dot{\boldsymbol{C}} = 0 \tag{3.10}$$

is evaluated, to determine the internal heat sources. Above, the time derivative of the internal energy $\dot{e} = \dot{\psi} + \dot{\eta}\,\theta + \eta\,\dot{\theta}$ is already incorporated. In line with e.g. Felder et al. [2020b, 2022]; Reuvers et al. [2024a], the heat capacity is approximated by a constant value $c_T = -\theta\,(\partial^2\psi)/(\partial\theta^2) = c_T(\chi, \theta)$ in this work and determined experimentally. The specific expression for c_T above and below the glass transition regime can be found in Tab. 3.8. An overview of the equations in their final form in the reference configuration is provided in Tab. 3.3.

3.5 Generation of repeating unit cells and comparison of different randomization methods

In this section, the generation of repeating unit cells (RUCs) is described in detail. Various randomization methods for the distribution of unidirectional glass fibers are tested and compared

Table 3.3: Overview over the constitutive equations in the reference configuration.

Elasto-plastic contribution	Visco-elastic contribution
Stresses $\boldsymbol{S}_1 = \mu_1(\boldsymbol{C}_p^{-1} - \boldsymbol{C}^{-1}) + \frac{\Lambda_1}{2}\left(\frac{\det(\boldsymbol{C})}{\det(\boldsymbol{C}_p)} - 1\right)\boldsymbol{C}^{-1} - 3K_1\alpha_T(\theta-\theta_0)\boldsymbol{C}^{-1}$ $\bar{\boldsymbol{X}} = c\,(\boldsymbol{C}_{pi}^{-1} - \boldsymbol{C}_p^{-1})$ $\boldsymbol{Y} = \boldsymbol{C}\boldsymbol{S}_1 - \boldsymbol{C}_p\bar{\boldsymbol{X}}, \quad \boldsymbol{Y}_{\text{kin}} = \boldsymbol{C}_p\bar{\boldsymbol{X}}$ Yield function $\Phi_p = 3\,J_2 + (m-1)\,\sigma_t^0\,I_1 - m\,(\sigma_t^0)^2$ $I_1 = \text{tr}(\boldsymbol{Y}), \quad J_2 = \frac{1}{2}\,\text{tr}((\text{dev}(\boldsymbol{Y}))^2), \quad m = \sigma_c^0(\chi,\theta)/\sigma_t^0(\chi,\theta)$ Evolution equations $\dot{\boldsymbol{C}}_p = \dot{\lambda}_p\,(6\,\text{dev}(\boldsymbol{Y}) + 2\,(m-1)\,\sigma_t^0)\,\boldsymbol{C}_p, \quad \dot{\boldsymbol{C}}_{pi} = 2\,\dot{\lambda}_p\,\frac{b}{c}\,\text{dev}(\boldsymbol{Y}_{\text{kin}})\,\boldsymbol{C}_{pi}$ $\dot{\lambda}_p \geq 0, \quad \Phi_p \leq 0, \quad \dot{\lambda}_p\,\Phi_p = 0$ Heat generation due to plastic dissipation $r_1 = \bar{r}_p = \frac{1}{2}\,\boldsymbol{C}\left(\boldsymbol{S}_1 - \theta\,\frac{\partial \boldsymbol{S}_1}{\partial\theta}\right) : \boldsymbol{C}_p^{-1}\,\dot{\boldsymbol{C}}_p - \frac{1}{2}\left(\bar{\boldsymbol{X}} - \theta\,\frac{\partial\bar{\boldsymbol{X}}}{\partial\theta}\right) : \dot{\boldsymbol{C}}_p$ $+\frac{1}{2}\,\boldsymbol{C}_p\left(\bar{\boldsymbol{X}} - \theta\,\frac{\partial\bar{\boldsymbol{X}}}{\partial\theta}\right) : \boldsymbol{C}_{pi}^{-1}\,\dot{\boldsymbol{C}}_{pi}$	Stress $\boldsymbol{S}_2 = \mu_2(\boldsymbol{C}_v^{-1} - \boldsymbol{C}^{-1}) + \frac{\Lambda_2}{2}\left(\frac{\det(\boldsymbol{C})}{\det(\boldsymbol{C}_v)} - 1\right)\boldsymbol{C}^{-1}$ $-3\,K_2\,\alpha_T\,(\theta-\theta_0)\boldsymbol{C}^{-1}$ Evolution equation $\dot{\boldsymbol{C}}_v = \left(\frac{1}{\tau\mu_2}\,\text{dev}(\boldsymbol{C}\boldsymbol{S}_2) + \frac{2}{9\tau K_2}\,\text{tr}(\boldsymbol{C}\boldsymbol{S}_2)\,\boldsymbol{I}\right)\boldsymbol{C}_v$ Heat generation due to viscous dissipation $r_2 = \bar{r}_v = \frac{1}{2}\,\boldsymbol{C}\left(\boldsymbol{S}_2 - \theta\,\frac{\partial \boldsymbol{S}_2}{\partial\theta}\right) : \boldsymbol{C}_v^{-1}\,\dot{\boldsymbol{C}}_v$
Second Piola-Kirchhoff stress $\boldsymbol{S} = \boldsymbol{S}_1 + \boldsymbol{S}_2$ Heat flux $\boldsymbol{q}_0 = -J\,\lambda_T\,\boldsymbol{C}^{-1}\,\text{Grad}(\theta)$	Elastic heat generation $r_e = \theta\left(\frac{\partial \boldsymbol{S}_1}{\partial\theta} : \frac{1}{2}\,\dot{\boldsymbol{C}} + \frac{\partial \boldsymbol{S}_2}{\partial\theta} : \frac{1}{2}\,\dot{\boldsymbol{C}}\right)$ Entropy $\eta = -\partial\psi/\partial\theta$

to microscopic pictures of the PA6 composite material used for the experiments in Sec. 3.3. Furthermore, mesh and size convergence studies are conducted to identify a valid RUC that will be used for comparison with the experimental results. Throughout the generation of the RUCs, the focus lied on the process automation to minimize the effort for e.g. the convergence studies. Therefore, the Abaqus - Python interface was used to generate a plug-in application that allows for automatic RUC generation and testing with mechanical and thermal periodic boundary conditions (PBCs).

3.5.1 Unit cell generation

The automatic generation of repeating unit cells is separated into three main steps. Firstly, the random distribution of the UD fibers is carried out using three different randomization methods. Next, the geometry of the unit cell is generated, followed by the automatic generation of the mesh and the corresponding periodic boundary conditions (PBCs). The input parameters for the Abaqus-Python plug-in are the constant fiber volume fraction $\varphi_f = 40$ % and the diameter of the roving glass fibers (17 μm) as well as the number of fibers n_f that determine the size of the RUC. The fibers are modeled as cylinders under the assumption of a perfectly round cross-section, and no inhomogeneities along the fiber direction. Note here that the fibers in weft direction needed for structural support during production (approximately 3 % of the total fiber volume content) are neglected. Moreover, the height and width of the RUCs are chosen to be equal, in that way, the dimensions of the RUC are a priori known when evaluating the input quantities given above. Three different randomization schemes are used to generate the random fiber distribution, namely the so-called randomized method (see e.g. Poggenpohl et al. [2022*b*]), the random sequential adsorption (RSA) method (see e.g. Hinrichsen et al. [1986]) and a variation of the RSA method based on microscopic images, which is referred to as clustered RSA (CRSA) in the following.

The randomized method is based on a repetition of a regular grid of initally two fibers that resemble square closest packing in 2D (see Fig.3.9 a)). Each fiber is shifted by a random value with respect to its original position. Hereby, the shift is restricted such that overlapping of the individual fibers is prevented (see Fig. 3.9 a)). The number of fibers for this randomization method is limited to certain even numbers ($n_{f,\text{randomized}} = 2n^2, n \in \mathbb{N}$), based on the base cell for square closest packing and the restriction to quadratic RUC dimensions.

RUCs resulting from the random sequential adsorption method consist of sequentially generated random fiber coordinates within the limits of the RUC size. Each fiber is placed in the RUC and only those fibers are adsorbed that do not overlap with already existing ones (see Fig. 3.10 a)). Otherwise, the coordinates are discarded, and new ones are generated

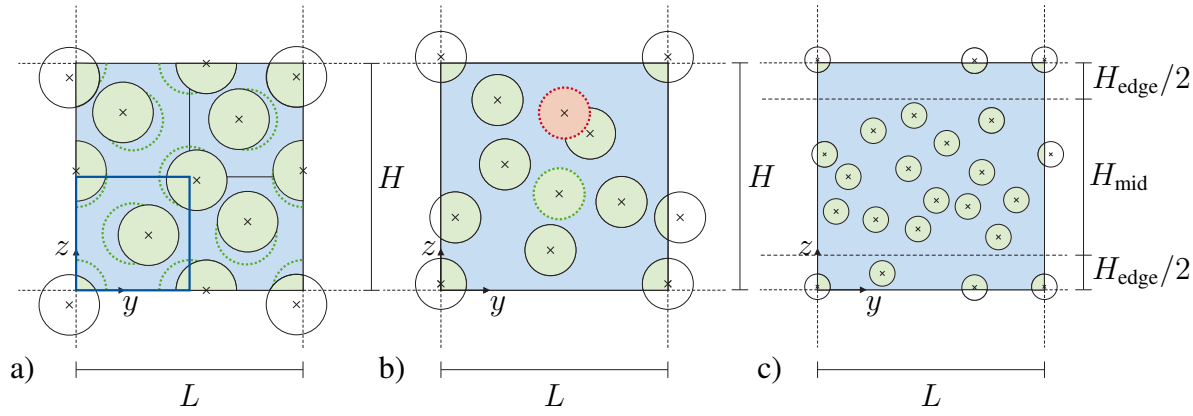

Figure 3.9: Random fiber distribution generated with a) randomized method (blue box marks base cell of two fibers) b) random sequential adsorption (RSA) method c) clustered RSA (CRSA) method.

until the desired fiber volume fraction is reached (see Fig. 3.9 b)). In addition, narrow gaps between the fibers and small or rather sharp matrix regions in the corners or the edges (see Fig. 3.10 b)) that lead to insufficient mesh quality or problems during mesh creation are prevented as well. This step is especially important since the mesh is generated automatically with a predefined element size. Therefore, mesh refinement in those areas is a priori not possible and would require manual intervention. In comparison, the RSA method shows a higher degree of clustering, whereas the fiber distribution in the RUCs generated with the randomized method is more even. These differences are reflected in the resulting RUC behavior and, therefore, as well in the resulting effective material properties of the composite, as will be shown in Sec. 3.5.3. Generally, both methods are suited to describe a random fiber distribution and the choice should be made on the basis of microscopic pictures. If, for instance, the fiber content is relatively high, however, the randomized method is the preferred choice since a valid fiber distribution with the RSA method is unlikely or requires various attempts that result in increased computation time. A saturation in the RSA approach with circular disks is reached with a maximum fiber volume fraction of approximately 54.7 % according to the literature (cf. Feder [1980]; Hinrichsen et al. [1986]). Comparing the microscopic images in Fig. 3.2 with images of RUCs with both randomization methods, the authors conclude that the RSA method better approximates the visible clustering of fibers. Nonetheless, areas can be indicated where no fibers are prominent, similar to a laminate structure. This effect stems from the production process, as discussed in Sec. 3.3.3. However, the laminate like structure is not incorporated in the RUCs yet. Thus, a third set of RUCs is generated for comparison using a variation of the RSA method, here referenced as clustered RSA (CRSA). To achieve a higher degree of

fiber clustering, the assumption is made that the majority of the fibers lie in the middle of the RUC, while the upper and lower edge consists mainly of matrix material, see Fig. 3.9 c) for a visual reference. To achieve a random fiber distribution in each part, the RSA method is used. The resulting new parameters, namely the height of the middle area $H_{\text{mid}} = H - H_{\text{edge}}$ and the fiber volume content in this part $\varphi_{\text{mid}} = \varphi_{\text{fibers}} - \varphi_{\text{edge}}$ of the RUC need to be determined. Here, values between 0.5 and 0.9 for the ratio of H_{mid}/H and values between 0.75 and 0.95 for the ratio of the fiber volume fraction $\varphi_{\text{mid}}/\varphi_{\text{fibers}}$ are realized in a preliminary parametric study and further tested and visually compared to the microscopic pictures. In addition, it is made sure that the resulting RUC behavior differed from that of the RUCs generated with the RSA method, resulting in $H_{\text{mid}}/H = 0.6$ and $\varphi_{\text{mid}}/\varphi_{\text{fibers}} = 0.9$. It should be noted that the clustered RSA method results in varying material behavior in y- and z-direction (see Sec. 3.5.3), thus thwarting the assumption of transversal isotropy. Consequently, experiments in all three directions are necessary to validate this method.

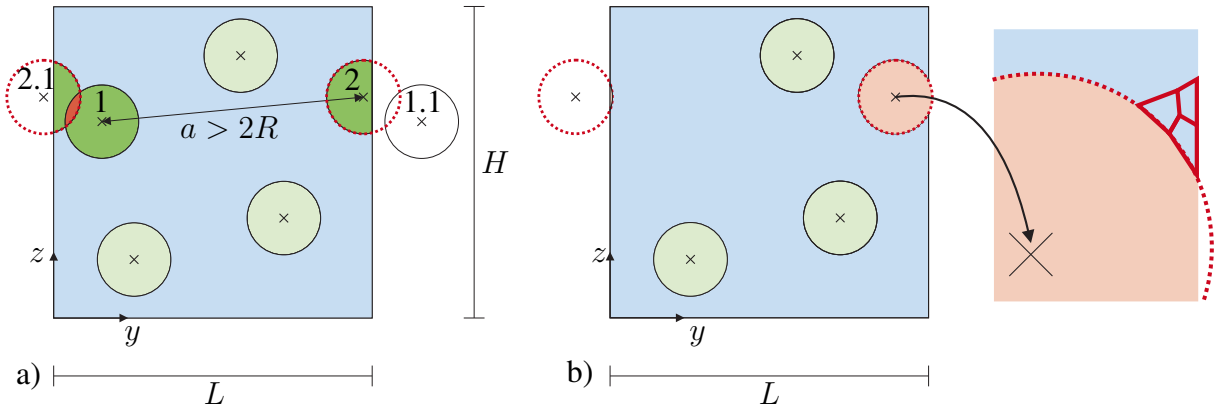

Figure 3.10: a) Rejection of overlapping fibers after projection b) Abortion of fiber coordinates that lead to narrow gaps and sharp corners to circumvent poor mesh quality.

After the fiber distributions are found and the geometries are generated using a sequence of boolean cuts, the mesh is generated automatically using eight node hexahedral elements with reduced integration (C3D8RT) from the Abaqus element library. Their performance has been compared to fully integrated elements for several uniaxial strain states combined with the RSA method. Here, the computation time of the reduced elements was significantly lower compared to the fully integrated elements, especially, due to the large history array of the complex nonlinear matrix material model. In the next step, periodic boundary conditions are created from the node set, applying Abaqus specific so-called equation constraints at the edges, faces and vertices of the RUC that mirror the local fluctuations of the current configuration at the respective boundaries. More specifically, PBCs prescribe a constant difference in displacement

and / or temperature between nodes that share the same reference coordinates in all but one direction (see e.g. Miehe [2002]; Kanit et al. [2003]; Nguyen et al. [2011]). Hereby, the difference in displacement and / or temperature can either be zero or non-zero depending on the applied far field strain or temperature state. During the generation of the PBCs it is made sure that no node is over-constraint by excluding the respective nodes from the node sets of the edges, faces and vertices. For a detailed description on how to apply Abaqus specific displacement equation constraints, the reader is kindly referred to Omairey et al. [2019]. An example for temperature equation constraints can be found in Tian et al. [2019].

The material model formulation used for the polyamide 6 matrix material can be found in Sec. 3.4 with the experimentally identified mechanical parameters in Appendix 3.8.1. For the fibers, an isotropic linear thermo-elastic material model from the Abaqus material library was chosen for simplicity, since the glass fibers behave purely elastically over the considered temperature range ($\theta = 23 - 150^\circ$ C). The corresponding material parameters can be found in Sec. 3.6.

3.5.2 Homogenization scheme

Based on the hypothesis of equal virtual work density on the microscopic ($*_m$) and macroscopic ($*_M$) level, the Hill-Mandel condition (see Hill [1963, 1967]) with the thermal extension by Özdemir et al. [2007] states the equivalence of the product of the volume averages and the volume average of the products for a representative volume on the micro level

$$\delta W_M = \{\delta W_m\}_{\Omega_0} \tag{3.11}$$

$$\Leftrightarrow$$

$$\{\boldsymbol{P}_m\}_{\Omega_0} : \{\delta \boldsymbol{F}_m\}_{\Omega_0} - \{\boldsymbol{q}_{0,m}\}_{\Omega_0} \cdot \{\mathrm{Grad}_m(\theta_m)\}_{\Omega_0} = \{\boldsymbol{P}_m : \delta \boldsymbol{F}_m\}_{\Omega_0} - \{\boldsymbol{q}_{0,m} \cdot \mathrm{Grad}_m(\theta_m)\}_{\Omega_0}, \tag{3.12}$$

with the microscopic first Piola-Kirchhoff stress tensor $\boldsymbol{P}_m$ and the conjugated deformation gradient $\boldsymbol{F}_m$ as well as the microscopic heat flux $\boldsymbol{q}_{0,m}$ with respect to the reference configuration and the temperature gradient $\mathrm{Grad}_m(\theta_m)$. In line with Özdemir et al. [2007], the time variation of the heat storage on the microscale is neglected due to the negligibly small representative volume. Here, $\{*\}_{\Omega_0}$ denotes the volume average

$$\{*\}_{\Omega_0} = \frac{1}{V_{\Omega_0}} \int_{\Omega_0} (*) \mathrm{dV}, \tag{3.13}$$

with V_{Ω_0} as the volume of Ω_0. The displacement as well as the temperature PBCs described in Sec. 3.5.1 are known to satisfy the Hill-Mandel condition (cf. Van der Sluis et al. [2000]; Özdemir et al. [2007]). Consequently, the stress of a macroscale material point $\boldsymbol{P}_M$ complies with the averaged stress of a volume element on the microscale and the same relation holds for the heat flux

$$\boldsymbol{P}_M = \{\boldsymbol{P}_m\}_{\Omega_0} \tag{3.14}$$

$$\boldsymbol{q}_{0,M} = \{\boldsymbol{q}_{0,m}\}_{\Omega_0}. \tag{3.15}$$

Using Abaqus specific equation constraints, $\boldsymbol{P}_M$ is obtained from the reaction force of the corresponding reference point divided by the reference area (see e.g. Omairey et al. [2019]). To obtain the elastic effective material parameters in the three material directions, six uniaxial strain states are applied successively on the RUCs under isothermal conditions at each test temperature. The corresponding tensile or shear loading conditions are shown schematically in Fig. 3.11 together with the associated material parameters. The macroscopic heat flux $\boldsymbol{q}_{0,M}$ equally follows from the averaged heat flux over the RUC domain, assuming stationary heat conduction. In order to obtain the direction dependent effective thermal conductivity a temperature gradient is applied successively on two opposing sides in each material direction (cf. Tian et al. [2019]). Since the effect of the temperature on the conductivity of the GFRP is negligibly small (cf. Sec. 3.3.5), the effective thermal conductivity is calculated in Sec. 3.6 independently of the temperature.

3.5.3 Statistical evaluation

In this section, the representativeness of the RUCs is examined in a statistical manner. Therefore, several convergence studies are conducted to investigate the fluctuations introduced by the random fiber distributions. Note here that the investigations are carried out up to 5% maximum strain in line with the experimental results of Sec. 3.3. To model larger deformations, these convergence studies need to be extended to verify the RUCs. This is, however, omitted here to reduce the computational effort.

Mesh convergence study

For the mesh convergence study, three RUC geometries generated with the randomization methods from Sec. 3.5.1 are considered. The corresponding in-plane dimensions are derived from the number of fibers and the fiber volume fraction ($\varphi = 40$ %) and measure 116.7 μm x

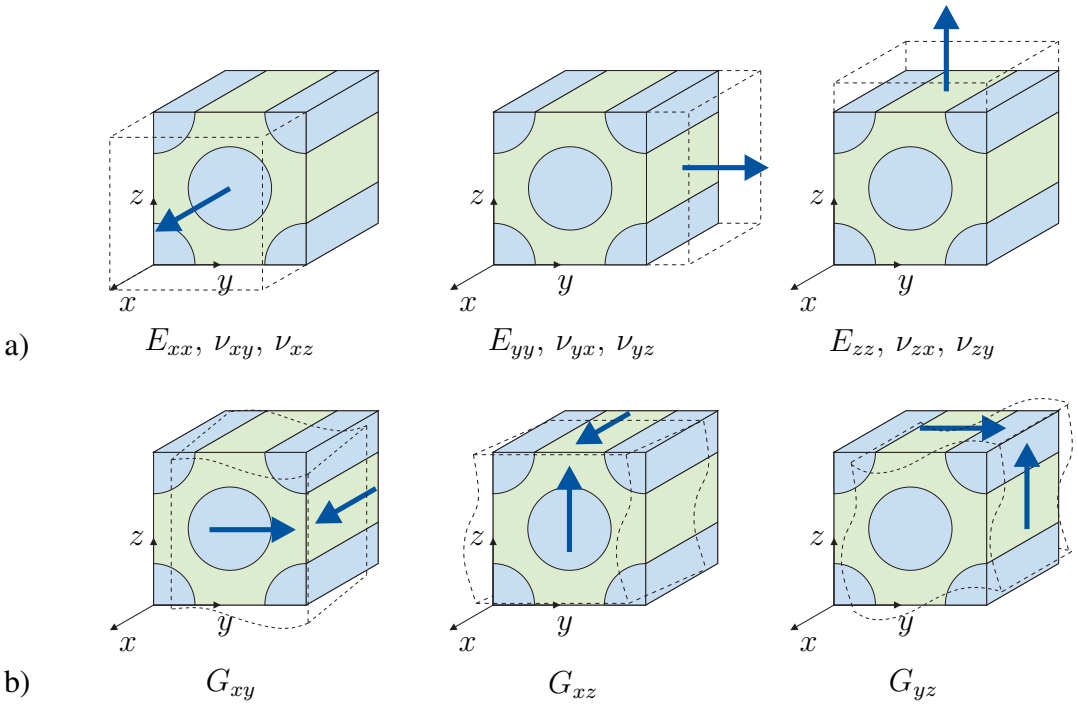

Figure 3.11: Schematic representation of the boundary conditions in terms of the six uniaxial strain states for deriving the effective elastic material properties. a) Monotonic, uniaxial tension b) Pure shear

116.7 μm for the RSA and CRSA method with $n_f = 24$ and 101.07 μm x 101.07 μm for the randomized method with $n_f = 18$. In fiber direction, only one element over the thickness is considered, which results in a material behavior comparable to plane strain. Different mesh sizes ranging from 1 to 3 μm are evaluated in steps of 0.5 μm. Regarding the boundary conditions, a constant temperature of $150°$ C is chosen since at elevated temperatures, plastic yielding in the PA6 matrix occurs already at small strains compared to room temperature (cf. Tab. 3.9). Here, the highest DOC of the matrix $\chi = 0.29$ is used to determine the matrix material parameters from Tab. 3.9. Monotonic, uniaxial tension in y-direction is the tested load case (see Fig. 3.11 a2). The simulations are terminated at a strain of 5% and the resulting stresses and strains are computed as volume averages of the whole domain Ω_0. In Fig. 3.12 a), the homogenized stresses at maximum strain are shown over the element size for the different randomization methods.

For the RSA and the CRSA method, a pronounced mesh dependence is visible, whereas the results of the randomized method show almost instantaneously converged behavior. This can be attributed to the lower amount of fiber clustering in the randomized method. Comparing the RSA based methods in more detail, a direct correlation between the amount of fiber clustering

and the mesh convergence is visible. The higher the amount of fiber clustering, the smaller element size is needed to achieve a converged result. Next, to determine the mesh size at which convergence is achieved, the relative errors are computed as the difference in the resulting homogenized stress from the current mesh size compared to the stress of the next coarser mesh. Here, a change < 1 % is regarded as a converged solution. Overall, mesh convergence is achieved for all three fiber distributions. In terms of the randomized method, an element size of 2.5 μm is already assumed to show the converged solution, whereas for the RSA and CRSA method a size of 1.0 μm is sufficient. Therefore, a mesh size of 1.0 μm is adopted for the subsequent simulations.

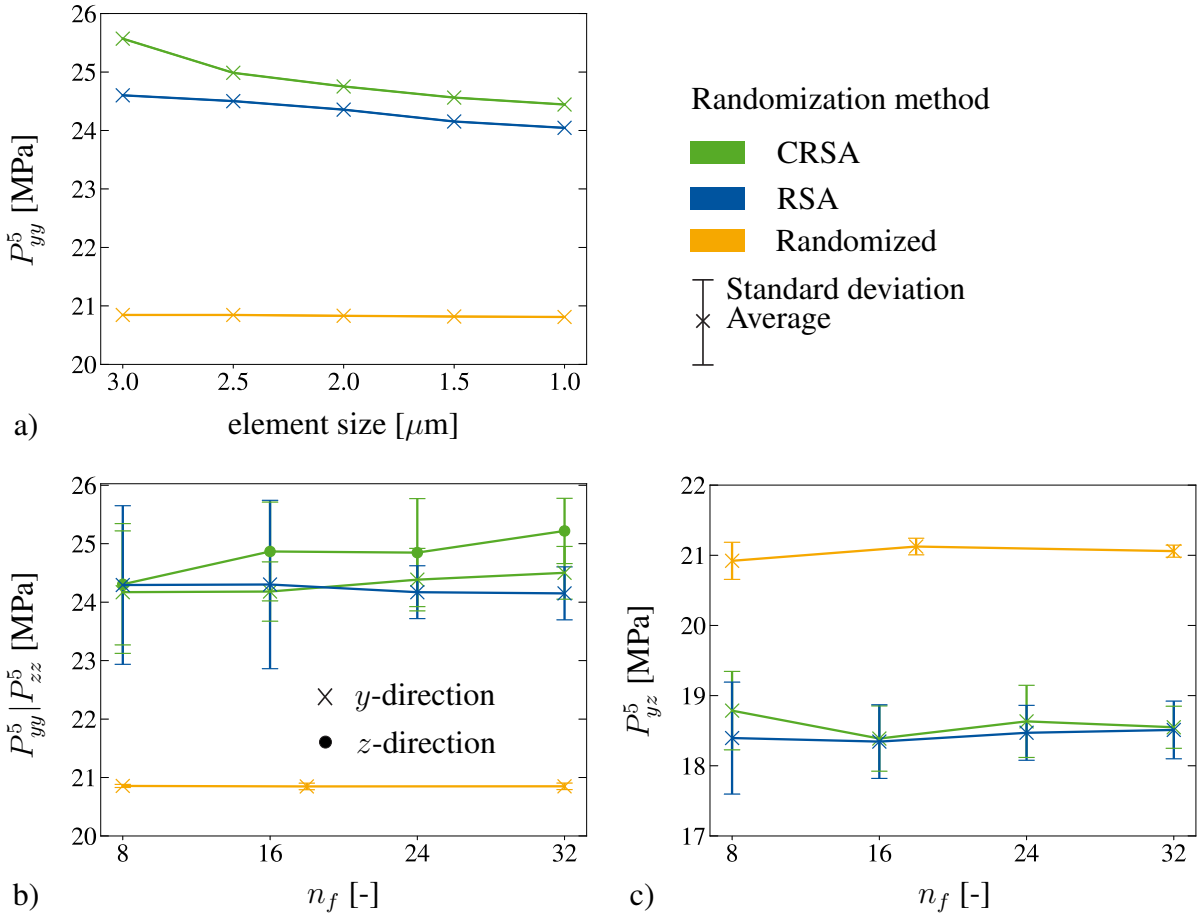

Figure 3.12: a) Mesh convergence study b) Size convergence study: Tension in y-direction (Standard deviation indicated by the error bars) c) Size convergence study: Pure shear in yz-direction (Standard deviation indicated by the error bars). For the corresponding periodic boundary conditions, the reader is referred to Fig. 3.11. P^5_* indicates the engineering stress (1. Piola-Kirchhoff stress) at 5% strain.

Size convergence study

A size convergence study is performed for varying sizes of RUCs generated with all three randomization methods. Again, the number of fibers n_f is used as a measure for the overall RUC size since the fiber volume fraction and the fiber diameter are assumed to be constant. Due to the random fiber distribution, for every randomization method and number of fibers, 10 different RUCs are generated. Hence, the average is used for comparison together with the standard deviation indicated by the error bars. The RUCs are tested in in-plane tension (y-direction) and in-plane shear (yz-direction) (see Fig. 3.11 a2 and b3). Further, in-plane tension simulations in z-direction are conducted for the CRUCs to investigate their direction dependence. Similar to the convergence study for the mesh density, the stresses and strains are computed as volume averages of the whole domain Ω_0 and the computation is terminated at a maximum strain of 5%.

The results of the size convergence study are shown in Fig. 3.12 b) and c) for both loading cases. In line with the results for the mesh density study, the randomized method yields almost instantaneously converged results for all RUC sizes. Moreover, compared to the other two methods, the standard deviation is very small, due to the low amount of fiber clustering. In contrast to the RSA based methods, the material response in y-direction is less stiff for the randomized method, whereas in the case of pure shear, the stiffest material response is present. Thus, a direct correlation between the amount of fiber clustering and the overall in-plane material response can be drawn, where a higher amount of clustering generally leads to a higher difference between tensile and shear behavior.

In terms of the convergence criterion, the deviation to the previous realization is adopted as previously done for the mesh convergence study. Consequently, $n_f = 18$ can be regarded as the converged RUC size for the randomized method. Compared to the randomized method, the RSA and the CRSA method show pronounced differences between the shear and tensile response. Here, the CRSA method results in a slightly stiffer material behavior, especially in the tensile load case. In general, the standard deviation decreases with increasing RUC size and similar to the mesh convergence study, the amount of fiber clustering influences the convergence rate. At 24 fibers, convergence is reached for the RSA method, whereas 32 fibers are needed for the clustered RSA method in z-direction. Interestingly enough, in y-direction convergence for the CRSA is already reached for 24 fibers. Additionally, in this direction, the unit cell response is similar to the RSA method. In the following, $n_f = 32$ is chosen for all unit cells as the common denominator.

3.6 Unit cell identification and validation against experimental results

3.6.1 Parameter identification

In Reuvers et al. [2024a], the thermomechanically coupled matrix model for polyamide 6 was developed, characterized and validated with mechanical and thermal experimental data. Therefore, a staggered parameter identification procedure was used on the isothermal model to obtain a set of mechanical and thermal material parameters for each test temperature. Here, a novel blending technique of the polymer PA6 together with cyclic olefin copolymer (COC) during specimen production allowed testing on a broad variety of stable DOCs. The resulting material model is valid for DOCs between 15% and 29%. In the following, a brief overview of the identification scheme is given:

1. The total Young's modulus E_{tot} was obtained from the initial slope of the true stress-strain relations for different DOCs. Next, the exponential dependence of the Young's modulus on the crystallinity was found using nonlinear regression. In contrast to the Young's modulus, the Poisson's ratio calculated via the negative ratio of the measured transverse and longitudinal strain, showed no clear dependence on the DOC. Hence, it was chosen as a constant ν_{tot}.

2. Based on a post-processing scheme introduced by Amin et al. [2006], uniaxial long-term relaxation tests at various strain states revealed a nonlinear dependence of the relaxation time τ on the visco-elastic overstress $\boldsymbol{\tau}_2$ and the corresponding strain state represented by the visco-elastic right Cauchy-Green tensor $\boldsymbol{C}_v$ (see Fig. 3.13). Similar to the Poisson's ratio, no clear dependence on the DOC was visible, in line with the assumption of the visco-elastic part corresponding mainly to the amorphous response of the material. For the relaxation time, the power-law-type function $\tau = \tau_0 ||\boldsymbol{B}_v||^{\gamma} \exp(-\delta ||\boldsymbol{\tau}_2||)$ was chosen. Here, a dependence on the visco-elastic left Cauchy-Green tensor $\boldsymbol{B}_v = \boldsymbol{F}_v \boldsymbol{F}_v^T$ and the Kirchhoff overstress $\boldsymbol{\tau}_2$ was introduced. The temperature dependent material parameters $\tau_0(\theta), \gamma(\theta)$ and $\delta(\theta)$ were identified using nonlinear curve fitting.

3. Above room temperature, it was not possible to directly obtain the yield stress in tension σ_t^0 and compression σ_c^0 from monotonic or cyclic tension and compression test. Hence, these material parameters together with the parameters related to nonlinear Armstrong Frederick hardening (b, c) were identified using a nonlinear multiple curve fitting procedure. Firstly, the ideal parameters for each DOC were governed using a single fit

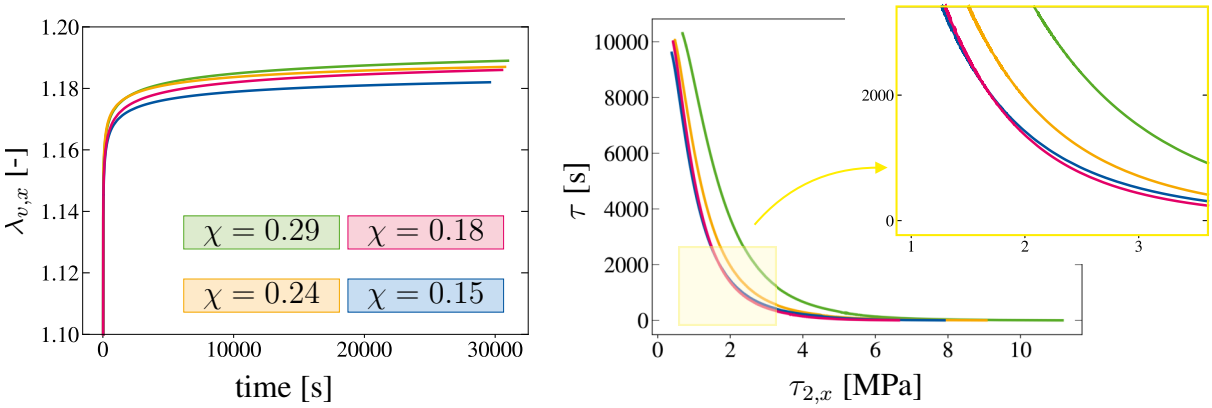

Figure 3.13: Results of the visco-elastic post-processing procedure from Reuvers et al. [2024a]: Inelastic stretch over time and relaxation time over Kirchhoff stress for an exemplary temperature of 100°C and various DOCs χ.

independent of the crystallinity. Next, the results for each parameter were plotted over the DOC and a linear trend line was identified using a multi curve fit. In this way, the dependence on the DOC was found and incorporated into the model for each test temperature.

4. Finally, the parameters related to the thermal characteristics of the model as the conductivity λ_t, specific heat capacity c_T, the thermal expansion coeffcient α_T and the density ρ_0 were determined experimentally. Similar to the Young's modulus, a dependence on the DOC was found using linear regression.

Parameter		23° C	100° C	150° C
E_{tot}	[MPa]	3800	832.0	484.89
ν_{tot}	[-]	0.35	0.45	0.45
σ_t^0	[MPa]	25.0	2.6	2.51
c	[MPa]	17.756	162.39	171.25
b	[MPa]	1.276	147.445	158.90
$\tau = \tau_0(\theta)\,\|\|\boldsymbol{B}_v\|\|^{\gamma(\theta)} \exp(-\delta(\theta)\,\|\|\boldsymbol{\tau}_2\|\|)$	τ_0 [s]	1853.653	1035.238	573.899
	γ [-]	4.57	4.3	4.289
	δ [-]	0.539	0.759	0.873

Table 3.4: Mechanical matrix material parameters for $\chi = 0.41$ at all test temperatures.

The complete set of mechanical and thermal parameters for the matrix material model up to a DOC of 29% is provided in Tabs. 3.9 and 3.8 in the Appendix. In the current work, the DSC results of the composite material revealed a DOC of $\chi \approx 0.41$ (cf. Sec. 3.3), which is beyond the identified parameter range. The extrapolated parameters from Tabs. 3.9 and

3.8 were tested for their suitability and compared to the experimental results from Sec. 3.3, however, only the thermal parameters as well as the crystallinity independent parameters for the visco-elastic branch were suitable. In Reuvers et al. [2024a], DIC was used only for the visco-elastic tests to exploit the post-processing procedure by Amin et al. [2006]. All other test results were converted to true stress and strain results under the assumption of incompressibilty. Hence, it is reasonable that extrapolated values from these results do not correspond to the current experimental data, which was obtained using DIC in all test cases. To obtain suitable parameters for the Young's modulus, the yield stress as well as the two hardening parameters, nonlinear curve fitting was used. Due to the lack of compression data above room temperature, the tension-compression asymmetry in yielding was neglected ($m = 1.0$). An overview of the mechanical parameters for a DOC of $\chi \approx 0.41$ is presented in Tab. 3.4. For the glass fibers, the temperature independent parameters were supplied by the manufacturer and can be found in Tab. 3.5.

E_{fiber}	ν_{fiber}	$\alpha_{T,\text{fiber}}$	$c_{T,\text{fiber}}$	$\lambda_{T,\text{fiber}}$	$\rho_{0,\text{fiber}}$
[GPa]	[-]	[10^{-6}/K]	[J/gK]	[W/mK]	[g/cm^3]
73	0.22	5.0	803	1.35	2.58

Table 3.5: Mechanical and thermal glass fiber material parameters.

3.6.2 Comparison of RUC and experimental results as well as further numerical calculations

Mechanical results

In order to derive the effective mechanical material properties and compare the results to the experimental findings from Sec. 3.3, the six uniaxial strain states (see Fig. 3.11) are applied successively on the RUCs. For each randomization method, 10 different RUCs are evaluated under isothermal conditions. The averaged results are shown in Tab. 3.6 for the three test temperatures together with the standard deviation s. Generally, the material stiffness tensor of transverse isotropic materials is defined by the following five material parameters: $E_{xx}, E_{yy}, \nu_{xy}, G_{xy}, G_{yz}$, where the symmetry between y- and z-direction is already exploited. This symmetry is, however, weakened for the CRSA method, where a high degree of clustering in $z-$direction leads to differences in the in-plane material characteristics. Consequently, the resulting material behavior from the CRSA method is orthotropic and defined by the following nine material constants: $E_{xx}, E_{yy}, E_{zz}, \nu_{xy}, \nu_{xz}, \nu_{yz}, G_{xy}, G_{xz}, G_{yz}$. In Tab. 3.6, all nine material constants are presented for completeness, even though in the case of the randomized

or RSA method the material constants are reduced to six. As expected, the material stiffness in x-direction is higher compared to the stiffness in y- and z-direction due to the dominant fiber influence. Moreover, the dependence on the temperature is least pronounced in fiber direction, which corresponds to the finding of Gröger et al. [2021] and the three-point-bending tests in Sec. 3.3. A more detailed overview of the reduction in material stiffness with increasing temperature is presented in Fig. 3.14, where the experimental material stiffness from tensile and three-point-bending tests are compared to the simulative results. The simulative results at room temperature are in good agreement with the experimental data. Above the glass transition, the predicted material stiffness in fiber direction deviates from the tensile response as expected due to the 2D measurement error discussed in Sec. 3.3. Interestingly enough, the temperature dependence in x-direction is more pronounced for the results of the bending tests compared to the RUC results and findings from Gröger et al. [2021]. The authors suspect that this softening might be related to delamination effects at the interface between fibers and matrix, which could be confirmed by a microscopic examination of the test specimens directly after testing or DIC measurements during testing. Another possibility could be a reduction in stiffness of the glass fibers resulting from the temperature increase. For example in Jenkins et al. [2015] a reduction in fiber stiffness was reported after thermal conditioning for 25 minutes at 200°C, suggesting that the stiffness decreased already between room and elevated temperatures. Hereby, the thermal conditioning time is similar to the heating phase for the experiments in Sec. 3.3. This decrease in fiber stiffness is, however, not accounted for in the RUC simulations (cf. Tab. 3.5) due to the lack of data from the manufacturer.

As indicated in Tab. 3.6, the material stiffness in y- and z-direction as well as the shear moduli G_{xy} and G_{zx} show no significant deviation for the randomization and the RSA method. The high degree of fiber clustering in the CRSA method, however, leads to pronounced differences at room temperature that are negligible above the glass transition.

The Poisson's ratios ν_{xy} and ν_{xz} correspond well with the experimental findings from Sec. 3.3 above the glass transition. However, at room temperature, the RUC results show an increased lateral contraction compared to the experimental results. Interestingly enough, below the glass transition, the Poisson's ratios ν_{xy} and ν_{xz} are independent of the randomization method, and the differences at higher temperatures are only minor. In terms of the standard deviation, the results correspond with those of the convergence studies in Sec. 3.5, where the standard deviation of the randomized method is smaller compared to the RSA and CRSA methods. This finding translates to the stress fields for an exemplary temperature of 100°C in Fig 3.15 and $\varepsilon = 0.25$, where the randomized method shows the most homogeneous stress distribution in all directions. Hereby, stress peaks are mainly visible in regions with increased fiber clustering.

$n = 10$	Randomization method	E_{xx} [MPa]	E_{yy} [MPa]	E_{zz} [MPa]	ν_{xy} [-]	ν_{xz} [-]	ν_{yz} [-]	G_{xy} [MPa]	G_{zx} [MPa]	G_{yz} [MPa]
23°C	Randomized	31350.23	7417.33	7460.11	0.29	0.29	0.50	45.50	44.99	6651.27
s		0.249	21.651	27.396	0.0003	0.0003	0.002	0.153	0.133	24.391
	RSA	31352.74	8374.29	8388.99	0.29	0.29	0.44	46.31	46.46	5847.62
s		0.345	188.741	154.343	0.006	0.006	0.011	0.615	0.804	148.625
	CRSA	31332.06	8871.82	8463.88	0.29	0.29	0.43	44.59	49.06	5667.99
s		34.717	131.550	104.993	0.001	0.001	0.010	0.367	0.622	79.094
100°C	Randomized	29563.95	1776.92	1779.63	0.35	0.35	0.78	9.78	9.94	1465.10
s		0.259	6.280	6.697	0.0007	0.0007	0.002	0.027	0.036	10.883
	RSA	29567.14	2219.74	2223.35	0.35	0.35	0.72	10.19	10.21	1236.72
s		0.485	84.704	80.705	0.004	0.004	0.012	0.206	0.147	52.849
	CRSA	29547.14	2390.97	2350.33	0.34	0.36	0.71	10.94	9.72	1171.88
s		33.877	76.597	70.923	0.003	0.003	0.010	0.175	0.096	26.188
150°C	Randomized	29351.08	1123.51	1127.57	0.35	0.35	0.79	5.76	5.85	1020.05
s		0.232	5.794	6.465	0.0007	0.0007	0.002	0.016	0.022	7.690
	RSA	29353.08	1447.69	1450.47	0.35	0.35	0.73	6.01	6.02	835.92
s		0.365	62.314	58.262	0.004	0.004	0.012	0.125	0.089	39.207
	CRSA	29332.82	1584.72	1538.37	0.34	0.36	0.72	6.46	5.72	791.60
s		33.817	54.129	48.874	0.003	0.003	0.010	0.106	0.058	19.882

Table 3.6: Effective elastic material parameters for various material directions and randomization methods at temperatures below and above the glass transition. The standard deviation is indicated by s.

This phenomenon is particularly evident in the CRSA method, where slight band formation is also visible in the yy- and xy-directions. In fiber direction, no significant differences between the stress fields of all randomization methods are present in line with the results for the material stiffness E_{xx} in Tab. 3.6. Here, the fibers are the load bearing component, as indicated by the stress field.

A detailed comparison of experimental and simulative results beyond the elastic material regime is presented in Fig. 3.16 for the material response perpendicular to the fibers at all respective test temperatures. The results for the RSA and CRSA method are in good agreement with the experimental data, whereas the randomized method yields a softer material response similar to the convergence study results from Sec. 3.5. Consequently, the authors conclude that both the RSA and the CRSA method are eligible for the present material. For a further selection, additional tests, such as for example, shear tests or a detailed microscopic examination of the underlying fiber distribution beyond the investigations in Sec. 3.3 would be necessary, which was, however, beyond the scope of this work. Nonetheless, both RSA and CRSA method yield valid results in comparison to the experiments and can be used to generate a data basis for the identification of the macroscopic material model.

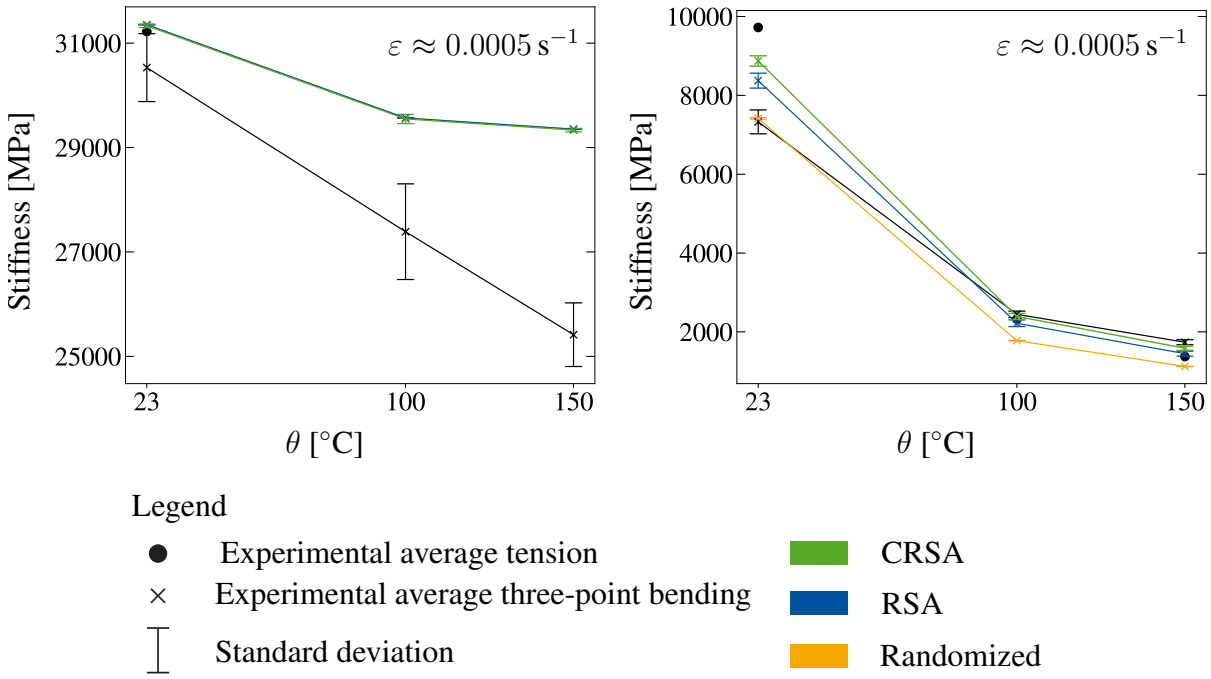

Figure 3.14: Comparison of experimental and simulative material stiffness in x- and y-direction for various temperatures and randomization methods.

Thermal results

To determine the effective thermal conductivity tensor from the averaged heat flux over the RUC domain a series of $n = 10$ tests is performed for each randomization method. Therefore, a temperature difference $\Delta T = 1\mathrm{K}$ is successively applied in x-, y- and z-direction under steady-state heat transfer conditions as stated in Sec. 3.5. In Reuvers et al. [2024a], the conductivity of the polyamide 6 matrix was found to be dependent on the degree of crystallinity, however, the temperature influence was negligibly small (cf. Tab. 3.8). For the conductivity of the glass fibers no temperature influence is reported by the manufacturer in the considered temperature range. Consequently, the effective thermal conductivity tensor of the composite is derived only at room temperature. The results of the computations are given in Tab. 3.7 as the mean value together with the standard deviation s. For all computations, the off-diagonal entries of the thermal conductivity tensor were four or more orders of magnitude smaller than the entries on the main diagonal and are, thus, considered as null $\lambda_{xy} = \lambda_{yx} = \lambda_{xz} = \lambda_{zx} = \lambda_{yz} = \lambda_{zy} \approx 0$. Hence, only the conductivities in x-, y- and z-direction are presented.

Similar to the mechanical results, the in-ply conductivities for the randomized and RSA methods are approximately equal, with the randomized method having the lowest standard deviation. For the CRSA method, the thermal conductivity in z-direction is higher compared

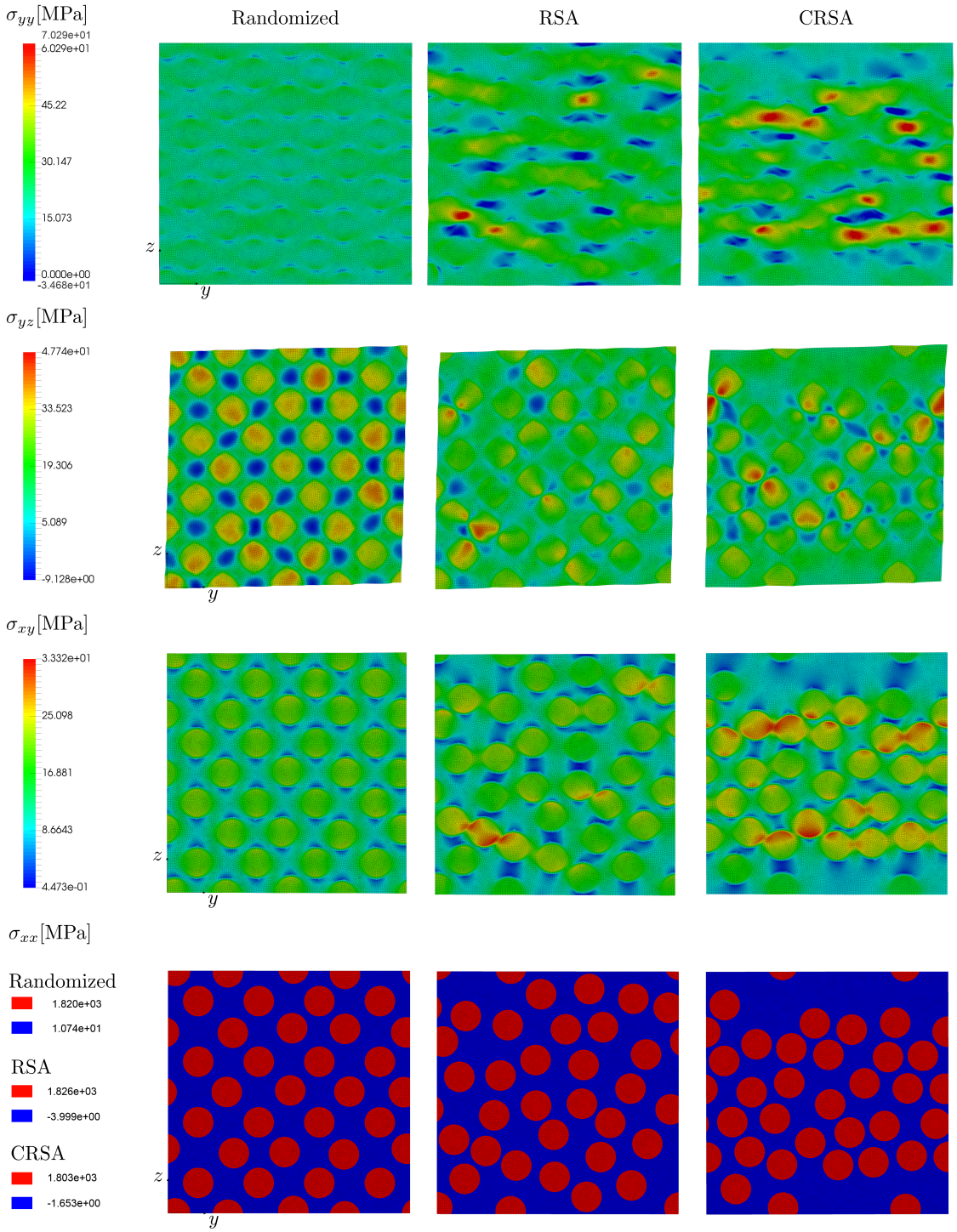

Figure 3.15: Exemplary in-plane stress fields (Cauchy stress) for all three randomization methods at $\varepsilon = 0.025$ and 100°C after application of the far field strains in the corresponding material directions.

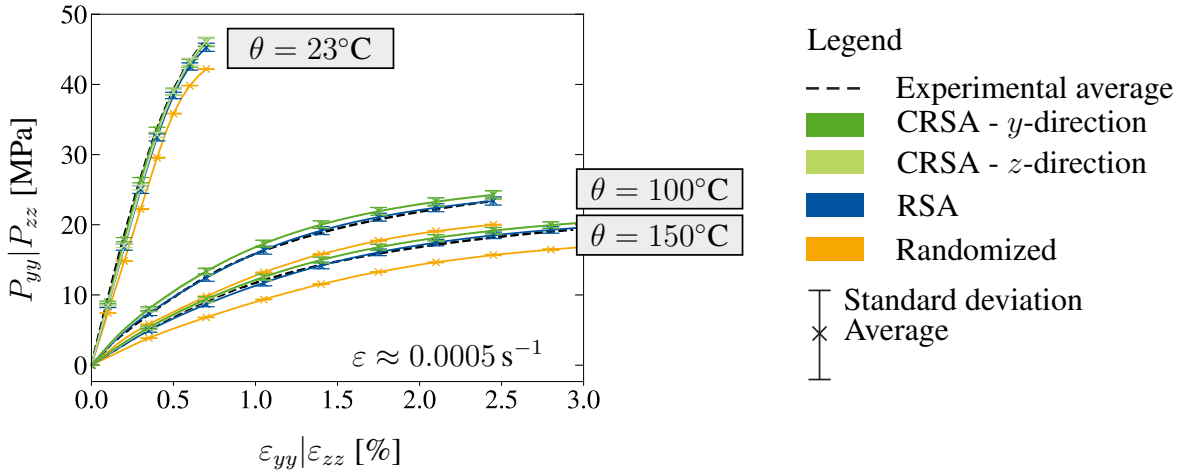

Figure 3.16: Comparison of experimental and simulative results perpendicular to the fiber direction for various temperatures and randomization methods.

n=10	Randomization method	λ_{xx} [W/mK]	λ_{yy} [W/mK]	λ_{zz} [W/mK]
	Randomized	0.7991	0.5919	0.5894
s		0.0015	0.0009	0.0008
	RSA	0.8040	0.5947	0.5944
s		0.0028	0.0033	0.0035
	CRSA	0.8022	0.5840	0.6073
s		0.0042	0.0028	0.0026

Table 3.7: Effective thermal conductivity for various material directions and randomization methods (s denotes the standard deviation). $\lambda_{xy} = \lambda_{yx} = \lambda_{xz} = \lambda_{zx} = \lambda_{yz} = \lambda_{zy} \approx 0$.

to the conductivity in y-direction, which can be attributed to the higher degree of clustering resulting in a layered structure. Generally, all results in y- and z-direction correspond well with the experimentally determined values in z-direction of 0.5889 W/mK for 23° and 0.6365 W/mK as the median over all test temperatures (cf. Fig. 3.7). In fiber direction, the thermal conductivity is fiber dominated and, thus, higher compared to the in-ply results for all randomization methods. Interestingly enough, the anisotropic thermal conductivity is not material-induced but rather geometry induced since both material constituents are thermally isotropic on their own. To give an insight on local differences between the randomization methods, exemplary heat flux fields resulting from the application of a temperature difference in x-, y- and z-direction are shown in Fig. 3.17. Here, the in-ply heat flux field of the randomized method is the most homogeneous, whereas directional dependencies can clearly be

indicated for the RSA and CRSA method. Slight band formation is visible for the RSA and CRSA method in y- and z-direction throughout all realizations, however, most pronounced for the heat flux of the CRSA RUC in y-direction, resulting from the high degree of fiber clustering. In x-direction, the heat flux fields of all randomization methods show no significant differences, consistent with the findings in Tab. 3.7.

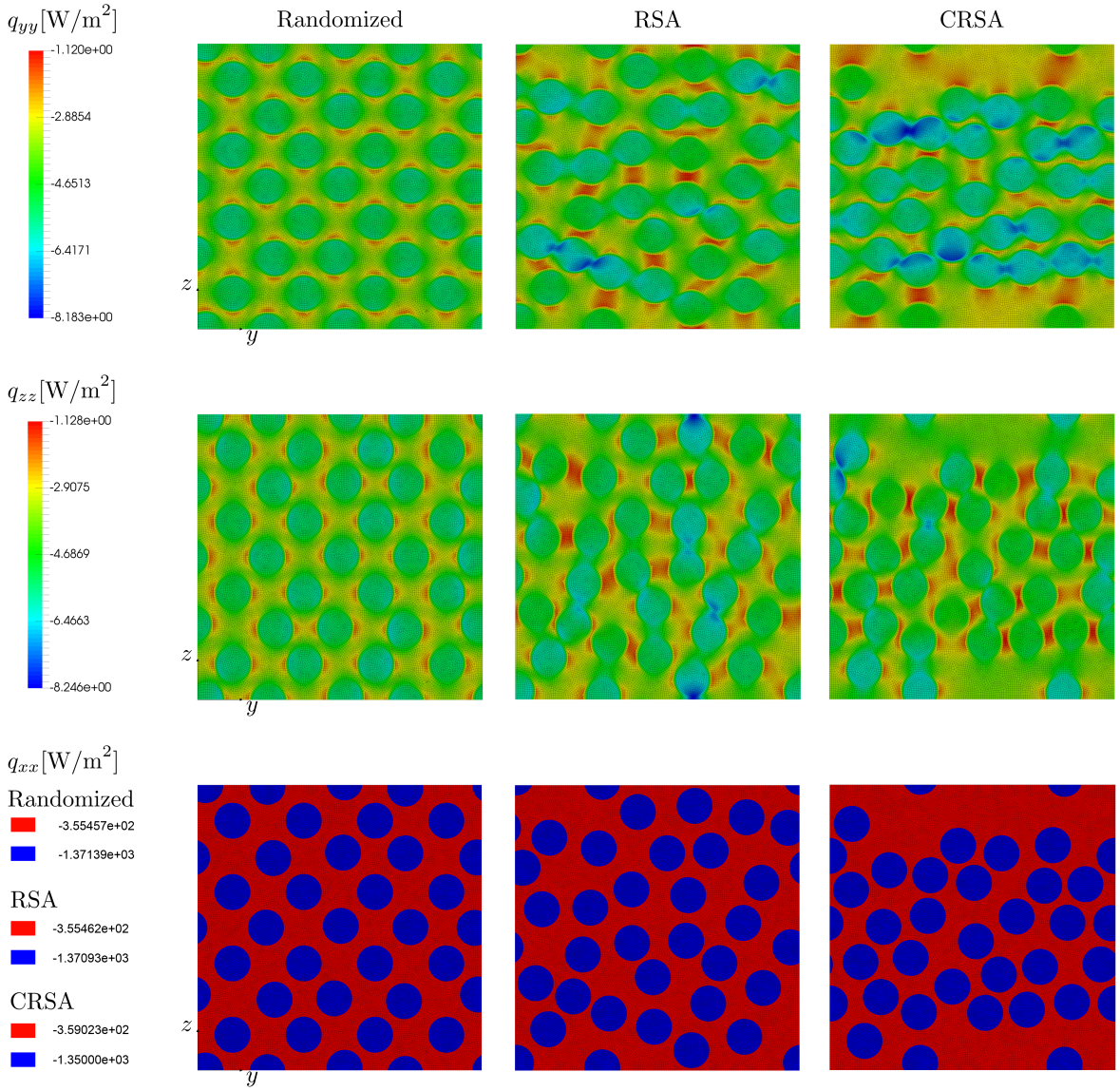

Figure 3.17: In-plane heat flux field for all three randomization methods after application of a 1K temperature difference in in x-, y- and z-direction.

3.7 Conclusion and outlook

In this work, a computational micromechanics framework was presented, incorporating thermal and mechanical effects on the microscale to predict the homogenized material behavior of an experimentally tested glass fiber reinforced polyamide 6 single ply. To this end, monotonic and cyclic experimental tests were conducted in various material directions, e.g. tension, compression and bending, including testing at various temperatures and strain rates. The results showed the materials' direction dependency due to the unidirectional reinforcement and confirmed the temperature and strain rate dependency mainly perpendicular to the fibers, where the polyamide 6 material dominates the material response. Additional tensile tests under varying fiber angle displayed the nonlinear influence of the fiber angle on the composite material behavior. Furthermore, the material was thermally characterized, including a TMA, DSC and *Hot-Disc* measurements indicating a temperature influence on the thermal material parameters. Next, a thermomechanically coupled material model formulation for the PA6 matrix was summarized that captures the nonlinear visco-elastic, elasto-plastic material behavior, incorporating the Bauschinger effect via nonlinear kinematic hardening together with a tension-compression asymmetry in yielding. The degree of crystallinity enters the constitutive equations as a constant input quantity to account for the effect of the underlying material morphology on the overall material behavior, as well as the interplay between the biphasic matrix microstructure and applied thermal conditions. In Reuvers et al. [2024a], the model formulation was already identified for polyamide 6 blends for a range of DOCs between 15 and 29% and extended up to 41 % in this contribution with the presented experimental results. Together with an elastic material model for the glass fibers, the presented matrix model formulation was used in the context of repeating unit cell simulations. Therefore, various randomization methods were tested during the generation of the unit cells to predict the random fiber distribution. Here, the focus lied on process automation. Consequently, a plug-in was developed using the Abaqus-Python interface. In the following, a statistical investigation, where the Hill-Mandel condition was exploited to obtain homogenized mechanical and thermal results indicated the necessary mesh and unit cell size to achieve converged results. The comparison of experimental and numerical mechanical and thermal results showed a strong agreement and confirmed the applicability of the repeating unit cells. In terms of the mechanical results, the RSA and CRSA methods were found to reflect the material behavior best, whereas the effect of the randomization method ,for example, on the effective thermal parameters was negligible. In general, the authors would recommend to use the CRSA method, which showed to be more accurate regarding the production induced orthotropic material behavior and the

visual comparison with the microscopic images. Moreover, the high amount of fiber clustering might be able to reproduce delamination phenomena if damage effects were incorporated in the matrix material. In the present case, however, the small plate thickness limited completing the mechanical and thermal experimental study for all three material directions. Thus, the RSA method provides a simpler solution, with the reduction from orthotropic to transversely isotropic material behavior. In the future, the established and experimentally validated unit cells will be used for the development of a broad data basis for the single ply response of glass fiber reinforced polyamide 6, enabling testing on additional temperatures and strain rates. Furthermore, previously unseen loading conditions, as for example shear, can be examined without the accompanying experimental effort. The concept can also be adjusted to cater for altered material design, as for example, using a different fiber volume content or exchanging the underlying material constituents, given that the knowledge of their individual material behavior is known. This data basis will then be used in an upcoming publication to identify a homogenized macroscopic material model, accounting for the underlying micro-thermomechanical effects through the presented framework. The macromodel will be tested in the context of thermoforming simulations to demonstrate the enhancements made through the inclusion of the crystallinity dependence and the thermo-mechanical coupling in the formulation.

3.8 Appendix

Table 3.8: Set of thermal material parameters at different temperatures from Reuvers et al. [2024a].

Function	Parameter at:	23° C	50° C	100° C	130° C	150° C
$\alpha_T(\chi) = c_9(\theta)\chi + c_{10}(\theta)$	$c_9[10^{-4}/\text{K}]$	-0.2601	-0.3586	-5.857	-3.336	-2.238
	$c_{10}[10^{-4}/\text{K}]$	0.8756	1.218	3.122	2.565	2.431
$c_T(\chi) = c_{11}(\theta)\,\theta + c_{12}(\theta)$	c_{11}[J/gK]	0.00471	0.00401	0.00401	0.00401	0.00401
	c_{12} [J/gK]	1.25313	1.52299	1.52299	1.52299	1.52299
$\lambda_T(\chi) = c_{13}\chi + c_{14}$	c_{13}[W/mK]	0.4338	0.4338	0.4338	0.4338	0.4338
	c_{14}[W/mK]	0.1855	0.1855	0.1855	0.1855	0.1855
$\rho_0(\chi) = c_{15}\chi + c_{16}$	c_{15} [g/mm^3]	0.4878	0.4878	0.4878	0.4878	0.4878
	c_{16} [g/mm^3]	0.9897	0.9897	0.9897	0.9897	0.9897

Remark: The reader is kindly reminded, that although some coefficients of the identified functions determining the material parameters, are negative, the material parameters themselves are always positive for the range of DOCs ($\chi = 0.15 - 0.29$) the model spans.

3.8.1 Mechanical and thermal material parameters for the polyamide 6 matrix model

Table 3.9: Set of mechanical material parameters at different temperatures for a range of DOC between 15 and 29% from Reuvers et al. [2024a].

Function	Parameter at:	23° C	50° C	100° C	130° C	150° C
$E_{\text{tot}}(\chi) = C_1(\theta)\exp(C_2(\theta)\,\chi)$	C_1 [MPa]	2397	2270*	143.1	96.875	102.1
$E_2 = E_{\text{tot}} - E_1$	C_2 [-]	0.9106	-0.8716*	5.133	5.565	5.373
$E_1 = m_E(\chi)E_{\text{tot}}$	m_E [-]					
$m_E = 1.07143\chi + 0.38935$						
$\nu_{\text{tot}}(\theta) = \nu_1 = \nu_2$	[-]	0.35	0.45	0.45	0.45	0.45
$\sigma_c^0 = c_1(\theta)\chi + c_2(\theta)$	c_1 [MPa]	72.19	138.8	26.95	20.86	13.19
	c_2 [MPa]	41.96	-21.913	-3.192	-2.969	-1.436
$\sigma_t^0 = c_3(\theta)\chi + c_4(\theta)$	c_3 [MPa]	72.19	131.24	25.38	20.27	12.93
	c_4 [MPa]	41.96	-20.984	-3.006	-2.884	-1.407
$c = c_5(\theta)\chi + c_6(\theta)$	c_5 [MPa]	$c = 17.756$**	20.86	834.5	597.3	523.8
	c_6 [MPa]		92.213	-94.56	-69.42	-67.89
$b = c_7(\theta)\chi + c_8(\theta)$	c_7 [-]	$b = 1.276$**	0	355.4	150.2	196.3
	c_8 [-]		60.438	-53.15	-22.39	-28.3
$\tau = \tau_0(\theta)\,\|\|\boldsymbol{B}_v\|\|^{\gamma(\theta)}\exp(-\delta(\theta)\,\|\|\boldsymbol{\tau}_2\|\|)$	τ_0 [s]	1853.653	1511.952	1035.238	737.245	573.899
	γ [-]	4.57	4.416	4.3	4.872	4.289
	δ [-]	0.539	0.814	0.759	0.866	0.873

* inconsistent results due to testing in the glass transition regime

** constant values obtained for $\chi = 0.29$ only, due to early failure of the remaining blends

Remark: The reader is kindly reminded, that although some coefficients of the identified functions determining the material parameters, are negative, the material parameters themselves are always positive for the range of DOCs ($\chi = 0.15 - 0.29$) the model spans.

4 Article 3: An anisotropic thermo-mechanically coupled constitutive model for glass fiber reinforced polyamide 6 including crystallization kinetics

This article was published as:

Reuvers, M., Dannenberg, C., Kulkarni, S., Johlitz, M., Lion, A., Reese, S. and Brepols, T. [2025], 'An anisotropic thermo-mechanically coupled constitutive model for glass fiber reinforced polyamide 6 including crystallization kinetics', *International Journal of Plasticity* **189**, 104341.

Disclosure of the individual authors' contributions to the article:

M. Reuvers revieved the existing literature, derived the constitutive framework, implemented the material model as a user-defined material model (UMAT/UMATHT) into the commercial Finite Element software *ABAQUS*/Standard, was responsible for model identification and validation and carried out all computational examples, interpreted the results, and wrote the article. C. Dannenberg implemented the crystallization kinetics neural network in the Tensorflow environment and was responsible for the interpretation of the results. S. Kulkarni carried out the differential scanning calorimetry and thermoforming experiments and contributed to the discussion of the results. M. Johlitz, A. Lion, T. Brepols and S. Reese gave conceptual advice, contributed to the discussion of the results, proofread the article and made valuable suggestions for improvement. All authors approved the publication of the final version of the manuscript.

4.1 Abstract

In order to achieve process stability in the industrial thermoforming of fiber reinforced polymers (FRPs), typically, cost- and time-intensive trial-and-error-processes are required. The experimental boundary conditions, as well as the material composition and component design optimization, are highly dependent on material phenomena related to various material scales and constituents. It is therefore necessary to develop finite element constitutive models that are validated against experimental results and incorporate various material phenomena in order to reduce the experimental effort and evaluate the composite's performance with reliable predictions. In this work, an existing thermo-mechanically coupled constitutive model for polyamide 6 is extended in a thermodynamically consistent manner to represent the anisotropic composite behavior, including anisotropic conduction, thermal expansion as well as internal heat generation associated with irreversible processes. Furthermore, the crystallization process is incorporated using experimental standard (S-DSC) and flash (F-DSC) differential scanning calorimetry results. The thermal and mechanical model parameters of the homogenized macroscopic material formulation are identified and the model response is successfully validated with a data base comprising both experimental and virtual results. Finally, the model capabilities are assessed in several thermo-mechanical structural computations, including a 3D thermoforming example in comparison with experimental results. In particular, the influence of the anisotropy on material self-heating, thermal expansion and the resulting crystalline state is investigated, demonstrating the potential of this new approach to efficiently and accurately predict FRPs in the future. Our source code, data, and exemplary input files are available under `https://doi.org/10.5281/zenodo.15052983`.

4.2 Introduction

Fiber-reinforced polymers (FRPs) are now prevalently employed in applications that necessitate superior thermo-mechanical properties alongside weight reduction and cost-effective mass production. These composite materials are fabricated using a diverse array of constituents, especially semi-crystalline thermoplastics as matrix materials, with recyclability and reusability increasingly becoming pivotal considerations in the design process. Despite their widespread adoption across various industries, the precise prediction and optimization of forming processes, such as thermoforming or injection molding, frequently remain dependent on trial and error methodologies. Often, the resulting products exhibit undesirable deformations post-forming, necessitating extensive and costly experimental adjustments to refine the process parameters. The intricate behavior of the polymeric matrix material, which undergoes a second order phase transition around the glass transition temperature, poses significant challenges for accurate prediction and remains an active area of research (see, e.g., Srivastava et al. [2010]; Hadipeykani et al. [2020]; Xie et al. [2020]). In instances involving a semi-crystalline polymer matrix, the non-isothermal crystallization process during cooling is crucial not only for the complex interaction between fiber and matrix at their interface but also for the material's ultimate performance and subsequent processing ability, further complicating the forming process (see e.g. Yoshida et al. [2022]). In this context, the formation of crystal phases occurs within a temperature environment that is both temporally and locally evolving. This has a significant impact on the relevant parameters for the heat transfer and thus, ultimately, the temperature field within the polymer. In turn, the temperature field determines the process of crystallization, resulting in a two-way coupling of the temperature field and the crystallization process (cf. Dietz [1981]; Ayoub et al. [2011]). Consequently, the need arises for including a macroscopic description of the crystallization process into the thermo-mechanically coupled material model for the resulting composite.

Naturally, the morphology of the underlying microstructure has a significant influence on the resulting material response as well (cf. e.g. Ayoub et al. [2011]; Dörr [2021]). Especially, since FRPs are industrially processed at high temperatures near the melt with the objective of achieving a stable crystalline state upon cooling. The resulting degree of crystallinity (DOC) is, however, mostly determined prior to or after the application of mechanical loadings and not during the experimental procedure itself. To this end, in this work on unidirectionally glass fiber reinforced polyamide 6 two decoupled processes are considered, similar to (Felder et al. [2020b]). At first, the non-isothermal crystallization from the melt is treated as a thermo-chemical problem, where stress-free conditions are assumed based on a relaxed static melt to

obtain the evolution of the DOC ($\dot{\chi} \geq 0$ and $\boldsymbol{\sigma} \approx \mathbf{0}$). Thus, changes in the crystal configurations or inhomogeneous crystal phases can be identified based on, for example, varying cooling rates or temperature gradients inside the composite resulting from e.g. anisotropic thermal behavior of the composite. Furthermore, analyzing the exothermic latent heat during crystallization in a fully coupled scheme is crucial for the identification of local temperature gradients within the material. To this end, the crystallization kinetics are incorporated by means of a non-isothermal modification of the Avrami equation (cf. Avrami [1939]; Nakamura et al. [1973]; Felder et al. [2020b]), introducing a cooling rate dependency and simultaneously taking into account the backcoupling with the temperature field. The model is identified with S-DSC and F-DSC data from Kulkarni et al. [2023]. Subsequently, the thermo-mechanical problem of the composite is solved, where the DOC enters the model as a constant input quantity, similar to, for example, Felder et al. [2020b]; Ayoub et al. [2011]; Abdul-Hameed et al. [2014] and external mechanical and thermal boundary conditions are applied ($\dot{\chi} = 0$ and arbitrary $\boldsymbol{\sigma}$).

Once the resulting crystalline state of the material is reached, the mechanical response of the composite is characterized by a nonlinear transversely isotropic material behavior. Additionally, thermo-mechanical coupling effects occur in terms of material self-heating and associated thermal softening, especially at high loading rates (see e.g. Krairi et al. [2019]; Felder et al. [2020a,b]; Hao et al. [2022a]). In the past, the primary focus has been on the derivation of suitable material formulations, predominantly related to the polymer matrix, due to its complex nonlinear material behavior. Some examples include phenomenological models incorporating viscous or visco-plastic effects (see e.g. Boyce et al. [2000]; Ayoub et al. [2010]; Krairi and Doghri [2014]; Felder et al. [2020a]) as well as fewer available extensions to thermo-mechanically coupled approaches in e.g. Khan et al. [2006]; Anand et al. [2009]; Srivastava et al. [2010]; Shen et al. [2019]; Felder et al. [2020b], to name a few. For the composite, several micromechanical approaches exist, where unit cells or representative volume elements are employed to generate a homogenized macroscopic material response (see e.g. González and LLorca [2007]; Melro et al. [2013*a*]; Naya et al. [2017]; Bahloul et al. [2021]; Reuvers et al. [2024b]). These approaches are however more suited for investing micromechanical phenomena and gathering virtual or effective material data and are not feasible for investigating forming processes due to their extensive computational cost. In addition, again only a few of these works consider non-isothermal conditions. For engineering applications, macromechanical polymer composite models were proposed by, for example Reese [2003*b*]; Mehdipour et al. [2019] as well as data-driven approaches using neural networks, see El Kadi [2006]; Dey et al. [2023]. More recent studies on thermoforming simulations include several non-isothermal effects in their macroscopic approaches (see e.g.

Machado et al. [2016]; Guzman-Maldonado et al. [2016]; Dörr et al. [2019]; Dörr [2021], however, apart from Dörr et al. [2019]; Dörr [2021]) they are limited to temperatures above the crystallization onset. The present work is settled in between engineering application and sophisticated, physics-based model development. In contrast to Dörr et al. [2019]; Dörr [2021], who incorporated the evolution of crystallinity mainly to account for the phase transition between the molten and the solid state, in this work, the resulting absolute degree of crystallinity enters the thermo-mechanical formulation as a constant input quantity. Moreover, in contrast to Dörr et al. [2019]; Dörr [2021], the present work exploits the concept of structural tensors (see e.g. Boehler [1979]; Zhang and Rychlewski [1990]; Reese et al. [2001]; Reese [2003*b*]) to model anisotropy. For polymeric materials this idea was adopted in, for example, Holzapfel and Gasser [2001]; He et al. [2021]. Another popular application is the field of biomechanics in, for example, human tissues (see e.g. Taç et al. [2024]; Martonová et al. [2024]). In Vladimirov et al. [2010], the concept of structural tensors has been used to model anisotropic finite elasto-plasticity, whereas Reese et al. [2021] utilized structural tensors to model damage in elasto-plastic materials. However, with regard to the extension of this approach to anisotropic thermal problems, very few contributions have been made thus far. In this context, Al-Kinani [2014] introduced a macroscopic description of the heat flux for transversely isotropic materials and further extended the theory to model anisotropic thermal expansion employing a split of the deformation gradient into a thermal and a mechanical part. This split is well-known in the literature to model thermo-mechanically coupled problems (see e.g. Stojanovic et al. [1964]; Lu and Pister [1975]; Lion [1997*a*]; Felder et al. [2022]). Besides the split of the deformation gradient, other approaches employ a general representation of the twice integrated heat capacity, where a suitable choice of the internal energy is necessary to include thermal expansion into the free energy (see e.e. Chadwick [1974]; Reese [2003*a*]). Both methods are commonly used in thermo-mechanically coupled material formulations, however, in this work the thermal expansion term will be introduced via the choice of the internal energy. For anisotropic materials, this was previously done briefly in Groß et al. [2019, 2020] and further works of the authors, who introduced a fiber deformation tensor based on a structural tensor. However, no numerical investigations regarding the thermal anisotropy were conducted and the suitability of the chosen thermal energetic terms were not evaluated. To the authors' knowledge, there is no comparable constitutive framework available in the literature, which investigates anisotropic thermal problems together with the corresponding complex mechanical and crystallization interactions related to fiber-reinforced semi-crystalline polymers (FRSCPs). Moreover, the presented material formulation is experimentally verified over multiple material scales and incorporates micro-thermo-mechanical phenomena over an unprecedentedly wide range of

process parameters.

In the following, the anisotropic thermo-chemically, thermo-mechanically coupled material model is presented in Sec. 4.3 as an extension of the model by Reuvers et al. [2024a]. The unidirectional (UD) fiber-induced anisotropy is accounted for by an additional anisotropic thermo-elastic energetic contribution together with macroscopic anisotropic thermal conduction. A novel aspect of this work is the formulation of the anisotropic thermal expansion term based on a general derivation of the internal energy. In addition, the crystallization process is introduced in a thermodynamically consistent manner according to Felder et al. [2020b]. A comparison of the model response to experimental and virtual composite data is shown in Sec. 4.4 for various fiber angles, following model identification for a wide range of crystallinities between 15 and 40 %. The capabilities of the model, to accurately predict anisotropic thermal expansion as well as self-heating are presented in Sec. 4.5, together with further complex structural examples covering the influence of the thermal anisotropy on the crystallization behavior as well as thermo-mechanical loading scenarios and a 3D thermoforming example in comparison to experimental results. Finally, a conclusion is drawn in Sec. 4.6 and an outlook on future model applications and enhancements is given.

4.3 Constitutive equations

This work is thought out as the final step of an approach for developing a valid macroscopic material model for fiber-reinforced polymers in the context of thermoforming, incorporating computational micromechanics and virtual material testing to reduce the experimental effort necessary for characterizing the material formulation for a wide range of crystalline states. Consequently, the thermo-mechanically coupled model equations presented here, are an extension of an already existing and experimentally characterized material model from Reuvers et al. [2024a]. The adjustments include the extension from isotropic to anisotropic thermo-mechanical material behavior to account for the reinforcing agent. It is assumed that a perfect bond between fibers and the matrix is achieved due to the application of bonding agents during production. Consequently, delamination effects are not considered in this work as well as residual stresses resulting from thermal gradients and the different mechanical and thermal properties of the constituents. The reader is kindly reminded that the DOC is introduced as a constant input quantity for the thermo-mechanically coupled material model. Its absolute value is determined through an independent thermo-chemical process, similar to Felder et al. [2020b], which represents the crystallization of the polymer matrix from the molten state. In the following, the equations related to the crystallization from the static melt ($\dot{\chi} \geq 0$ and

$\boldsymbol{\sigma} \approx \mathbf{0}$) are denoted with I. For the equations related to the thermo-mechanical behavior of the composite ($\dot{\chi} = 0$ and arbitrary $\boldsymbol{\sigma}$), the prefix II is introduced. Throughout the text, the following notational conventions are employed:

a, A	Scalar quantity	$\mathrm{sym}(\boldsymbol{A})$	$\frac{1}{2}(\boldsymbol{A} + \boldsymbol{A}^T)$
$\boldsymbol{a}$	First order tensor	$\mathrm{dev}(\boldsymbol{A})$	$\boldsymbol{A} - \frac{1}{3}\,\mathrm{tr}(\boldsymbol{A})\boldsymbol{I}$
$\boldsymbol{A}$	Second order tensor	$\mathrm{Grad}(\boldsymbol{A})$	Gradient of $\boldsymbol{A}$ with respect to the reference configuration
$\boldsymbol{I}$	Identity tensor	$\mathrm{grad}(\boldsymbol{A})$	Gradient of $\boldsymbol{A}$ with respect to the current configuration
$\mathbb{A}$	Fourth order tensor	$\mathrm{Div}(\boldsymbol{A})$	Divergence of $\boldsymbol{A}$ with respect to the reference configuration
$\dot{(*)}$	Total derivative with respect to time	:	Double contraction
$(\boldsymbol{A})^T$	Transpose of $\boldsymbol{A}$	$\lvert\boldsymbol{A}\rvert$	$\sqrt{\mathrm{tr}(\boldsymbol{A}^T\boldsymbol{A})}$
$(\boldsymbol{A})^{-1}$	Inverse of $\boldsymbol{A}$	$(*)_n$	Quantity from last converged time step
$\mathrm{tr}(\boldsymbol{A})$	Trace of $\boldsymbol{A}$	$\bar{(*)}$	Quantity in the reference configuration
$\det(\boldsymbol{A})$	Determinant of $\boldsymbol{A}$		

4.3.1 Kinematics

In line with Reuvers et al. [2024a], the deformation gradient $\boldsymbol{F}$ is split into an elastic ($\boldsymbol{F}_{e1}$) and plastic ($\boldsymbol{F}_p$) (see e.g. Eckart [1948]; Kröner [1959]; Lee [1969]) as well as an elastic ($\boldsymbol{F}_{e2}$) and a viscous ($\boldsymbol{F}_v$) part (see e.g. Sidoroff [1974]; Lubliner [1985]; Lion [1997a]; Reese and Govindjee [1998])

$$\boldsymbol{F} = \boldsymbol{F}_{e1}\,\boldsymbol{F}_p \;= \boldsymbol{F}_{e2}\,\boldsymbol{F}_v \tag{4.1}$$

to account for the visco-elastic, elasto-plastic material behavior of the polymeric matrix. An additional split of the plastic deformation gradient $\boldsymbol{F}_p = \boldsymbol{F}_{pe}\,\boldsymbol{F}_{pi}$ according to e.g. Lion [2000]; Dettmer and Reese [2004] is introduced to model nonlinear kinematic hardening. Thus, the following local intermediate configurations ic_1, ic_1^i and ic_2 are introduced (cf. Fig. 4.1).

4.3.2 Helmholtz free energy

The total Helmholtz free energy is expressed in terms of the right Cauchy-Green tensor $\boldsymbol{C} = \boldsymbol{F}^T\boldsymbol{F}$ and the elastic right Cauchy-Green like tensors of the intermediate configurations as

$$\begin{aligned}
\boldsymbol{C}_{e1} &= \boldsymbol{F}_{e1}^T\,\boldsymbol{F}_{e1} = \boldsymbol{F}_p^{-T}\,\boldsymbol{C}\,\boldsymbol{F}_p^{-1}, \quad \boldsymbol{C}_{pe} = \boldsymbol{F}_{pe}^T\,\boldsymbol{F}_{pe} = \boldsymbol{F}_{pi}^{-T}\,\boldsymbol{C}_p\,\boldsymbol{F}_{pi}^{-1}, \\
\boldsymbol{C}_{e2} &= \boldsymbol{F}_{e2}^T\,\boldsymbol{F}_{e2} = \boldsymbol{F}_v^{-T}\,\boldsymbol{C}\,\boldsymbol{F}_v^{-1},
\end{aligned} \tag{4.2}$$

where $\boldsymbol{C}_p = \boldsymbol{F}_p^T\boldsymbol{F}_p$ denotes the plastic right Cauchy-Green tensor. To consider the fiber induced anisotropy resulting in transversely isotropic material behavior, a structural tensor

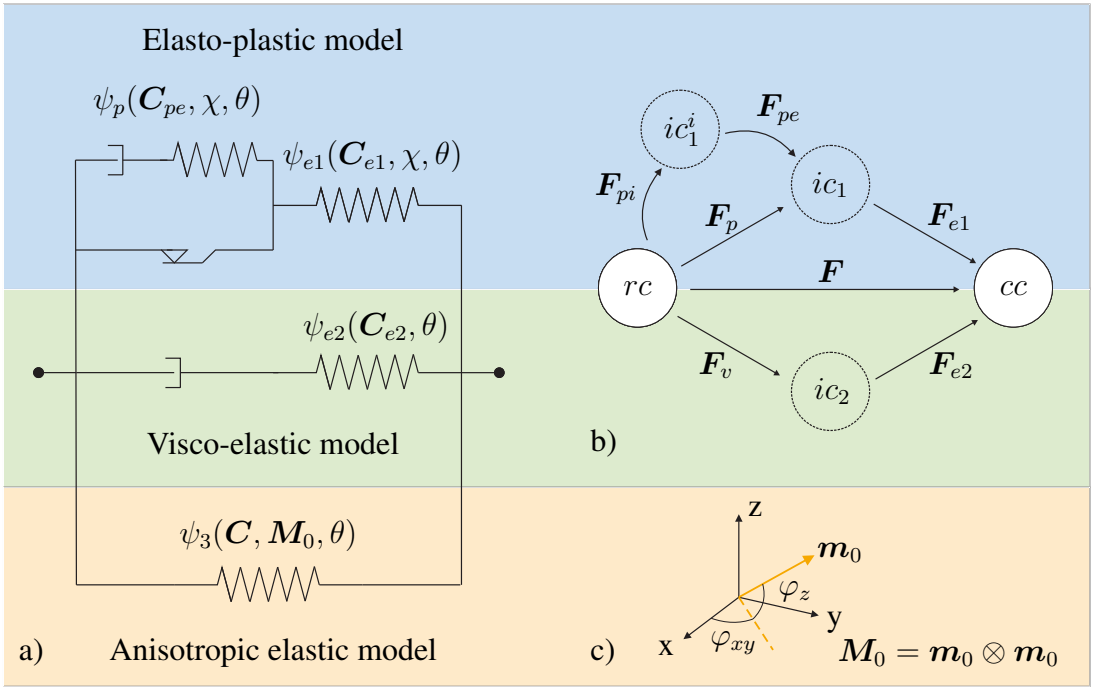

Figure 4.1: a) Schematic illustration of the constitutive model, b) Multiplicative splits of the deformation gradient (rc-reference and cc-current configuration), c) Definition of the structural tensor $\boldsymbol{M}_0$ in the reference configuration.

$\boldsymbol{M}_0 = \boldsymbol{m}_0 \otimes \boldsymbol{m}_0$ is introduced in the reference configuration. Here, $\boldsymbol{m}_0$ denotes a first order tensor oriented in the direction of the fibers as

$$\boldsymbol{m}_0 = \big(\cos(\varphi_{xy})\cos(\varphi_z)\big)\boldsymbol{e}_1 + \big(\sin(\varphi_{xy})\cos(\varphi_z)\big)\boldsymbol{e}_2 + \big(\sin(\varphi_z)\big)\boldsymbol{e}_3, \tag{4.3}$$

with the fiber angles φ_{xy} and φ_z according to Fig. 4.1 c. Consequently, two additional invariants (Eq. 4.5) are defined (see e.g. Spencer [1971]; Reese [2003*b*]; Holthusen et al. [2020]) that extend the set of the conventional ones (Eq. 4.4)

$$I_1 = \mathrm{tr}(\boldsymbol{C}), \quad I_2 = \frac{1}{2}\big(\mathrm{tr}(\boldsymbol{C})^2 - \mathrm{tr}(\boldsymbol{C}^2)\big), \quad I_3 = \det(\boldsymbol{C}) \tag{4.4}$$

$$I_4 = \mathrm{tr}(\boldsymbol{C}\boldsymbol{M}_0) = \lambda_F^2, \quad I_5 = \mathrm{tr}(\boldsymbol{C}^2\boldsymbol{M}_0). \tag{4.5}$$

Please note that $\boldsymbol{M}_0 = \boldsymbol{M}_0^2$ holds, therefore no further invariants depending on $\boldsymbol{M}_0^2$ need to be considered. Here, the fourth invariant can be interpreted as the squared stretch in fiber direction λ_F^2. In line with Fig. 4.1 and the assumption of two independent processes (I Thermo-chemical crystallization of the polymer melt and II Thermo-mechanical composite

behavior), the Helmholtz free energy is defined as an additive decomposition

$$\text{I} \qquad \psi(\chi,\theta) = \psi_\chi(\chi,\theta) + \psi_c(\theta), \tag{4.6}$$

$$\begin{aligned}\text{II} \qquad \psi(\boldsymbol{C},\boldsymbol{C}_{e1},\boldsymbol{C}_{e2},\boldsymbol{C}_{pe},\chi,\theta,\boldsymbol{M}_0) = \psi_1(\boldsymbol{C}_{e1},\boldsymbol{C}_{pe},\chi,\theta) + \psi_2(\boldsymbol{C}_{e2},\theta) \\ + \psi_3(I_1,I_4,I_5,\boldsymbol{M}_0,\theta) + \psi_c(\theta),\end{aligned} \tag{4.7}$$

whith the chemical potential ψ_χ depending on the absolute degree of crystallinity χ. Here, ψ_1 and ψ_2 denote the elasto-plastic and visco-elastic energetic contributions, respectively, and ψ_3 incorporates the fiber induced anisotropy. The elasto-plastic energetic part, ψ_1 is further decomposed into an elastic ψ_{e1} and a plastic ψ_p part

$$\psi_1(\boldsymbol{C}_{e1},\boldsymbol{C}_{pe},\chi,\theta) = \psi_{e1}(\boldsymbol{C}_{e1},\chi,\theta) + \psi_p(\boldsymbol{C}_{pe},\chi,\theta), \tag{4.8}$$

depending on the constant absolute DOC χ. Finally, an unspecified caloric part ψ_c is added to both state potentials in order to ensure flexibility regarding the choice of the function for the heat capacity c_T (cf. Felder et al. [2022]; Reuvers et al. [2024a]). As indicated in Eq. 4.6 and 4.7, all energetic contributions jointly depend on the temperature θ. It should be noted that the free energy of crystallization is related solely to the polymeric matrix material, as the fibers are not subjected to the formation of crystalline structures and remain unaltered throughout the process. Although, several contributions in the literature report the fibers as nucleation agents (see e.g. Klein et al. [1995]; Manchado et al. [2000]), DSC tests on fiber-reinforced and pure polyamide 6 samples did not support these findings. Thus, the influence of the reinforcement on the crystallization is neglected.

4.3.3 Second law of thermodynamics: Clausius-Duhem inequality

In order to derive thermodynamically consistent constitutive equations, the local form of the Clausius-Duhem inequality with respect to the reference configuration

$$\text{I} \qquad -\rho_0(\dot{\psi} + \eta\,\dot{\theta}) - \frac{1}{\theta}\,\boldsymbol{q}_0 \cdot \text{Grad}(\theta) \geq 0, \tag{4.9}$$

$$\text{II} \qquad \boldsymbol{S} : \frac{1}{2}\,\dot{\boldsymbol{C}} - \rho_0(\dot{\psi} + \eta\,\dot{\theta}) - \frac{1}{\theta}\,\boldsymbol{q}_0 \cdot \text{Grad}(\theta) \geq 0, \tag{4.10}$$

is evaluated separately for the two processes. Here, the second Piola-Kirchhoff stress tensor $\boldsymbol{S}$ is introduced along with the entropy η as well as the material density per unit reference volume ρ_0 and the heat flux in the reference configuration $\boldsymbol{q}_0$. Inserting the time derivative of Eq. 4.6

and 4.7 in Eq. 4.9 and 4.10, respectively, yields

$$\text{I} \qquad -\rho_0\left(\frac{\partial\psi}{\partial\theta}+\eta\right)\dot{\theta}-\rho_0\frac{\partial\psi}{\partial\chi}\,\dot{\chi}-\frac{1}{\theta}\,\boldsymbol{q}_0\cdot\text{Grad}(\theta)\geq 0, \tag{4.11}$$

$$\begin{aligned}\text{II} \qquad & \boldsymbol{S}:\frac{1}{2}\,\dot{\boldsymbol{C}}-\rho_0\left(\frac{\partial\psi}{\partial\boldsymbol{C}_{e1}}:\dot{\boldsymbol{C}}_{e1}+\frac{\partial\psi}{\partial\boldsymbol{C}_{pe}}:\dot{\boldsymbol{C}}_{pe}+\frac{\partial\psi}{\partial\boldsymbol{C}_{e2}}:\dot{\boldsymbol{C}}_{e2}\right)\\ & -\rho_0\left(\frac{\partial\psi}{\partial I_1}\frac{\partial I_1}{\partial\boldsymbol{C}}+\frac{\partial\psi}{\partial I_4}\frac{\partial I_4}{\partial\boldsymbol{C}}+\frac{\partial\psi}{\partial I_5}\frac{\partial I_5}{\partial\boldsymbol{C}}\right):\dot{\boldsymbol{C}}-\rho_0\left(\frac{\partial\psi}{\partial\theta}+\eta\right)\dot{\theta}-\frac{1}{\theta}\,\boldsymbol{q}_0\cdot\text{Grad}(\theta)\geq 0.\end{aligned} \tag{4.12}$$

After a series of mathematical operations (cf. Reuvers et al. [2024a]), Eq. 4.12 is reformulated and the following stress quantities are introduced for the thermo-mechanically coupled process II. The second Piola-Kirchhoff stress $\boldsymbol{S}_1$ and the Mandel stress $\boldsymbol{M}_1$ corresponding to the elasto-plastic part are defined as

$$\boldsymbol{S}_1=2\rho_0\boldsymbol{F}_p^{-1}\,\frac{\partial\psi_{e1}}{\partial\boldsymbol{C}_{e1}}\,\boldsymbol{F}_p^{-T},\quad \boldsymbol{M}_1=2\rho_0\boldsymbol{C}_{e1}\,\frac{\partial\psi_{e1}}{\partial\boldsymbol{C}_{e1}}, \tag{4.13}$$

together with the back stress $\boldsymbol{X}$ related to kinematic hardening and the Mandel stress $\boldsymbol{M}_{1,\text{kin}}$ corresponding to kinematic hardening

$$\boldsymbol{X}=2\rho_0\,\boldsymbol{F}_{pe}\,\frac{\partial\psi_p}{\partial\boldsymbol{C}_{pe}}\,\boldsymbol{F}_{pe}^{T},\quad \boldsymbol{M}_{1,\text{kin}}=2\rho_0\,\boldsymbol{C}_{pe}\frac{\partial\psi_p}{\partial\boldsymbol{C}_{pe}}. \tag{4.14}$$

Similarly, the second Piola-Kirchhoff stress $\boldsymbol{S}_2$ and the Mandel stress $\boldsymbol{M}_2$ related to the visco-elastic part follow to

$$\boldsymbol{S}_2=2\rho_0\boldsymbol{F}_v^{-1}\,\frac{\partial\psi_2}{\partial\boldsymbol{C}_{e2}}\,\boldsymbol{F}_v^{-T},\quad \boldsymbol{M}_2=2\rho_0\boldsymbol{C}_{e2}\,\frac{\partial\psi_2}{\partial\boldsymbol{C}_{e2}}. \tag{4.15}$$

Lastly, the second Piola-Kirchhoff stress tensor $\boldsymbol{S}_3$ incorporating the fiber induced anisotropy is defined as

$$\boldsymbol{S}_3=2\rho_0\left(\frac{\partial\psi_3}{\partial I_1}\,\boldsymbol{I}+\frac{\partial\psi_3}{\partial I_4}\,\boldsymbol{M}_0+\frac{\partial\psi_3}{\partial I_5}\,(\boldsymbol{C}\boldsymbol{M}_0+\boldsymbol{M}_0\boldsymbol{C})\right). \tag{4.16}$$

Here, the partial derivatives of the invariants are already evaluated. Since the Clausius-Duhem inequality must hold for arbitrary processes, the total second Piola-Kirchhoff stress tensor $\boldsymbol{S}$ and the entropy are chosen following the Coleman-Noll procedure (Coleman and Noll [1961]) as

$$\boldsymbol{S}=\boldsymbol{S}_1+\boldsymbol{S}_2+\boldsymbol{S}_3,\quad \eta=-\partial\psi/\partial\theta. \tag{4.17}$$

Moreover, the heat flux in the reference configuration is introduced according to Duhamel's law as

$$\boldsymbol{q}_0 = -\boldsymbol{\kappa}_0 \operatorname{Grad}(\theta), \tag{4.18}$$

where the thermal conductivity tensor $\boldsymbol{\kappa}_0$ is defined according to Al-Kinani [2014] as

$$\boldsymbol{\kappa}_0 = J \left(I_4^{-1} \left(\lambda_{T,f} - \lambda_{T,n} \right) \boldsymbol{M}_0 + \lambda_{T,n} \boldsymbol{C}^{-1} \right). \tag{4.19}$$

Here, $J = \det(\boldsymbol{F})$ and the thermal conductivities $\lambda_{T,f}$ and $\lambda_{T,n}$ along the fiber direction and normal to it are introduced as positive scalar quantities. For glass fiber reinforced polyamide 6 $\lambda_{T,f} > \lambda_{T,n}$ holds. Consequently, $\boldsymbol{\kappa}_0$ is positive definite, fulfilling the entropy inequality. For a more detailed derivation of the transverse isotropic heat flux, the reader is kindly referred to Appendix 4.7.1. Inserting the relations from Eqs. 4.17 and 4.18 into Eq. 4.11 and Eqs. 4.13 to 4.18 back into Eq. 4.12 leads to the reduced forms of the dissipation inequality

$$\text{I} \qquad -\rho_0 \frac{\partial \psi}{\partial \chi} \dot{\chi} \geq 0, \tag{4.20}$$

$$\text{II} \qquad (\boldsymbol{M}_1 - \boldsymbol{X}) : \boldsymbol{D}_p + \boldsymbol{M}_{1,\text{kin}} : \boldsymbol{D}_{pi} + \boldsymbol{M}_2 : \boldsymbol{D}_v \geq 0, \tag{4.21}$$

where $\boldsymbol{D}_{(*)} = \operatorname{sym}(\boldsymbol{L}_{(*)})$ denotes the symmetric part of the corresponding velocity gradient $\boldsymbol{L}_{(*)} = \dot{\boldsymbol{F}}_{(*)} \boldsymbol{F}_{(*)}^{-1}$ with $(*) = \{p, pi, v\}$.

4.3.4 Evolution equations

To ensure positive internal dissipation, a set of evolution equations is chosen, which fulfills the remaining dissipation inequality in Eqs. 4.20 and 4.21.

4.3.4.1 Non-isothermal crystallization kinetics (I)

The evolution equation for the non-isothermal crystallization kinetics is derived from the experimentally determined relative degree of crystallinity

$$\chi_c(t) = \frac{\int_{t_{\text{on}}}^{t} \dot{h}(t) \mathrm{dt}}{\Delta h_m} \tag{4.22}$$

that lies between zero (fully amorphous state) and one (end of the crystallization process) for any arbitrary time step. The change in the specific enthalpy Δh_m is obtained by integrating the specific heat flux curve $\dot{h}(t)$ from differential scanning calorimetry (DSC) results inbetween the onset t_{on} and end t_{end} time of the crystallization process. Relating the specific enthalpy at

time t to the specific fusion enthalpy of a 100% crystalline material Δh_0^{100}, yields the absolute degree of crystallinity

$$\chi(t) = \frac{\int_{t_{\text{on}}}^{t} \dot{h}(t)\text{dt}}{\Delta h_0^{100}} = \chi_c(t)\,\frac{\Delta h_m}{\Delta h_0^{100}}. \tag{4.23}$$

Here, the value of $\Delta h_0^{100} = 190$ J/g is adopted from Campoy et al. [1998]. Numerically, in the present work, the relative degree of crystallinity is approximated by means of the modified Nakamura-Ziabicki model (cf. Nakamura et al. [1973]; Ziabicki [1976])

$$\chi_c = 1 - \exp\left(-\int_t K_c\,dt\right)^{n_A} \tag{4.24}$$

based on the well-known Avrami equation (see Avrami [1939, 1940] and Appendix 4.7.2) with the Avrami index n_A and an empirical function for the crystal growth rate

$$K_c = K_{max}\exp\left(-\frac{4\ln(2)\,(\theta-\theta_{max})^2}{D^2}\right). \tag{4.25}$$

All three material parameters K_{max}, θ_{max} and D are directly related to the results of the DSC analysis (cf. Kulkarni et al. [2023]). Finally, the relation for the evolution of the absolute degree of crystallinity is obtained by the time derivative of Eq. 4.23 together with Eqs. 4.24 and 4.25

$$\dot{\chi} = n_A\,K_c(1-\chi_c)\left(\int_{t_{\text{on}}}^{t} K_c\,dt\right)^{n_A-1}\frac{\Delta h_m}{\Delta h_f^{100}}. \tag{4.26}$$

4.3.4.2 Thermo-mechanical composite behavior (II)

For the elasto-plastic part, a Tschoegl-type yield criterion (see e.g. Tschoegl [1971]; Ghorbel [2008]; Melro et al. [2013*b*]) is adopted

$$\Phi_p = 3J_{2,p} + (m-1)\,\sigma_t^0 I_{1,p} - m\,(\sigma_t^0)^2 \leq 0, \tag{4.27}$$

using the first ($I_{1,p} = \text{tr}(\boldsymbol{\Sigma})$) and second ($J_{2,p} = 1/2\,\text{tr}((\text{dev}(\boldsymbol{\Sigma}))^2)$) invariant of the relative stress $\boldsymbol{\Sigma} = \boldsymbol{M}_1 - \boldsymbol{X}$. Here, the ratio $m = \sigma_c^0(\chi,\theta)/\sigma_t^0(\chi,\theta)$ between the initial yield stress in compression σ_c^0 and tension σ_t^0 introduces a tension-compression flow asymmetry known for polymeric materials (Ghorbel [2008]). Under the assumption of associative plasticity, the plastic flow rule and the evolution equation for modeling nonlinear Armstrong-Frederick

kinematic hardening (Armstrong et al. [1966]) follow to

$$\boldsymbol{D}_p = \dot{\lambda}_p \frac{\partial \Phi_p}{\partial \boldsymbol{\Sigma}} = \dot{\lambda}_p \left(3\,\mathrm{dev}(\boldsymbol{\Sigma}) + (m-1)\,\sigma_t^0\,\boldsymbol{I} \right), \quad \boldsymbol{D}_{pi} = \dot{\lambda}_p \frac{b}{c}\,\mathrm{dev}(\boldsymbol{M}_{1,\mathrm{kin}}), \tag{4.28}$$

with the plastic multiplier $\dot{\lambda}_p$ and the material parameters $b(\chi,\theta)$ and $c(\chi,\theta)$ depending on the DOC and the temperature. To conclude the set of elasto-plastic evolution equations, the Karush-Kuhn-Tucker conditions $\dot{\lambda}_p \geq 0$, $\Phi_p \leq 0$, $\dot{\lambda}_p\,\Phi_p = 0$ are introduced. Subsequently, the evolution of the visco-elastic part is chosen from Reese and Govindjee [1998] as

$$\boldsymbol{D}_v = \frac{1}{2\tau\mu_2}\,\mathrm{dev}(\boldsymbol{M}_2) + \frac{1}{9\tau K_2}\,\mathrm{tr}(\boldsymbol{M}_2)\,\boldsymbol{I}, \tag{4.29}$$

where $K_2(\theta)$ and $\mu_2(\theta)$ denote the temperature-dependent bulk[1] and shear moduli, related to the material stiffness by the Lamé constants. The relaxation time τ is chosen as a nonlinear function

$$\tau = \tau_0\,|\boldsymbol{B}_v|^{\gamma}\exp(-\delta\,|\boldsymbol{\tau}_2|) \tag{4.30}$$

of the norm of the viscous left Cauchy-Green tensor $\boldsymbol{B}_v = \boldsymbol{F}_v\boldsymbol{F}_v^T$ as well as of the viscous Kirchhoff stress $\boldsymbol{\tau}_2$ based on an experimental post-processing scheme by Amin et al. [2006], exploited in Reuvers et al. [2024a]. In Eq. 4.30, the temperature-dependent material parameters $\tau_0(\theta), \gamma(\theta)$ and $\delta(\theta)$ are introduced.

4.3.5 First law of thermodynamics: energy balance

The heat generation due to the exothermic crystallization process, elastic, viscous and plastic effects are derived from the local form of the energy balance in the reference configuration

$$\text{I} \qquad \rho_0\,(\dot{\psi} + \dot{\eta}\,\theta + \eta\,\dot{\theta}) + \mathrm{Div}(\boldsymbol{q}_0) = 0, \tag{4.31}$$

$$\text{II} \qquad \rho_0\,(\dot{\psi} + \dot{\eta}\,\theta + \eta\,\dot{\theta}) + \mathrm{Div}(\boldsymbol{q}_0) - \boldsymbol{S} : \frac{1}{2}\,\dot{\boldsymbol{C}} = 0. \tag{4.32}$$

Here, the time derivative of the internal energy $\dot{e} = \dot{\psi} + \dot{\eta}\,\theta + \eta\,\dot{\theta}$ with the entropy rate as $\dot{\eta} = -\partial\dot{\psi}/\partial\theta$ is already included. Analogously to Sec. 4.3.3, several mathematical operations are utilized to reformulate Eqs. 4.31 and 4.32 in order to derive the corresponding expressions

[1] The bulk moduli $K_*, * = \{1,2\}$ are defined by the two Lamé constants μ_* and Λ_* as $K_* = \Lambda_* + \frac{2\mu_*}{3}$.

for the temperature field

$$\text{I} \qquad \rho_0 c_T \dot{\theta} = r_\chi - \text{Div}(\boldsymbol{q}_0), \tag{4.33}$$

$$\text{II} \qquad \rho_0 \, c_T \, \dot{\theta} = r_e + r_p + r_v - \text{Div}(\boldsymbol{q}_0). \tag{4.34}$$

Here, the following abbreviations for heat generated due to the formation of crystals r_χ, the elastic r_e, plastic r_p and viscous r_v heat generation terms

$$\text{I} \quad r_\chi = \rho_0 \left(-\frac{\partial \psi}{\partial \chi} + \theta \, \frac{\partial^2 \psi}{\partial \theta} \right) \dot{\chi} \tag{4.35}$$

$$\text{II} \quad r_e = \theta \left(\frac{\partial \boldsymbol{S}_1}{\partial \theta} + \frac{\partial \boldsymbol{S}_2}{\partial \theta} + \frac{\partial \boldsymbol{S}_3}{\partial \theta} \right) : \frac{1}{2} \, \dot{\boldsymbol{C}} \tag{4.36}$$

$$\text{II} \quad r_p = \left(\boldsymbol{M}_1 - \theta \, \frac{\partial \boldsymbol{M}_1}{\partial \theta} \right) : \boldsymbol{D}_p - \left(\boldsymbol{X} - \theta \, \frac{\partial \boldsymbol{X}}{\partial \theta} \right) : \boldsymbol{D}_p + \left(\boldsymbol{M}_{1,\text{kin}} - \theta \, \frac{\partial \boldsymbol{M}_{1,\text{kin}}}{\partial \theta} \right) : \boldsymbol{D}_{pi} \tag{4.37}$$

$$\text{II} \quad r_v = \left(\boldsymbol{M}_2 - \theta \, \frac{\partial \boldsymbol{M}_2}{\partial \theta} \right) : \boldsymbol{D}_v \tag{4.38}$$

are introduced and the heat flux is defined according to Eq. 4.18. Noteworthy, anisotropic elastic heat generation follows naturally from the anisotropic definition of the stress in Eq. 4.16. Furthermore, the specific heat capacity is introduced as

$$c_T = -\theta \, \frac{\partial^2 \psi}{\partial \theta^2}. \tag{4.39}$$

In line with e.g. Felder et al. [2020b, 2022]; Reuvers et al. [2024a], in the following the heat capacity is approximated by a constant value $c_T = c_T(\chi, \theta)$.

4.3.6 Specific energy choice

The authors would like to note that the prior derivation was performed in a general manner to allow for flexibility regarding the specific choice of the energy terms in order to account for a multitude of unidirectional reinforced composite materials. In order to conclude the constitutive framework, a set of energies is chosen that is suitable for modeling glass fiber reinforced polyamide 6.

4.3.6.1 Free energy related to crystallization (I)

The free energy related to the crystallization process is chosen as

$$\psi_\chi = \frac{\rho_{0,m}}{\rho_0} \Delta h_f^{100} \, \frac{\theta - \theta_{\text{on}}}{\theta_{\text{on}}} \chi, \tag{4.40}$$

in line with Kulkarni et al. [2023]; Felder et al. [2020b]; Kelly et al. [2016]. Here, the phase transformation from the purely amorphous melt is initiated as soon as the onset temperature is reached ($\theta \leq \theta_{on}$) and the corresponding free energy becomes negative (see e.g. Turnbull and Fisher [1949]; Mandelkern et al. [1954]). Thus, the temperature ratio $(\theta - \theta_{\text{on}})/\theta_{\text{on}}$ essentially serves as a switch. Moreover, the ratio between the density of the polymeric matrix $\rho_{0,m}$ and the density of the composite ρ_0 is introduced. Now, using Eq. 4.23 together with Eq. 4.40, a relation between the heat signal obtained through the DSC experiments per unit time and reference volume and the heat source $r_\chi = \rho_{m,0} \, \Delta h_f^{100} \, \dot{\chi} = \rho_{m,0} \, \dot{h}$ is found according to Zinet et al. [2010]; Kugele et al. [2017].

4.3.6.2 Free energies related to the thermo-mechanical composite behavior (II)

With regard to the elasto-plastic part, a compressible Neo-Hookean-type energy with an additional term for isotropic volumetric thermal expansion is chosen for ψ_{e1} alongside a nonlinear plastic defect energy ψ_p to model Armstrong-Frederick kinematic hardening

$$\begin{aligned} \psi_{e1} = \; & \frac{\mu_1}{2} \left(\text{tr}(\boldsymbol{C}_{e1}) - 3\right) - \mu_1 \ln\left(J_{e1}\right) + \frac{\Lambda_1}{4} \left(\det(\boldsymbol{C}_{e1}) - 1 - 2\ln(J_{e1})\right) \\ & - 3\, K_1 \alpha_{T,n} \left(\theta - \theta_0\right) \ln(J_{e1}), \end{aligned} \tag{4.41}$$

$$\psi_p = \frac{c}{2} \left(\text{tr}(\boldsymbol{C}_{pe}) - 3\right) - c \ln(\sqrt{\det(\boldsymbol{C}_{pe})}). \tag{4.42}$$

Here, $J_{e1} = \det(\boldsymbol{F}_{e1})$ is the determinant of the elastic part of the deformation gradient. Besides, the two Lamé constants $\mu_1(\chi, \theta)$ and $\Lambda_1(\chi, \theta)$, the elasto-plastic bulk modulus K_1 and the thermal expansion coefficient $\alpha_{T,n}$ perpendicular to the fiber direction are introduced as material quantities. Furthermore, $c(\chi, \theta)$ and the dimensionless parameter $b(\chi, \theta)$ the latter of which only shows up in the evolution equation (cf. Eq. 4.28) are the material parameters related to nonlinear kinematic hardening. Thus, the second Piola Kirchhoff stress $\boldsymbol{S}_1$ as well as the thermodynamic conjugate force of kinematic hardening in the reference configuration

follow to

$$\boldsymbol{S}_1 = \mu_1(\boldsymbol{C}_p^{-1} - \boldsymbol{C}^{-1}) + \frac{\Lambda_1}{2}\left(\frac{\det(\boldsymbol{C})}{\det(\boldsymbol{C}_p)} - 1\right)\boldsymbol{C}^{-1} - 3K_1\alpha_{T,n}(\theta - \theta_0)\boldsymbol{C}^{-1} \tag{4.43}$$

$$\bar{\boldsymbol{X}} = c\,(\boldsymbol{C}_{pi}^{-1} - \boldsymbol{C}_p^{-1}). \tag{4.44}$$

For the visco-elastic part, the energy ψ_{e2} is defined as a compressible Neo-Hookean-type energy as well, extended with a thermal expansion term

$$\begin{aligned}\psi_2 = {} & \frac{\mu_2}{2}\left(\mathrm{tr}(\boldsymbol{C}_{e2}) - 3\right) - \mu_2 \ln(J_{e2}) + \frac{\Lambda_2}{4}\left(\det(\boldsymbol{C}_{e2}) - 1 - 2\ln(J_{e2})\right) \\ & - 3\,K_2\alpha_{T,n}(\theta - \theta_0)\ln(J_{e2}),\end{aligned} \tag{4.45}$$

where $\mu_2(\theta)$ and $\Lambda_2(\theta)$ are the viscous Lamé constants, K_2 the visco-elastic bulk modulus and $J_{e2} = \det(\boldsymbol{F}_{e2})$ holds. Hence, the viscous second Piola Kirchhoff stress follows to

$$\boldsymbol{S}_2 = \mu_2(\boldsymbol{C}_v^{-1} - \boldsymbol{C}^{-1}) + \frac{\Lambda_2}{2}\left(\frac{\det(\boldsymbol{C})}{\det(\boldsymbol{C}_v)} - 1\right)\boldsymbol{C}^{-1} - 3K_2\alpha_{T,n}\,(\theta - \theta_0)\,\boldsymbol{C}^{-1}. \tag{4.46}$$

Lastly, the energy related to the anisotropic contribution of the fibers is chosen as

$$\begin{aligned}\psi_3 = {} & \frac{1}{\alpha}\,K_{ani1}\,(I_4 - 1)^{\alpha} + \frac{1}{\beta}\,K_{ani2}\,(I_5 - 1)^{\beta} + \frac{1}{\zeta}\,K_{coup}\,(I_1 - 3)^{\zeta}(I_4 - 1)^{\zeta} \\ & - K_{therm}\,(\alpha_{T,f} - \alpha_{T,n})\,(\theta - \theta_0)\,\sqrt{I_4},\end{aligned} \tag{4.47}$$

with the stiffness-like material parameters K_{ani1}, K_{ani2}, K_{coup} and K_{therm}, the exponents α, β and ζ as well as the thermal expansion coefficient in fiber direction $\alpha_{T,f}$. The mechanical part of the anisotropic energy ψ_3 is chosen based on Reese et al. [2001]; Holthusen et al. [2020], whereas the term related to anisotropic thermal expansion is newly introduced by the authors. Note here that in order to ensure a stress-free state for $\boldsymbol{C} = \boldsymbol{I}$ and $\theta = \theta_0$, it is necessary that the exponents are selected to $\alpha, \beta, \zeta \geq 2$ (see e.g. Holthusen et al. [2020]). In contrast to Eqs. 4.41 and 4.45, where a volumetric thermal expansion was introduced, the expansion term of the anisotropic energy part ψ_3 is chosen depending on the stretch in fiber direction $\lambda_F = \sqrt{I_4}$ via the invariant I_4. Thus, the resulting thermal expansion from Eq. 4.47 occurs solely in fiber direction. The total anisotropic volume-temperature relation can be calculated from Eq. 4.17 and is similar to the one by Al-Kinani [2014], who initially proposed the concept of transversely isotropic thermal expansion in the context of a split of the deformation gradient into a thermal and mechanical part. In this work, however, the deformation gradient $\boldsymbol{F}$ and the temperature θ are introduced as individual and independent state variables. Consequently, the

Helmholtz free energy is chosen based on a generalized approach, where the twice integrated specific heat capacity is the starting point. This well-known approach has been developed for isotropic thermo-elastic rubberlike materials in Chadwick [1974] and was extended to isotropic thermo-viscoelastic materials in Reese [2003*a*]. In Chadwick [1974], two physically motivated assumptions are introduced that result in restrictions for the choice of the free energy density. Both criteria were adopted for the extension of the theory to anisotropic thermo-elastic material behavior in Eq. 4.47. Although, in this case, the postulated volume-temperature relation reduces to a stretch-temperature relation through the fourth invariant to introduce transverse anisotropy. Since the corresponding expansion term is invented by the authors and the concept of anisotropic thermo-elasticity has not been discussed in detail in the literature yet, a detailed numerical investigation is performed in Sec. 4.5. Finally, following, Eq. 4.47, the second Piola Kirchhoff stress tensor $\boldsymbol{S}_3$ incorporating the fiber induced anisotropy takes the form

$$\begin{aligned}\boldsymbol{S}_3 =& K_{ani1}\,(I_4-1)^{\alpha-1}\boldsymbol{M}_0 + K_{ani2}\,(I_5-1)^{\beta-1}(\boldsymbol{C}\boldsymbol{M}_0+\boldsymbol{M}_0\boldsymbol{C})\\ &+ K_{coup}\,(I_1-3)^{\zeta-1}(I_4-1)^{\zeta}\boldsymbol{I} + K_{coup}\,(I_1-3)^{\zeta}(I_4-1)^{\zeta-1}\boldsymbol{M}_0\\ &- \frac{1}{2}\,K_{therm}\,(\alpha_{T,f}-\alpha_{T,n})\,(\theta-\theta_0)\,(\sqrt{I_4})^{-1}\,\boldsymbol{M}_0.\end{aligned} \tag{4.48}$$

Note on thermodynamic consistency and algorithmic treatment

For the proof of thermodynamic consistency and the numerical implementation into an Abaqus mechanical (UMAT) and thermal (UMATHT) user material subroutine exploiting an exponential mapping algorithm for the thermo-mechanical process, the reader is kindly referred to Reuvers et al. [2024a], where the model formulation for the polymeric matrix material was derived in detail. Note here that the automatic differentiation tool *AceGen* Korelc [2009] was used to obtain the material sensitivities. The extension to a transversely isotropic material formulation for modeling unidirectional fiber-reinforced polymers through the addition of an elastic energy $\psi_3(\boldsymbol{C}, \boldsymbol{M}_0, \theta)$ a priori fulfills the second law of thermodynamics as shown in Eq. 4.17. Moreover, the thermodynamic consistency of the transversely isotropic heat flux $\boldsymbol{q}_0$ was ensured by a suitable choice for the thermal conductivity tensor $\boldsymbol{\kappa}_0$ in Eq. 4.19 in the Appendix. Consequently, the extended model formulation satisfies the entropy inequality principle. The pull-back of the model equations allows the application of the exponential map algorithm which automatically preserves the symmetry of the internal variables and the material's incompressibility (cf. Vladimirov et al. [2008]). Hence, only the quantities with respect to the reference configuration are derived from the specific choice of the Helmholtz free

Elasto-plastic contribution	Visco-elastic contribution	Anisotropic elastic contribution
Stresses $\boldsymbol{S}_1 = \mu_1(\boldsymbol{C}_p^{-1} - \boldsymbol{C}^{-1}) + \frac{\Lambda_1}{2}\left(\frac{\det(\boldsymbol{C})}{\det(\boldsymbol{C}_p)} - 1\right)\boldsymbol{C}^{-1}$ $-3K_1\alpha_{T,n}(\theta - \theta_0)\boldsymbol{C}^{-1}$ $\bar{\boldsymbol{X}} = c\,(\boldsymbol{C}_{pi}^{-1} - \boldsymbol{C}_p^{-1})$ $\boldsymbol{Y} = \boldsymbol{C}\boldsymbol{S}_1 - \boldsymbol{C}_p\bar{\boldsymbol{X}}, \quad \boldsymbol{Y}_{\text{kin}} = \boldsymbol{C}_p\bar{\boldsymbol{X}}$ Yield function $\Phi_p = 3\,J_{2,p} + (m-1)\,\sigma_t^0\,I_{1,p} - m\,(\sigma_t^0)^2$ $I_{1,p} = \text{tr}(\boldsymbol{Y}), \quad J_{2,p} = \frac{1}{2}\,\text{tr}((\text{dev}(\boldsymbol{Y}))^2)$ Evolution equations $\dot{\boldsymbol{C}}_p = \dot{\lambda}_p\,(6\,\text{dev}(\boldsymbol{Y}) + 2\,(m-1)\,\sigma_t^0)\,\boldsymbol{C}_p,$ $\dot{\boldsymbol{C}}_{pi} = 2\,\dot{\lambda}_p\,\frac{b}{c}\,\text{dev}(\boldsymbol{Y}_{\text{kin}})\,\boldsymbol{C}_{pi}$ Heat generation due to plastic dissipation $r_1 = \bar{r}_p = \frac{1}{2}\,\boldsymbol{C}\left(\boldsymbol{S}_1 - \theta\,\frac{\partial \boldsymbol{S}_1}{\partial\theta}\right) : \boldsymbol{C}_p^{-1}\,\dot{\boldsymbol{C}}_p$ $-\frac{1}{2}\left(\bar{\boldsymbol{X}} - \theta\,\frac{\partial \bar{\boldsymbol{X}}}{\partial\theta}\right) : \dot{\boldsymbol{C}}_p$ $+\frac{1}{2}\,\boldsymbol{C}_p\left(\bar{\boldsymbol{X}} - \theta\,\frac{\partial \bar{\boldsymbol{X}}}{\partial\theta}\right) : \boldsymbol{C}_{pi}^{-1}\,\dot{\boldsymbol{C}}_{pi}$	Stress $\boldsymbol{S}_2 = \mu_2(\boldsymbol{C}_v^{-1} - \boldsymbol{C}^{-1}) + \frac{\Lambda_2}{2}\left(\frac{\det(\boldsymbol{C})}{\det(\boldsymbol{C}_v)} - 1\right)\boldsymbol{C}^{-1}$ $-3\,K_2\,\alpha_{T,n}\,(\theta - \theta_0)\boldsymbol{C}^{-1}$ Evolution equation $\dot{\boldsymbol{C}}_v = \left(\frac{1}{\tau\mu_2}\,\text{dev}(\boldsymbol{C}\boldsymbol{S}_2) + \frac{2}{9\tau K_2}\,\text{tr}(\boldsymbol{C}\boldsymbol{S}_2)\,\boldsymbol{I}\right)\boldsymbol{C}_v$ Heat generation due to viscous dissipation $r_2 = \bar{r}_v = \frac{1}{2}\,\boldsymbol{C}\left(\boldsymbol{S}_2 - \theta\,\frac{\partial \boldsymbol{S}_2}{\partial\theta}\right) : \boldsymbol{C}_v^{-1}\,\dot{\boldsymbol{C}}_v$	Stress $\boldsymbol{S}_3 = K_{ani1}\,(I_4 - 1)^{\alpha-1}\boldsymbol{M}_0 +$ $K_{ani2}\,(I_5 - 1)^{\beta-1}(\boldsymbol{C}\boldsymbol{M}_0 + \boldsymbol{M}_0\boldsymbol{C})$ $+K_{coup}\,(I_1 - 3)^{\zeta-1}(I_4 - 1)^{\zeta}\boldsymbol{I} +$ $K_{coup}\,(I_1 - 3)^{\zeta}(I_4 - 1)^{\zeta-1}\boldsymbol{M}_0 -$ $\frac{K_{therm}}{2}\,(\alpha_{T,f} - \alpha_{T,n})\,(\theta - \theta_0)\,\frac{\boldsymbol{M}_0}{\sqrt{I_4}}$ $I_1 = \text{tr}(\boldsymbol{C}),$ $I_4 = \text{tr}(\boldsymbol{C}\boldsymbol{M}_0), \quad I_5 = \text{tr}(\boldsymbol{C}^2\boldsymbol{M}_0)$ Structural tensor $\boldsymbol{M}_0 = \boldsymbol{m}_0 \otimes \boldsymbol{m}_0$
Second Piola-Kirchhoff stress $\boldsymbol{S} = \boldsymbol{S}_1 + \boldsymbol{S}_2 + \boldsymbol{S}_3$	Elastic heat generation $r_e = \theta\left(\frac{\partial \boldsymbol{S}_1}{\partial\theta} + \frac{\partial \boldsymbol{S}_2}{\partial\theta} + \frac{\partial \boldsymbol{S}_3}{\partial\theta}\right) : \frac{1}{2}\,\dot{\boldsymbol{C}}$	Heat flux $\boldsymbol{q}_0 = -\boldsymbol{\kappa}_0\,\text{Grad}(\theta)$ $\boldsymbol{\kappa}_0 = J\left(I_4^{-1}\,(\lambda_{T,f} - \lambda_{T,n})\,\boldsymbol{M}_0 + \lambda_{T,n}\boldsymbol{C}^{-1}\right)$

Table 4.1: Overview over the constitutive equations in the reference configuration.

energy. A comprehensive overview of the thermo-mechanical model equations in the reference configuration is provided in Tab. 4.1. For the algorithmic treatment of the crystallization process, the reader is kindly referred to Appendix 4.7.3. The thermodynamic consistency of the crystallization process is fulfilled since $\dot{\chi} \geq 0$ holds and the derivative of the energy related to crystallization ψ_χ with respect to χ is negative for $\theta < \theta_{\text{on}}$. The authors would like to kindly remind the reader that the crystallization process is by choice direction-dependent and the thermodynamic consistency only holds for the crystallization from the melt. Modeling the melting of the crystalline phase would require a fully coupled scheme that is out of the scope of this work.

4.4 Parameter identification

4.4.1 Non-isothermal crystallization kinetics (I)

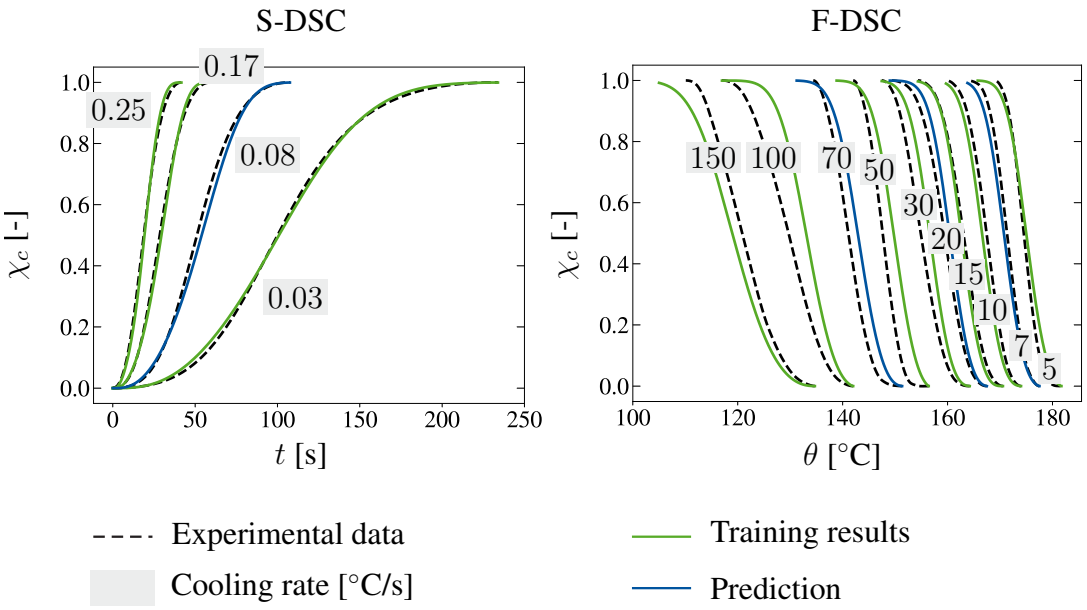

Figure 4.2: Identification results and predictions for training with S-DSC and F-DSC data.

The material parameters of the crystallization process are identified based on S-DSC and F-DSC results by Kulkarni et al. [2023] for cooling rates between 0.033 to $3000°\text{C}/\text{s}$. For more informations on the experimental procedure and an in-depth discussion of the results, the reader is kindly referred to the aforementioned literature resource. The experimentally determined enthalpy of fusion for the S-DSC and F-DSC tests can be found in Fig. 4.17 a) in the Appendix 4.7.4. It should be noted that the enthalpy of fusion for cooling rates lower than

0.25 °C/s was approximately constant, thus, the value of 57.9 J/g is adopted for all S-DSC tests. An overview of the crystallization onset temperatures θ_{on} read off from the DSC curves is presented in Fig. 4.17 b) in the Appendix. The remaining material parameters K_{max}, θ_{max}, D and n_A are determined by a neural network using a combination of feed-forward and recurrent layers in the TensorFlow environment to calculate the mean squared error (MSE) between the model and experimentally determined relative DOC. In contrast to Felder et al. [2020b]; Kulkarni et al. [2023], who determined an individual set of parameters per cooling rate, a linear cooling rate dependency of type $\langle\bullet\rangle = w_i\,\dot{\theta} + b_i$ is introduced for each material parameter in the present work. Thus, the quality of the fit is slightly compromised compared to the individual parameter sets, however, the amount of model parameters is significantly reduced. The results of the identification procedure are presented in Fig. 4.2 for the S-DSC and F-DSC tests. Here, data from cooling rates that were used for identification are shown in green, whereas previously unseen data is shown in blue. Moreover, an overview over the parameters is shown in Tab. 4.2. Note here that the constituents of the material quantities were not constrained during the training process. Thus, the resulting parameters and their trends should not be interpreted according to the physical meaning stated in for example Kugele [2020]. Rather, they should be regarded as numerical input values for an empirical function.

S-DSC	w_i	b_i	F-DSC	w_i	b_i
K_{max}	0.1159	0.005328	K_{max}	0.1123	0.0307
$\hat{D}^*$	-0.1198	0.04084	$\hat{D}^*$	2.45 10^{-6}	-0.0009
θ_{max}	-42.7741	197.5829	θ_{max}	-0.54258	166.0976
n_A	-	2.95638	n_A	-0.0053	2.9815

Table 4.2: Identification results for the modified Nakamura-Ziabicki model. The material parameters are approximated by $\langle\bullet\rangle = w_i\,\dot{\theta} + b_i$. $^*\hat{D} = -4\ln(2)/D^2$.

4.4.2 Thermo-mechanical composite behavior (II)

In order to identify the macroscopic material model from Sec. 4.3, experimental data and data generated through virtual experiments from Reuvers et al. [2024a,b] are used. In these works a data base was successively established, commencing with the derivation and experimental identification of a thermo-mechanically coupled material formulation for polyamide 6 blends in Reuvers et al. [2024a]. The model formulation was then employed on the composite's mesoscale to generate repeating unit cells (RUCs) with different randomization methods for a single material ply in Reuvers et al. [2024b]. The RUC results were validated against an experimental study on glass fiber reinforced polyamide 6. Furthermore, the RUC generated

with the random sequential adsorption (RSA) method was utilized to construct a virtual data base for the transverse isotropic composite. In this way, data was obtained for a variety of temperatures both below and above the glass transition regime, as well as for a broad range of crystallinities between 15% and 41%. In the following, the crystallinity-independent viscous parameters from Reuvers et al. [2024a] will be used during the identification process, as no supplementary relaxation tests were conducted on the composite. Moreover, the assumption of $\sigma_c^0 = \sigma_t^0$ is made, due to the lack of compression data above room temperature. The parameter K_{coup} is maintained constant during identification, as a parameter study conducted prior to model identification revealed a negligibly small influence under tension. The impact of this material quantity is more pronounced under shear states, which fall beyond the scope of this work. A nonlinear curve fitting procedure in *MATLAB* is employed to identify the remaining mechanical material parameters, specifically $E_1, E_2, \sigma_t^0, c, b, K_{ani1}$ and K_{ani2}. Therefore, the average engineering stress and strain material data of ten RUCs from Reuvers et al. [2024b] with a fiber angle of 0° and 90°, are used to calculate the mean squared error. Here, the genetic algorithm is chosen in conjunction with the Downhill-Simplex algorithm for parameter optimization. For a detailed description of the fitting procedure, the reader is kindly referred to Reuvers et al. [2024a]. Prior to model identification, a mesh convergence study is conducted up to 5% strain for monotonic tension. The results indicate that for a fiber angle of 0° and 90° a single element with unhindered lateral contraction is sufficient to obtain a converged solution. For the identification procedure, isothermal conditions are assumed, consequently, a C3D8 element is selected. Finally, the strain rate for identification is chosen as $\dot{\varepsilon}_x = 0.0005$ s^{-1}, in accordance with the experimental results from Reuvers et al. [2024a,b]. Since, the experimental study from Reuvers et al. [2024b] was conducted using digital image correlation (DIC), whereas in Reuvers et al. [2024a] DIC was used only for the visco-elastic tests to exploit the post-processing scheme by Amin et al. [2006], a difference between the local and global experimental measurements is observed. Moreover, the DOC of the composite tested in Reuvers et al. [2024b] is higher ($\chi = 0.41$) than the range tested in Reuvers et al. [2024a] ($\chi = 0.15 - 0.29$). It is likely that this discrepancy is due to production in two different facilities and the blend partner that was incorporated in Reuvers et al. [2024a] in order to achieve stable varying DOCs. These deviations inevitably impact the previous identifications of the matrix material model and, ultimately, the results of the virtual RUC experiments. To address these differences in identifying the macroscopic material model and simultaneously ensure the reproducibility of a wide range of DOCs, in the following, two parameter sets will be identified for each temperature. The first will be applied for $\chi = 0.41$, while the second will encompass $\chi = 0.15 - 0.29$. In Fig. 4.3 the results of the model identification

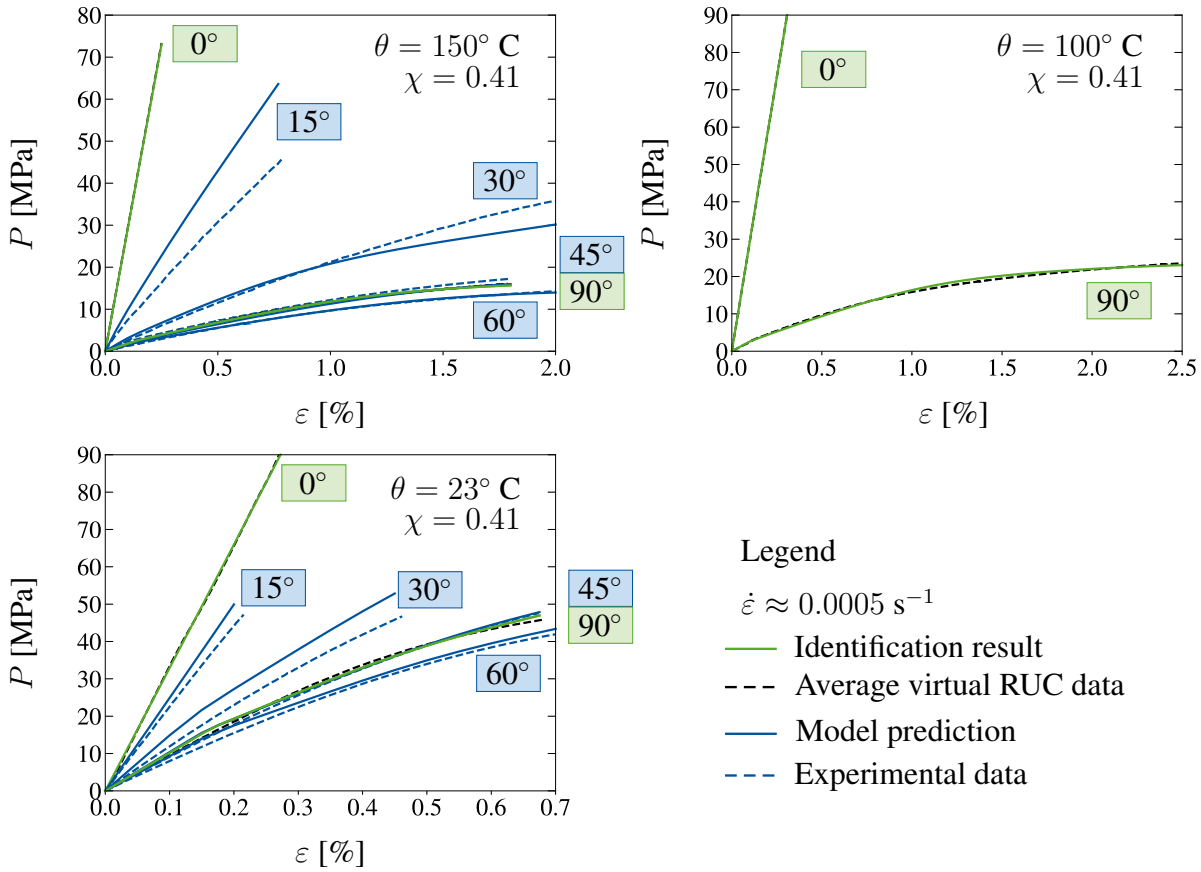

Figure 4.3: Identification results and model prediction for $\chi = 0.41$ under various fiber angles $0° \leq \varphi_{xy} \leq 90°$ ($\varphi_z = 0°$) and temperatures. Note here that results from ten RUCs were used to calculate the average.

procedure are shown for 23°C, 100°C and 150°C and a DOC of $\chi = 0.41$ as engineering stress P over engineering strain ε. Here, the experimental data and data generated through virtual experiments are shown in blue and black colored dashed lines, while the identification results are indicated with a solid green line. In general, the identified fiber angles of 0° and 90° correspond well with the RUC data for all three temperatures. To demonstrate the model's predictive capabilities, various fiber angles between 0° and 90° are tested and compared to experimental data for $\chi = 0.41$ (cf. Fig. 4.3). In this case, 125 C3D8 elements are required to achieve a converged solution due to the inhomogeneous stress state resulting from the fiber influence. The model prediction is in line with experimental results above 45° fiber angle, where the material response is dominated by the polymeric matrix material. Below 45 ° fiber angle, the deviation between simulation and experiment is more pronounced, especially in the nonlinear hardening regime. Moreover, in this regime, the initial model response is overly stiff compared to the experimental measurements (see Fig. 4.4 a)). Here, including the structural

tensor in the yield function or the energy of the elasto-plastic part could improve the results, specifically the transition between the visco-elastic and the visco-elastic, elasto-plastic regime. However, it remains unclear whether the relaxation behavior is influenced by the reinforcement as well. Consequently, relaxation tests need to be conducted prior to improving the model formulation. With regard to the results for $\chi = 0.15 - 0.29$, three crystallinities are used for

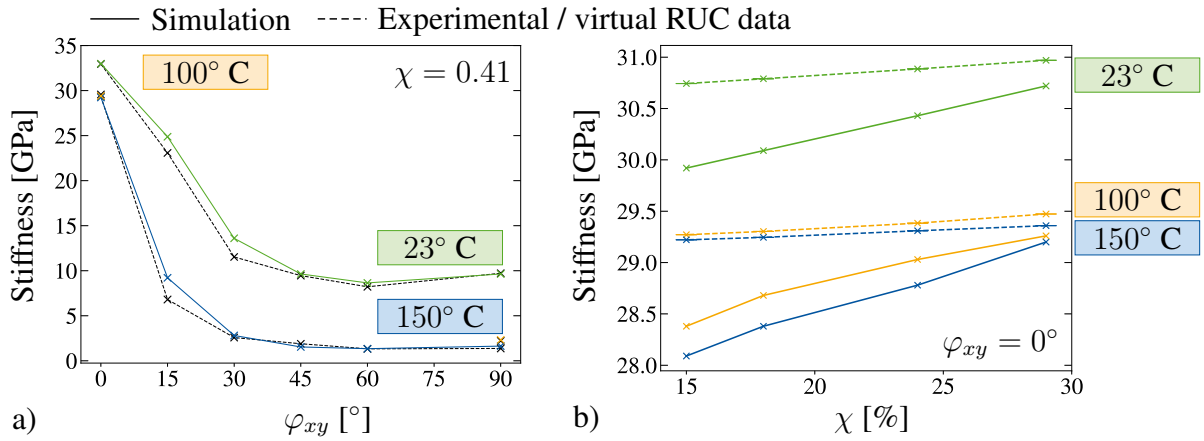

Figure 4.4: a) Comparison of material stiffness for $\chi = 0.41$ at various temperatures and fiber angles $0° \leq \varphi_{xy} \leq 90°$ ($\varphi_z = 0°$). b) Comparison of material stiffness for $\chi = 0.15 - 0.29$ at $\varphi_{xy} = 0°$ and $\varphi_z = 0°$ for various temperatures.

identification purposes, with one DOC reserved for verification ($\chi = 0.18$), similar to Reuvers et al. [2024a]. For these DOCs only virtually generated RUC data is available with 0° and 90° fiber angle. Consequently, a single element test is sufficient for identification purposes. The virtual data was obtained using ten RUCs generated with the RSA method from Reuvers et al. [2024b] together with the identified matrix material model from Reuvers et al. [2024a]. Hence, the averaged RUC response is used for model identification and the standard deviation is provided in the corresponding plots as well. Since the fiber properties are independent of the DOC, the parameters K_{ani1} and K_{ani2} are already known from the identification procedure for $\chi = 0.41$. Therefore, only the parameters related to the elasto-plastic part ($\sigma_t^0, c, b,$) as well as the Young's moduli E_1 and E_2 need to be determined using nonlinear optimization. The results of the identification procedure are shown as engineering stress over strain in Fig. 4.5 for $\varphi_{xy} = 90°$ and as a comparison between material stiffnesses for $\varphi_{xy} = 0°$ in Fig. 4.4 b). As anticipated, good agreement between the virtual experiment and the simulation is observed for all three test temperatures (cf. Fig. 4.5). The model also captures the unseen DOC of $\chi = 0.18$ well, especially at 150° C. Conversely, in fiber direction, the deviation between the model response and the virtual experiment increases with decreasing DOC (see. Fig. 4.4 b)). This effect can be attributed to the crystallinity-dependent isotropic part of the formulation,

which results in a reduction in stiffness with decreasing DOC. Concurrently, the parameters K_{ani1} and K_{ani2}, which contribute to the overall material stiffness via the anisotropic part of the formulation, are assumed to be constant. In light of the findings presented in Fig. 4.4 b), it may be beneficial to revisit the crystallinity dependence of the model formulation in future work. This could be achieved by either modifying the nonlinear crystallinity dependence of the material parameters or by incorporating the structural tensor into the elasto-plastic and / or visco-elastic part of the formulation. The authors would recommend the latter approach, as the results presented in Fig. 4.3 demonstrate the necessity for the inclusion of the structural tensor into the elasto-plastic part as well to accurately capture the yielding and hardening behavior for fiber angles between $0°$ and $45°$.

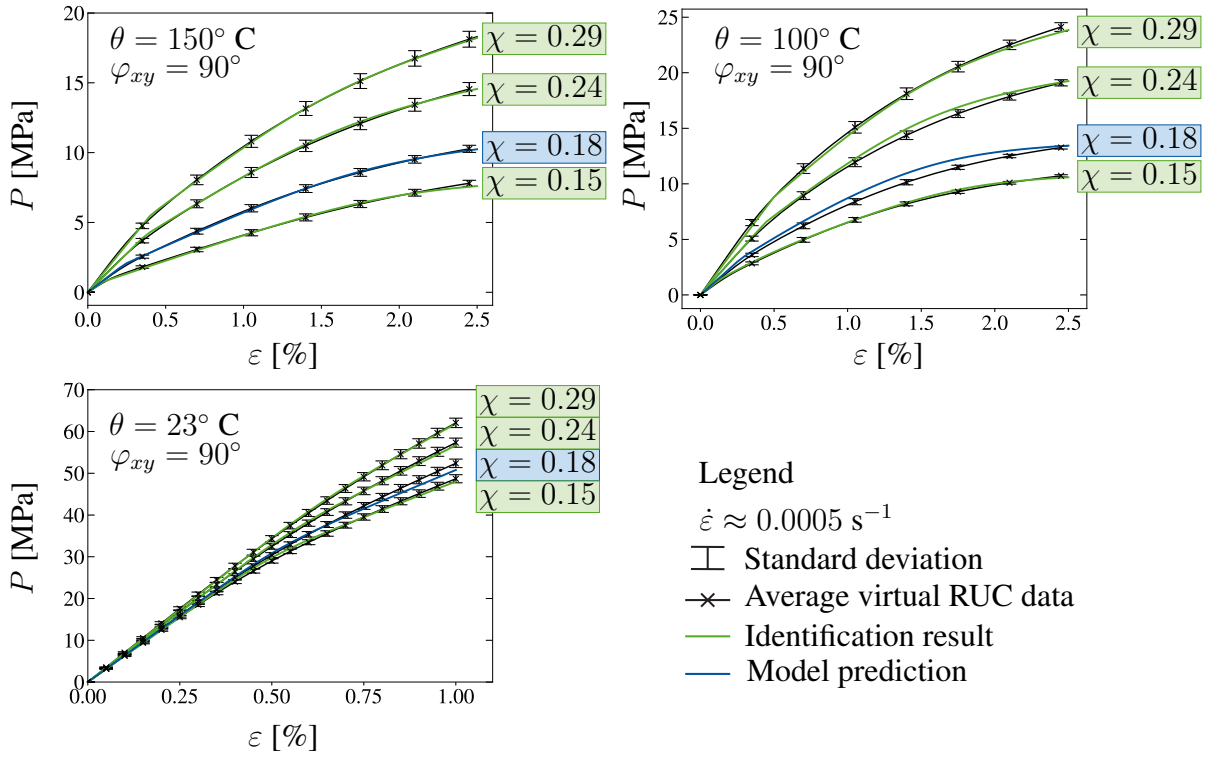

Figure 4.5: Identification results and model prediction for $\chi = 0.15 - 0.29$ at $\varphi_{xy} = 90°$ and $\varphi_z = 0°$ for various temperatures. Note here that results from ten RUCs were used to calculate the average and standard deviation.

An overview of the mechanical material parameters for $\chi = 0.41$ as well as $\chi = 0.15 - 0.29$. is provided in Tab. 4.3. It should be noted that the authors by no means claim that the identified parameter set is unique, given that the parameters of the visco-elastic branch were adopted from Reuvers et al. [2024a] and the identification was performed using only tensile data from a single strain rate. To improve the identification results, experimental data for multiple

strain rates, relaxation tests on the composite level and additional loading scenarios such as compression or shear would be necessary. Including these tests would, however, significantly increase the identification time. Moreover, prior to improving the identification procedure, the limitations of the presented formulation for fiber angles between $0°$ and $90°$ should be addressed. Therefore, the authors consider to use iCANNs (inelastic constitutive artificial neural networks) in the future for simultaneous model discovery and identification (see e.g. Holthusen et al. [2024]; Boes et al. [2024]; Holthusen et al. [2025a,b]) to accelerate model development. In order to identify the thermal stiffness-like parameter K_{therm}, ideally, an optical

		23° C		100° C		150° C	
Function	Parameter	$\chi = 0.41$	$\chi = 0.15 - 0.29$	$\chi = 0.41$	$\chi = 0.15 - 0.29$	$\chi = 0.41$	$\chi = 0.15 - 0.29$
$E_{\text{tot}} = C_1(\theta)\exp(C_2(\theta)\chi)$	C_1 = [MPa]	9306	4969	2324	500.9	1447	316
	C_2 =[-]	0	0.8184	0	3.632	0	4.33
$m_E = 1.07142\chi + 0.38935$	[-]	-		-		-	
$E_1^{\chi=0.15-0.29} = m_E(\chi)E_{\text{tot}}$	[MPa]	-			-		-
$E_2^{\chi=0.15-0.29} = E_{\text{tot}} - E_1$	[MPa]	-			-		-
$E_1^{\chi=0.41}$ =konst.	[MPa]	6514.2	-	1626.8	-	1012.9	-
$E_2^{\chi=0.41}$ =konst.	[MPa]	2791.8	-	697.2	-	434.1	-
ν_{tot}	[-]	0.35	0.35	0.45	0.45	0.45	0.45
$\sigma_t^0 = C_3\chi + C_4$	C_3 =[MPa]	0	95.22	0	33.86	0	21.57
	C_4 =[MPa]	10.769	17.27	1.694	-4.428	1.562	-2.863
$c = C_5\chi + C_6$	C_5 =[MPa]	0	399.1	0	1431	0	1359
	C_6 =[MPa]	2266.497	-2.474	508.224	-85.72	433.439	-198.1
$b = C_7\chi + C_8$	C_7 =[MPa]	0	-3376	0	842.7	0	677.2
	C_8 =[MPa]	19.898	1169	255.216	188.4	309.959	-101.3
$\tau = \tau_0(\theta)\,\|\|\boldsymbol{B}_v\|\|^{\gamma(\theta)}\exp(-\delta(\theta)\,\|\|\boldsymbol{\tau}_2\|\|)$	τ_0 [s]	1853.653	1853.653	1035.238	1035.238	573.899	573.899
	γ [-]	4.57	4.57	4.3	4.3	4.289	4.289
	δ [-]	0.539	0.539	0.759	0.759	0.873	0.873
K_{ani1}	[MPa]	3571.390	3571.390	3263.886	3263.886	3255.794	3255.794
K_{ani2}	[MPa]	2048.122	2048.122	2569.630	2569.63	2647.884	2647.884
K_{coup}*	[MPa]	100	100	100	100	100	100
$K_{therm} = \chi K_{therm,0}$*	$K_{therm,0}$[MPa]	ND	25862	ND	6897	ND	4138

Remark: The reader is kindly reminded, that, although some coefficients of the identified functions determining the material parameters, are negative, the material parameters themselves are always positive for the range of DOCs the model spans.
*not experimentally determined, ND = not determined

Table 4.3: Mechanical composite material parameters for $\chi = 0.41$ and $\chi = 0.15 - 0.29$ at all test temperatures.

measurement would be conducted, wherein the specimen is placed onto a heating table/plate and the actual deformation field is recorded using DIC (see e.g. Dudescu et al. [2013]; Singer et al. [2019]). This approach allows for the determination of the thermal expansion in both material directions. Subsequently, nonlinear optimization can be utilized to identify K_{therm}. Since, the aforementioned experimental results are, however, not available to the authors and the results from the thermo-mechanical analysis are by no means sufficient to identify K_{therm}, artificial values in the order of magnitude of the remaining material stiffnesses are introduced. Noteworthy, a parameter study of the stiffness-like parameter K_{therm} is not performed in the current manuscript. The reader is kindly advised to carefully review their chosen parameter set, as thermal shrinkage might occur in fiber direction upon heating beyond the thermo-elastic regime, due to the complex interplay between visco-elastic, elasto-plastic and anisotropic

mechanical and thermal phenomena. The remaining thermal composite material parameters are presented in Tab. 4.4 and are derived directly from the experimentally and the virtually generated data from Reuvers et al. [2024b]. As shown previously in Reuvers et al. [2024a], the influence of the DOC on the thermal matrix parameters is negligibly small. For the composite, this influence is even less pronounced due to the reinforcing fibers, and will thus be neglected. Consequently, only the temperature dependence will be considered.

Parameter		23° C	100° C	150° C
$\alpha_{T,n}$	[10^{-6}/K]	53	82	96
$\alpha_{T,f}$	[10^{-6}/K]	1	7	9
$\lambda_{T,n}$	[W/mK]	0.59	0.59	0.59
$\lambda_{T,f}$	[W/mK]	0.80	0.80	0.80
$c_T(\theta)$	[J/gK]	0.798989	0.6162	0.98295
ρ_0	[g/cm^3]	1.8	1.8	1.8

Table 4.4: Thermal composite material parameters independent of the DOC at all test temperatures.

4.5 Numerical examples

In this section, the model's capabilities to capture the coupling effects between, thermal, chemical and mechanical influencing factors are assessed, following the identification with experimental results. Sec. 4.5.1 addresses the thermo-mechanical coupling in terms of material self-heating in a single element computation. Subsequently, anisotropic thermal expansion and anisotropic heat generation are investigated in Sec. 4.5.2. The influence of the anisotropic thermal field on the crystallization behavior is studied in Sec. 4.5.3 by solving a staggered thermo-mechanically coupled boundary value problem. Finally, in Sec. 4.5.4 a complete thermoforming procedure is performed together with a comparison of the experimental and numerical results for model verification. For all computations, fully integrated C3D8T elements are used and the fiber angle φ_z is set to zero. The temperature-dependent material parameters are linearly interpolated between the identified values from Tabs. 4.3 and 4.4. Note here that the presented material parameters are not extrapolated beyond the identification range presented in Sec. 4.4. Therefore, in scenarios with boundary conditions outside the identification limits, the closest identified parameters are used to prevent errors due to extrapolation as, for example, negative values.

4.5.1 Material self-heating

To study the influence of the fibers on the internal self-heating, a single C3D8T element with unit length is subjected to monotonic, uniaxial extension with a loading rate of $\dot{\varepsilon}_{xx} = 0.01\,\mathrm{s}^{-1}$ until 15% strain. Subsequently, a relaxation step is introduced, where the strain is held constant for an additional 10 seconds. Two fiber angles are tested at $\theta = 150°$ C, namely $\varphi_{xy} = 90°$ and $\varphi_{xy} = 0°$, since all other fiber angles require multiple elements due to a resulting inhomogeneous stress state. Further fiber directions are investigated in a structural example in Sec. 4.5.2 and Sec. 4.5.3. For both computations, adiabatic conditions are assumed, meaning that no heat in- nor outflow at the surfaces of the specimen is permitted. The material parameters are chosen from Tabs. 4.3 and 4.4 for a DOC of 29%. Fig. 4.6,

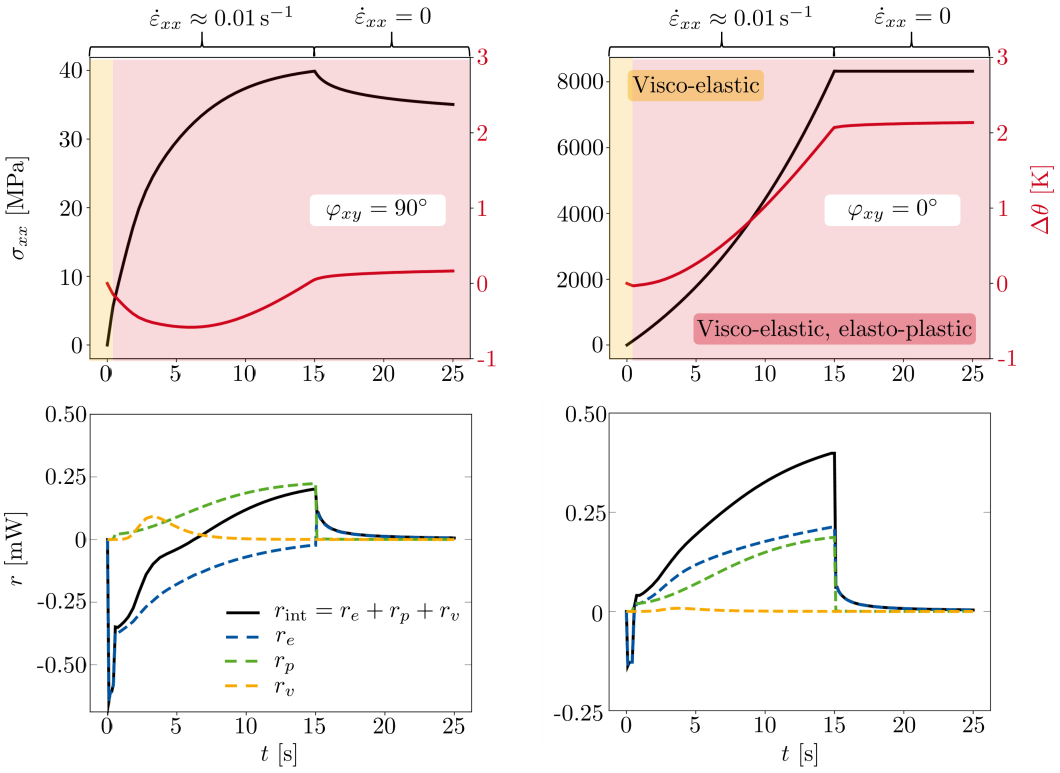

Figure 4.6: Single element subjected to monotonic, uniaxial extension ($\varepsilon_{xx}^{\max} = 0.15$) followed by a relaxation step under adiabatic conditions ($\theta = 150°$ C, $\chi = 0.29$). Left: tension normal to fiber direction $\varphi_{xy} = 90°$. Right: tension in fiber direction $\varphi_{xy} = 0°$. Top: Cauchy stress σ_{xx} over time in longitudinal direction and resulting change in temperature $\Delta\theta$. Bottom: Corresponding internal heat generation r_{int} and decomposition into elastic r_e, plastic r_p and viscous r_v parts.

shows the resulting Cauchy stress in x-direction, together with the corresponding change in temperature (top) and the depicted heat generation (bottom) for $\varphi_{xy} = 90°$ (left) and $\varphi_{xy} = 0°$

(right).

In the visco-elastic regime, thermo-elastic inversion is visible with a corresponding negative change in temperature, depending on the fiber angle φ_{xy}. This effect is more pronounced for $\varphi_{xy} = 90°$, where the material response in x-direction is dominated by the matrix material, due to the significantly higher coefficient of thermal expansion and the reduced influence of the fibers. Upon reaching the initial yield stress, plastic flow occurs, resulting in heat generation due to plastic dissipation r_p, independent of the fiber direction, together with a significant decrease in the elastic cooling. Compared to the plastic heat generation, the heat generated by viscous effects is significantly smaller. This finding is in line with Reese [2003a], where the loading rate was identified as the main influence on viscous thermal heating. At the start of relaxation, the plastic heat generation is reduced to almost zero, accompanied by a positive or negative jump in the elastic heat generation, depending on the fiber direction. Ultimately, at the end of the relaxation step, the total internal heat generation reduces to almost zero. With regard to the change in temperature, an increase with decreasing fiber angle is visible. For a fiber angle of 90°, the thermo-elastic cooling superimposes the viscous and plastic heat dissipation far into the visco-elastic, elasto-plastic regime. To validate the proposed formulation, a uniaxial tensile test would need to be conducted together with infrared thermography measurements. It should, however, be noted, that this example is of academic nature and rather a test of the material formulation itself, since the applied maximum strain lies beyond the fracture strain of the composite (cf. Reuvers et al. [2024b]).

4.5.2 Dogbone specimen: Anisotropic thermal expansion and material self-heating

In order to verify the novel theory chosen to model anisotropic thermal expansion, the structural example of an I-shaped specimen (type 1BA DIN EN ISO 527-2:2012) is investigated. The dimensions and boundary conditions are shown in Fig. 4.7 on the left with the experimental measurement length indicated in blue color. Here, the lower part of the specimen is fixed in all three principal directions. In a first series of computations, a mesh convergence study is conducted for $\varphi = 75°$ and $\varphi = 45°$ using C3D8T elements. In this case, only the displacement step between the times t_2 and t_3 as shown in Fig. 4.7 is considered. The results demonstrate a clear convergence trend (see Fig. 4.18 a in the Appendix), consequently, a structured mesh consisting of 13328 elements is assumed to be sufficient for the following considered problem. Subsequently, a more complex loading scenario is considered in order to account for thermal expansion. Initially, the specimen with a DOC of 29 % is heated up from room temperature

($\theta = 23°$ C) up to 50° C. Next, the temperature boundary conditions are held constant for 60 s to ensure a homogeneous temperature distribution within the structure. During the heating phase, the elongation in y-direction is constrained, resulting in the evolution of compressive stresses (see Fig. 4.7 on the lower right), which reach an almost constant value once the steady-state solution is obtained. Lastly, the temperature boundary conditions are removed and the upper part of the specimen is moved in y-direction with a loading speed of approximately $0.01\,\mathrm{s}^{-1}$ until a displacement of $u_y = 6.0$ mm is reached.

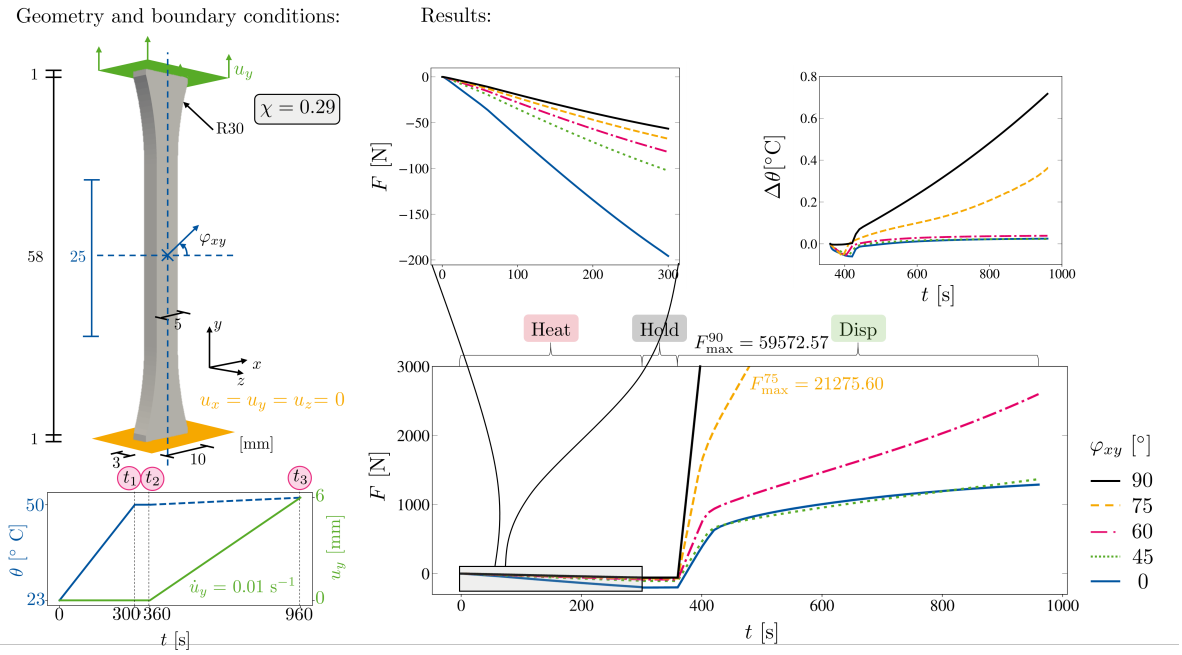

Figure 4.7: I-shaped specimen, geometry, boundary conditions and applied loading procedure (left). Resulting reaction force F over time and temperature increase due to internal heat generation during loading for varying fiber angles (right).

In Fig. 4.7 on the lower right, the reaction force in y-direction is displayed over time for varying fiber angles φ_{xy} between 0° and 90°. To increase the readability of the plot, the reaction forces are shown up to 3000 N. Above this number, only the maximum reaction force at t_3 is provided for 75° and 90° fiber angle. As expected, the reaction force first decreases during the heating phase, due to the hindered expansion in vertical direction. This effect is most pronounced when the fibers are orientated perpendicular to the loading direction ($\varphi_{xy} = 0°$), due to the higher thermal expansion of the polyamide 6 matrix compared to the glass fibers (cf. 4.7 upper left). As the fiber angle increases, the absolute value of the reaction force exhibits a nonlinear decrease. The lowest compressive reaction force is observed for a fiber angle of $\varphi_{xy} = 90°$, where the fibers are aligned with the loading direction. From the

results presented in Fig. 4.7, the authors conclude that the proposed formulation is indeed able to capture anisotropic thermal expansion. Moreover, comparing the magnitude of the negative reaction force with the tensile results, it becomes evident that thermal expansion plays a significant role in polymeric materials, particularly when considering the relatively modest applied temperature gradient. As a next step, the proposed ansatz must be validated with experimental DIC results. In addition, the formulation needs to be carefully examined with regard to the potential presence of residual internal stresses at the interface of the two constituents, which are common in polymeric composites with contrasting thermal properties. The homogenized approach might underestimate this phenomenon. Introducing a thermal coupling term, similar to the mechanical coupling term in Eq. 4.47, could be considered in future investigations.

Next the displacement is applied, which results in a complex interplay between different coupling phenomena. After the thermo-elastic inversion, the internal heat generation increases, leading to an increase in the temperature, here, shown in the upper right of Fig.4.7 for the center of the specimen. The corresponding contour plots for the internal heat generation r_{int} and true strain in loading direction at the end of the loading procedure ($t_3 = 960$ s) are shown in Fig. 4.8 for all tested fiber angles. In general, the internal heat generation is most pronounced when the fibers are aligned with the loading direction and decreases significantly with decreasing fiber angle, in line with the findings from Sec. 4.5.1. The dissipated heat is strongly associated with the strain field (cf. Fig. 4.8), where high local strains lead to increased heat generation. In addition, the strain contours align with the prescribed fiber angles.

4.5.3 Thermo-mechanically coupled boundary value problem

This section is concerned with a thermo-mechanically coupled boundary value problem from Felder et al. [2020b] to provide a direct comparison between the isotropic theory and the composite formulation presented in this work, which incorporates fiber-induced anisotropy. To this end, a symmetric plate with hole is subjected to a multi-step loading procedure (see Fig. 4.9). Contrary to Felder et al. [2020b], the whole structure is modeled, due to the anisotropic nature of the composite material model. Furthermore, multiple computations are conducted with varying fiber angles φ_{xy} to investigate the influence of anisotropic heat conduction on the crystallization process. Prior to testing, a convergence study was conducted (see Fig. 4.18 in the Appendix) on the displacement step, where 30760 fully integrated C3D8T elements were found to yield a converged solution. The mechanical and thermal boundary conditions are provided in Fig. 4.9, together with the loading procedure. Following the classical thermoforming process, the edges of the structure are first cooled down from a temperature close to the melt

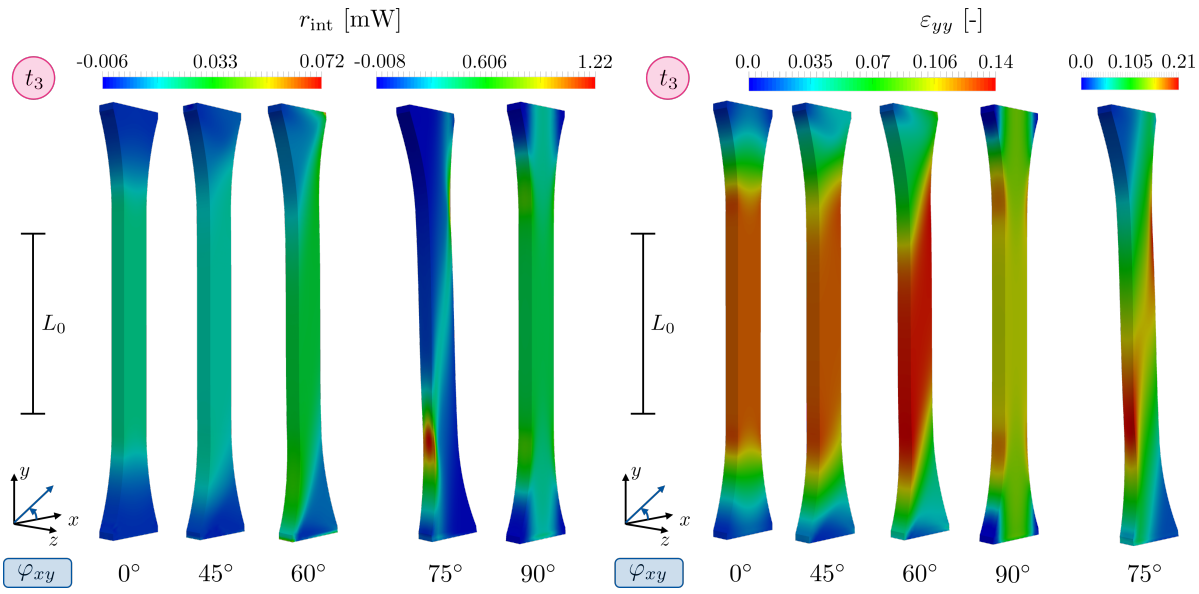

Figure 4.8: Contour plots for internal heat generation r_{int} and true strain in y-direction at $t_3 = 960$ s for all tested fiber angles. The experimental measurement length L_0 is highlighted for reference.

(200 °C) with varying cooling rates between 0.17 and 100 K/s, incorporating both S-DSC and F-DSC results. Once the target temperature of 100 °C is reached (t_1), the temperature is held constant for 180 s until t_2, in order to ensure a homogeneous distribution. Subsequently, the temperature boundary conditions are removed and a displacement is applied with a constant loading rate of 0.01 1/s until $u_x = 0.6$ mm (t_3) is reached. Lastly, the displacement is held constant for an additional 60 s to allow for stress relaxation. Fig. 4.10 illustrates the distribution of the absolute degree of crystallization χ, at the end of the holding step (t_2) for four cooling rates $\dot{\theta} = \{0.17, 10, 50, 100\}$ K/s and a fiber angle of 90°. Similar to the findings of Felder et al. [2020b], higher cooling rates result in a heterogeneous distribution of crystals, due to temperature gradients and non-constant cooling rates, whereas for the lowest (S-DSC) cooling rate an almost uniform distribution arises. In general, the DOC increases with decreasing cooling rate. Noteworthy, for all F-DSC rates, the majority of the crystallization occurs after the cooling step, between t_1 and t_2. Moreover, the released heat of fusion from the crystallization process increases with increasing cooling rate (cf. Fig 4.11 b), especially during the initial cooling step. This finding is reflected in the exemplary evolution of the temperature and DOC over time for one Gauss point, displayed in Fig. 4.10. Here, the typical crystallization kinetics for varying thermal treatments (i.e. higher overall degree of crystallinity and higher crystallization onset temperature for lower cooling rates) are depicted and the heat of fusion can be detected from the visible temperature rise after the crystallization onset. Noteworthy,

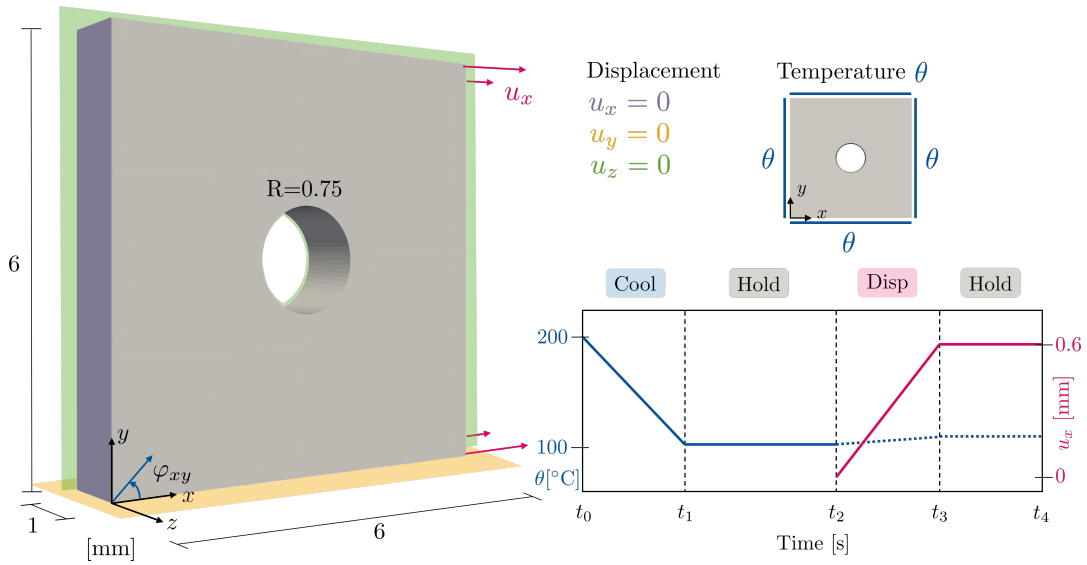

Figure 4.9: Plate with hole: geometry, boundary conditions and applied loading procedure.

the magnitude of the internal heat, generated during crystallization r_χ, is significantly higher compared to plastic and viscous dissipative phenomena. The influence of the fiber angle on the

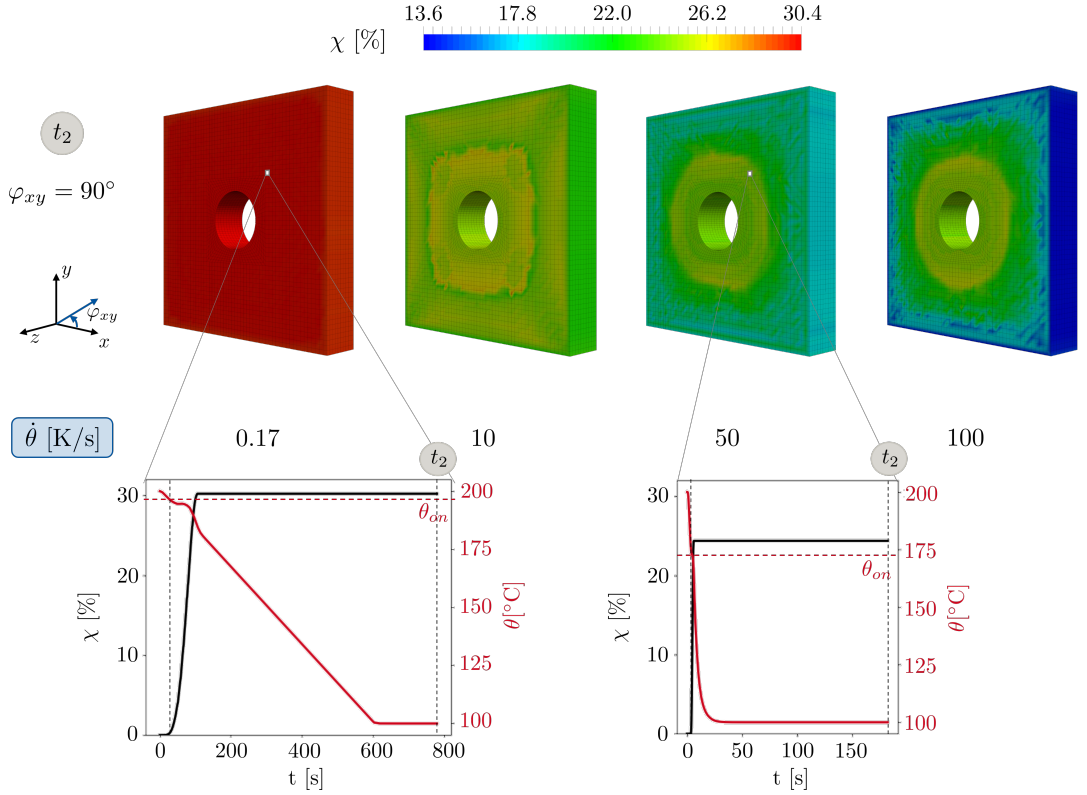

Figure 4.10: Resulting total degree of crystallinity for varying S-DSC and F-DSC cooling rates and evolution of the DOC for selected cooling rates.

crystallization process is illustrated in Fig. 4.11 a. Overall, the resulting degree of crystallinity is similar for all fiber angles and the influence of the thermal anisotropy on the resulting thermo-mechanical composite behavior in terms of the reaction force between t_2 and t_4 is negligibly small. However, local differences in the absolute DOC are clearly visible (cf. Fig. 4.11 a) and increase with increasing cooling rate. The authors believe that this is a result of the uniform temperature boundary conditions, which superimpose the influence of the anisotropic heat flux. Certainly, non-uniform temperature boundaries would result in more pronounced local differences and, consequently, differences in the resulting thermo-mechanical composite behavior. During the commercial thermoforming process the structure will most likely undergo a uniform thermal treatment. Therefore, the authors believe that it would be sufficient to neglect the fiber influence on the crystallization process in scenarios characterized by uniform thermal boundary conditions, where the objective is to determine the resulting DOC e.g. for later use as a constant input quantity. The dependence of the macroscopic mechanical response on the

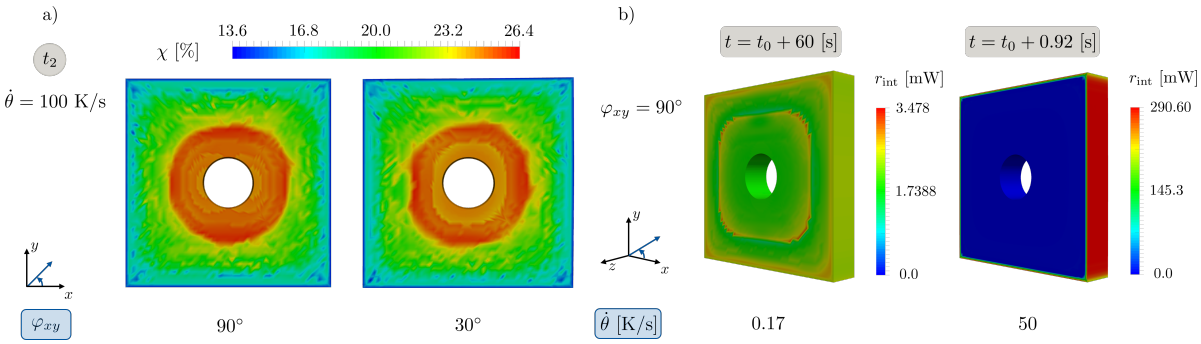

Figure 4.11: a) Comparison of the resulting degree of crystallinity for varying fiber angles. b) Comparison of the internal heat generation due to crystallization for varying cooling rates.

underlying microstructure and the fiber angle is clearly visible in the reaction force time relation provided in Fig. 4.12. Overall, the stiffness, the yield stress and the hardening stress increase with increasing degree of crystallinity. These effects are, however, more pronounced for higher fiber angles, whereas with decreasing fiber angle differences between the varying cooling rates are mostly visible in the relaxation step ($t_3 - t_4$), where the resulting change in the reaction force is related purely to the visco-elastic model part. Note here that the reaction force for $\varphi_{xy} = 90°$ between t_2 and t_3 is reduced due to the choice of hardening parameters. In contrast to Felder et al. [2020b], the temperature distribution is not provided, since notable changes in the thermal field due to inelastic deformation are observed only for a fiber angle of 15°. Similar to the findings in Sec. 4.5.1, the heat generated through inelastic phenomena is superimposed by thermo-elastic inversion. This effect was not reproduced by Felder et al. [2020b], who

neglected the elastic heat generation. Consequently, the overall change in temperature in this study is significantly higher. Furthermore, compared to Felder et al. [2020b], a significantly broader range of DOCs is investigated in this work, due to the composition of blends and the conduct of S-DSC and F-DSC tests.

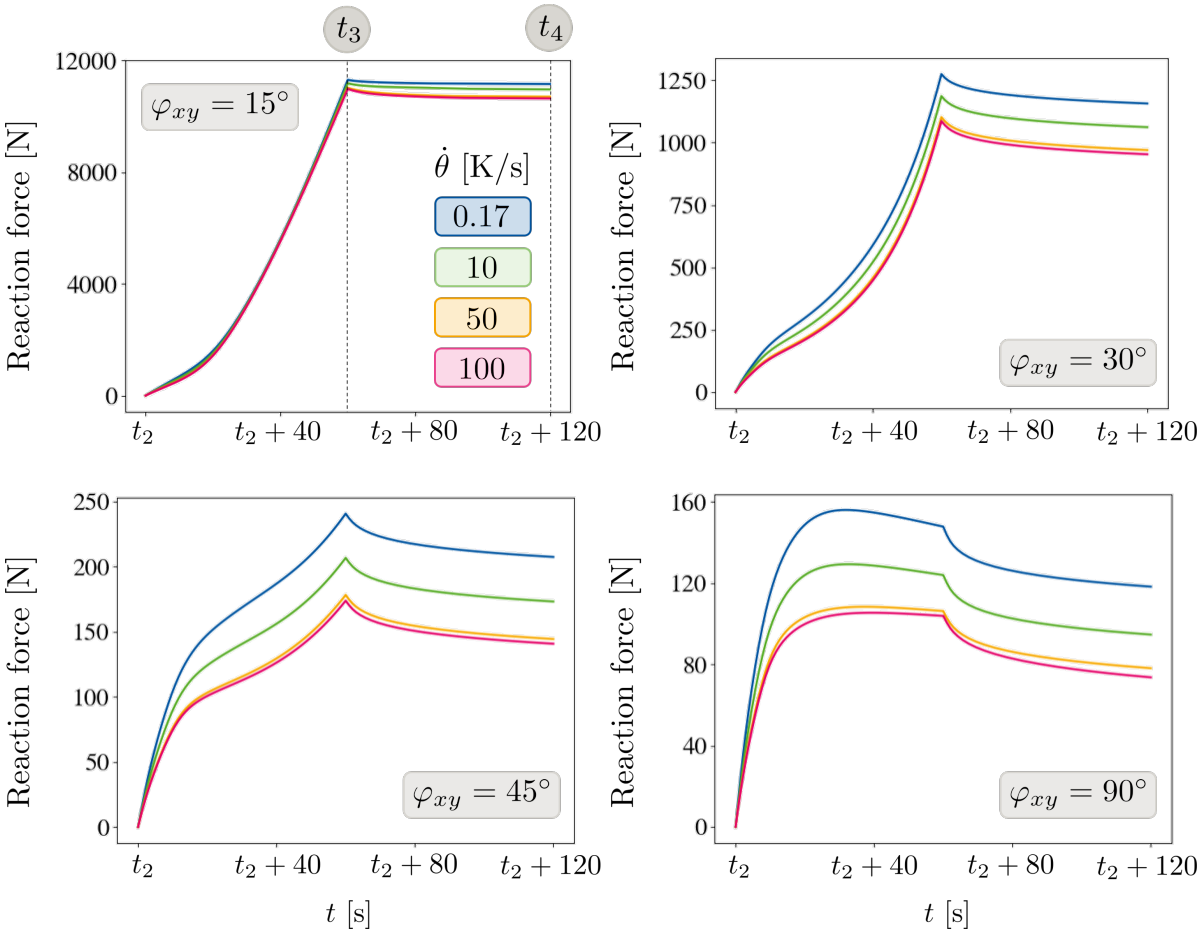

Figure 4.12: Reaction force time relation for various fiber angles and S-DSC as well as F-DSC cooling rates.

4.5.4 Thermoforming simulation in comparison to experimental results

In order to validate the proposed framework, a 3D thermoforming simulation on glass fiber reinforced polyamide 6 is conducted and, subsequently, compared to experimental results. The corresponding experiments are conducted at the University of the German Federal Armed Forces in Munich. To ensure comparability between the simulation and the experiment, the UD-reinforced composite material from Reuvers et al. [2024b], with a thickness of 5 mm,

which was employed prior to generating the data base (cf. Sec. 4.4.2) is used for testing. A schematic drawing of the experimental forming setup as well as the corresponding dimensions for the numerical boundary value problem are presented in Fig. 4.13. Note here that for all experimental procedures and simulations, the fiber direction is aligned with the x-axis (cf. Fig. 4.13 b).

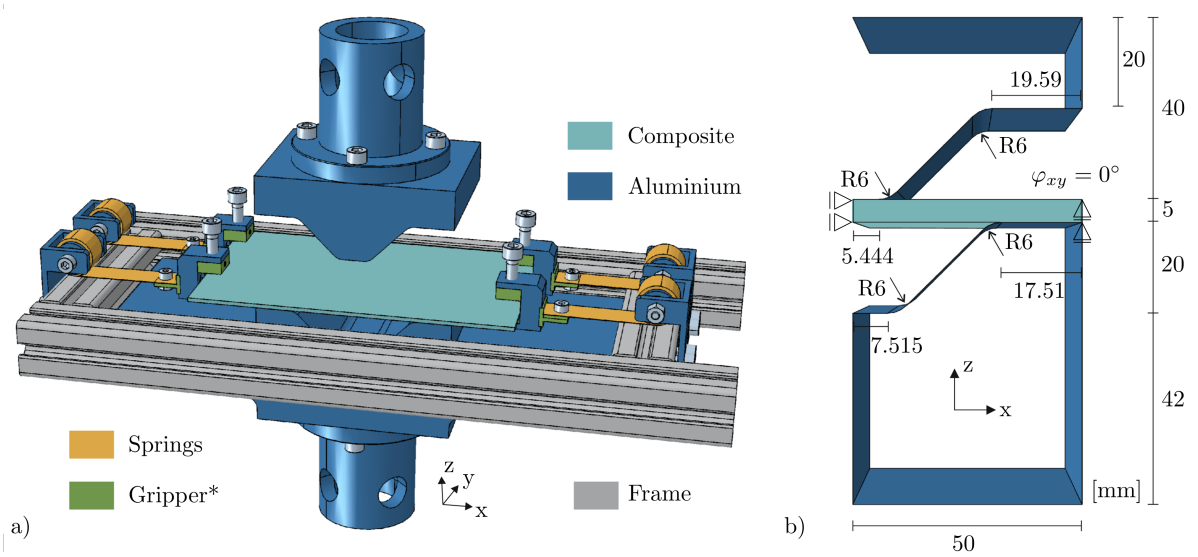

Figure 4.13: a) Experimental setup. *The grippers have been replaced with paper clips for testing. b) Geometry and boundary conditions. Symmetry boundary conditions are applied in x- and y-direction of the plate. The springs are neglected, since the simulation does not account for gravity effects. Instead, boundary conditions in y- and z-direction are applied to mimic the effect of the springs holding the plate in plane.

Prior to the forming procedure, the plate is stored in a *Nabertherm TR 60* drying oven until a homogenous plate temperature of 230° C is reached. A *K-type* thermocouple is inserted into the center of the plate through a 1 mm hole, thus enabling the temperature evolution to be monitored during the forming process. To ensure a smooth transition between the oven ($\theta = 230°$ C) and the *Zwick/Roell Z020* machine ($\theta = 21°$ C), equipped with aluminum punch and die, the plate is fixed in a specimen holder prior to heating. In order to prevent sagging of the specimen due to the high viscosity of the matrix material close to the melting point in combination with gravity, four springs are attached to the frame and the plate, each with a force below 1 N (cf. Fig. 4.13 a). In this way, a quick manual transfer to the *Zwick/Roell Z020* machine is ensured, while the heat loss of the plate is limited. Once the frame is in place, the forming is conducted with a displacement-controlled punch movement, together with a maximum prescribed compressive force of 3750 N. After the mold is closed, the force is held

constant for an additional 60 seconds to ensure cooling of the plate and, therefore, allow for crystallization of the polymeric matrix material. The maximum prescribed force is determined through a series of preliminary tests, where a higher compressive force resulted in extensive overflow or spillage of the material at the open sides of the mold in x- and y-direction. In the course of these experiments, the optimal temperature for both the punch and the die is determined as well, with room temperature yielding the most precise forming results. Note here that in industrial forming processes, punch and die, by default, are cooled down below room temperature after mold closure, which could not be replicated with the existing laboratory equipment.

The resulting plate deformation, after removal from the mold, is shown in Fig. 4.14. Overflow at the open sides of the mold and slight distortions within the plate are visible. These effects are most likely related to unsuitable fixtures of the specimen holder and the magnitude of the applied force. Given the limited laboratory facilities compared to an industrial production environment, the results are nonetheless impressive. The experimentally measured temperature evolution in the center of the plate is displayed in Fig. 4.15 b. Here, the temperature increase after the closing of the mold is related to the latent heat released during crystallization. It should be noted that the experiment was terminated after reaching 50° C in the center of the plate, which is significantly lower than the end temperature of crystallization t_{end} (cf. Fig. 4.2).

As shown in Fig. 4.13 b, symmetry conditions are exploited for the numerical boundary value problem. Consequently, only one quarter of the plate is computed, which significantly reduced the computation time. Moreover, in addition to the corresponding symmetry boundary conditions, fixtures in y- and z-direction are applied at the outer edge of the plate to mimic the effect of the springs holding the plate in the yz-plane (cf. Fig. 4.13 b). In this way, the initial bending of the plate into a v-shape is constrained in a manner analogous to the experimental procedure. Since the proposed model framework is formulated in two separate processes (I: thermo-chemical crystallization from the melt, II: thermo-mechanical composite behavior, cf. Sec. 4.3), two separate computations are performed: firstly purely mechanical forming (II) and, subsequently, cooling and crystallization (I). In comparison with the experimentally obtained temperature curve, the temperature change in the center of the specimen before mold closure is negligible, with the predominant temperature change occurring once the mold is fully closed and the plate is in contact with punch and die. Therefore, the authors' believe that the separation in two computations is reasonable. Note here that in order to model the thermoforming process in a single computation, a fully thermo-chemo-mechanically coupled model formulation would be necessary, which is beyond the scope of the work and would

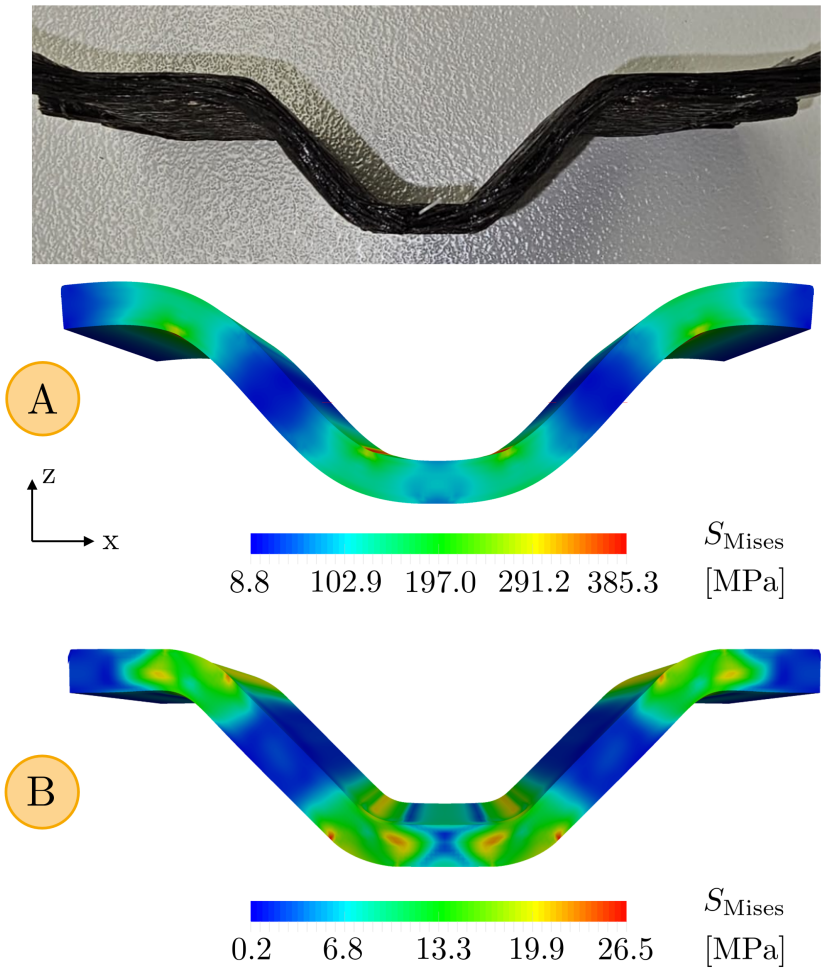

Figure 4.14: Resulting deformation and von Mises stress contours after forming ($t = 10$ s) in comparison to the experimental result. A) Anisotropic material behavior without friction B) Isotropic material behavior including friction.

require re-development of the formulation.

In the context of the mechanical forming, the loading is applied force-controlled, since Abaqus does not allow for displacement-controlled loading, together with a maximum prescribed force. Moreover, preliminary numerical studies have demonstrated that applying the corresponding experimental displacement instead of the force, results in excessive contact forces and, thus, a comparison with the experimental results is unfeasible. With regard to the mechanical contact conditions, hard contact is chosen in normal direction together with friction in tangential direction. The corresponding coefficient of friction ($\mu = 0.0507$) is taken from experimentally obtained values by Dörr [2021]. Note here that for the experiments in Dörr [2021] steel was used together with fiber reinforced PA6, as opposed to the aluminum fixtures

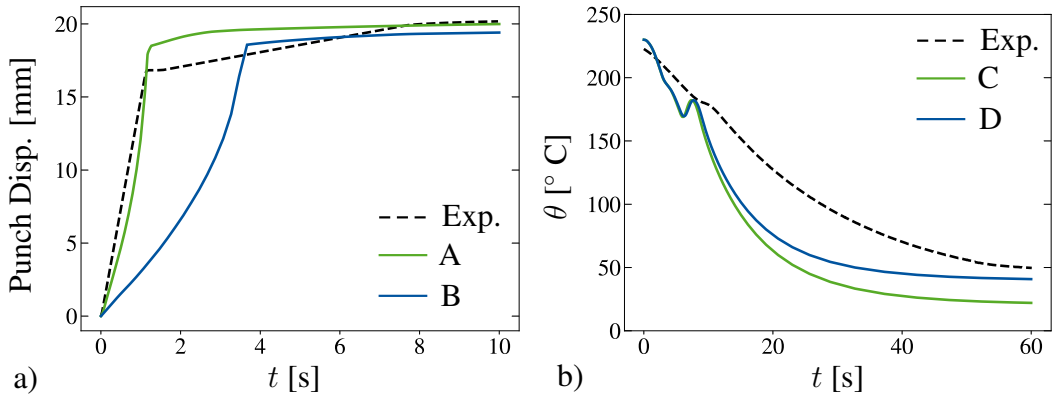

Figure 4.15: a) Punch displacement over time in comparison to experimental displacement. (A) Anisotropic material behavior without friction (B) Isotropic material behavior including friction. b) Temperature evolution in the middle of the plate im comparison to temperature sensor measurements. (C) Punch and die $\dot{\theta} = 0$ (D) Punch and die $\dot{\theta} \neq 0$.

in the current work. During the computations, the anisotropic material model in combination with friction resulted in an overly stiff material response, and, thus, in an incomplete forming due to the relatively low compressive force. Therefore, two computations were conducted, firstly, anisotropic material behavior without friction (A) and, secondly, isotropic material behavior including frictional effects (B). A relatively fine discretization was needed for the computation including anisotropic material behavior (80000 elements, structured mesh), since the high stiffness contrast between x- and y- direction is prone to buckling effects.

The resulting mechanical deformation of the composite is shown in Fig. 4.14 for both computations in comparison to the experimental result. Although both material configurations result in a deformed shape similar to the experiment, the deformation of the computation with isotropic material behavior and frictional effects (B) is more pronounced, especially with regard to the rounded corners, where the plate is bent. Furthermore, in these areas, the resulting von Mises stress is significantly higher for the anisotropic computation, which is the result of an overly stiff material response. This finding is reflected in the punch displacement over time (cf. Fig. 4.15 a). Here, the maximum punch displacement ($t = 10$ s) of the anisotropic calculation is lower than the isotropic value. Moreover, the initial punch displacement rate for the isotropic calculation is similar to the experimental findings, whereas the punch displacement for the anisotropic plate evolves slower and more non-linearly.

In comparison to the experimental result, the isotropic solution is able to capture the initial displacement increase, as well as the maximum punch displacement, despite the high stiffness of the Young's modulus (cf. Tab. 4.3) and the difference in the boundary conditions. Conversely,

the anisotropic solution is not able to capture the features of the experiment due to the overly stiff material response resulting from the fibers. The authors' believe that the fibers do not transfer a significant amount of load during the experimental forming procedure, due to the high viscosity of the polymeric matrix close to the melting point. This is, however, not reflected in the identified material formulation, where the composite has a high stiffness in fiber direction even at high temperatures (cf. Fig. 4.4 b). In addition, no experimental data is available for temperatures beyond 150° C and the extrapolated material parameters, similarly, result in a high stiffness in fiber direction. Consequently, the true material behavior most likely lies in between the presented results. In future studies, it is imperative to identify the material formulation at temperatures proximate to the melting point of the polymeric matrix. However, the corresponding experiments will be challenging due to the increased viscosity.

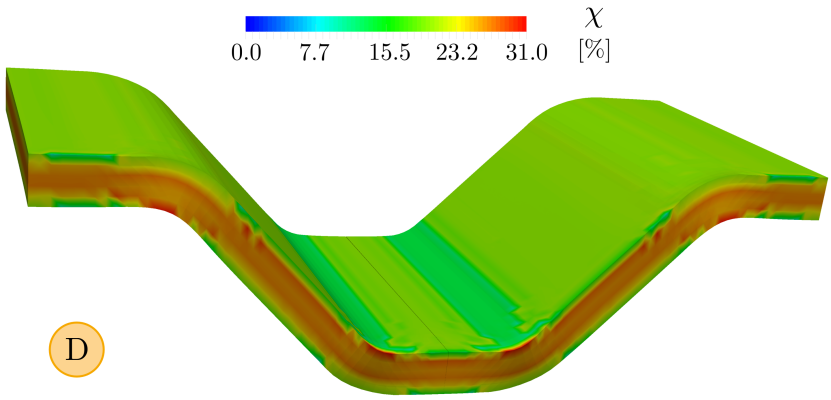

Figure 4.16: Resulting degree of crystallinity (DOC) after forming. D) Punch and die $\dot{\theta} \neq 0$.

With regard to the thermo-chemical calculation, isothermal deformable bodies with rigid constraints are used to approximate punch and die, thereby facilitating heat transfer between the different constituents. The gap conductance between tools and plate is adopted from Dörr [2021] measuring 1.05 mW/K. It should be emphasized that the corresponding experiments were conducted between steel and polyamide 6. In this study, the effects of radiation and convection are not considered, since the majority of the surface of the plate is enclosed by the punch and die. Moreover, in order to speed up the calculation, a coarser mesh discretization is chosen (10000 elements), compared to the mechanical computations. The corresponding temperature conditions for the plate ($\theta = 230°$ C) and punch/die ($\theta = 21°$ C) are applied instantaneously and heat conduction is allowed for 60 s thereafter. Two computations are conducted. Firstly, punch and die are held constant at $\theta = 21°$ C during the whole simulation (C) ($\dot{\theta} = 0$). For the second computation, no temperature boundaries are applied at the reference points of the rigid bodies, apart from the initial temperature field, to allow for heat

up (D) ($\dot{\theta} \neq 0$). During the experimental procedure, the tools are allowed to heat up, however, the thermal mass is higher due to the adjacent fixtures that are not included in the simulation. Moreover, in reality, punch and die are exposed to room temperature air, therefore, radiation and convection will lead to significant heat loss that is not accounted for in the presented computations.

An overview of the resulting crystalline state ($t = 60$ s) is provided in Fig. 4.16. Since the differences in the resulting DOC for calculations C and D are negligible, only the results from calculation D are shown. As anticipated, the crystallization process resulted in a higher DOC in the central region of the plate (cf. Fig. 4.16). This phenomenon can be attributed to the reduced cooling rate within the material relative to the exterior surface, which is directly exposed to the room temperature fixtures. The evolution of the temperature in the center of the plate is presented in Fig. 4.15 b, together with the experimentally obtained curve. Compared to the experiment, the plate cools down faster during both simulations. This effect is directly related to the choice of the gap conductance. To improve the results, thermal measurements need to be taken experimentally to determine the correct gap conductivity. Similar to the temperature evolution during the experimental procedure, a temperature increase related to exothermic crystallization is visible for both numerical examples. Here, the temperature increase is significantly higher and the crystallization occurs faster, shown by the narrowing of the peak, which is a result of the higher cooling rate. Overall, the differences between simulation C and D are negligible during the crystallization process, indicated by the uniform crystallization peak. After crystallization is finished, the temperature evolution in the center of the plate of simulation D is, however, slowed down, due to temperature compensation between plate, punch and die. Thus, the final thermal state at $t = 60$ s for simulation D is closer to the experimentally measured value.

4.6 Conclusion and outlook

In this work, a finite strain, thermo-mechanically coupled constitutive framework was proposed for the analysis, prediction and optimization of glass fiber reinforced semi-crystalline polymers during the thermoforming process. This work is the conclusion of several experimental and simulative investigations on the individual constituents and multiple material scales, resulting in a validated and thermodynamically consistent composite model. To account for the fiber induced anisotropy, a thermo-mechanically coupled material framework for the polymer matrix was extended by exploiting the concept of structural tensors, introducing transversally anisotropic conduction, thermal expansion and internal heat sources. Moreover, the crystal-

lization process of the matrix material during cool-down from the melt was incorporated into the proposed formulation as a seperate thermo-chemical process. In order to complete model identification, the mechanical and thermal material parameters were subsequently identified with experimental and virtual data over multiple material levels. The model prediction was in good agreement with the experimental results, especially for higher fiber angles. However, in order to improve the results for lower fiber angles, the introduction of the structural tensor in the visco-elastic and / or elasto-plastic part of the formulation should be considered in the future, once the corresponding experiments are available. Nonetheless, it is remarkable that the framework is able to successfully predict fiber angles beyond $0°$ and $90°$, given that only data on uniaxial stress states was available for identification purposes.

The capabilities of the proposed framework were assessed in multiple numerical examples, firstly presenting the influence of the fiber angle on material self-heating. Next, the new approach regarding anisotropic thermal expansion was verified with a thermo-mechanically coupled boundary value problem with varying fiber angles. A multi-step loading procedure was applied on a plate with hole, where the phenomenological approach allowed to visualize the complex crystallization process on the microscale. Throughout multiple computations with varying fiber angles, the influence of the reinforcement on the resulting degree of crystallinity was evaluated. Moreover, the predicted heat of fusion from crystal growth was identified as an important influencing factor, especially for high cooling rates. The influence of the DOC on the macroscopic material response was mainly visible for high fiber angles or relaxation states. Compared to existing formulations, a significantly larger range of DOCs was depicted, due to blend composition and different DSC tests in preliminary works. Finally, a 3D thermoforming procedure was conducted and compared to experimental results, demonstrating the ability of the framework to successfully predict industrial forming processes. To the authors' knowledge, there exists no comparable experimentally validated constitutive framework for fiber-reinforced semi-crystalline polymers in the literature, which accounts for the crystallization kinetics as well as anisotropic thermal and mechanical behavior and the corresponding complex interactions over multiple material scales. Therefore, the authors' believe that this formulation provides a flexible and promising basis for further research.

In the future, the homogenized approach should be revised with regard to residual thermal stresses at the interface between fibers and matrix, resulting from contrasting thermal properties. As previously stated, incorporating the structural tensor in different parts of the model formulation might be necessary to improve the model response for inhomogenous stress states, depending on the application. Therefore, more complex structural problems resembling real themoforming processed should be computed and verified with experimental data. In order

to improve model identification, the experimental and virtual data base needs to be enriched with combined loading procedures and further experiments on the thermal expansion behavior. Based on promising results in the literature (see e.g. Flaschel et al. [2021, 2023]; Holthusen et al. [2024]; Boes et al. [2024]; Holthusen et al. [2025a,b]), neural networks could be introduced to facilitate model discovery and detect so far concealed or overlooked material effects in the experimental results, while at the same time reducing the identification effort. Besides, the thermo-mechanical model improvements, the presented macroscopic crystallization formulation does not yet account for the formation of local nuclei, different crystal configurations or cold crystallization. Especially the latter is of high importance for thermoforming with high cooling rates and would require a fully coupled modeling scheme.

4.7 Appendix

4.7.1 Transversely isotropic heat flux

The Cauchy heat flux vector $\boldsymbol{q}$ is introduced according to Duhamel's law as

$$\boldsymbol{q} = -\boldsymbol{\kappa}\,\mathrm{grad}(\theta), \tag{4.49}$$

where $\boldsymbol{\kappa}$ denotes the symmetric second order thermal conductivity tensor with respect to the current configuration. Next, in order to describe transversely isotropic materials, where the thermal conductivity in fiber direction $\lambda_{T,f}$ differs from the orthogonal directions $\lambda_{T,n}$, the conductivity tensor is defined as

$$\boldsymbol{\kappa} = (\lambda_{T,f} - \lambda_{T,n})\boldsymbol{m} \otimes \boldsymbol{m} + \lambda_{T,n}\boldsymbol{I} = (\lambda_{T,f} - \lambda_{T,n})\boldsymbol{M} + \lambda_{T,n}\boldsymbol{I}, \tag{4.50}$$

in line with e.g. Al-Kinani [2014]; Tröger and Hartmann [2022]. Here, $\boldsymbol{M}$ is the structural tensor with respect to the current configuration, which is given by

$$\boldsymbol{M} = \boldsymbol{m} \otimes \boldsymbol{m} = \boldsymbol{F}\,\boldsymbol{M}_0\boldsymbol{F}^T\,\frac{1}{\boldsymbol{C} : \boldsymbol{M}_0} \quad \text{with} \quad \boldsymbol{m} = \boldsymbol{F}\,\boldsymbol{m}_0\,\frac{1}{|\boldsymbol{F}\boldsymbol{m}_0|}. \tag{4.51}$$

Using the Piola transformation $\boldsymbol{q}_0 = J\,\boldsymbol{F}^{-1}\,\boldsymbol{q}$ with $J = \det(\boldsymbol{F})$ as well as the relation $\mathrm{grad}(\theta) = \boldsymbol{F}^{-T}\,\mathrm{Grad}(\theta)$, the heat flux in the reference configuration follows to

$$\boldsymbol{q}_0 = -J\,\boldsymbol{F}^{-1}\left((\lambda_{T,f} - \lambda_{T,n})\boldsymbol{M} + \lambda_{T,n}\boldsymbol{I}\right)\boldsymbol{F}^{-T}\,\mathrm{Grad}(\theta) = -\boldsymbol{\kappa}_0\,\mathrm{Grad}(\theta). \tag{4.52}$$

The heat conductivity tensor with respect to the reference configuration $\boldsymbol{\kappa}_0$ can be rewritten to

$$\begin{aligned}
\boldsymbol{\kappa}_0 &= J\,\boldsymbol{F}^{-1}\left((\lambda_{T,f} - \lambda_{T,n})\boldsymbol{M} + \lambda_{T,n}\boldsymbol{I}\right)\boldsymbol{F}^{-T} \\
&= J\left((\lambda_{T,f} - \lambda_{T,n})\,\boldsymbol{F}^{-1}\boldsymbol{M}\boldsymbol{F}^{-T} + \lambda_{T,n}\,\boldsymbol{F}^{-1}\boldsymbol{F}^{-T}\right) \\
&= J\left(I_4^{-1}\,(\lambda_{T,f} - \lambda_{T,n})\,\boldsymbol{M}_0 + \lambda_{T,n}\,\boldsymbol{C}^{-1}\right),
\end{aligned} \tag{4.53}$$

using Eq. 4.51 together with the relation for the fourth invariant $I_4 = \mathrm{tr}(\boldsymbol{C}\boldsymbol{M}_0)$.

4.7.2 Avrami equation

In the field of material science, the Avrami equation (cf. Avrami [1939, 1940]) is a widely used mathematical model for describing isothermal phase transformations. In the context of polymer crystallization, the model describes the transformation from the amorphous phase to the thermodynamically more stable crystalline phase. The relative degree of crystallinity defined as $0 \leq \chi_c(t) \leq 1$ at time t is expressed as

$$\chi_c = 1 - \exp(-K\, t^{n_A}). \tag{4.54}$$

Here, K is the temperature-dependent crystallization rate constant and n_A the Avrami index which contains information on nucleation and growth geometry Di Lorenzo and Silvestre [1999]. For information on the limitations of the isothermal theory, the reader is kindly referred to Wunderlich [1976].

4.7.3 Algorithmic implementation of the crystallization process

The backward Euler method is used to discretize the evolution equation for the total degree of crystallinity (cf. Eq. 4.26), yielding

$$\chi = \chi_n + \Delta t\, n_A\, K_c \underbrace{\exp\!\left(\left(-\int_{t_{on}}^{t} K_c\, dt\right)^{n_A}\right)}_{(1-\chi_c)} \left(\int_{t_{on}}^{t} K_c\, dt\right)^{n_A-1} \frac{\Delta h_m}{\Delta h_f^{100}}. \tag{4.55}$$

Next, the integrals are approximated by means of the trapezoidal rule

$$\int_{t_{on}}^{t} K_c(\theta)\, dt = \underbrace{\int_{t_{on}}^{t_n} K_c(\theta)\, dt}_{\mathcal{I}_n} + \int_{t_n}^{t} K_c(\theta)\, dt \approx \mathcal{I}_n + \sum_{i=2}^{N} \frac{K_c(\theta_i) + K_c(\theta_{i-1})}{2}\,(t_i - t_{i-1}), \tag{4.56}$$

with the approximated solution of the last converged time step $\mathcal{I}_n$. The current time step Δt is further divided into N subtimesteps with linear interpolation of the temperature in-between. As soon as the onset temperature θ_{on} is reached and the crystallization process is initiated, the onset time t_{on} is determined.

4.7.4 Crystallization enthalpy and onset temperature

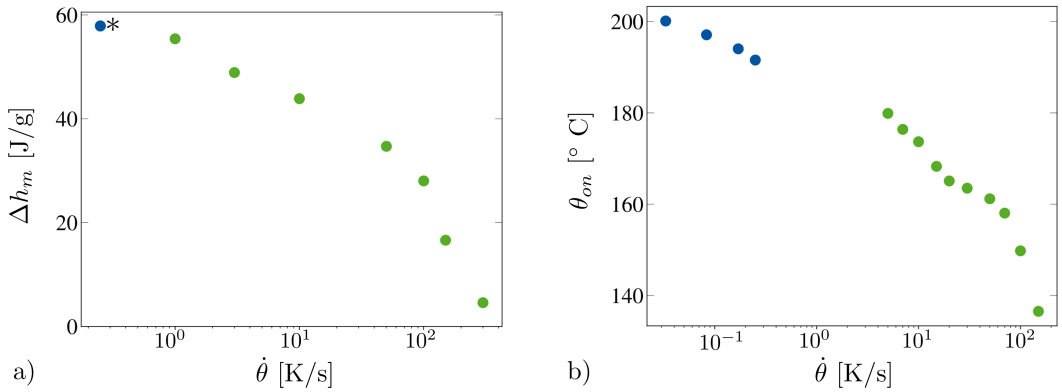

Figure 4.17: a) Enthalpy of fusion for S-DSC and F-DSC data (*For cooling rates lower than 0.25°C/s the enthalpy of fusion remained almost constant, thus the value of 57.9 J/g is adopted for all S-DSC tests), b) Crystallization onset temperature for S-DSC and F-DSC data.

4.7.5 Convergence study results

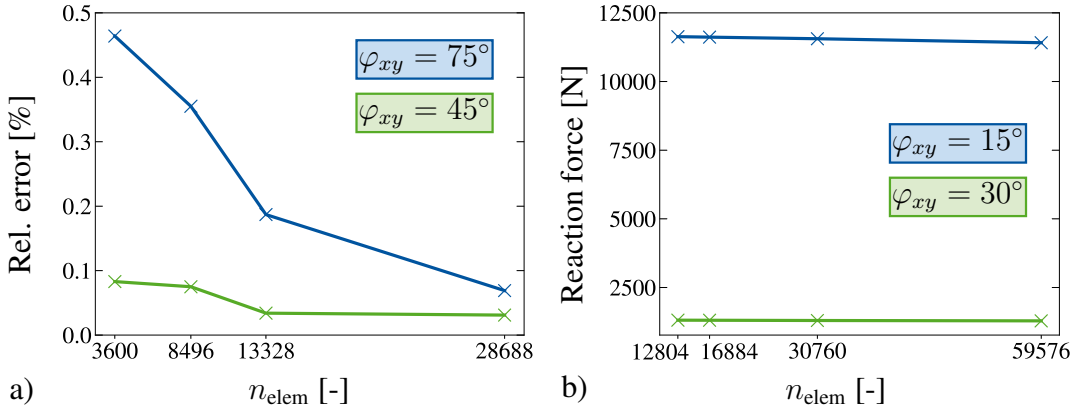

Figure 4.18: Convergence studies for a) Dogbone specimen with $\varphi_{xy} = 45°$ and $75°$ for various numbers of elements n_{elem} (1752, 3600, 8496, 13328, 28688). b) Plate with hole with $\varphi_{xy} = 15°$ and $30°$ for various numbers of elements n_{elem} (12804, 16884, 30760, 59576).

5 Conclusions and Outlook

The present dissertation was concerned with a bottom-up multi-step process across various scales for the development of a multiphysics modeling approach for fiber-reinforced polymers. In order to capture industrial (thermo-)forming processes, important corresponding coupling phenomena as well as phase transformations were taken into account, both numerically and experimentally.

Starting on the microscale, in the first article, a thermo-mechanically coupled constitutive model for polyamide 6 blends was proposed, identified, and validated. To this end, a nonlinear visco-elastic and elasto-plastic contribution were combined in a thermodynamically consistent manner. To account for the Bauschinger effect, nonlinear kinematic hardening was incorporated together with a tension-compression asymmetry in yielding, where the hydrostatic pressure sensitivity was included and the yield criterion accounts for the DOC and the temperature. The temperature field was fully coupled with the mechanical part of the model to account for self-heating effects, as well as thermal expansion and thermal softening. Finally, the material parameters were assumed to be functions of the temperature as well as the degree of crystallinity, which served as a constant input quantity. Based on the analysis of an extensive experimental study at various temperatures, comprising tensile and compression loading conditions, relaxation tests, and a thermal analysis, the temperature-dependent effect of the degree of crystallinity was investigated. To this end, a novel blending technique was introduced –compounding polyamide 6 with an amorphous co-polymer– to achieve a particularly broad range of degrees of crystallinity (ranging from $\chi = 0.15$ to $\chi = 0.29$), which are stable regarding time and temperature. Continuing with the aim of reproducing a wide range of processing conditions, strain rates over two decades, and temperatures below and above the glass transition regime were tested. The experimental study provided important insights into the complex dependencies of the material on the temperature, strain rate, and DOC and closed several gaps left in earlier works. Interestingly, apart from thermal expansion, the dependence of the mechanical material behavior on the DOC was more pronounced compared to the thermal material response. Regarding the blending technique, unfortunately, side effects were visible during testing, for example, a reduced material strength below the glass transition regime,

related to the increasing number of phase boundaries. In the future, further additives should be tested for compounding in terms of co-polymer choice and the application of compatibilizers. Moreover, the use of crystallization agents instead of blending techniques could be investigated to maintain the broad range of crystallinities without compromising the experimental results, especially below the glass transition. In order to obtain a set of material parameters for each test temperature, a successive identification procedure was proposed, testing various nonlinear functions for the relaxation time. Here, the identification proved to be more difficult compared to studies that took into account a smaller range of crystallinities. In the future, the optimization algorithms and the identification procedure could be revised to achieve more accurate results. Moreover, the presented article was mostly limited to a linear dependence on the DOC. Here, the use of nonlinear dependencies in terms of power laws or higher-order polynomial functions could improve the identification results even further. Nonetheless, the identification results were in very good agreement with the experimental data. In terms of model validation and prediction, the structural example was reflected well. However, the relaxation behavior was reproduced less accurately compared to the tensile results, which can be related to the wide range of strain rates (two decades) that were considered.

In Chapter 3, the polymeric matrix model was employed in a computational micromechanics framework, analyzing mechanical and thermal effects of fiber-reinforced polyamide 6. Therefore, firstly, an experimental study on unidirectionally glass fiber reinforced polyamide 6 was conducted, incorporating monotonic and cyclic tension, compression, and bending tests at various temperatures, strain rates, and material directions. Since the dependence on the DOC was already investigated in the previous experimental study (cf. 2), only one DOC was taken into account, which significantly reduced the overall experimental effort. The experimental study revealed the materials' direction dependency and the nonlinear influence of the fiber angle. As expected, the materials' dependence on the temperature, as well as the strain rate, was more pronounced perpendicular to the fibers. Moreover, the material was thermally characterized. In order to perform the micromechanical and microthermal analysis, repeating unit cells were generated with a focus on process automization. Several randomization methods were implemented to reflect the random fiber distribution, and their effect on the resulting material behavior was statistically evaluated. The comparison of the effective material response of the micromechanical and microthermal analysis with the experimental results showed a strong agreement and, thus, confirmed the applicability of micromechanics to generate virtual data. In order to set up a data base for model identification of the homogenized macromodel, the virtual experiments were carried out to reflect the considered range of DOCs and load cases. In the future, the present study should be extended even further to account for varying fiber

volume fractions. Accordingly, the macroscopic material model maintains its validity in the context of material optimization and altered part design.

As the final step of the hierarchical multiscale approach, a thermo-mechanically coupled constitutive theory for glass fiber reinforced polyamide 6 was proposed in Chapter 4. Therefore, the matrix framework from Chapter 2 was extended with mechanical and thermal anisotropy and characterized with the virtual and experimental data base from 3. Moreover, the crystallization kinetics were incorporated by means of a non-isothermal modification of the Avrami model to account for microstructural phase transformations. Throughout the multi-step process, the emphasis was placed on preserving the validity of the employed models across a broad spectrum of processing conditions. Consequently, both S-DSC and F-DSC results were utilized to identify the crystallization process. The results of the identification procedure generally were in good agreement with the virtual and experimental data base. However, for fiber angles between $0° \leq \varphi_{xy} \leq 45°$, it was evident that further model refinement was needed. In the future, incorporating the structural tensor in different parts of the model towards a more phenomenological approach might improve the results for inhomogeneous stress states. Nonetheless, the results were remarkable considering that only data for uniaxial stress states ($\varphi_{xy} = 0°$ and $\varphi_{xy} = 90°$) was used for model identification. In order to evaluate the capabilities of the presented constitutive framework, a series of numerical examples were conducted. The presented study investigated the influence of the fiber-induced anisotropy on the mechanical and thermal composite response, as well as the crystallization behavior, with a focus particularly on anisotropic material self-heating and anisotropic thermal expansion. Finally, a thermoforming simulation is conducted and, subsequently, compared to experimental results, demonstrating the ability of the framework to successfully predict industrial forming processes. Thus, concluding the objective of the hierarchical multiscale approach.

Overall, the aim of maintaining a wide range of processing conditions (specifically for the degree of crystallinity, strain rate, and temperature) throughout a hierarchical multiscale approach is reached. Moreover, the number of experiments could be successfully reduced by focusing on individual constituents and pivotal influencing factors on each material scale while simultaneously introducing elaborate material modeling schemes and virtual experiments where needed. Clearly, the studies on each material level will help to reduce the number of experiments in the future by indicating which effects and constituents have the highest impact. Nonetheless, further research in this field is undoubtedly necessary, as indicated in different places throughout the conclusion. Obviously, the experimental study should be extended to account for shear- and combined loading procedures, such as, for example, combined cyclic tension and compression tests. Based on these results, a more accurate or experimentally

determined yield criterion could be proposed. Moreover, the quality of the compression results must be improved by revising the current experimental set-up. In terms of the considered processing conditions, the employed test temperatures were limited to a range between 23° C and 150° C. Thus, limiting the abilities of the framework to accurately predict thermoforming at a temperature of around 230° C. Consequently, in the future, it is imperative to include experiments at temperatures close to the melting point. The corresponding tests will, however, be extremely challenging due to the increased viscosity of the material.

From a modeling perspective, the influence of the pressure on the crystallization process should be considered in future works given the predominant processing conditions during thermoforming. Moreover, inter- and intraply delamination effects are not accounted for yet. Most importantly, the current macroscopic modeling framework consists of two decoupled processes (I Thermo-chemical crystallization of the polymer melt and II Thermo-mechanical solidified composite behavior). Therefore, the presented thermoforming simulation was conducted in two separate computations. The derivation of a thermodynamically consistent thermo-chemo-mechanically coupled constitutive theory in the future would be desirable.

Apart from the aforementioned experimental and modeling considerations, especially model identification on multiple material levels proved to be very time-consuming and repetitive as a result of the wide range of process parameters. Moreover, the aforementioned proposed changes to the formulation would require recalibration. To overcome this problem and, simultaneously, reduce the time needed for model identification and verification, neural networks should be considered in the future. Promising results in the literature (see e.g. Flaschel et al. [2021, 2023]; Holthusen et al. [2024]; Boes et al. [2024]; Holthusen et al. [2025a,b]) demonstrated their ability to facilitate model development while identifying the material parameters at the same time through sufficient training. Additionally, in this way, concealed or overlooked material effects in the experimental results might be detectable. The challenge for these novel approaches certainly will be the choice of experiments that are used for training, the quality of the experimental data, and the associated postprocessing. Moreover, currently model discovery is restricted to mechanical, phenomenological single scale models. The literature review provided in the introduction already discussed several hierarchical and concurrent multiscale approaches successfully incorporating neural networks by, for example, replacing micromechanics. The application in the context of model discovery is, however, yet unexplored, similar to multiphysical material behavior incorporating coupling effects. Therefore, a key future task is to develop strategies for incorporating data from multiple scales as well as multiphysics into constitutive artificial neural networks.

List of Figures

List of Tables

Bibliography

Abdul-Hameed, H., Messager, T., Zaïri, F. and Naït-Abdelaziz, M. [2014], 'Large-strain viscoelastic–viscoplastic constitutive modeling of semi-crystalline polymers and model identification by deterministic/evolutionary approach', *Computational Materials Science* **90**, 241–252.

Aboudi, J., Arnold, S. and Bednarcyk, B. [2012], *Micromechanics of composite materials: a generalized multiscale analysis approach*, Butterworth-Heinemann.

Ahzi, S., Makradi, A., Gregory, R. and Edie, D. [2003], 'Modeling of deformation behavior and strain-induced crystallization in poly (ethylene terephthalate) above the glass transition temperature', *Mechanics of Materials* **35**(12), 1139–1148.

Al-Kinani, R. [2014], *Thermo-mechanical coupling of transversely isotropic materials using high-order finite elements*, Papierflieger-Verlag.

Ames, N., Srivastava, V., Chester, S. and Anand, L. [2009], 'A thermo-mechanically coupled theory for large deformations of amorphous polymers. Part II: Applications', *International Journal of Plasticity* **25**(8), 1495–1539.

Amin, A., Lion, A., Sekita, S. and Okui, Y. [2006], 'Nonlinear dependence of viscosity in modeling the rate-dependent response of natural and high damping rubbers in compression and shear: Experimental identification and numerical verification', *International Journal of Plasticity* **22**(9), 1610–1657.

Anand, L., Ames, N., Srivastava, V. and Chester, S. [2009], 'A thermo-mechanically coupled theory for large deformations of amorphous polymers. Part I: Formulation', *International Journal of Plasticity* **25**(8), 1474–1494.

Anand, L. and Gurtin, M. [2003], 'A theory of amorphous solids undergoing large deformations, with application to polymeric glasses', *International Journal of Solids and Structures* **40**(6), 1465–1487.

Armstrong, P. J., Frederick, C. et al. [1966], *A mathematical representation of the multiaxial Bauschinger effect*, Vol. 731 of *CEGB Report RD/B/N731*, Central Electricity Generating Board and Berkeley Nuclear Laboratories, Research & Development Department.

Arruda, E., Boyce, M. and Jayachandran, R. [1995], 'Effects of strain rate, temperature and thermomechanical coupling on the finite strain deformation of glassy polymers', *Mechanics of Materials* **19**(2-3), 193–212.

Avrami, M. [1939], 'Kinetics of phase change. I General theory', *The Journal of chemical physics* **7**(12), 1103–1112.

Avrami, M. [1940], 'Kinetics of phase change. II transformation-time relations for random distribution of nuclei', *The Journal of chemical physics* **8**(2), 212–224.

Ayoub, G., Zaïri, F., Fréderix, C., Gloaguen, J.-M., Naït-Abdelaziz, M., Seguela, R. and Lefebvre, J.-M. [2011], 'Effects of crystal content on the mechanical behaviour of polyethylene under finite strains: Experiments and constitutive modelling', *International Journal of Plasticity* **27**(4), 492–511.

Ayoub, G., Zaïri, F., Nait-Abdelaziz, M. and Gloaguen, J.-M. [2010], 'Modelling large deformation behaviour under loading–unloading of semicrystalline polymers: Application to a high density polyethylene', *International Journal of Plasticity* **26**(3), 329–347.

Bahloul, A., Doghri, I. and Adam, L. [2021], 'Linking a phase field model for polymer crystallization to full-field micromechanical simulations of semi-crystalline polymers', *Computational Materials Science* **199**, 110685.

Bahrololoumi, A., Shaafaey, M., Ayoub, G. and Dargazany, R. [2022], 'Thermal aging coupled with cyclic fatigue in cross-linked polymers: Constitutive modeling & FE implementation', *International Journal of Solids and Structures* **252**, 111800.

Bai, X., Bessa, M., Melro, A., Camanho, P., Guo, L. and Liu, W. [2015], 'High-fidelity micro-scale modeling of the thermo-visco-plastic behavior of carbon fiber polymer matrix composites', *Composite Structures* **134**, 132–141.

Barbero, E., Lonetti, P. and Sikkil, K. [2005], 'Finite element continuum damage modeling of plain weave reinforced composites', *Composites Part B: Engineering* **37**(2-3), 137–147.

Bargmann, S., Klusemann, B., Markmann, J., Schnabel, J., Schneider, K., Soyarslan, C. and Wilmers, J. [2018], 'Generation of 3d representative volume elements for heterogeneous materials: A review', *Progress in Materials Science* **96**, 322–384.

Barriere, T., Gabrion, X. and Holopainen, S. [2019], 'A compact constitutive model to describe the viscoelastic-plastic behaviour of glassy polymers: Comparison with monotonic and cyclic experiments and state-of-the-art models', *International Journal of Plasticity* **122**, 31–48.

Bednarcyk, B., Stier, B., Simon, J.-W., Reese, S. and Pineda, E. [2015], 'Meso-and micro-scale modeling of damage in plain weave composites', *Composite Structures* **121**, 258–270.

Bergström, J. S. and Boyce, M. C. [1998], 'Constitutive modeling of the large strain time-dependent behavior of elastomers', *Journal of the Mechanics and Physics of Solids* **46**(5), 931–954.

Bishara, D., Xie, Y., Liu, W. and Li, S. [2023], 'A state-of-the-art review on machine learning-based multiscale modeling, simulation, homogenization and design of materials', *Archives of computational methods in engineering* **30**(1), 191–222.

Boehler, J.-P. [1979], 'A simple derivation of representations for non-polynomial constitutive equations in some cases of anisotropy', *ZAMM-Journal of Applied Mathematics and Mechanics/Zeitschrift für Angewandte Mathematik und Mechanik* **59**(4), 157–167.

Boes, B., Simon, J.-W. and Holthusen, H. [2024], 'Accounting for plasticity: An extension of inelastic constitutive artificial neural networks', *arXiv preprint arXiv:2407.19326* .

Boisse, P., Zouari, B. and Gasser, A. [2005], 'A mesoscopic approach for the simulation of woven fibre composite forming', *Composites science and technology* **65**(3-4), 429–436.

Bonet, J. and Burton, A. [1998], 'A simple orthotropic, transversely isotropic hyperelastic constitutive equation for large strain computations', *Computer methods in applied mechanics and engineering* **162**(1-4), 151–164.

Bouvard, J.-L., Ward, D. K., Hossain, D., Nouranian, S., Marin, E. B. and Horstemeyer, M. F. [2009], 'Review of hierarchical multiscale modeling to describe the mechanical behavior of amorphous polymers', *Journal of Engineering Materials and Technology* **131**(4).

Boyce, M., Parks, D. and Argon, A. [1988], 'Large inelastic deformation of glassy polymers. Part I: Rate dependent constitutive model', *Mechanics of Materials* **7**(1), 15–33.

Boyce, M., Socrate, S. and Llana, P. [2000], 'Constitutive model for the finite deformation stress-strain behavior of poly(ethylene terephthalate) above the glass transition', *Polymer* **41**(6), 2183–2201.

Brepols, T., Wulfinghoff, S. and Reese, S. [2020], 'A gradient-extended two-surface damage-plasticity model for large deformations', *International Journal of Plasticity* **129**, 102635.

Campoy, I., Gomez, M. A. and Marco, C. [1998], 'Structure and thermal properties of blends of nylon 6 and a liquid crystal copolyester', *Polymer* **39**(25), 6279–6288.

Chadwick, P. [1974], 'Thermo-mechanics of rubberlike materials', *Philosophical Transactions of the Royal Society of London. Series A, Mathematical and Physical Sciences* **276**(1260), 371–403.

Chevalier, J., Camanho, P., Lani, F. and Pardoen, T. [2019], 'Multi-scale characterization and modelling of the transverse compression response of unidirectional carbon fiber reinforced epoxy', *Composite Structures* **209**, 160–176.

Coleman, B. and Noll, W. [1961], 'Foundations of linear viscoelasticity', *Reviews of Modern Physics* **33**(2), 239.

Cowie, J. M. G. and Arrighi, V. [2007], *Polymers: Chemistry and physics of modern materials*, CRC press.

Cundiff, K., Ayoub, G. and Benzerga, A. [2022], 'Modeling the viscoplastic behavior of a semicrystalline polymer', *International Journal of Solids and Structures* **254**, 111920.

Daniel, I., Luo, J.-J., Schubel, P. and Werner, B. [2009], 'Interfiber/interlaminar failure of composites under multi-axial states of stress', *Composites Science and Technology* **69**(6), 764–771.

Dettmer, W. and Reese, S. [2004], 'On the theoretical and numerical modelling of Armstrong-Frederick kinematic hardening in the finite strain regime', *Computer Methods in Applied Mechanics and Engineering* **193**(1-2), 87–116.

Dey, A., Welschinger, F., Schneider, M., Gajek, S. and Böhlke, T. [2023], 'Rapid inverse calibration of a multiscale model for the viscoplastic and creep behavior of short fiber-reinforced thermoplastics based on Deep Material Networks', *International Journal of Plasticity* **160**, 103484.

Di Lorenzo, M. and Silvestre, C. [1999], 'Non-isothermal crystallization of polymers', *Progress in Polymer Science* **24**(6), 917–950.

Dietz, W. [1981], 'Sphärolithwachstum in Polymeren', *Colloid and Polymer Science* **259**, 413–429.

Doerr, D., Joppich, T., Kugele, D., Henning, F. and Kaerger, L. [2019], 'A coupled thermo-mechanical approach for finite element forming simulation of continuously fiber-reinforced semi-crystalline thermoplastics', *Composites Part A: Applied Science and Manufacturing* **125**, 105508.

Dörr, D. [2021], *Simulation of the thermoforming process of UD fiber-reinforced thermoplastic tape laminates*, KIT Scientific Publishing.

dos Santos, W., De Sousa, J. and Gregorio Jr., R. [2013], 'Thermal conductivity behaviour of polymers around glass transition and crystalline melting temperatures', *Polymer Testing* **32**(5), 987–994.

dos Santos, W., Mummery, P. and Wallwork, A. [2005], 'Thermal diffusivity of polymers by the laser flash technique', *Polymer testing* **24**(5), 628–634.

Doshev, P., Tomova, D., Wutzler, A. and Radusch, H.-J. [2005], 'Morphology and mechanical properties of reactive and non-reactive COC/EOC blends', *Journal of Polymer Engineering* **25**(5), 375–392.

Doufas, A., McHugh, A. and Miller, C. [2000], 'Simulation of melt spinning including flow-induced crystallization: Part I. Model development and predictions', *Journal of Non-Newtonian Fluid Mechanics* **92**(1), 27–66.

Drucker, D. C. and Prager, W. [1952], 'Soil mechanics and plastic analysis or limit design', *Quarterly of Applied Mathematics* **10**(2), 157–165.

Dudescu, C., Botean, A. and Hardau, M. [2013], 'Thermal expansion coefficient determination of polymeric materials using digital image correlation', *Materiale plastice* **50**(1), 55–59.

Dusunceli, N. and Colak, O. [2008], 'Modelling effects of degree of crystallinity on mechanical behavior of semicrystalline polymers', *International Journal of Plasticity* **24**(7), 1224–1242.

Eckart, C. [1948], 'The thermodynamics of irreversible processes. IV. The theory of elasticity and anelasticity', *Physical Review* **73**(4), 373.

El Kadi, H. [2006], 'Modeling the mechanical behavior of fiber-reinforced polymeric composite materials using artificial neural networks—A review', *Composite structures* **73**(1), 1–23.

Farrokh, B. and Khan, A. [2010], 'A strain rate dependent yield criterion for isotropic polymers: Low to high rates of loading', *European Journal of Mechanics-A/Solids* **29**(2), 274–282.

Feder, J. [1980], 'Random sequential adsorption', *Journal of Theoretical Biology* **87**(2), 237–254.

Felder, S., Vu, N. A., Reese, S. and Simon, J.-W. [2020], 'Modeling the effect of temperature and degree of crystallinity on the mechanical response of Polyamide 6', *Mechanics of Materials* **148**, 103476.

Felder, S. and Holthusen, H. and Hesseler, S. and Pohlkemper, F. and Gries, T. and Simon, J.-W. and Reese, S. [2020], 'Incorporating crystallinity distributions into a thermo-mechanically coupled constitutive model for semi-crystalline polymers', *International Journal of Plasticity* **135**, 102751.

Felder, S., Kopic-Osmanovic, N., Holthusen, H., Brepols, T. and Reese, S. [2022], 'Thermo-mechanically coupled gradient-extended damage-plasticity modeling of metallic materials at finite strains', *International Journal of Plasticity* **148**, 103142.

Feyel, F. and Chaboche, J.-L. [2000], 'Fe2 multiscale approach for modelling the elastovis-coplastic behaviour of long fibre sic/ti composite materials', *Computer methods in applied mechanics and engineering* **183**(3-4), 309–330.

Flaschel, M., Kumar, S. and De Lorenzis, L. [2021], 'Unsupervised discovery of interpretable hyperelastic constitutive laws', *Computer Methods in Applied Mechanics and Engineering* **381**, 113852.

Flaschel, M., Kumar, S. and De Lorenzis, L. [2023], 'Automated discovery of generalized standard material models with euclid', *Computer Methods in Applied Mechanics and Engineering* **405**, 115867.

Fornes, T. D. and Paul, D. R. [2003], 'Crystallization behavior of nylon 6 nanocomposites', *Polymer* **44**(14), 3945–3961.

Gajek, S., Schneider, M. and Böhlke, T. [2021], 'An FE–DMN method for the multiscale analysis of short fiber reinforced plastic components', *Computer Methods in Applied Mechanics and Engineering* **384**, 113952.

Gajek, S., Schneider, M. and Böhlke, T. [2022], 'An FE-DMN method for the multiscale analysis of thermomechanical composites', *Computational Mechanics* **69**(5), 1087–1113.

Garofalo, F. [1963], 'An empirical relation defining the stress dependence to minimum creep rate in metals', *Transactions of the Metallurgical Society of AIME* **227**, 351.

Geers, M., Kouznetsova, V. and Brekelmans, W. [2010], 'Multi-scale computational homogenization: Trends and challenges', *Journal of computational and applied mathematics* **234**(7), 2175–2182.

Ghorbel, E. [2008], 'A viscoplastic constitutive model for polymeric materials', *International Journal of Plasticity* **24**(11), 2032–2058.

Ghorbel, E., Hadriche, I., Casalino, G. and Masmoudi, N. [2014], 'Characterization of thermomechanical and fracture behaviors of thermoplastic polymers', *Materials* **7**(1), 375–398.

Gierden, C., Kochmann, J., Waimann, J., Kinner-Becker, T., Sölter, J., Svendsen, B. and Reese, S. [2021], 'Efficient two-scale FE-FFT-based mechanical process simulation of elasto-viscoplastic polycrystals at finite strains', *Computer Methods in Applied Mechanics and Engineering* **374**, 113566.

Gierden, C., Kochmann, J., Waimann, J., Svendsen, B. and Reese, S. [2022], 'A review of FE-FFT-based two-scale methods for computational modeling of microstructure evolution and macroscopic material behavior', *Archives of Computational Methods in Engineering* **29**(6), 4115–4135.

González, C. and LLorca, J. [2007], 'Mechanical behavior of unidirectional fiber-reinforced polymers under transverse compression: Microscopic mechanisms and modeling', *Composites Science and Technology* **67**(13), 2795–2806.

Gröger, B., Hornig, A., Hoog, A. and Gude, M. [2021], 'Temperature dependent modelling of fibre-reinforced thermoplastic organo-sheet material for forming and joining process simulations', *Key Engineering Materials* **883**, 49–56.

Groß, M., Dietzsch, J. and Röbiger, C. [2019], Locking-free higher-order energy-momentum schemes for thermo-viscoelastic fiber-reinforced materials derived by the principle of virtual power, *in* 'AIP Conference Proceedings', Vol. 2116, AIP Publishing.

Groß, M., Dietzsch, J. and Röbiger, C. [2020], 'Non-isothermal energy–momentum time integrations with drilling degrees of freedom of composites with viscoelastic fiber bundles and curvature–twist stiffness', *Computer Methods in Applied Mechanics and Engineering* **365**, 112973.

Gudimetla, M. and Doghri, I. [2017], 'A finite strain thermodynamically-based constitutive framework coupling viscoelasticity and viscoplasticity with application to glassy polymers', *International Journal of Plasticity* **98**, 197–216.

Guzman-Maldonado, E., Hamila, N., Naouar, N., Moulin, G. and Boisse, P. [2016], 'Simulation of thermoplastic prepreg thermoforming based on a visco-hyperelastic model and a thermal homogenization', *Materials & Design* **93**, 431–442.

Hachour, K., Zaïri, F., Naït-Abdelaziz, M., Gloaguen, J.-M., Aberkane, M. and Lefebvre, J.-M. [2014], 'Experiments and modeling of high-crystalline polyethylene yielding under different stress states', *International Journal of Plasticity* **54**, 1–18.

Hadipeykani, M., Aghadavoudi, F. and Toghraie, D. [2020], 'A molecular dynamics simulation of the glass transition temperature and volumetric thermal expansion coefficient of thermoset polymer based epoxy nanocomposite reinforced by CNT: a statistical study', *Physica A: Statistical Mechanics and its Applications* **546**, 123995.

Hao, P., Laheri, V., Dai, Z. and Gilabert, F. [2022], 'A rate-dependent constitutive model predicting the double yield phenomenon, self-heating and thermal softening in semi-crystalline polymers', *International Journal of Plasticity* **153**, 103233.

Hao, P., Spronk, S., Van Paepegem, W. and Gilabert, F. [2022], 'Hydraulic-based testing and material modelling to investigate uniaxial compression of thermoset and thermoplastic polymers in quasistatic-to-dynamic regime', *Materials & Design* **224**, 111367.

Haward, R. and Thackray, G. [1968], 'The use of a mathematical model to describe isothermal stress-strain curves in glassy thermoplastics', *Proceedings of the Royal Society of London. Series A. Mathematical and Physical Sciences* **302**(1471), 453–472.

He, G., Liu, Y., Hammi, Y., Bammann, D. and Horstemeyer, M. [2021], 'A combined viscoelasticity-viscoplasticity-anisotropic damage model with evolving internal state variables applied to fiber reinforced polymer composites', *Mechanics of Advanced Materials and Structures* **28**(17), 1775–1796.

Herráez, M., González, C., Lopes, C., De Villoria, R. G., LLorca, J., Varela, T. and Sánchez, J. [2016], 'Computational micromechanics evaluation of the effect of fibre shape on the transverse strength of unidirectional composites: an approach to virtual materials design', *Composites Part A: Applied Science and Manufacturing* **91**, 484–492.

Hill, R. [1963], 'Elastic properties of reinforced solids: some theoretical principles', *Journal of the Mechanics and Physics of Solids* **11**(5), 357–372.

Hill, R. [1967], 'The essential structure of constitutive laws for metal composites and polycrystals', *Journal of the Mechanics and Physics of Solids* **15**(2), 79–95.

Hine, P., Lusti, H. and Gusev, A. [2002], 'Numerical simulation of the effects of volume fraction, aspect ratio and fibre length distribution on the elastic and thermoelastic properties of short fibre composites', *Composites science and technology* **62**(10-11), 1445–1453.

Hinrichsen, E., Feder, J. and Jøssang, T. [1986], 'Geometry of random sequential adsorption', *Journal of statistical physics* **44**, 793–827.

Hinton, M., Kaddour, A. and Soden, P. [2004], 'A further assessment of the predictive capabilities of current failure theories for composite laminates: comparison with experimental evidence', *Composites Science and Technology* **64**(3-4), 549–588.

Holmes, D., Loughran, J. and Suehrcke, H. [2006], 'Constitutive model for large strain deformation of semicrystalline polymers', *Mechanics of Time-Dependent Materials* **10**, 281–313.

Holthusen, H., Brepols, T. and Reese, S.and Simon, J.-W. [2020], 'An anisotropic constitutive model for fiber-reinforced materials including gradient-extended damage and plasticity at finite strains', *Theoretical and Applied Fracture Mechanics* **108**, 102642.

Holthusen, H., Rothkranz, C., Lamm, L., Brepols, T. and Reese, S. [2023], 'Inelastic material formulations based on a co-rotated intermediate configuration - Application to bioengineered tissues', *Journal of the Mechanics and Physics of Solids* **172**, 105174.

Holthusen, H.and Lamm, L., Brepols, T., Reese, S. and Kuhl, E. [2024], 'Theory and implementation of inelastic constitutive artificial neural networks', *Computer Methods in Applied Mechanics and Engineering* **428**, 117063.

Holthusen, H., Brepols, T., Linka, K. and Kuhl, E. [2025], 'Automated model discovery for tensional homeostasis: Constitutive machine learning in growth and remodeling', *Computers in Biology and Medicine* **186**, 109691.

Holthusen, H., Linka, K., Kuhl, E. and Brepols, T. [2025], 'A generalized dual potential for inelastic Constitutive Artificial Neural Networks: A JAX implementation at finite strains', *arXiv preprint arXiv:2502.17490* .

Holzapfel, G. and Gasser, T. [2001], 'A viscoelastic model for fiber-reinforced composites at finite strains: Continuum basis, computational aspects and applications', *Computer methods in applied mechanics and engineering* **190**(34), 4379–4403.

Holzapfel, G. and Simo, J. [1996], 'Entropy elasticity of isotropic rubber-like solids at finite strains', *Computer Methods in applied mechanics and engineering* **132**(1-2), 17–44.

Jenkins, P., Yang, L., Liggat, J. and Thomason, J. [2015], 'Investigation of the strength loss of glass fibre after thermal conditioning', *Journal of Materials Science* **50**, 1050–1057.

Johlitz, M., Scharding, D., Diebels, S., Retka, J. and Lion, A. [2010], 'Modelling of thermo-viscoelastic material behaviour of polyurethane close to the glass transition temperature', *ZAMM-Journal of Applied Mathematics and Mechanics/Zeitschrift für Angewandte Mathematik und Mechanik: Applied Mathematics and Mechanics* **90**(5), 387–398.

Johnsen, J., Clausen, A., Grytten, F., Benallal, A. and Hopperstad, O. [2019], 'A thermo-elasto-viscoplastic constitutive model for polymers', *Journal of the Mechanics and Physics of Solids* **124**, 681–701.

Jordan, B., Gorji, M. and Mohr, D. [2020], 'Neural network model describing the temperature- and rate-dependent stress-strain response of polypropylene', *International Journal of Plasticity* **135**, 102811.

Kalaprasad, G., Pradeep, P., Mathew, G., Pavithran, C. and Thomas, S. [2000], 'Thermal conductivity and thermal diffusivity analyses of low-density polyethylene composites reinforced with sisal, glass and intimately mixed sisal/glass fibres', *Composites Science and Technology* **60**(16), 2967–2977.

Kanit, T., Forest, S., Galliet, I., Mounoury, V. and Jeulin, D. [2003], 'Determination of the size of the representative volume element for random composites: statistical and numerical approach', *International Journal of solids and structures* **40**(13-14), 3647–3679.

Kästner, M., Obst, M., Brummund, J., Thielsch, K. and Ulbricht, V. [2012], 'Inelastic material behavior of polymers–experimental characterization, formulation and implementation of a material model', *Mechanics of Materials* **52**, 40–57.

Kehrer, L., Keursten, J., Hirschberg, V. and Böhlke, T. [2023], 'Dynamic mechanical analysis of PA 6 under hydrothermal influences and viscoelastic material modeling', *Journal of Thermoplastic Composite Materials* p. 08927057231155864.

Kelly, A., Stebner, A. and Bhattacharya, K. [2016], 'A micromechanics-inspired constitutive model for shape-memory alloys that accounts for initiation and saturation of phase transformation', *Journal of the Mechanics and Physics of Solids* **97**, 197–224.

Khan, A., Lopez-Pamies, O. and Kazmi, R. [2006], 'Thermo-mechanical large deformation response and constitutive modeling of viscoelastic polymers over a wide range of strain rates and temperatures', *International Journal of Plasticity* **22**(4), 581–601.

Khan, M., Mabrouki, T., Vidal-Sallé, E. and Boisse, P. [2010], 'Numerical and experimental analyses of woven composite reinforcement forming using a hypoelastic behaviour. Application to the double dome benchmark', *Journal of materials processing technology* **210**(2), 378–388.

Klein, N., Selivansky, D. and Marom, G. [1995], 'The effects of a nucleating agent and of fibers on the crystallization of nylon 66 matrices', *Polymer composites* **16**(3), 189–197.

Kochmann, J., Manjunatha, K., Gierden, C., Wulfinghoff, S., Svendsen, B. and Reese, S. [2019], 'A simple and flexible model order reduction method for FFT-based homogenization problems using a sparse sampling technique', *Computer Methods in Applied Mechanics and Engineering* **347**, 622–638.

Kopal, I., Harničárová, M., Valíček, J. and Kušnerová, M. [2017], 'Modeling the temperature dependence of dynamic mechanical properties and visco-elastic behavior of thermoplastic polyurethane using artificial neural network', *Polymers* **9**(10), 519.

Korelc, J. [2009], 'Automation of primal and sensitivity analysis of transient coupled problems', *Computational mechanics* **44**, 631–649.

Krairi, A. and Doghri, I. [2014], 'A thermodynamically-based constitutive model for thermoplastic polymers coupling viscoelasticity, viscoplasticity and ductile damage', *International Journal of Plasticity* **60**, 163–181.

Krairi, A., Doghri, I., Schalnat, J., Robert, G. and Van Paepegem, W. [2019], 'Thermomechanical coupling of a viscoelastic-viscoplastic model for thermoplastic polymers: Thermodynamical derivation and experimental assessment', *International Journal of Plasticity* **115**, 154–177.

Kröner, E. [1959], 'Allgemeine Kontinuumstheorie der Versetzungen und Eigenspannungen', *Archive for Rational Mechanics and Analysis* **4**, 273–334.

Kugele, D. [2020], 'Experimentelle und numerische Untersuchung des Abkühlverhaltens thermoplastischer Gelegelaminate in der Prozesskette'.

Kugele, D., Dörr, D., Wittemann, F., Hangs, B., Rausch, J., Kärger, L. and Henning, F. [2017], Modeling of the non-isothermal crystallization kinetics of polyamide 6 composites during thermoforming, *in* 'AIP Conference Proceedings', Vol. 1896, AIP Publishing.

Kulkarni, S., Loos, K., Lion, A. and Johlitz, M. [2022], Thermoforming: Identification of process-relevant ranges for strain, strain rate, cooling rate, and degree of crystallinity through preliminary simulations, *in* 'Lectures Notes on Advanced Structured Materials', Springer, pp. 303–314.

Kulkarni, S., Reuvers, M.-C., Brepols, T., Reese, S., Johlitz, M. and Lion, A. [2023], 'Characterization of crystallization kinetics in polyamide 6 with a focus on modeling the thermoforming process: experiments, modeling, simulations', *Continuum Mechanics and Thermodynamics* pp. 1–17.

Kulkarni, S., Reuvers, M., Brepols, T., Reese, S., Johlitz, M. and Lion, A. [2025], A Constitutive Model of Finite Viscoelasticity for Polyamide 6 Considering Degree of Crystallinity, *in* 'Lectures Notes on Advanced Structured Materials 3', Springer, pp. 275–300.

Le Goff, R., Poutot, G., Delaunay, D., Fulchiron, R. and Koscher, E. [2005], 'Study and modeling of heat transfer during the solidification of semi-crystalline polymers', *International Journal of Heat and Mass Transfer* **48**(25-26), 5417–5430.

Lee, E. [1969], 'Elastic-plastic deformation at finite strains', *Journal of Applied Mechanics* **36**(1), 1 – 6.

Li, H., Wang, Y., Zhang, C. and Zhang, B. [2016], 'Effects of thermal histories on interfacial properties of carbon fiber/polyamide 6 composites: Thickness, modulus, adhesion and shear strength', *Composites Part A: Applied Science and Manufacturing* **85**, 31–39.

Li, J., Romero, I. and Segurado, J. [2019], 'Development of a thermo-mechanically coupled crystal plasticity modeling framework: application to polycrystalline homogenization', *International Journal of Plasticity* **119**, 313–330.

Lin, X., Liu, Y., Chen, X., Wu, Y., Cui, L., Mao, L., Zheng, W. and Lin, M. [2020], 'Reactive compatibilization of polyamide 6/olefin block copolymer blends: Phase morphology, rheological behavior, thermal behavior, and mechanical properties', *Materials* **13**(5), 1146.

Lion, A. [1997*a*], 'On the large deformation behaviour of reinforced rubber at different temperatures', *Journal of the Mechanics and Physics of Solids* **45**(11-12), 1805–1834.

Lion, A. [1997*b*], 'A physically based method to represent the thermo-mechanical behaviour of elastomers', *Acta Mechanica* **123**(1-4), 1–25.

Lion, A. [1998], 'Thixotropic behaviour of rubber under dynamic loading histories: experiments and theory', *Journal of the Mechanics and Physics of Solids* **46**(5), 895–930.

Lion, A. [1999], 'Strain-dependent dynamic properties of filled rubber: a non-linear viscoelastic approach based on structural variables', *Rubber chemistry and technology* **72**(2), 410–429.

Lion, A. [2000], 'Constitutive modelling in finite thermoviscoplasticity: A physical approach based on nonlinear rheological models', *International Journal of Plasticity* **16**(5), 469–494.

Lion, A. and Johlitz, M. [2016], 'A thermodynamic approach to model the caloric properties of semicrystalline polymers', *Continuum Mechanics and Thermodynamics* **28**, 799–819.

Lion, A., Liebl, C., Kolmeder, S. and Peters, J. [2010], 'Representation of the glass-transition in mechanical and thermal properties of glass-forming materials: A three-dimensional theory based on thermodynamics with internal state variables', *Journal of the Mechanics and Physics of Solids* **58**(9), 1338–1360.

Lion, A., Mittermeier, C. and Johlitz, M. [2017], 'Heat capacities and volumetric changes in the glass transition range: a constitutive approach based on the standard linear solid', *Continuum Mechanics and Thermodynamics* **29**, 1061–1079.

Lion, A., Peters, J. and Kolmeder, S. [2011], 'Simulation of temperature history-dependent phenomena of glass-forming materials based on thermodynamics with internal state variables', *Thermochimica acta* **522**(1-2), 182–193.

Lu, S. and Pister, K. [1975], 'Decomposition of deformation and representation of the free energy function for isotropic thermoelastic solids', *International Journal of Solids and Structures* **11**(7-8), 927–934.

Lubliner, J. [1985], 'A model of rubber viscoelasticity', *Mechanics Research Communications* **12**(2), 93–99.

Luo, H., Fu, Z., Jing, B., Shi, J., Zou, X. and Dai, W. [2009], 'Tensile behaviors of polyamide 6/UHLE blends', *Journal of Materials Science* **44**, 3694–3701.

Machado, M., Murenu, L., Fischlschweiger, M. and Major, Z. [2016], 'Analysis of the thermomechanical shear behaviour of woven-reinforced thermoplastic-matrix composites during forming', *Composites Part A: Applied Science and Manufacturing* **86**, 39–48.

Maldonado, E., Bigot, N., Denis, Y. and Hamila, N. [2025], Thermomechanical modeling and experimental characterization of continuous fiber-reinforced thermoplastic composites at forming temperatures, *in* 'Advanced Structural Textile Composites Forming', Elsevier, pp. 355–388.

Manaia, J. P., Pires, F. A., de Jesus, A. M. P. and Wu, S. [2020], 'Mechanical response of three semi crystalline polymers under different stress states: Experimental investigation and modelling', *Polymer Testing* **81**, 106156.

Manchado, M., Blagiotti, J., Torre, L. and Kenny, J. [2000], 'Effects of reinforcing fibers on the crystallization of polypropylene', *Polymer Engineering & Science* **40**(10), 2194–2204.

Mandelkern, L., Quinn, F. and Flory, P. [1954], 'Crystallization kinetics in high polymers. I. Bulk polymers', *Journal of applied Physics* **25**(7), 830–839.

Martonová, D., Peirlinck, M., Linka, K., Holzapfel, G., Leyendecker, S. and Kuhl, E. [2024], 'Automated model discovery for human cardiac tissue: Discovering the best model and parameters', *Computer Methods in Applied Mechanics and Engineering* **428**, 117078.

Maurel-Pantel, A., Baquet, E., Bikard, J., Bouvard, J. and Billon, N. [2015], 'A thermo-mechanical large deformation constitutive model for polymers based on material network description: Application to a semi-crystalline polyamide 66', *International Journal of Plasticity* **67**, 102–126.

Mears, D. R., Pae, K. D. and Sauer, J. A. [1969], 'Effects of hydrostatic pressure on the mechanical behavior of polyethylene and polypropylene', *Journal of Applied Physics* **40**(11), 4229–4237.

Mehdipour, H., Camanho, P. and Belingardi, G. [2019], 'Elasto-plastic constitutive equations for short fiber reinforced polymers', *Composites Part B: Engineering* **165**, 199–214.

Melro, A., Camanho, P., Pires, F. A. and Pinho, S. [2013*a*], 'Micromechanical analysis of polymer composites reinforced by unidirectional fibres: Part II–Micromechanical analyses', *International Journal of Solids and Structures* **50**(11-12), 1906–1915.

Melro, A., Camanho, P., Pires, F. and Pinho, S. [2013*b*], 'Micromechanical analysis of polymer composites reinforced by unidirectional fibres: Part I–Constitutive modelling', *International Journal of Solids and Structures* **50**(11-12), 1897–1905.

Menczel, J. D. and Prime, R. B. [2009], *Thermal analysis of polymers: Fundamentals and applications*, John Wiley & Sons.

Menyhárd, A. and Varga, J. [2006], 'The effect of compatibilizers on the crystallisation, melting and polymorphic composition of β-nucleated isotactic polypropylene and polyamide 6 blends', *European polymer journal* **42**(12), 3257–3268.

Miehe, C. [2002], 'Strain-driven homogenization of inelastic microstructures and composites based on an incremental variational formulation', *International Journal for numerical methods in engineering* **55**(11), 1285–1322.

Mudra, I. and Balázs, G. [1998], 'Comparative study of efficiency of nucleating agents in PA-6', *Journal of Thermal Aanalysis and Calorimetry* **52**, 355–361.

Müller, S., Kästner, M., Brummund, J. and Ulbricht, V. [2011], 'A nonlinear fractional viscoelastic material model for polymers', *Computational Materials Science* **50**(10), 2938–2949.

Mulliken, A. and Boyce, M. [2006], 'Mechanics of the rate-dependent elastic–plastic deformation of glassy polymers from low to high strain rates', *International Journal of Solids and Structures* **43**(5), 1331–1356.

Nagarajan, K., Levon, K. and Myerson, A. [2000], 'Nucleating agents in polypropylene', *Journal of thermal analysis and calorimetry* **59**(1-2), 497–508.

Nakamura, K., Katayama, K. and Amano, T. [1973], 'Some aspects of nonisothermal crystallization of polymers. II. Consideration of the isokinetic condition', *Journal of Applied Polymer Science* **17**(4), 1031–1041.

Narayan, S. and Anand, L. [2021], 'Fracture of amorphous polymers: A gradient-damage theory', *Journal of the Mechanics and Physics of Solids* **146**, 104164.

Naya, F., González, C., Lopes, C., Van der Veen, S. and Pons, F. [2017], 'Computational micromechanics of the transverse and shear behavior of unidirectional fiber reinforced polymers including environmental effects', *Composites Part A: Applied Science and Manufacturing* **92**, 146–157.

Nguyen, V.-D., Lani, F., Pardoen, T., Morelle, X. P. and Noels, L. [2016], 'A large strain hyperelastic viscoelastic-viscoplastic-damage constitutive model based on a multi-mechanism non-local damage continuum for amorphous glassy polymers', *International Journal of Solids and Structures* **96**, 192–216.

Nguyen, V., Stroeven, M. and Sluys, L. [2011], 'Multiscale continuous and discontinuous modeling of heterogeneous materials: a review on recent developments', *Journal of Multiscale Modelling* **3**(04), 229–270.

Nikolov, S. and Doghri, I. [2000], 'A micro/macro constitutive model for the small-deformation behavior of polyethylene', *Polymer* **41**(5), 1883–1891.

Nikolov, S., Doghri, I., Pierard, O., Zealouk, L. and Goldberg, A. [2002], 'Multi-scale constitutive modeling of the small deformations of semi-crystalline polymers', *Journal of the Mechanics and Physics of Solids* **50**(11), 2275–2302.

Norton, F. H. [1929], 'The creep of steel at high temperatures', *(No Title)* .

Omairey, S., Dunning, P. and Sriramula, S. [2019], 'Development of an ABAQUS plugin tool for periodic RVE homogenisation', *Engineering with Computers* **35**, 567–577.

Özdemir, I., Brekelmans, W. and Geers, M. [2007], 'Computational homogenization for heat conduction in heterogeneous solids', *International journal for numerical methods in engineering* **73**(2), 185–204.

Özdemir, I., Brekelmans, W. and Geers, M. [2008], 'Fe2 computational homogenization for the thermo-mechanical analysis of heterogeneous solids', *Computer Methods in Applied Mechanics and Engineering* **198**(3-4), 602–613.

Ozkoc, G., Bayram, G. and Bayramli, E. [2007], 'Effects of olefin-based compatibilizers on the morphology, thermal and mechanical properties of ABS/polyamide-6 blends', *Journal of Applied Polymer Science* **104**(2), 926–935.

Parodi, E., Peters, G. W. M. and Govaert, L. E. [2018], 'Prediction of plasticity-controlled failure in polyamide 6: Influence of temperature and relative humidity', *Journal of Applied Polymer Science* **135**(11), 45942.

Perin, D., Dorigato, A. and Pegoretti, A. [2023], 'Thermoplastic self-healing polymer blends for structural composites: Development of polyamide 6 and cyclic olefinic copolymer blends', *Journal of Applied Polymer Science* **140**(16), e53751.

Pisani, W., Radue, M., Chinkanjanarot, S., Bednarcyk, B., Pineda, E., Waters, K., Pandey, R., King, J. and Odegard, G. [2019], 'Multiscale modeling of peek using reactive molecular dynamics modeling and micromechanics', *Polymer* **163**, 96–105.

Poggenpohl, L., Brepols, T., Holthusen, H., Wulfinghoff, S. and Reese, S. [2021], 'Towards brittle damage in carbon fiber reinforced plastics: A gradient extended approach', *Composite Structures* **255**, 112911.

Poggenpohl, L., Holthusen, H. and Simon, J.-W. [2022*a*], 'Failure zone homogenization at mode ii and mixed mode loading including gradient-extended damage and interface debonding at finite strains', *Composite Structures* **298**, 115997.

Poggenpohl, L., Holthusen, H. and Simon, J.-W. [2022*b*], 'Failure zone homogenization for modeling damage-and debonding-induced softening in composites including gradient-extended damage at finite strains', *International Journal of Plasticity* **154**, 103277.

Popa, C., Fleischhauer, R., Schneider, K. and Kaliske, M. [2014], 'Formulation and implementation of a constitutive model for semicrystalline polymers', *International Journal of Plasticity* **61**, 128–156.

Qi, Z., Hu, N., Li, G., Zeng, D. and Su, X. [2019], 'Constitutive modeling for the elastic-viscoplastic behavior of high density polyethylene under cyclic loading', *International Journal of Plasticity* **113**, 125–144.

Rabiej, M. and Rabiej, S. [2021], 'Application of the artificial neural network for identification of polymers based on their x-ray diffraction curves', *Computational Materials Science* **186**, 110042.

Radermacher, A. and Reese, S. [2016], 'POD-based model reduction with empirical interpolation applied to nonlinear elasticity', *International Journal for Numerical Methods in Engineering* **107**(6), 477–495.

Rae, P. J., Brown, E. N. and Orler, E. B. [2007], 'The mechanical properties of poly (ether-ether-ketone)(peek) with emphasis on the large compressive strain response', *Polymer* **48**(2), 598–615.

Raju, K., Tay, T.-E. and Tan, V. [2021], 'A review of the fe 2 method for composites', *Multiscale and Multidisciplinary Modeling, Experiments and Design* **4**, 1–24.

Reese, S. [2003*a*], 'A micromechanically motivated material model for the thermo-viscoelastic material behaviour of rubber-like polymers', *International Journal of Plasticity* **19**(7), 909–940.

Reese, S. [2003*b*], 'Meso-macro modelling of fibre-reinforced rubber-like composites exhibiting large elastoplastic deformation', *International Journal of Solids and Structures* **40**(4), 951–980.

Reese, S., Brepols, T., Fassin, M., Poggenpohl, L. and Wulfinghoff, S. [2021], 'Using structural tensors for inelastic material modeling in the finite strain regime–a novel approach to anisotropic damage', *Journal of the Mechanics and Physics of Solids* **146**, 104174.

Reese, S. and Christ, D. [2008], 'Finite deformation pseudo-elasticity of shape memory alloys–Constitutive modelling and finite element implementation', *International Journal of Plasticity* **24**(3), 455–482.

Reese, S. and Govindjee, S. [1997], 'Theoretical and numerical aspects in the thermo-viscoelastic material behaviour of rubber-like polymers', *Mechanics of Time-Dependent Materials* **1**(4), 357–396.

Reese, S. and Govindjee, S. [1998], 'A theory of finite viscoelasticity and numerical aspects', *International Journal of Solids and Structures* **35**(26-27), 3455–3482.

Reese, S., Raible, T. and Wriggers, P. [2001], 'Finite element modelling of orthotropic material behaviour in pneumatic membranes', *International journal of solids and structures* **38**(52), 9525–9544.

Regrain, C., Laiarinandrasana, L., Toillon, S. and Saï, K. [2009], 'Multi-mechanism models for semi-crystalline polymer: Constitutive relations and finite element implementation', *International Journal of Plasticity* **25**(7), 1253–1279.

Reuvers, M., Kulkarni, S., Boes, B., Felder, S., Wutzler, A., Johlitz, M., Lion, A., Brepols, T. and Reese, S. [2024], 'A thermo-mechanically coupled constitutive model for semi-crystalline polymers at finite strains: Mechanical and thermal characterization of polyamide 6 blends', *Continuum Mechanics and Thermodynamics* **36**, 657–698.

Reuvers, M., Dannenberg, C., Kulkarni, S., Loos, K., Johlitz, M., Lion, A., Reese, S. and Brepols, T. [2024], 'Experimental investigation and micromechanical analysis of glass fiber reinforced polyamide 6', *Mechanics of Materials* **199**, 105144.

Rezasefat, M., Mostafavi, Y., Ma, D. and Manes, A. [2023], 'A hybrid micro-macro mechanical damage model to consider the influence of resin-rich zones on the transverse tensile behaviour of unidirectional composites', *Composite Structures* **308**, 116714.

Richeton, J., Ahzi, S., Vecchio, K., Jiang, F. and Adharapurapu, R. [2006], 'Influence of temperature and strain rate on the mechanical behavior of three amorphous polymers: Characterization and modeling of the compressive yield stress', *International Journal of Solids and Structures* **43**(7-8), 2318–2335.

Richeton, J., Ahzi, S., Vecchio, K., Jiang, F. and Makradi, A. [2007], 'Modeling and validation of the large deformation inelastic response of amorphous polymers over a wide range of temperatures and strain rates', *International Journal of Solids and Structures* **44**(24), 7938–7954.

Ricker, A., Gierig, M. and Wriggers, P. [2023], 'Multiplicative, Non-Newtonian Viscoelasticity Models for Rubber Materials and Brain Tissues: Numerical Treatment and Comparative Studies', *Archives of Computational Methods in Engineering* pp. 1–39.

Rodriguez, A., Mansoor, B., Ayoub, G., Colin, X. and Benzerga, A. [2020], 'Effect of UV-aging on the mechanical and fracture behavior of low density polyethylene', *Polymer Degradation and Stability* **180**, 109185.

Román, A., Qin, S., Rodríguez, J., González, L., Zavala, V. and Osswald, T. [2022], 'Natural rubber blend optimization via data-driven modeling: The implementation for reverse engineering', *Polymers* **14**(11), 2262.

Saba, N. and Jawaid, M. [2018], 'A review on thermomechanical properties of polymers and fibers reinforced polymer composites', *Journal of Industrial and Engineering Chemistry* **67**, 1–11.

Schmid, E. and Boas, W. [2013], *Kristallplastizität mit besonderer Berücksichtigung der Metalle*, Vol. 17, Springer-Verlag.

Schmidt, A., Gierden, C., Fechte-Heinen, R., Reese, S. and Waimann, J. [2025], 'Efficient thermo-mechanically coupled and geometrically nonlinear two-scale FE-FFT-based modeling of elasto-viscoplastic polycrystalline materials', *Computer Methods in Applied Mechanics and Engineering* **435**, 117648.

Schmidt, A., Gierden, C., Waimann, J., Svendsen, B. and Reese, S. [2023], 'Two-scale FE-FFT-based thermo-mechanically coupled modeling of elasto-viscoplastic polycrystalline materials at finite strains', *PAMM* **22**(1), e202200172.

Schneider, M. [2021], 'A review of nonlinear fft-based computational homogenization methods', *Acta Mechanica* **232**(6), 2051–2100.

Schröder, J. [2014], A numerical two-scale homogenization scheme: the FE2-method, *in* 'Plasticity and beyond: microstructures, crystal-plasticity and phase transitions', Springer, pp. 1–64.

Segal, L. [1979], 'The thermal expansion of reinforced nylon-6 composites through the matrix glass transition temperature', *Polymer Engineering & Science* **19**(5), 365–372.

Selmi, A., Doghri, I. and Adam, L. [2011], 'Micromechanical simulations of biaxial yield, hardening and plastic flow in short glass fiber reinforced polyamide', *International Journal of Mechanical Sciences* **53**(9), 696–706.

Sevenois, R., Hao, P., Van Paepegem, W. and Gilabert, F. [2022], 'Numerical study on the effect of matrix self-heating on the thermo-visco-plastic response of continuous fiber-reinforced polymers under transverse tensile loading', *Polymers* **14**(10), 1941.

Shan, G.-F., Yang, W., Yang, M., Xie, B., Feng, J. and Fu, Q. [2007], 'Effect of temperature and strain rate on the tensile deformation of polyamide 6', *Polymer* **48**(10), 2958–2968.

Sharma, P., Sambale, A., Stommel, M., Maisl, M., Herrmann, H.-G. and Diebels, S. [2020], 'Moisture transport in PA6 and its influence on the mechanical properties', *Continuum Mechanics and Thermodynamics* **32**, 307–325.

Shen, F., Kang, G., Lam, Y., Liu, Y. and Zhou, K. [2019], 'Thermo-elastic-viscoplastic-damage model for self-heating and mechanical behavior of thermoplastic polymers', *International Journal of Plasticity* **121**, 227–243.

Shepherd, J., McDowell, D. L. and Jacob, K. [2006], 'Modeling morphology evolution and mechanical behavior during thermo-mechanical processing of semi-crystalline polymers', *Journal of the Mechanics and Physics of Solids* **54**(3), 467–489.

Shojaei, A. and Li, G. [2013], 'Viscoplasticity analysis of semicrystalline polymers: a multiscale approach within micromechanics framework', *International Journal of Plasticity* **42**, 31–49.

Sidoroff, F. [1974], 'Un modèle viscoélastique non linéaire avec configuration intermédiaire.', *Journal de mécanique* **13**, 679 – 713.

Singer, G., Sinn, G., Lichtenegger, H., Veigel, S., Zecchini, M. and Wan-Wendner, R. [2019], 'Evaluation of in-situ shrinkage and expansion properties of polymer composite materials for adhesive anchor systems by a novel approach based on digital image correlation', *Polymer Testing* **79**, 106035.

Spahn, J., Andrä, H., Kabel, M. and Müller, R. [2014], 'A multiscale approach for modeling progressive damage of composite materials using fast fourier transforms', *Computer Methods in Applied Mechanics and Engineering* **268**, 871–883.

Spencer, A. J. M. [1971], 'Part III. Theory of invariants', *Continuum Physics* **1**, 239–353.

Srivastava, V., Chester, S., Ames, N. and Anand, L. [2010], 'A thermo-mechanically-coupled large-deformation theory for amorphous polymers in a temperature range which spans their glass transition', *International Journal of Plasticity* **26**(8), 1138–1182.

Stein, E. and Sagar, G. [2008], 'Convergence behavior of 3D finite elements for Neo-Hookean material', *Engineering Computations* **25**(3), 220–232.

Stier, B., Simon, J.-W. and Reese, S. [2015*a*], 'Comparing experimental results to a numerical meso-scale approach for woven fiber reinforced plastics', *Composite structures* **122**, 553–560.

Stier, B., Simon, J.-W. and Reese, S. [2015*b*], 'Numerical and experimental investigation of the structural behavior of a carbon fiber reinforced ankle-foot orthosis', *Medical Engineering & Physics* **37**(5), 505–511.

Stojanovic, R., Djuric, S. and Vujosevic, L. [1964], 'On finite thermal deformations', *Archiwum Mechaniki Stosowanej* **16**, 103–108.

Strobl, G. R. [1997], *The physics of polymers*, Vol. 2, Springer.

Taç, V., Linka, K., Sahli-Costabal, F., Kuhl, E. and Tepole, A. [2024], 'Benchmarking physics-informed frameworks for data-driven hyperelasticity', *Computational mechanics* **73**(1), 49–65.

Temizer, I. and Wriggers, P. [2011], 'Homogenization in finite thermoelasticity', *Journal of the Mechanics and Physics of Solids* **59**(2), 344–372.

Tian, W., Qi, L., Chao, X., Liang, J. and Fu, M. [2019], 'Numerical evaluation on the effective thermal conductivity of the composites with discontinuous inclusions: Periodic boundary condition and its numerical algorithm', *International Journal of Heat and Mass Transfer* **134**, 735–751.

Tröger, J.-A. and Hartmann, S. [2022], 'Identification of the thermal conductivity tensor for transversely isotropic materials', *GAMM-Mitteilungen* **45**(3-4), e202200013.

Tschoegl, N. [1971], Failure surfaces in principal stress space, *in* 'Journal of Polymer Science Part C: Polymer symposia', Vol. 32, Wiley Online Library, pp. 239–267.

Turnbull, D. and Fisher, J. [1949], 'Rate of nucleation in condensed systems', *The Journal of chemical physics* **17**(1), 71–73.

Uchida, M. and Tada, N. [2013], 'Micro-, meso- to macroscopic modeling of deformation behavior of semi-crystalline polymer', *International Journal of Plasticity* **49**, 164–184.

Uchida, M., Yoshida, T., Okada, E., Touji, M. and Kaneko, Y. [2024], 'Mechanical modeling of polyamide 6 obtained from different thermal histories', *Polymer* **296**, 126770.

Unger, J. and Könke, C. [2008], 'Coupling of scales in a multiscale simulation using neural networks', *Computers & Structures* **86**(21-22), 1994–2003.

Unger, J. and Könke, C. [2009], 'Neural networks as material models within a multiscale approach', *Computers & structures* **87**(19-20), 1177–1186.

Van der Sluis, O., Schreurs, P., Brekelmans, W. and Meijer, H. [2000], 'Overall behaviour of heterogeneous elastoviscoplastic materials: effect of microstructural modelling', *Mechanics of Materials* **32**(8), 449–462.

Van Dommelen, J., Parks, D., Boyce, M., Brekelmans, W. and Baaijens, F. [2003], 'Micromechanical modeling of the elasto-viscoplastic behavior of semi-crystalline polymers', *Journal of the Mechanics and Physics of Solids* **51**(3), 519–541.

van Dommelen, J., Poluektov, M., Sedighiamiri, A. and Govaert, L. [2017], 'Micromechanics of semicrystalline polymers: Towards quantitative predictions', *Mechanics Research Communications* **80**, 4–9.

Vanclooster, K., Lomov, S. and Verpoest, I. [2009], 'Experimental validation of forming simulations of fabric reinforced polymers using an unsymmetrical mould configuration', *Composites Part A: Applied Science and Manufacturing* **40**(4), 530–539.

Varandas, L., Catalanotti, G., Melro, A., Tavares, R. and Falzon, B. [2020], 'Micromechanical modelling of the longitudinal compressive and tensile failure of unidirectional composites: The effect of fibre misalignment introduced via a stochastic process', *International journal of solids and structures* **203**, 157–176.

Vaughan, T. and McCarthy, C. [2010], 'A combined experimental–numerical approach for generating statistically equivalent fibre distributions for high strength laminated composite materials', *Composites Science and Technology* **70**(2), 291–297.

Vladimirov, I., Pietryga, M. and Reese, S. [2008], 'On the modelling of non-linear kinematic hardening at finite strains with application to springback - Comparison of time integration algorithms', *International Journal for Numerical Methods in Engineering* **75**(1), 1–28.

Vladimirov, I., Pietryga, M. and Reese, S. [2010], 'Anisotropic finite elastoplasticity with nonlinear kinematic and isotropic hardening and application to sheet metal forming', *International Journal of Plasticity* **26**(5), 659–687.

Vogler, M., Rolfes, R. and Camanho, P. [2013], 'Modeling the inelastic deformation and fracture of polymer composites–Part I: Plasticity model', *Mechanics of Materials* **59**, 50–64.

Vujošević, L. and Lubarda, V. [2002], 'Finite-strain thermoelasticity based on multiplicative decomposition of deformation gradient', *Theoretical and applied mechanics* (28-29), 379–399.

Wang, J., Peng, L., Deng, Y., Lai, X., Fu, M. and Ni, J. [2019], 'A finite strain thermodynamically-based constitutive modeling and analysis of viscoelastic-viscoplastic deformation behavior of glassy polymers', *International Journal of Plasticity* **122**, 135–163.

Wang, W., Dai, Y., Zhang, C., Gao, X. and Zhao, M. [2016], 'Micromechanical modeling of fiber-reinforced composites with statistically equivalent random fiber distribution', *Materials* **9**(8), 624.

Weiss, J. A., Maker, B. and Govindjee, S. [1996], 'Finite element implementation of incompressible, transversely isotropic hyperelasticity', *Computer methods in applied mechanics and engineering* **135**(1-2), 107–128.

Wicht, D., Schneider, M. and Böhlke, T. [2021], 'Computing the effective response of heterogeneous materials with thermomechanically coupled constituents by an implicit fast fourier transform-based approach', *International Journal for Numerical Methods in Engineering* **122**(5), 1307–1332.

Wulfinghoff, S., Fassin, M. and Reese, S. [2017], 'A damage growth criterion for anisotropic damage models motivated from micromechanics', *International Journal of Solids and Structures* **121**, 21–32.

Wunderlich, B. [1976], *Macromolecular physics, Vol. 2: crystal nucleation, growth, annealing*, Academic Press New York.

Wunderlich, B. [2003], 'Reversible crystallization and the rigid–amorphous phase in semicrystalline macromolecules', *Progress in polymer science* **28**(3), 383–450.

Xie, R., Weisen, A., Lee, Y., Aplan, M., Fenton, A., Masucci, A., Kempe, F., Sommer, M., Pester, C., Colby, R. et al. [2020], 'Glass transition temperature from the chemical structure of conjugated polymers', *Nature communications* **11**(1), 893.

Yoshida, T., Nakane, T., Uchida, M. and Kaneko, Y. [2022], 'Mechanical modeling and testing of different polyamides considering molecular chain structure, crystallinity, and large strains', *International Journal of Solids and Structures* **239**, 111419.

Young, R. and Lovell, P. [2011], *Introduction to polymers*, CRC press.

Zhang, J. and Rychlewski, J. [1990], 'Structural tensors for anisotropic solids', *Archives of Mechanics* **42**(3), 267–277.

Ziabicki, A. [1976], *Fundamentals of fibre information: the science of fibre spinning and drawing*, London: Wiley.

Zinet, M., El Otmani, R., Boutaous, M. and Chantrenne, P. [2010], 'Numerical modeling of nonisothermal polymer crystallization kinetics: Flow and thermal effects', *Polymer Engineering & Science* **50**(10), 2044–2059.